

1 **Alpacas in Space - An Autobiography**
2

3 By
4

5 JOSEPH LEVINE
6 DISSERTATION
7

8 Submitted in partial satisfaction of the requirements for the degree of
9
10 DOCTOR OF PHILOSOPHY

11 in
12

13 Physics
14

15 in the
16

17 OFFICE OF GRADUATE STUDIES
18
19 of the
20

21 UNIVERSITY OF CALIFORNIA
22

23 DAVIS
24

25 Approved:
26

27 J. Anthony Tyson, Chair
28

30 S. Mani Tripathi
31

33 Brian Kolner
34

36 Committee in Charge
37

38 2025

39

Abstract

40 comment: This is my qual write up and is here only as a place holder. Don't edit this
41 yet It is believed that a large majority of the mass in the universe comes from an as yet
42 undetermined source. This claim stems originally from work performed in 1933 by Fritz
43 Zwicky who noticed a discrepancy between measured velocities of galaxies within the Coma
44 Cluster and velocities predicted by applying the virial theorem. He wrote

45 *If this [experimental result] would be confirmed we would get the surprising result
46 that dark matter is present in much greater amount than luminous matter [1].*

47 Vera Rubin furthered this work by measuring velocities of stars rotating in the M31 galaxy
48 and concluded there must be additional non-luminous mass (originally published in [2],
49 and shown in Fig.0.1). Studies of other phenomena, such as lensing (see [**lensing2**]) have
50 confirmed the existence of this dark matter, and it is currently one of the major mysteries
51 in modern physics.

52 Since the 1980's, the leading theories have consisted of an unknown species of elementary
53 particle. The search for weakly interacting massive particles (WIMPs) have dominated
54 the budgets and schedules of the dark matter search effort but have yet to provide any
55 experimental evidence.

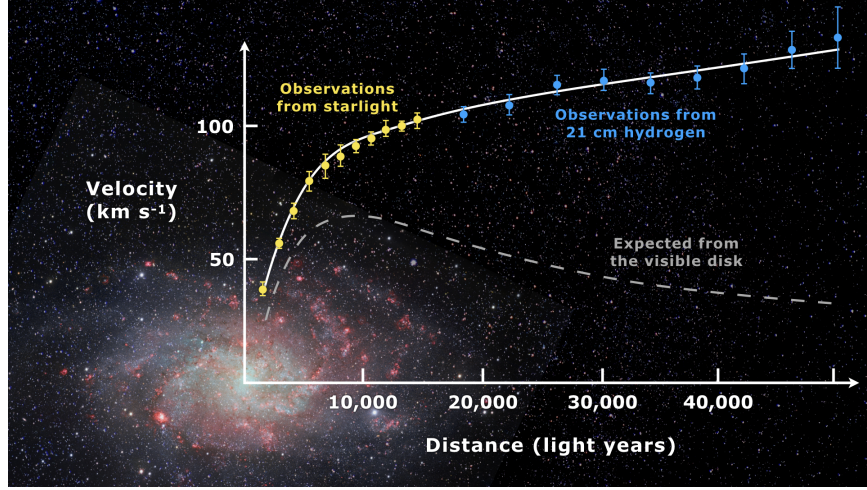


Figure 0.1: Expected vs observed velocity distributions of M33

56 In light of this, the 2017 community report on dark matter [3] highlights a need for a multi-
 57 experiment program in which many small scale experiments (< \$10M) split up to cover the
 58 vast landscape of potential dark matter candidates (see Fig. 0.2). Since very little is known
 59 about the dark matter, it is a playground for theoretical physicists to invent candidates.

60 This overwhelming search should be narrowed down.

61 The enormous mass range splits nicely into two regimes; waves and particles. At a mass of
 62 order 1eV the inter-particle spacing \approx wavelength. Lighter than this it is more convenient
 63 to think of dark matter as a wave. Alternatively, dark matter candidates heavier than this
 64 are more conveniently modeled as exhibiting particle-like behavior. The Dark E-Field Radio
 65 experiment searches for dark photons in the nano- to milli-eV mass range where dark matter
 66 is best described as a wave. This property means one would search for a dark photon using
 67 wave-like detectors, e.g. antennas.

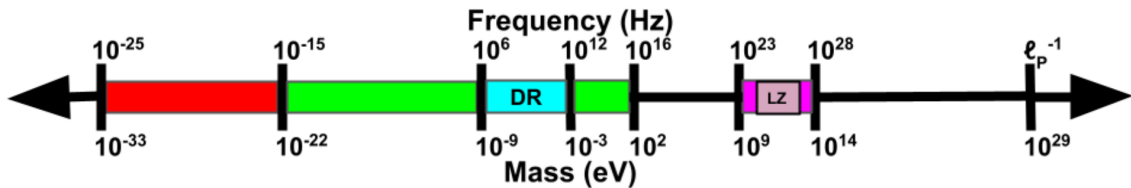


Figure 0.2: Cartoon depicting the mass scales over which dark matter may be found. Corresponding frequencies shown above. At heavy mass scales $> \mathcal{O}(1\text{ eV})$ the dark matter would behave like a particle, while on the lighter end it would behave like a wave. The Dark Radio Experiment searches at radio/microwave frequencies (blue) for a hidden photon using an antenna and spectrum analyzer. LUX-ZEPLIN Experiment (LZ) also shown.

68 comment: Discussion from paper. Good to pull from

69 This experiment extends the earlier results of our pilot experiment [4], which was designed to
 70 demonstrate feasibility of the Dark E-field Radio technique. The pilot experiment was run
 71 over the same frequency range as the experiment reported here, but did not make use of the
 72 calibration techniques to approximate statistical uniformity, nor did it fully account for the
 73 resonant enhancement of the cavity. In this paper we describe how we randomize antenna
 74 positions by moving it many times during the run. In addition, we detail EM simulations
 75 which give the average relation between the E-field at the antenna and the voltage into
 76 the LNA, accounting for resonant enhancement of the cavity. A 2^{24} -point FFT produces a
 77 spectrum dominated by background thermal noise which varies gradually with frequency.

78 We then searched over the full 50-300 MHz frequency span for any narrow-band dark photon
 79 signal of at least 5% global significance. Optimally filtering the resulting spectrum, we detect
 80 a single candidate which we are able to identify as interference, likely from our electronics.

81 Rejecting this candidate, we obtain a null result for any signal which could be attributed
82 to the dark photon in our frequency range. The resulting 95% exclusion limit for the dark
83 photon kinetic coupling ϵ is then obtained over this mass range of 0.2-1.2 μeV . Our null result
84 is a factor of ≈ 100 more sensitive than current astrophysical limits.

85 Ultimately, we can apply this detection technique at higher frequencies, ultimately going up
86 to the sub-THz band. This will require new antennas and microwave electronics. Cryogenic
87 cavities and LNAs could improve our sensitivity by an order of magnitude.

88 **Contents**

89	Contents	vi
90	List of Figures	ix
91	List of Tables	xii
92	1 The Dark Matter Story	1
93	1.1 The History of Dark Matter	2
94	1.1.1 Early ideas in dark matter	2
95	1.1.2 Into the modern era	3
96	1.1.2.1 Galactic rotation curves	7
97	1.1.3 Local dark matter density measurements	7
98	1.2 From “History” to “Current Events”	7
99	1.2.1 Modern evidence and observations of dark matter	8
100	1.2.1.1 The cosmic microwave background	8
101	1.2.1.2 Gravitational lensing	8
102	1.2.1.3 MOND and the bullet cluster	8
103	1.3 MACHOs, WIMPs and WISPs, oh my!	9
104	1.4 Dark Photon Physics	9
105	1.5 Detection Strategy: a Resource Allocation Problem	10
106	2 Experiment Overview and Design	11
107	2.1 Sources of Power in Measured Spectrum	14
108	2.1.1 Thermal Noise	14
109	2.1.1.1 Blackbody Electric Field Density	14
110	2.1.1.2 Antenna Noise	17
111	2.1.1.3 Dicke radiometer equation	20
112	2.1.2 Dark Photon Signal	25
113	2.1.3 Radio Frequency Interference	27
114	2.1.4 Amplifier Chain Noise	28
115	2.1.5 ADC effects	32
116	2.1.5.1 Spurious signals	33
117	2.1.5.2 ADC noise	33

118	2.2	Toy Analysis	34
119	2.2.1	Signal significance	36
120	2.2.1.1	Computing an exclusion limit	38
121	2.2.2	Predicted time to detection	42
122	2.3	Thermal Noise in A Cavity: Thermal Wiggles	44
123	2.3.1	Theory of thermal radiation in a cavity	44
124	2.3.2	Inspection of thermal noise spectra	48
125	2.3.3	A simple resonator: shorted coax cable	49
126	2.3.3.1	RF circulators	52
127	2.3.4	A simpler resonator: shorted coax cable and circulator	55
128	2.3.5	A more complex resonator: antenna in room	57
129	2.3.6	Effective temperature of amplifier	59
130	2.3.7	Intentional breaking of thermal equilibrium	62
131	2.3.8	Relation of antenna S_{11} to thermal noise without a circulator	69
132	2.3.9	Discussion of Thermal Wiggles	72
133	2.4	Reverberation Chambers and Statistical Uniformity	73
134	2.4.1	Deterministic solutions to electromagnetic waves in cavities	75
135	2.4.2	Statistical approach to electromagnetic waves in cavities	79
136	2.5	System Design	80
137	2.5.1	Shielded room	83
138	2.5.2	Antenna	84
139	2.5.3	Terminator and fiber-optic switch control	88
140	2.5.4	Signal conditioning	88
141	2.5.4.1	Low noise amplifier	89
142	2.5.4.2	Secondary amplifier	89
143	2.5.4.3	Band pass filter	90
144	2.5.4.4	Putting together a signal conditioning chain	91
145	2.5.5	Veto antenna	94
146	2.5.6	12 V power system	95
147	2.5.7	GPU-Based Real-Time Spectrum Analyzer	98
148	3	System Characterization and Data Acquisition System	102
149	3.1	Measurement of Amplifier Chain Performance	103
150	3.1.1	Y-factor method	103
151	3.1.2	Confirming gain with tracking generator measurement	111
152	3.1.3	System stability over a run period	112
153	3.2	Measurement of shielding effectiveness and radio frequency interference	116
154	3.3	Spectrum Analyzer Characterization	122
155	3.3.1	Spectrum analyzer calibration	122
156	3.3.2	Spurious signal performance of the ADC	123
157	3.3.3	ADC clock performance	125
158	3.3.4	Real-time data collection efficiency	126

159	4 Data Acquisition, Data Analysis and Calibration	128
160	4.1 Data Acquisition	130
161	4.1.1 Raw data, S_o	131
162	4.2 Data Analysis	134
163	4.2.1 Fit background, $\hat{B}(\nu)$	136
164	4.2.2 Normalized spectrum, S_o^{norm}	138
165	4.2.3 Signal-matched filter	139
166	4.2.4 Monte Carlo: pseudo experiments	142
167	4.2.5 Rejection of a single candidate	147
168	4.3 Calibration	148
169	4.3.1 Average effective aperture, $\langle A_e(\nu) \rangle$	149
170	4.3.2 Simulation of $\langle \tilde{Q} A_e \rangle$	150
171	4.3.3 Correction and uncertainty of $\langle \tilde{Q} A_e \rangle$	153
172	4.4 Hardware Injection Test	157
173	4.4.1 Injection test prerequisites	157
174	4.4.1.1 Determination of required injected power	157
175	4.4.1.2 Proxy dark photon signal injection	160
176	4.4.2 Performing the injection test	162
177	4.4.3 Inspection of Data	166
178	4.5 Results	170
179	4.5.1 Discussion of uncertainties	170
180	5 Beyond 300 MHz	173
181	5.1 Preliminary Run 1B results	174
182	5.2 Mixer System	174
183	5.3 Cryogenics	174
184	A Overview of RTSA code base	175
185	A Tips for using the RTSA system	177
186	B Data structure and processing	178
187	B.1 Writing data	178
188	B.2 Reading and averaging data	182
189	Bibliography	185

¹⁹⁰ List of Figures

191	0.1	Expected vs observed velocity distributions of M33	iii
192	0.2	Dark matter mass regimes	iv
193	2.1	Overview of Dark E-field Radio experiment	13
194	2.2	Blackbody electric field spectral density from radio to UV frequencies	16
195	2.3	An antenna and matched resistor in cavities which are in thermal equilibrium.	19
196	2.4	Simulated antenna noise voltage at room temperature in the time domain	21
197	2.5	Simulated antenna noise power spectral density at room temperature in the frequency domain	22
199	2.6	Effect of averaging on simulated antenna noise power spectral density at room temperature in the frequency domain	24
201	2.7	Schematic of LNA adding input referred noise	28
202	2.8	Schematic of cascade of amplifiers and their added noise	30
203	2.9	Cascaded noise temperature for system with two amplifiers	31
204	2.10	Input-referred power spectral density from simplified simulation	36
205	2.11	Noise spectrum containing sub-detection-threshold signal	40
206	2.12	Noise spectrum containing sub-detection-threshold signal, various number of averages	41
208	2.13	Predicted time to detection for the toy analysis spectra	43
209	2.14	Two cavities in thermal equilibrium of arbitrary shape, material and physical contents contain equivalent radiation fields	45
211	2.15	A cavity with a small hole behaves like a black body as long as the probability of absorption $\ll 1$. The probability of absorption at each reflection is given by the emissivity, so the total probability of <i>reflection</i> is the emissivity raised to the power of the average number of bounces. Figure from Wikipedia.	47
215	2.16	Output-referred Vivaldi antenna and terminator spectra as measured through Run 1A amplifier chain	49
217	2.17	A coax cable with a short on the end and a matched measurement device on the other behaves like a “closed-open” resonator. Replacing the short termination with an open (not shown here) produces a similar resonator, though with a 180-degree phase shift.	51
221	2.18	Power spectrum of short and open terminations at the end of 1.85 m of RG400 coax cable	51
223	2.19	Schematic symbol of a circulator	52

224	2.20 Photo of Teledyne C-0S03A-3M RF circulator	53
225	2.21 3-port, frequency-dependent S-parameter data for Teledyne C-0S03A-3M circulator	54
226	2.22 A coax cable with a short on one end and a circulator isolating the system from the amplifier.	56
228	2.23 Power spectrum of 185 cm coax resonator as measured through circulator.	56
229	2.24 Schematic of experimental set-up using circulator to isolate antenna from ampli- fier effects	58
231	2.25 Normalized power spectrum for Vivaldi antenna in the room with and without circulator	58
233	2.26 Schematic of set-up to measure the noise emerging <i>out</i> of an amplifiers input . . .	61
234	2.27 Power spectrum of noise emerging <i>out</i> of the input of an amplifier's input	61
235	2.28 Setup to create hot and cold terminator	63
236	2.29 Spectra resulting from the antenna and circulator set up at a variety of temper- atures above room temperature	65
238	2.30 Spectra resulting from the antenna and circulator set up with the terminator 210 K above and below room temperature	67
240	2.31 Sum of normalized spectra shown in Fig. 2.30	68
241	2.32 $1 - S_{11} ^2$ and the normalized antenna spectrum over plotted	70
242	2.33 Correlation of $1 - S_{11} ^2$ and the normalized antenna spectrum	71
243	2.34 Modal density for an electromagnetic cavity with dimensions of the shielding room	77
244	2.35 Pictures of conductor configurations in shielded room	78
245	2.36 Measured S_{11} with different conductors in shielded room	78
246	2.37 Schematic of the RF receiver system	81
247	2.38 Photo of dark radio lab	82
248	2.39 AB-900A biconical antenna free space effective aperture, simulated, measured and theoretical	86
250	2.40 simulated AB-900A biconical antenna free space complex input impedance, vs measured biconical data	87
252	2.41 Through gain (S_{21}) of bandpass filter	93
253	2.42 Schematic of Run 1A Amplifier chain	94
254	2.43 Schematic of Interlock board	96
255	2.44 Photo of lead-acid battery and slow turn on circuit	97
256	2.45 Real time DAQ data stream.	100
257	3.1 Cartoon showing Y-factor data	104
258	3.2 Raw output power spectra used to compute the gain and noise temperature for the Run 1.4 amplifier chain using the Y-factor method	106
260	3.3 Y-factor data from Run 1.4 amplifier chain at a single frequency (625 MHz) . .	107
261	3.4 Frequency dependent noise temperature of Run 1.4 amplifier chain, measured using the Y-factor method	108
263	3.5 Frequency-dependent gain of the Run 1.4 amplifier chain, measured using the Y-factor method	109
265	3.6 Run 1.4 terminator, input-referred power spectral density	110

266	3.7	Gain vs. frequency of Run 1.4 amplifier chain	111
267	3.8	Gain vs. LNA voltage of Run 1.4 amplifier chain	113
268	3.9	Voltage at LNA vs. time	114
269	3.10	Frequency-averaged power spectral density vs. time of the terminator from Run 270 1.4	115
271	3.11	Photo of setup to measure Shielding effectiveness of shielded room	118
272	3.12	Shielding effectiveness of shielded room, 50-300 MHz	119
273	3.13	Shielding effectiveness of shielded room, 125-3000 MHz	120
274	3.14	Spectrum from veto antenna during 300 MHz data run	121
275	3.15	Scan of terminated input of Teledyne spectrum analyzer system to measure spur 276 performance	124
277	3.16	Acquisition efficiency for GPU-based Real-time spectrum analyzer	127
278	4.1	Run 1A averaged, output-referred antenna power spectrum S_o	132
279	4.2	Run 1A averaged, output-referred, antenna and terminator power spectra	133
280	4.3	Flow chart outlining the logic of signal processing in the detection algorithm of 281 sections 4.2.1 through 4.2.3.	135
282	4.4	Fitting background \hat{B} in the presence of a synthetic signal.	138
283	4.5	Normalized, output-referred power spectrum S_o^{norm}	140
284	4.6	S_o^{norm} after it has been passed through a matched filter.	142
285	4.7	Result of Monte Carlo pseudo experiments on signal detection.	145
286	4.8	Limit on output-referred total integrated signal power, P_o^{lim}	146
287	4.9	Screenshot of COMSOL simulation GUI for two-antenna validation	152
288	4.10	Simulated vs measured $\langle S_{21} \rangle$	153
289	4.11	Corrected average effective aperture.	155
290	4.12	Schematic of hardware injection test	158
291	4.13	Average S parameters of hardware injection test	159
292	4.14	Histogram of frequencies used for hardware injection test	162
293	4.15	Output-referred power spectral density from the hardware injection test	164
294	4.16	Standard deviation of output-referred power spectral density from the hardware 295 injection test, computed with median absolute deviation	165
296	4.17	Output-referred power spectrum from hardware injection test, various levels of 297 zoom	167
298	4.18	Normalized, output-referred power spectrum from hardware injection test, various 299 levels of zoom	168
300	4.19	Matched filtered, output-referred power spectrum from hardware injection test, 301 various levels of zoom	169
302	4.20	Zoom of 95 % exclusion limit on ϵ from Dark E-field Radio run 1A	171
303	4.21	Dark photon limits of various experiments with this work shown in red	172
304	A.1	Real-time heads up window for data acquisition.	181

³⁰⁵ List of Tables

306 2.1	Statistics of simple Monte Carlo simulation for probability of signal detection in the toy analysis	42
308 2.2	Direction, coordinate, and length measurements of shielded room in lab 314. Note that Fig. 2.38 is looking south, so x is right-left and z in into the page. Note that these are the mean values of several measurements. The room was found to be about 5mm out of square, so these should be interpreted as ± 5 mm.	84
312 2.3	Specifications for the Pasternack PE15A1012-E. The voltage is regulated internally, so the exact voltage supplied is not critical, though there is a slight gain dependence on voltage since a higher voltage causes the amp to run warmer, see Fig 3.8.	89
316 2.4	Specifications for the Mini-Circuits ZKL-1R5+ as measured with 9.05 V bias. There is no internal regulator, so the voltage is set using an external regulator (built around a TI LM317 [60]).	90
319 2.5	Specifications for the custom, real time spectrum analyzer used for run 1A.	99
320 4.1	Run 1.4 Details. Many specifications are related and can be computed from each other but are listed for reference. The efficiency differs from that calculated in Fig. 3.16 mainly because of switching to terminator and brief daily pauses to move the antenna.	130
324 4.2	Threshold parameters that are part of the detection algorithm and Monte Carlo. X is the significance of the analysis. It is a parameter passed to the detection algorithm which specifies the significance threshold. The quantity $100\% - Y$ is the statistical power of the analysis. It is a parameter in the MC, which specifies a threshold on signal power where a given signal is detected in $100\% - Y$ of the MC iterations. We choose both X and Y = 5%.	144
330 A.1	Example database file.	179

331

Acknowledgments

332 Thank you to: Ben

333 Dave Hemmer

334 Nathan IT

335 Monda

336 emiljia

337 Bill Tuck

338 Buchholtz/Ayars/Nelson/Kagan/Clare/Patrova/Rick Danner/pechkis

339 parents

340 janet/joel

341 baba/papa

342 Belva

343 chatGPT

344 Mr Keye

345 Bill Nye

346 pechkis

347 hepcat

348 paul

349 Self plagiarism statement <https://journals.aps.org/copyrightFAQ.html>

350 As the author of an APS-published article, may I include my article or a portion
351 of my article in my thesis or dissertation? Yes, the author has the right to use
352 the article or a portion of the article in a thesis or dissertation without requesting
353 permission from APS, provided the bibliographic citation and the APS copyright
354 credit line are given on the appropriate pages.

355 <https://grad.ucdavis.edu/preparing-filing-your-thesis-or-dissertation>

356 Published or publishing pending material may be used with permission from the
357 copyright owner, if not you, and the Graduate Chair, if you are not the first-
358 author. See the Copyright FAQ for information about permissions when using
359 published material.

360 Material you have authored, and which has been previously published or is pend-
361 ing publishing, may be used in its published format with three exceptions: 1)
362 Margins - You must maintain 1" margins on all sides throughout the paper. 2)
363 Pagination - page numbers must follow the UC Davis standards. 3) The title
364 page must follow UC Davis standards and you must include an overall abstract.

365 comment: Need to add note about github and where code comes from

³⁶⁶ Chapter 1

³⁶⁷ The Dark Matter Story

368

If we start making a list of things that aren't here, we could be here all night. You know, pens for instance. Let's stick with things we can see.

Wheatley

369 While there are many ways to begin a thesis on a dark matter search (of which many
370 hundreds are written every year), I have opted to prioritize narrative over completeness. I
371 will aim to answer the following questions:

- 372 • Why do we believe there to be some mysterious “dark matter” which we can’t even
373 see?
- 374 • Can we back up this prediction?
- 375 • What is the best way to balance answering this question with the economic reality of
376 finite money?

377 There will be a few digressions along the way, however the goal of this chapter is simply
378 to motivate what brought society to the point of paying young scientists to put antennas in
379 metal boxes and measure noise.

380 1.1 The History of Dark Matter

381 1.1.1 Early ideas in dark matter

382 The fundamental idea that things exist which can not be easily observed by human senses is
383 not a new one. Following a long history of discovery of previously unobserved phenomena,
384 the study of dark matter began to take shape around the end of the 19th century with the
385 discovery of dark regions among areas with a high density of stars [5]. It was Lord Kelvin
386 who began a dynamical study of the motions of stars in order to tease out the weight of

387 the luminiferous aether (who's "existence is a fact that can not be questioned" as stated
388 in his 1901 lecture which is transcribed on page 260 of [6]). Eventually the theory of the
389 aether would give way to special relativity, which ruled out a potential candidate for the
390 dark regions. This proposing of dark matter candidates and their rejection is a cycle that
391 continues to this day, and is the topic of this thesis.

392 1.1.2 Into the modern era

393 1905, known as Einstein's miracle year, ushered in a new era of "modern physics". The
394 aether that Lord Kelvin was trying to weigh was accepted as non-existent, but that didn't
395 answer the questions of galactic dynamics which were posed by those who believed in it.
396 Fritz Zwicky is credited with the first discovery of dark matter in 1933 [1], though it was
397 not widely accepted at this time. This lack of acceptance was in part due to his technique
398 of "morphological analysis" which is similar to arranging refrigerator magnets to arrive at
399 creative solutions¹. The many "creative" solutions are simultaneously to the benefit and
400 detriment of this technique. To quote Stephen Maurer[7],

401 *When researchers talk about neutron stars, dark matter, and gravitational lenses,*
402 *they all start the same way: "Zwicky noticed this problem in the 1930s. Back then,*
403 *nobody listened..."*.

404 It even seems if Zwicky himself didn't believe his own result[1],

¹This analogy is from a class I took from Andrew Wetzel at U.C. Davis. In researching it for this thesis, it is surprisingly accurate

405 *If this [experimental result] would be confirmed we would get the surprising result
 406 that dark matter is present in much greater amount than luminous matter [1].*

407 comment: Tony summarizes virial therm this in his '97 physics today article, p. 1 [8] In
 408 retrospect however, this idea is seemingly on firm theoretical footing. The viral theorem is a
 409 well known from statistical mechanics. It was formalized 1870 by Rudolf Clausius (English
 410 translation can be found here [9]). The name *virial* was coined by Clausius. Kinetic energy
 411 was, at the time, referred to as *vis viva* latin for “living force”. The plural of vis is virias,
 412 and since the theorem is concerned with many particles each with their own vis vita the
 413 name *virial* theorem was chosen. The theorem is derived briefly here (following chapter 3 of
 414 Goldstein[10]) since it is informative, however the reader can skip to Eq. 1.6 for the result
 415 as it applies to galacite dynamics.

416 The “virial” the system is defined as

$$G \equiv \sum_{i=1}^N \mathbf{r}_i \cdot \mathbf{p}_i \quad (1.1)$$

417 Where \mathbf{r}_i is the position of the ith particle and \mathbf{p}_i is it's momentum, $m_i \mathbf{v}_i$.

418 By the product rule, the time derivative of G is

$$\dot{G} = \sum_{i=1}^N (\dot{\mathbf{r}}_i \cdot \mathbf{p}_i + \mathbf{r}_i \cdot \dot{\mathbf{p}}_i) . \quad (1.2)$$

419 Since the first term is really $m_i \mathbf{v}_i \cdot \mathbf{v}_i$ it can be seen as twice the kinetic energy, $2T$. The
 420 second term can be simplified by Newton's second law, $\mathbf{F} = \dot{\mathbf{p}}$. So,

$$\dot{G} = 2T + \sum_{i=1}^N (\mathbf{r}_i \cdot \mathbf{F}_i) . \quad (1.3)$$

Solving for the time-averaged, time-derivative of G ,

$$\begin{aligned}\bar{\dot{G}} &= \frac{1}{T} \int_0^\tau dt \dot{G} \\ &= \frac{G(\tau) - G(0)}{\tau}\end{aligned}$$

421 Where T is the period the average is taken over, not to be confused with the Kinetic energy.

422 In the case that the system is bound together (i.e. $\mathbf{r}_i, \mathbf{p}_i > \infty$), G is finite and as τ
423 approaches ∞ , $\bar{\dot{G}}$ approaches 0

424 Returning to Eq. 1.2, we can now say

$$\overline{T} = -\frac{1}{2} \overline{\sum_{i=1}^N (\mathbf{r}_i \cdot \mathbf{F}_i)}, \quad (1.4)$$

425 A familiar statement of the virial theorem, where the term on the right hand side is
426 known as *the virial of Clausius*.

427 While incredibly general (one can pull the ideal gas law out of this in just a few steps,
428 see again Ch. 3 of Goldstein [10]), we are concerned not with a jar filled with gas in some
429 lab, but with “gas” of stars (among which all labs are contained!).

430 To specify the equation to that of galactic dynamics, recognize for a conservative central
431 force, $\mathbf{F} = -\nabla U$ and $\mathbf{r} \cdot \mathbf{F} = rF$. If U is in a power law, i.e. of the form $k r^{n+1}$, it can quickly
432 be seen that the virial of Clausius of Eq. 1.4 can be written $\frac{n+1}{2} \overline{U}$.

433 For a problem involving an inverse square force as we are concerned with, $n = -2$, and we
434 arrive at the well known result which is usually just called “the virial theorem”, though as we
435 have seen, it reaches much deeper than a simple statement of kinetic vs potential energies
436 for galaxies:

$$\overline{T} = -\frac{1}{2}\overline{U}. \quad (1.5)$$

437 Finally following Edington's 1916 paper [11] we can form a useful formula which ul-
 438 timately gave a clue to the existence of dark matter. By setting $T = 1/2M\overline{v^2}$ and $U =$
 439 $GM^2/2R$ where M is the total mass of a cluster or galaxy, v is it's velocity, and R is it's
 440 radius, we arrive at

$$M \approx \frac{2R\overline{v^2}}{G} \quad (1.6)$$

441 As pointed out by Bertone [12], one of the earliest "clean" arguments for the existence
 442 of dark matter is known as the timing argument. It was derived by Kahn and Woltjer [13].
 443 The basic idea is given the negative red-shift (i.e. blue-shift) of the Andromeda galaxy, they
 444 are approaching (at 125 km/s), an indication that they are bound system. Given that the
 445 period of this system must be less than the age of the universe (assumed to be 10^{10} yr), a
 446 lower bound can be set on the reduced mass of the system (since orbital period T is inversely
 447 proportional to the reduced mass).

448 In the years following these arguments, WWII brought unprecedeted destruction, the
 449 reconstruction of which slowed the progress of all science that was not essential to the war
 450 effort, especially in Europe. The focus of astronomy and astrophysics largely shifted to
 451 stellar structure and evolution, in large part due to the work and understanding of nuclear
 452 reactions around this time. The war also brought with it advances in radar technology. At
 453 the end of the war, the German occupation forces left large amounts of radar equipment

454 strewn about Europe. This included a large number of 7.5 m Würzburg antennas designed
455 to 54 cm aircraft radar, but were also sensitive to the famous Hydrogen 21[cm] line [14]. This
456 would play a major role in what was to come.

457 **1.1.2.1 Galactic rotation curves**

458 **1.1.3 Local dark matter density measurements**

459 **comment: Add plots of local dark matter density estimate.**

460 Good figure 2 of historical DM density through 2014 by Read [15]. Also Figure 1 explains
461 the difference between local and global density of DM

462 Read is also an author on [16], which has a nice figure 1 showing a continuation of this
463 out to 2021

464 This is questionable (not peer-reviewed, 2 citations) but has a good overview of Gaia,
465 and gets DM density using data release 3 [17]

466 **1.2 From “History” to “Current Events”**

467 As pointed out by Trimble, “Practicing scientists will normally put the cut between history
468 and current events at the time when they started reading the literature for themselves,
469 probably early in graduate school.” [18]. While that puts my personal cut-off around 2020,
470 the cut-off of the Dark E-field Radio group is closer to the mid-1960’s, a fruitful time for
471 research into dark matter.

472 A characteristic shift in the dark matter problem occurs in this era of current events.
473 Instead of asking “is there dark matter (and if so how much)”, we ask “what is this stuff?!”.
474 To be sure, the first question is still relevant today and the ever more precise answer was
475 outlined in Sec. 1.1.3. This section is concerned with more modern evidence for dark matter,
476 which tend to point to the modern non-baryonic particle models, which the Dark E-Field
477 Radio Experiment is searching for.

478 **1.2.1 Modern evidence and observations of dark matter**

479 **1.2.1.1 The cosmic microwave background**

480 Billy and Ben’s thesis

481 **1.2.1.2 Gravitational lensing**

482 -ben thesis

483 -tony 92 article// -J. A. Tyson, G. P. Kochanski, and I. P. Dell’Antonio, Detailed mass map
484 of CL0024+1654 from strong lensing

485 **1.2.1.3 MOND and the bullet cluster**

486 -history of dark matter bertone

487 - billy and ben

488 - D. Clowe, M. Bradac, A. H. Gonzalez, M. Markevitch, S. W. Randall, et al., A direct
489 empirical proof of the existence of dark matter,

490 **1.3 MACHOs, WIMPs and WISPs, oh my!**

491 -Billy thesis sec 1.2

492 - G. Bertone, D. Hooper, and J. Silk, Particle dark matter: Evidence, candidates and con-
493 straints

494 **1.4 Dark Photon Physics**

495 - Ben's thesis

496

$$|\mathbf{E}_{\text{ant}}| \approx \epsilon \sqrt{\frac{2}{\varepsilon_0} \rho_{\text{DM}}}, \quad (1.7)$$

497 Tony says 9/23/25– Production mechanisms: fluctuation occurs early in inflation or mis-
498 alignment mechanism.

499

500 two scales cross, peter graham Point out that DP doesn't have a thermal origin like a
501 WIMP does

502 **1.5 Detection Strategy: a Resource Allocation**

503 **Problem**

504 - US Cosmic Visions 2017

505

506 Chapter 2

507 Experiment Overview and Design

508 A month in the laboratory can often save an

hour in the library.

Frank Westheimer

509 Veljko Radeka said of detectors “One would imagine that in each particular case the best
510 solution is arrived at by 1) the detector design to maximize the significant signal, 2) reduction
511 of noise at its physical source, and 3) optimum filtering of signal and noise.” [19]. While
512 he was referring to position sensitive particle detectors, the same three principles apply to
513 this experiment. Put more directly, the goal is to maximize the signal to noise ratio. The
514 detector in this case is a low-noise, wide-band radio receiver system searching not for discrete
515 instances of particle-like interactions, but for coherent waves which are constant over long
516 periods. The signal is a small excess of narrow-band, radio frequency power received by an
517 antenna in a cavity. The noise is the white, thermal background due to the 300 K walls. An
518 overview of the entier experiment is shown in Fig. 2.1.

519 This chapter begins with Sec. 2.1, devoted to exploring the sources of power in the mea-
520 sured spectrum. It walks through several back-of-the-envelope calculations to follow the
521 signal and noises as they progress from fields in free space through a simplified detector.
522 Section 2.2 takes the next step; it simulates these signals and noises and shows a frame-
523 work for statistical data analysis. These two sections serve to build up intuition about the
524 experiment which will explain design choices discussed in the later chapters. Furthermore,
525 this section is useful because the actual experiment will report a null result, i.e. a lack of
526 detection of a signal on a background. By following a signal *forward* through the system
527 and toy data analysis, it will be more clear how to infer an exclusion limit from a power
528 spectrum and working *backward* through the experiment. In the following two sections, 2.3
529 and 2.4, effects will be introduced that were not apparent from the simplistic analysis of
530 the first section. The final section, 2.5, details each piece of the system. Measurements of

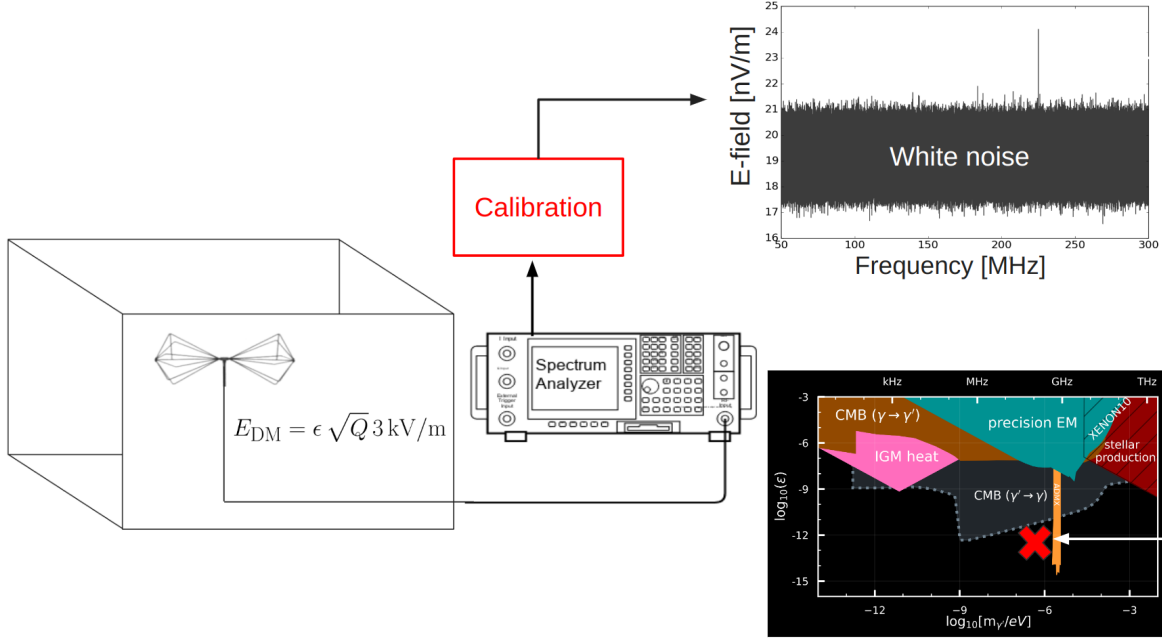


Figure 2.1: Overview of Dark E-field Radio experiment. The free space electric field strength was calculated in Sec. 1.4, and will be modified to include the Q of the cavity in Sec. 2.1.2. The design of the system is outlined in this chapter, while it's performance is measured in Ch. 3. The use of the system, its calibration, and setting a limit are all discussed in Ch. 4. **comment: Remake this. Change E_{DM} to E_{ant} , 3kV to 4.5kV, change limit plot. Image from google slide called "schematic"**

531 system performance are put off until Ch. 3).

532 A note on experiment “run numbers”. Run 1A is the 50-300 MHz run. There have been
 533 four attempts at collecting run 1A data. The final, published data run was collected between
 534 May 10 and May 19, 2023 and is called run 1.4 or run 1p4 throughout my power points and
 535 file names. I will refer to this run interchangeably as run 1A or run 1.4. Strictly speaking, it
 536 should be run 1A.4, but if I change it now it will be inconsistent with file names. When you
 537 forget about this note, you will have a hard time finding data in my file structure, especially

538 as future runs are completed.

539 **2.1 Sources of Power in Measured Spectrum**

540 This section will break down each term in the following equation for the input-referred power

$$P_i = \text{Thermal Noise} + \text{Dark Photon Signal} + \text{RFI} + \text{Amp Chain Noise} + \text{ADC Effects}/G, \quad (2.1)$$

541 where G is a gain factor. While convenient, this word equation is not rigorous, and relies
542 on the following subsections 2.1.1 - 2.1.5 for definition.

543 **2.1.1 Thermal Noise**

544 **2.1.1.1 Blackbody Electric Field Density**

545 This subsection estimates the noise-like¹ electric field in free space due to black body ra-
546 diation. It assumes to be in *some* enclosure in that the ambient temperature is known to
547 be 300 K and not, for example, the 3.6 K of the sky. The enclosure considered is assumed
548 to be "black" in that all radiation impinging on its surface is absorbed. This assumption is
549 introduced in Sec. 2.1.1.2 and investigated further in Sec. 2.3.

550 Planck's law gives the black body spectral energy density as

$$u_\nu(\nu, T) d\nu = \frac{8\pi h\nu^3}{c^3} \frac{1}{e^{h\nu/kT} - 1} d\nu \quad \left[\frac{J}{m^3} \right]. \quad (2.2)$$

¹"Noise-like" simply means that the power contained in a signal is proportional to the bandwidth measured. Noise-like signals are more conveniently described as a power spectral density (PSD) which we will describe with the symbol S . As we will see, coherent signals that have finite width in frequency space $\Delta\nu_{\text{sig}}$ can share this property if the measurement bandwidth $\Delta\nu_{\text{RF}} \lesssim \Delta\nu_{\text{sig}}$, even though one wouldn't think of a coherent signal as being "noise-like"

551 This is frequently written in terms of spectral radiance,

$$B_\nu(\nu, T) d\nu = \frac{2h\nu^3}{c^2} \frac{1}{e^{h\nu/kT} - 1} d\nu d\Omega \quad \left[\frac{W}{m^2} \right]. \quad (2.3)$$

552 Integrating this isotropic radiance over a solid angle 4π sr as well as a small frequency

553 band $\Delta\nu$ gives the flux density $|\mathbf{S}|$ (AKA, the magnitude of the Poynting vector),

$$\begin{aligned} |\mathbf{S}| &= \int_0^{4\pi} \int_\nu^{\nu+\Delta\nu} B_\nu(\nu, T) d\nu d\Omega \\ &= \int_0^{4\pi} \int_\nu^{\nu+\Delta\nu} \frac{2h\nu^3}{c^2} \frac{1}{e^{h\nu/kT} - 1} d\nu d\Omega \quad \left[\frac{W}{m^2} \right]. \\ &\approx \frac{8\pi h\nu^3}{c^2} \frac{1}{e^{h\nu/kT} - 1} \Delta\nu \end{aligned} \quad (2.4)$$

554 Poynting's theorem relates this flux density to the RMS electric field

$$|\mathbf{S}| = \frac{|E_{rms}|^2}{\eta} \quad \left[\frac{W}{m^2} \right], \quad (2.5)$$

555 where η is the impedance of free space. Equating Eqs. 2.4 and 2.5 and solving for the

556 electric field gives

$$\frac{|E_{rms}|}{\sqrt{\Delta\nu}} = \sqrt{\eta \frac{8\pi h\nu^3}{c^2} \frac{1}{e^{h\nu/kT} - 1}} \quad \left[\frac{V}{m \cdot \sqrt{Hz}} \right], \quad (2.6)$$

557 and is plotted in Fig. 2.2.

558 Eq. 2.6 breaks up nicely into two regimes,

$$\frac{|E_{rms}|}{\sqrt{\Delta\nu}} = \begin{cases} \sqrt{\eta \frac{8\pi kT\nu^2}{c^2}} & \text{Rayleigh-Jeans regime } (h\nu \ll kT) \\ \sqrt{\eta \frac{8\pi h\nu^3}{c^2} e^{-h\nu/kT}} & \text{Wien approximation } (h\nu \gg kT) \end{cases} \quad \left[\frac{V}{m \cdot \sqrt{Hz}} \right]. \quad (2.7)$$

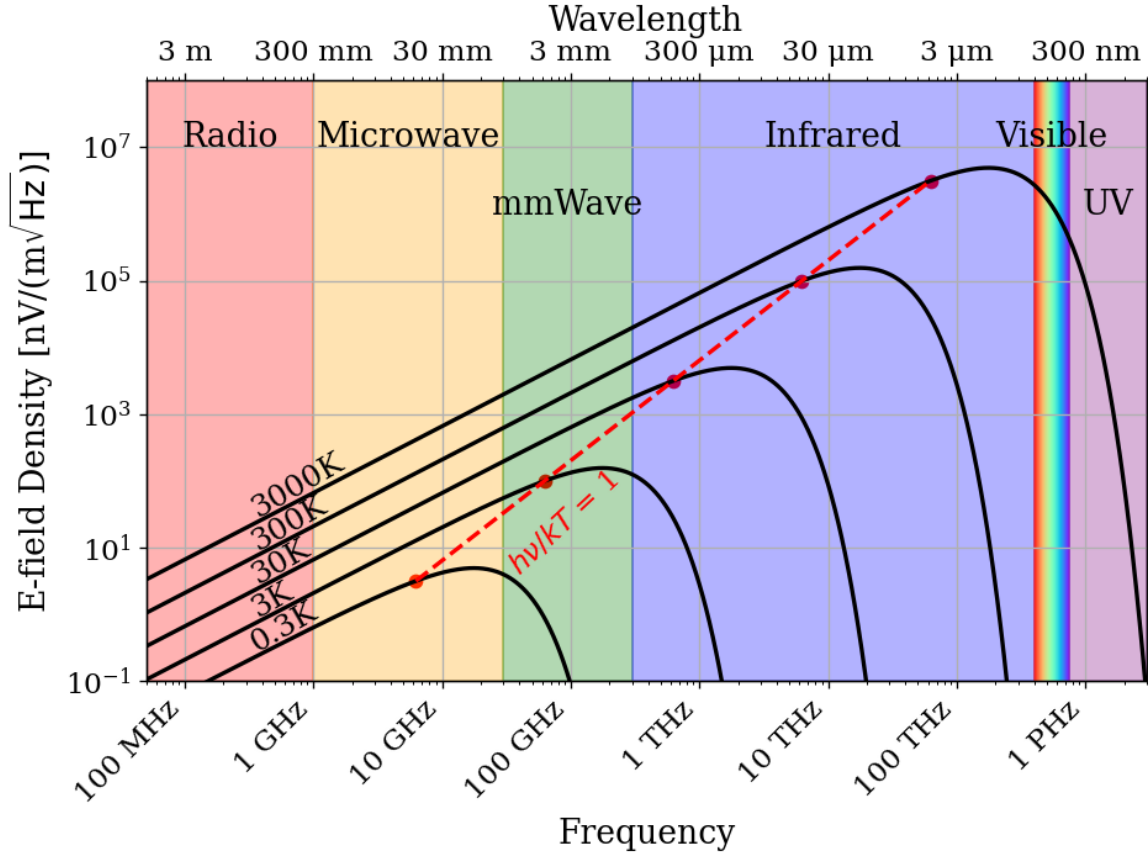


Figure 2.2: Blackbody electric field spectral density from radio to UV frequencies. A variety of temperatures are shown in black. The dashed red curve and red points indicate where along the black curves $h\nu = kT$, i.e. where Eq. 2.7 breaks up between the Rayleigh-Jeans regime to the Wien approximation. Note that these points are only a function of ν and T ; their vertical placement is chosen to lie on their respective curve but has no physical significance. The dark radio experiment is firmly in the Rayleigh-Jeans regime.

559 At frequencies and temperatures where the experiment is operated ($< 300 \text{ MHz}$ and
 560 300 K), $h\nu/kT \lesssim 5 \times 10^{-5}$ suggesting the Rayleigh-Jeans approximation is valid. At 300 K ,
 561 this yields electric field spectral densities of 1 and $6 \text{ nV}/(\text{m}\sqrt{\text{Hz}})$ at 50 and 300 MHz respec-
 562 tively.

563 It is interesting to note, however, that for cryogenic experiments operating at a few GHz

564 and in the sub K range (A common technique; see for example [20–22]), $h\nu/kT \approx 1$ and
 565 the full form of Eq. 2.6 must be used. This is shown at frequencies and temperatures to the
 566 right of the red dashed line in Fig. 2.2.

567 **2.1.1.2 Antenna Noise**

568 An antenna's effective aperture, $A_e [\text{m}^2]$, represents the effective area that it has to collect
 569 power density or irradiance [W/m^2] from an incident Poynting vector,

$$P_A = |\mathbf{S}| A_e, \quad (2.8)$$

570 Where $|\mathbf{S}|$ is the magnitude of the incident Poynting vector and P_r is the power received at
 571 the antenna which is available at its terminals.

572 A_e is a directional quantity which varies with the antenna's directivity $D(\Omega)$, where Ω
 573 represents solid angle around the antenna. It varies with frequency ν , though it is generally
 574 discussed in terms of wavelength λ . Three matching parameters are introduced to describe
 575 how much actual power the antenna is able to deliver to a transmission line; p the polarization
 576 match of the wave to the antenna, m the impedance match of the antenna to the transmission
 577 line and η_a the efficiency of the antenna which represents how much power is absorbed
 578 compared to that lost to Joule heating of the antenna. p , m and η_a are all real, dimensionless
 579 and vary between 0 and 1.

$$A_e \equiv \frac{\lambda^2}{4\pi} D(\Omega) p m \eta_a. \quad (2.9)$$

580 This definition follows [23], though some authors do not include p in the definition [24,
 581 25].

582 A simple derivation of the direction-averaged effective aperture based on thermodynamics
 583 will provide intuition. An isotropic antenna placed in a cavity at temperature T will be
 584 illuminated by randomly polarized, isotropic radiation of the form given by the Rayleigh-
 585 Jeans limit of Eq. 2.4, $|\mathbf{S}| = 8\pi kT\Delta\nu\nu^2/c^2$. The power received by the antenna can be found
 586 by Eq. 2.8,

$$\begin{aligned} P_A &= \langle A_e \rangle \frac{1}{2} |\mathbf{S}| \\ &= \langle A_e \rangle \frac{4\pi kT\nu^2}{c^2} \Delta\nu, \end{aligned} \tag{2.10}$$

587 Where the factor of $1/2$ is introduced to account for the random polarization and the $\langle \rangle$
 588 indicate an average aperture over all angles around the antenna. If a resistor is placed in
 589 a second cavity, also at temperature T , it will deliver its Johnson-Nyquist noise power [26,
 590 27]

$$P_R = kT\Delta\nu \tag{2.11}$$

591 into a matched transmission line. This is shown in Fig. 2.3. The second law of thermo-
 592 dynamics makes a very powerful statement here; the net power flow between antenna and
 593 terminator must equal 0 if the two temperatures are indeed equivalent. This means $P_R = P_A$
 594 or Eq. 2.10 = Eq. 2.12,

$$\langle A_e \rangle \frac{4\pi kT\nu^2}{c^2} \Delta\nu = kT\Delta\nu \tag{2.12}$$

595 or,

$$\begin{aligned} \langle A_e \rangle &= \frac{c^2}{4\pi\nu^2} \quad [\text{m}^2] \\ &= \frac{\lambda^2}{4\pi} \end{aligned} \quad (2.13)$$

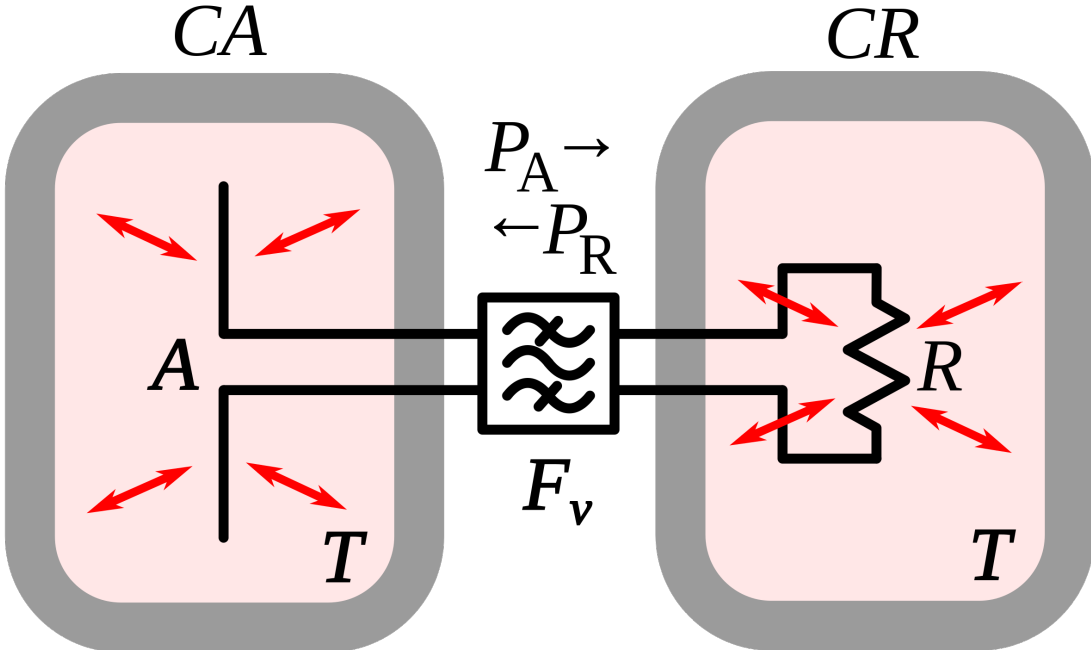


Figure 2.3: An antenna and matched resistor in cavities which are in thermal equilibrium. They are connected by a narrow filter permitting a narrow frequency band $\Delta\nu$. Image from Wikipedia, and is similar to the thought experiment proposed by Dicke [28].

596 This allows us to conclude that the power spectral density S_{ant} received by an antenna
 597 surrounded by an isotropic temperature is simply $kT\Delta\nu$ in the Rayleigh-Jeans limit of room
 598 temperatures and standard electronic frequencies. This result is independant of frequency,
 599 which can be understood by the reciprocal frequency dependence of the blackbody radiation
 600 (Eq. 2.4) and the average effective aperature (Eq. 2.13). The result is an antenna power
 601 which is equivalent to the well known result for a resistor at 290 K,

$$S_{\text{ant}} = 3.9 \times 10^{-22} [\text{W}/\text{Hz}] = -174 [\text{dBm}/\text{Hz}]. \quad (2.14)$$

602 Note that S_{ant} indicates power spectral density and should not be confused with \mathbf{S} which
 603 indicates a Poynting vector.

604 **2.1.1.3 Dicke radiometer equation**

605 Equation 2.14 gave the mean of a power spectrum which is inherently noisy. We will now
 606 show the origin of this spectrum.

607 An enclosure who's electrically-lossy walls contain free charge carriers at finite temper-
 608 ature will radiate incoherently by the fluctuation dissipation theorem. This theorem is
 609 the underlying principal of phenomena such as Brownian motion [29] and Johnson-Nyquist
 610 noise [26, 27], but was not generally proven until 1951 by Callen and Wellton [30]. The
 611 random thermal fluctuation of the charge carriers will radiate a black-body spectrum. Ob-
 612 serving the electric field in the time domain, one can imagine the radiation arriving at a
 613 detector at a wide variety of random frequencies and phases. This is incoherent noise in that
 614 at each time domain sample is independent of the one proceeding it ². The detector will
 615 produce a voltage which can be modeled as Gaussian with zero mean and standard deviation
 616 $\sigma = \sqrt{S_{\text{ant}} \Delta \nu_{\text{RF}} |Z|}$ where Z is the system impedance (here 50Ω). This is shown for a room
 617 temperature antenna (or equivalently a room temperature resistor, see Fig. 2.3) in Fig. 2.4.

²The hidden assumption here is that blackbody radiation is totally incoherent. It actually has a coherence time $\tau_c \approx 2 \times 10^{-14} \text{ s}$ at 300 K [31]. For this statement to hold, the sample time $\tau_s \gg \tau_c$. For run 1A, $\tau_s = 1/800 \text{ MHz} = 1.25^{-9} \text{ s}$, 5 orders of magnitude more than τ_c

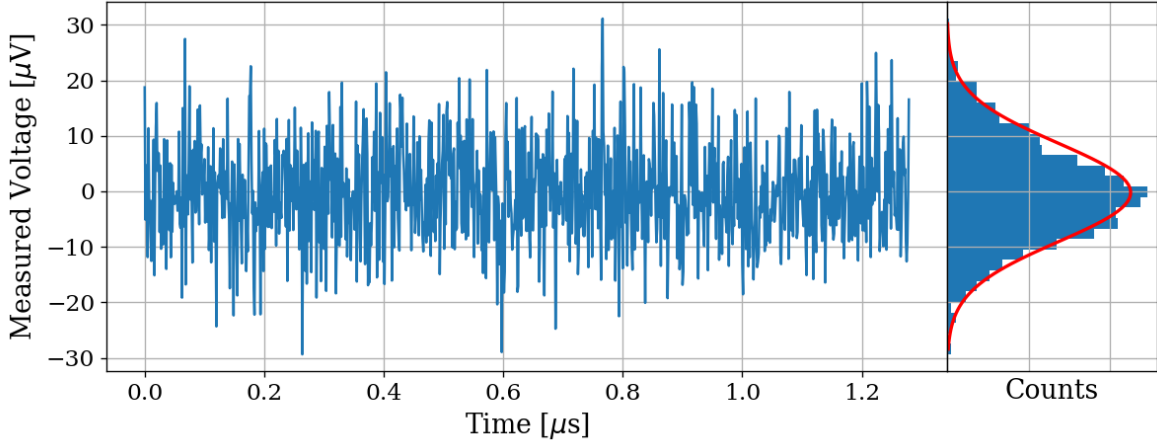


Figure 2.4: Simulated antenna noise voltage at room temperature in the time domain. Sample rate $\nu_s = 800\text{MHz}$ and number of samples $N = 2^{10} = 1024$. Bin width $\Delta\nu_{\text{RF}} = \nu_s/N \approx 800\text{ kHz}$. Data are binned and plotted as a histogram to the right. Best fit Gaussian is shown on the histogram in red with $\mu = -0.199\text{ }\mu\text{V}$ and $\sigma = 8.86\text{ }\mu\text{V}$. Counts have been normalized such that the bins add up to unity.

618 The next step in converting this time domain voltage signal to a frequency domain
 619 power spectral density (PSD). The first step is taking a discrete Fourier transform. This is
 620 usually implemented with an algorithm known as a fast Fourier transform (FFT), so that
 621 $\tilde{V} = \text{FFT}(V)$. In order to convert to a power spectrum, a non-trivial normalization prefactor
 622 must be included;

$$S = \frac{2}{N^2 |Z|} |\Re(\tilde{V})[:N//2]|^2, \quad (2.15)$$

623 where N is the number of samples, Z is the system impedance, and [:N//2] is python notation
 624 for the second half of the samples contained in the \tilde{V} array. Performing this operation on
 625 the data in Fig. 2.4 yealds the data in Fig. 2.5

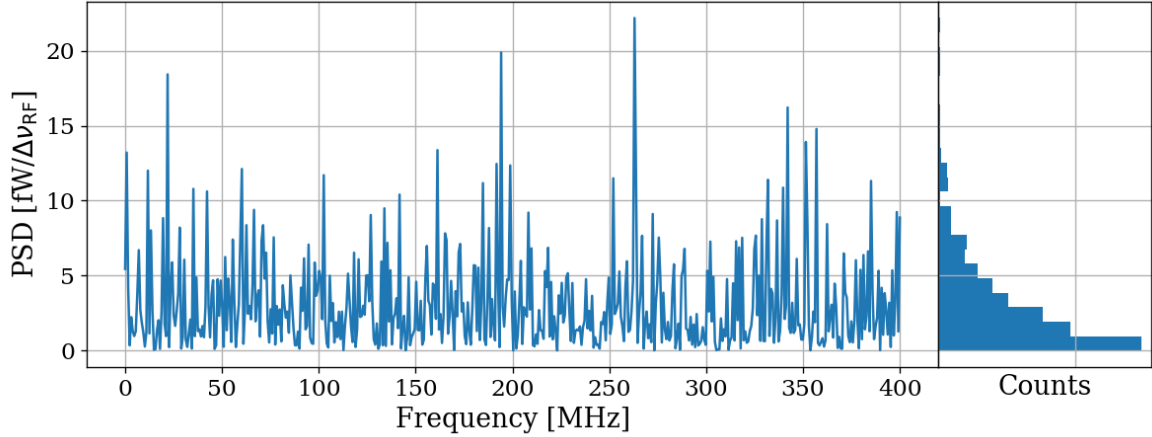


Figure 2.5: Simulated antenna noise power spectral density (PSD) at room temperature in the frequency domain. Sample rate $\nu_s = 800\text{MHz}$ and number of samples $N = 2^{10} = 1024$. Bin width $\Delta\nu_{\text{RF}} = \nu_s/N \approx 800\text{ kHz}$. Data are binned and plotted as a histogram to the right. Counts have been normalized such that the bins add up to unity.

626 The peculiar PDF of the histogram shown in Fig. 2.5 is known as a χ^2 distribution with
 627 1 degree of freedom and comes about because power is a positive-definite quantity and the
 628 standard deviation of the PSD is greater than it's mean.

629 However, by averaging many of the these power spectra together the central limit theorem
 630 dictates that we can expect the resulting PDF to be Gaussian. The transition from χ^2 to
 631 Gaussian distributed spectra is shown in Fig. 2.6.

632 Finally, this averaged power spectrum can be modeled with the Dicke radiometer equa-
 633 tion. The measured power (assuming only thermal noise) is given by

$$P_{\text{ant}} = kT\Delta\nu \left(1 \pm \frac{1}{\sqrt{\Delta\nu\tau}} \right) \quad [\text{W}]. \quad (2.16)$$

634 Here τ is the total acquisition time and so $\Delta\nu\tau$ is equivalent to the number of spectra

635 that are averaged together. This can be nondimensionalized and written

$$\frac{P_{\text{ant}}}{kT\Delta\nu_{\text{RF}}} = 1 \pm \frac{1}{\sqrt{N}} \quad [\text{None}], \quad (2.17)$$

636 which will become important during data analysis which is the topic of Sec. 4.2.

637 For the remainder of this thesis, unless otherwise stated, it will be assumed enough
638 spectra have been averaged together that a PSD is Gaussian and scales with the square root
639 of total acquisition time according to Eq. 2.16.

640 Thus far the analysis has focused only on thermal noise, however there are other sources
641 of noise and interfering signals which must be considered, not to mention the actual dark
642 photon signal.

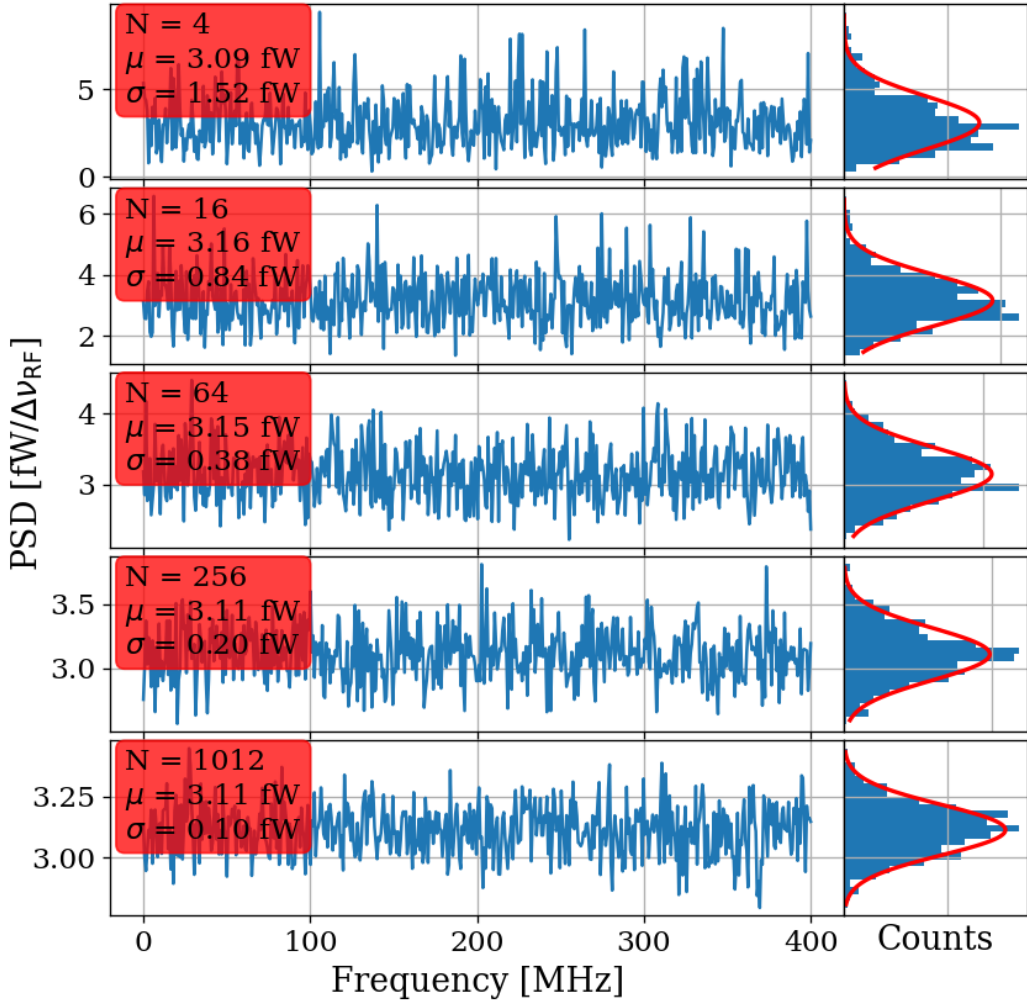


Figure 2.6: Effect of averaging on simulated antenna noise power spectral density (PSD) at room temperature in the frequency domain. Subplots show different number of averaged power spectra from $N = 4$ to 1024. Each subplot shows a factor of 4 times more averaging than the previous one. The Dicke radiometer equation predicts the standard deviation σ will scale like $N^{-1/2}$, once a large number of averages have been taken such that $\sigma \ll \mu$. Sample rate $\nu_s = 800\text{MHz}$ and number of samples $N = 2^{10} = 1024$. Bin width $\Delta\nu_{\text{RF}} = \nu_s/N \approx 800 \text{ kHz}$. Data are binned and plotted as a histogram to the right with a best fit Gaussian shown in red. Counts have been normalized such that the bins add up to unity. Note that the Y-axis scale changes between sub plots to show the improvement of the Gaussian fit. The standard deviation is indeed decreasing between plots.

643 **2.1.2 Dark Photon Signal**

644 The electric field of a kinetically mixed dark photon in free space $\mathbf{E}_{\text{ant}}^{\text{free space}}$ was shown in
645 Eq. 1.7. In a cavity, the E-field will be enhanced by the quality factor Q of the cavity. This
646 Q must be measured or simulated, but for this toy analysis we will assume it to be known
647 ³. The E-field inside the cavity then is

$$\mathbf{E}_{\text{ant}} = \mathbf{E}_{\text{ant}}^{\text{free space}} \sqrt{Q}, \quad (2.18)$$

648 since Q is proportional to power, i.e. \mathbf{E}^2 . This E-field will then need to be converted from
649 a wave in the cavity to a wave in a 50Ω transmission line by an antenna. Similar to the
650 thermal noise of the previous section, this electric field will be converted via the effective
651 aperture of the antenna. Similar to Q , aperture will be assumed to be known.

652 The total received power from a coherent signal inside the room then is

$$P = \frac{\mathbf{E}_{\text{ant}}^{\text{free space}^2}}{\eta} Q < A_e >, \quad (2.19)$$

653 where η is the impedance of free space.

654 The observed spread of the frequencies of the dark photon are in important effect which
655 determine system design. In the following paragraphs of this section, several sections of
656 Gramolin et al. [33] are summarized. Also note that the original calculation for the predicted
657 line shape this appears to be Michael Turner in 1990 [34].

658 A simple model of the dark photon line assumes it is monochromatic, i.e. it's line shape
659 is a delta function in frequency domain,

$$\nu_{\text{obs}} = \delta(\nu - \nu_{\text{DP}}). \quad (2.20)$$

³Typical values are in the ball park of 100. Some experiments have ultra-high Q cavities $\approx 10^{10}$ [32]

660 This is consistent with it's production add reference: misalignment mechanism/ch 1.

661 However, when observed in a frame other than its rest frame, the frequency of a (single)

662 dark photon will shift by an amount proportional to it's kinetic energy

$$\nu_{\text{obs}} = \left(1 + \frac{v_n^2}{2c^2}\right) \nu_{\text{DP}}, \quad (2.21)$$

663 where ν_{obs} is the observed frequency of the n th dark photon, v_n is its velocity, c is the speed

664 of light, and ν_{DP} is its rest frequency. The end result will be a signal that has some spread

665 in frequency, $\nu_{\text{DP}}/(\Delta\nu) \equiv Q_{\text{DP}} \approx 10^6$, with a line shape given by 2.24.

666 By summing over an infinity of dark photons of random phases and velocities (sampled

667 from the relative velocity of the dark matter halo), each with a frequency given by Eq. 2.21,

668 one can construct a PSD of the dark photon signal as measured on earth, S [W/Hz].

669 When performing a measurement, one records the voltage V emerging from a detector

670 for a period of time greater than the coherence of the dark photon $\tau_{\text{FFT}} \gg \tau_c$. The Fourier

671 transform of $V(t)$ is denoted $\tilde{V}(\nu)$

672 The signal will have a total power

$$P_0 = \frac{1}{\tau_{\text{FFT}}} \int_0^{\tau_{\text{FFT}}} \frac{V(t)^2}{|Z|} dt = \int_0^{1/\tau_{\text{FFT}}} S(\nu)^2 d\nu, \quad (2.22)$$

673 which is a statement of Parseval's theorem.

674 The normalized line shape is defined by dividing by P_0 ; $\lambda(\nu) \equiv S(\nu)/P_0$. This has the

675 property of being normalized to unity,

$$\int_0^\infty \lambda(\nu) d\nu = 1. \quad (2.23)$$

676 Finally, the result for this normalized line shape is

$$\lambda(\nu) = \frac{2 c^2}{\sqrt{\pi} v_0 v_{\text{lab}} \nu_{\text{DP}}} \exp \left(-\frac{\beta^2 v_0^2}{4 v_{\text{lab}}^2} - \frac{v_{\text{lab}}^2}{v_0^2} \right) \sinh \beta \quad \left[\frac{1}{\text{Hz}} \right], \quad (2.24)$$

677 where $|v_0| \approx 220$ km/s is the circular rotation speed of the Galaxy at the radius of the sun

678 (approximately 8 kpc), $v_{\text{lab}} \approx 233$ km/s is the relative velocity of the Sun to the rest frame

679 of the Galaxy and

$$\beta \equiv \frac{2 c v_{\text{lab}}}{v_0^2} \sqrt{\frac{2 (\nu - \nu_{\text{DP}})}{\nu_{\text{DP}}}}.$$

680 Equation 2.24 is used to generate Fig. 4.14. Note the quality factor $Q_{\text{DP}} \approx 10^6$ as

681 mentioned above.

682 2.1.3 Radio Frequency Interference

683 Radio Frequency Interference (RFI) includes any coherent interfering signals which can be

684 detected by the experiment. While noise is better described as a power spectral *density*

685 [W/Hz] or electric field *density* [V/(m $\sqrt{\text{Hz}}$)], RFI is made up of more narrow lines and is

686 discussed in terms of a power [W] or electric field [V/m]. In this experiment, RFI is mitigated

687 through the shielding effectiveness (SE) of the cavity. SE measurements and more details

688 about local RFI are discussed further in Sec. 2.5.1 and Sec. 3.2, and a plot of the local RFI

689 spectrum is shown in Fig. 3.14.

690 The peak RFI spike is at 186 MHz and approximately 100 $\mu\text{V}/\text{m}$, an energy density

691 of roughly 10^{-11} W/m². This will be reduced by the SE of the room (roughly 120 dB at

692 200MHz, see Fig. 3.11), but just like a coherent dark photon, it will be enhanced by the

693 Q/effective aperture. This will be right on the edge of detection, but in the actual data run
 694 it was not detected.

695 **2.1.4 Amplifier Chain Noise⁴**

696 Any amplifier will have some noise which it adds to an incoming signal which will degrade
 697 the signal to noise ratio (SNR) of the measurement ⁵. A low noise amplifier (LNA) is an
 698 amplifier which has been specifically designed to minimize the noise contribution. This
 699 process is shown schematically in Fig. 2.7.

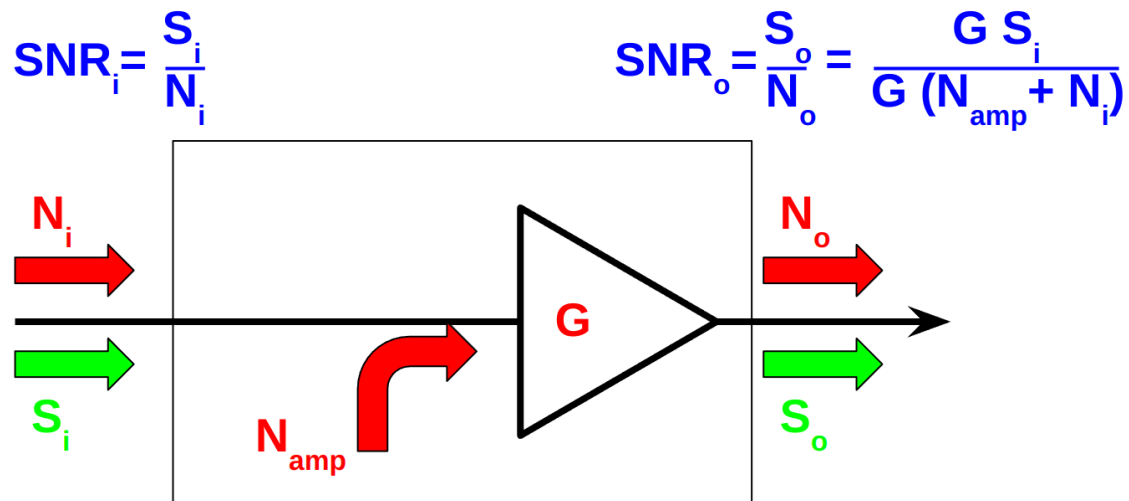


Figure 2.7: Schematic of LNA (with power gain G) adding input referred noise N_{amp} . Since N_{amp} is referred to the input, it can be directly added to the input noise which is itself input-referred. The ideal, noisless, amplifier is represented by the triangle, while the physical amplifier including noise is contained in the rectangle.

⁴Code for this section can be found at: <https://github.com/josephmlev/darkRadio/tree/master/thesis/ch2/CH2.ipynb>

⁵A great lecture on the subject by Prof. Greg Durgin can be found at [35]

700 The performance of an LNA is generally evaluated by its noise factor (F). F is defined
 701 to be the ratio the SNR at the input of an LNA to that at its output.

$$\begin{aligned}
 F &\equiv \frac{\text{SNR}_i}{\text{SNR}_o} \\
 &= \frac{S/N}{[S G]/[(N + N_{\text{amp}})G]} \\
 &= \frac{1}{1/[1 + N_{\text{amp}}/N]} \\
 &= 1 + \frac{N_{\text{amp}}}{N},
 \end{aligned} \tag{2.25}$$

702 where S and N are the signal and noise [W] presented to the LNA respectively, N_{amp} is
 703 the input-referred noise added by the LNA and G is the power gain. By factoring out the
 704 implicit $k \Delta\nu$ from $N = kT\Delta\nu$, we find

$$F = 1 + \frac{T_e}{T_0}, \tag{2.26}$$

705 where T_e is the noise temperature of a device and T_0 the temperature of the system being
 706 measured by the LNA.

707 Note that following the same derivation as Eq. 2.25, it is simple to show that the noise
 708 figure of an attenuator at temperature T with loss L is given by

$$F_{\text{att}} = 1 + \frac{(L - 1)T}{T_0}, \tag{2.27}$$

709 where T_0 is the reference temperature defined above. If $T = T_0$, Eq. 2.27 simplifies to
 710 $F_{\text{att}} = L$

711 In order to standardize device specifications for across system applications, it is common
 712 to choose a reference temperature T_0 of 290K. If not specified, it is generally safe to assume
 713 this has been done.

714 Noise factor is simply defined from noise figure,

$$\text{NF} \equiv 10\log_{10}(F). \quad (2.28)$$

715 When working with LNAs, all three measurements (T_e , F and NF) are frequently used
 716 and one must use Eqs. 2.26 and 2.28 to convert between them.

717 One important generalization is that of a cascaded series of amplifiers, shown schemati-
 718 cally in Fig. 2.8.

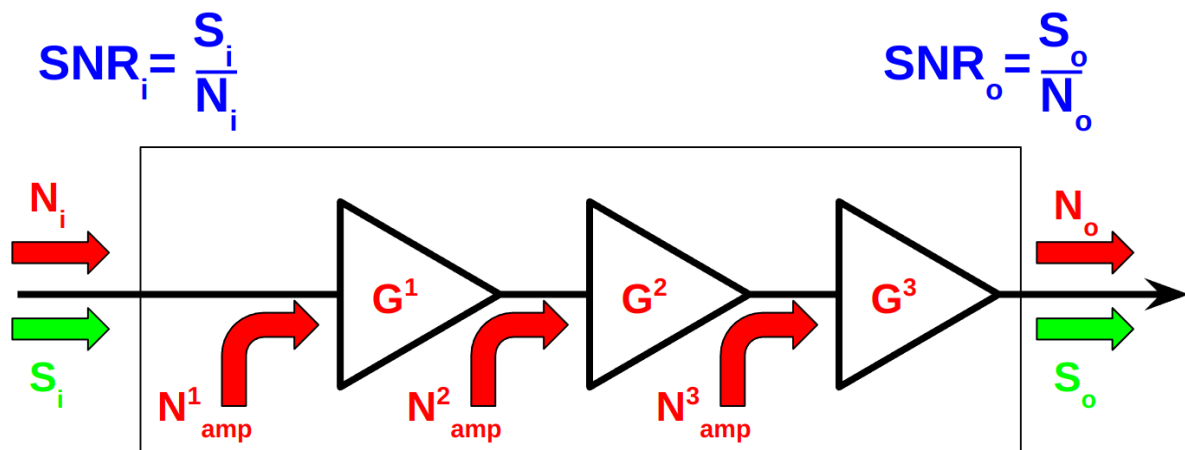


Figure 2.8: Schematic of cascade of $n = 3$ amplifiers and their added noise N_{amp}^n . Each amplifier has a gain of G^n . The SNR at the output is derived in Eq. 2.29. Note that superscripts in the figure and caption refer to index of each component and are not exponents.

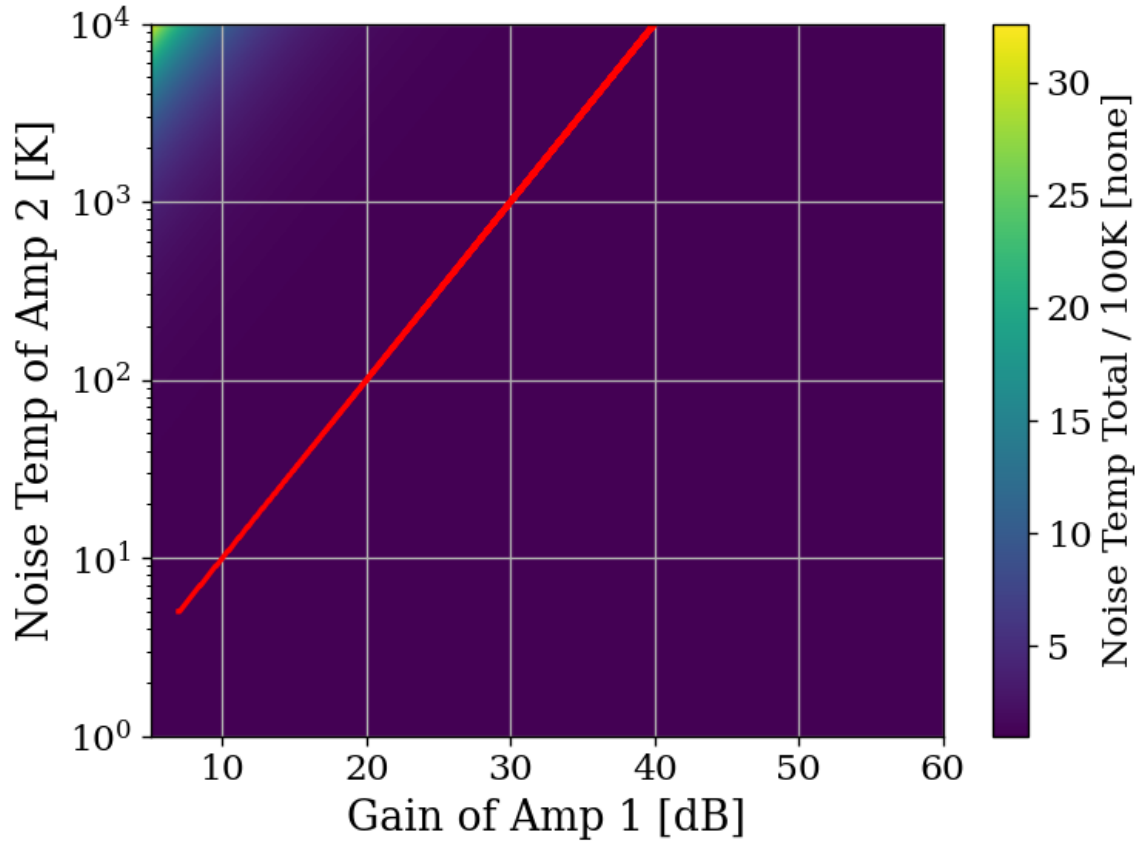


Figure 2.9: Cascaded noise temperature for system with $n = 2$ amplifiers, normalized to noise temperature of amplifier 1 (the so called LNA) = 100 K. Shown schematically (for $n = 3$) in Fig. 2.8. First amplifier's noise temperature and gain (40 dB and 100 K respectively) roughly equivalent to the LNA used in phase 1A of the experiment[36]. Red curve shows where the system's noise temperature is 1% higher than LNA noise temperature. This shows that for a 40 dB, 100 K LNA, in order to change the system noise temperature by 1 K, a second stage amplifier with a noise temperature of 10^4 would be required. Secondary amplifiers with noise temperatures closer to 500 K are realistic and inexpensive. Note that red curve should continue, but is cut off as a plotting artifact.

719 Here the total noise figure of n amplifiers can be shown to be

$$F_{\text{total}} = F_1 + \frac{F_2 - 1}{G_1} + \frac{F_3 - 1}{G_1 G_2} + \cdots + \frac{F_n - 1}{G_1 G_2 \cdots G_{n-1}}, \quad (2.29)$$

720 following the same derivation as Eq. 2.25. Since the noise temperature of a system depends

721 on the noise temperature a given amplifier divided by he gain which precedes it, a front-end
722 LNA with modest gain ensures the total noise figure of the the system is equal to it's noise
723 figure to very good approximation. This is shown in Fig. 2.9. We will use this approximation
724 and assert

$$\text{Amp Chain Noise} = \text{LNA Noise}, \quad (2.30)$$

725 Where LNA here is taken to mean the first gain stage in the amplifier chain
726 Noise figures are typically frequency dependant, though they vary slowly over frequency
727 and can be approximated as constant over narrow frequency bands. Noise figures are typically
728 given on the data sheet of the LNA [36], but can also be measured. Measurement of LNA
729 noise is covered in Sec. 3.1.1 and is shown in Fig. 3.4 (which is in good agreement with the
730 LNA's data sheet [36]).

731 The power contributed by the LNA's noise is simply given by

$$P_{\text{LNA}} = kT_e\Delta\nu \quad (2.31)$$

732 This is again the mean of a fluctuating power, just as 2.16.

733 2.1.5 ADC effects

734 “ADC effects” is a catch all term which refers to power introduced by an analog-to-digital
735 converter. It contains are a three components, listed in order of importance;

$$\text{ADC Effects} = \text{Spurious Signals} + \text{ADC Noise Floor} \quad (2.32)$$

736 Equation 2.29 shows that gain G introduced before a noisy element in the RF chain, will
737 reduce the relative contribution of that noise by a factor of G . The same idea applies to
738 ADC effects, though one must be careful with the language used to describe this; spurious
739 signals are not noise, and the experiment's output *is* mostly noise.

740 **2.1.5.1 Spurious signals**

741 Spurious signals (also known as spurs) are coherent signals which are introduced into the
742 signal path at the ADC⁶. They are likely caused by candidates caused by RFI due to various
743 clocks in the PC in close proximity to the ADC. The coherence of spurs means they will pop
744 up above the noise with more averaging. Spurs don't degrade the SNR of the experiment in
745 the same way a noisy amplifier chain would; instead, they produce false positive candidates
746 which must be excluded, similar to RFI discussed in Sec. 2.1.3. Similar to ADC noise,
747 they can be measured easily by terminating the input of the ADC and scanning. They are
748 investigated in Sec. 3.3.2 and shown in Fig. 3.15, where they are shown to be nearly negligible,
749 having been mitigated by the gain of the system. There is a single spur detected after a few
750 days (see Sec. 4.2.5), but for this simple analysis we will assume spurs are negligible.

751 **2.1.5.2 ADC noise**

752 ADC noise can simply be measured by terminating the input and taking a scan. This is is
753 the same procedure as with spurs, and can be seen in Fig. 3.15. The result is that ADC

⁶Note that these spurs described here are not the same as the spurs that are described by the ADC specification *spur free dynamic range* (SFDR). SFDR is measured in dBc, i.e. *relative* to a carrier. Since our "carrier" is broadband noise, each bin produces some spurs which are -66 dBc [37] relative to itself. The aggregate of these spurs are also broadband, and averages down with the experiment's noise. The SFDR spurs are negligible for an experiment which looks at a noise-like background.

754 noise is $\approx -130\text{dBm}/47.7\text{Hz}$; a factor of 10^5 lower than the thermal noise of the experiment
 755 $\approx -81\text{dBm}/47.7\text{Hz}$, both output-referred⁷, which agrees with the ADC's data sheet [37].
 756 Since ADC noise follows the same scaling as the experiment's thermal noise (Eq. 2.16), this
 757 factor of 10^5 is independent of averaging, and ADC noise is totally negligible.

758 2.2 Toy Analysis⁸

759 With each of the terms of Eq. 2.1 defined in the previous section, we will now perform and
 760 view several simulations of a simplified dark photon signal on a simplified background. This
 761 section should provide intuition about the process of detecting a weak, narrow signal on a
 762 background PSD of thermal noise. It is assumed the noise has been averaged a sufficient
 763 number of times such that it's PDF is Gaussian (discussed in Sec. 2.1.1.3). Furthermore,
 764 following the discussion of Sec. 2.1, Eq. 2.1 can be simplified by setting RFI and ADC
 765 Effects to zero and combining Thermal Noise (300 K) with Amp Chain Noise (100 K) into a
 766 single term which represents the total of the noise in the whole system, $S_{\text{sys}} = P_{\text{sys}}/\Delta\nu_{\text{RF}} =$
 767 $k(T_{\text{ant}} + T_{\text{LNA}})$. With these simplifications, the input-referred measured power of Eq. 2.1
 768 reduces to

$$P_i = P_{\text{DP}} + kT_{\text{sys}}\Delta\nu_{\text{RF}} \left[1 \pm \frac{1}{\sqrt{N}} \right], \quad (2.33)$$

769 where $T_{\text{sys}} \equiv 400$ K, realistic for the experiment that is being simulated. Also note that this
 770 equation assumes the dark photon's line shape is much more narrow than $\Delta\nu_{\text{RF}}$ such that the

⁷Technically it doesn't matter where they are referred since they are taken in ratio. As long as they are referred to the same point!

⁸Code for this section can be found at: <https://github.com/josephmlev/darkRadio/tree/master/thesis/ch2/toyAnalysis.ipynb>

771 measured input-referred dark photon power is independent of $\Delta\nu_{\text{RF}}$. In the simulations the
772 line shape will be modeled as a delta function as in Eq. 2.20. The signal will be introduced
773 simply by adding some power in a single bin to a Gaussian background in frequency domain.
774 Performing an FFT on a perfect (discretized) sine wave can cause it's power to be split among
775 adjacent bins depending on the ratio of the sample rate to the sine wave's frequency. This
776 can be minimized by windowning the the time-domain data as is discussed in Ch. 2 Sec. 2
777 of Ben Godfrey's thesis [38]. This effect is avoided by working in the frequency domain and
778 adding power to a single bin which is the method used here. A reminder that throughought
779 this thesis, code is available at github and is linked in the footnote of each section title.

780 With a simple simulation framework in place, we can now begin to generate signal-
781 containing-spectra. Figure 2.10 qualitatively shows the 400 K system noise (input-referred
782 antenna plus LNA) averaging down, leaving a small signal visible. Further subsections in
783 this section will quantify this.

784 With a basic conceptual framework in place, it is now simpler to quantify signal detection
785 and the uncertainty on how many averages are required to detect a signal and have that
786 detection be significant in that it isn't a random fluctuation (false positive).

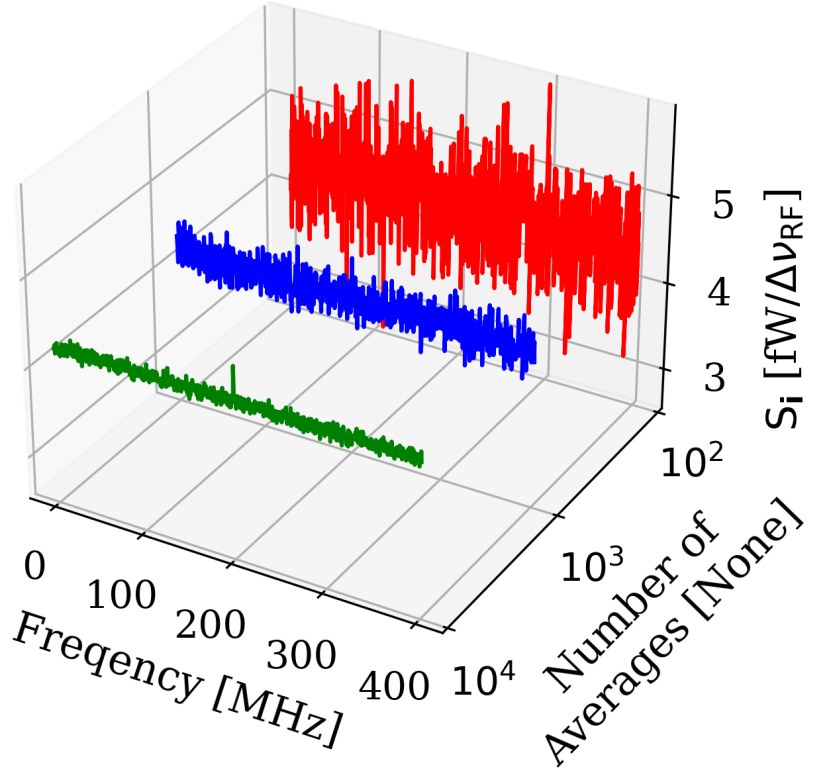


Figure 2.10: Input-referred power spectral density from simplified simulation illustrating noise averaging down to reveal a persistent, software-injected, dark photon proxy signal. The red, blue and green spectra represent 100, 1,000 and 10,000 averages respectively. The power of the signal P_{DP} is set to 0.4 fW and it only occupies a single bin. The mean of the noise is $\approx 4.3 \text{ fW}/\Delta\nu_{RF}$ where $\Delta\nu_{RF} \approx 0.78 \text{ MHz}$. The standard deviation ranges between $0.41 \text{ fW}/\Delta\nu_{RF}$ and $0.041 \text{ fW}/\Delta\nu_{RF}$ for 100 and 10,000 averages respectively. Note that this factor of 10 reduction in noise is predicted by the Dicke radiometer equation Eq. 2.16 for a factor of 100 times more averaging, as is shown in the red and green curves. Noise represents a 300 K antenna into a 100 K LNA for a total system temperature of 400 K. Signal is in a single bin at 200 MHz with a delta function line shape, defined in Eq. 2.20.

⁷⁸⁷ 2.2.1 Signal significance

⁷⁸⁸ The problem of the extraction of signal from noise is fundamentally a statistical one since,
⁷⁸⁹ in general, both the signal and noise are random variables. A method for computing a

790 *significance threshold* (ST) must be established, such that any bin containing more power
791 than this threshold is X % significant. In this way, it is possible to have some known
792 confidence a given signal was not just a random fluctuation.

793 The probability that all N bins are less than z standard deviations $z\sigma$ for a standard
794 Gaussian distribution is given by

$$P(\max < z\sigma) = \left\{ \frac{1}{2} \left[1 + \operatorname{erf} \left(\frac{z}{\sqrt{2}} \right) \right] \right\}^N, \quad (2.34)$$

795 where P is the probability, $\operatorname{erf}(z)$ is the standard error function and z is real. Setting
796 this equal to 100%–X (where X is the *significance* or the desired probability a fluctua-
797 tion crosses the $z\sigma$ threshold assuming no signal), and inverting $\operatorname{erf}(z)$ yields a significance
798 threshold (ST). A convenient significance that was used in [39] is X = 5% corresponding to
799 a 5% probability that an observed fluctuation above this ST is due to chance rather than a
800 significant effect (i.e., a signal). A 5% ST for $2^{10}/2 = 512$ frequency bins⁹ works out to 3.9σ .

801 It should be noted that it is common in physics to discuss “ 5σ significance”. This means
802 that a given experiment has a $1 - \operatorname{erf}(5/\sqrt{2})$ probability (about 1 in 3×10^6) of a false positive.
803 The analysis of these normal spectra involves testing many independent frequency bins to see
804 if any one of them exceeds some threshold. It is helpful to view these bins as “independent
805 experiments”, each involving a random draw from the same parent Gaussian distribution.
806 In this context, we discuss global significance (all of the bins) in contrast to local significance
807 (a single bin). Setting a global 5% significance threshold is equivalent to setting a local

⁹Note that a real FFT produces half the number of frequency bins as an output compared to the time domain sample it received, hence the factor of 2 established in Fig. 2.4

808 threshold of 3.9σ given 512 bins.

809 One concept that can assist in choosing the significance is known as the *cost* of a decision.

810 If an experiment requires a facility that charges by the hour and where the schedule is
811 set years in advance, a false positive is quite expensive since it will lead to publicity and,
812 ultimately, humiliation. A follow-up experiment will have to take out more expensive time
813 to verify the results, and until that happens, theorists will spend their time rewriting physics
814 to explain the result of a random fluctuation. In this case, the global significance should
815 be quite low to avoid these high-cost outcomes, hence the 5σ discussed in the previous
816 paragraph.

817 In the case of the dark radio experiment, a false positive is quite inexpensive. If a signal
818 is detected, just repeat the experiment. For run 1A, this is 9 days of averaging which is
819 mostly passive and is little more than an annoyance. If a signal is detected at the same
820 frequency, things become interesting. This concept of cost is discussed formally in Appendix
821 1 of Extraction of Signals From Noise by Wainstein and Zubakov [40].

822 For this reason, a significance of 5 % (i.e. 5 % chance of a false positive) is acceptable
823 for this experiment, where it is certainly not acceptable at the LHC.

824 **2.2.1.1 Computing an exclusion limit**

825 With the significance threshold (ST) defined for a spectrum containing a signal in the previ-
826 ous subsection, we turn briefly to the concept of an exclusion limit. In the actual experiment,
827 no signals were detected. In this case, the null result must be translated into an exclusion
828 limit, as in Fig. 4.21. While this section on toy analysis looks at small signals riding on noise

829 spectra, it can be easy to lose sight of the fact that no signal was observed.

830 It is tempting to draw a line above the spectrum, claim no signals were observed above
831 it, and cite that as the exclusion limit. This is the red dashed line in Fig. 2.11. However,
832 this line is riding on the thermal background and is actually significantly higher than the
833 true exclusion limit, which is shown in dashed green. The mean μ must be subtracted off
834 of this upper (red) line to compute the exclusion limit. In Fig. 2.12, the exclusion limit is
835 pushed down with additional averaging, resulting in a detection of a small signal shown as
836 an orange dot. The frequency-dependant exclusion limit from the actual run 1A data run is
837 shown in Fig. 4.8.

838 With the derivation of the significance threshold complete, the next subsection will focus
839 on predicting the amount of time.

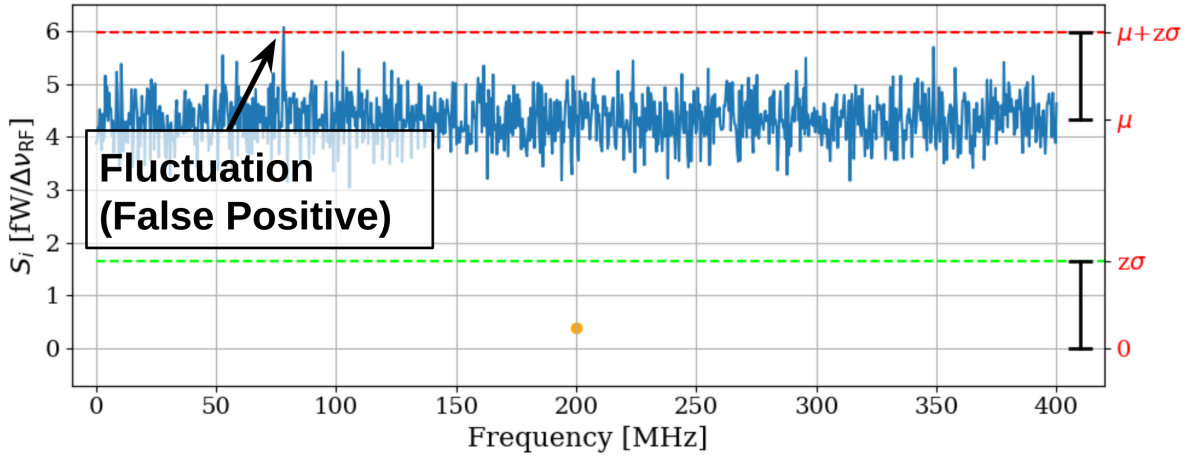


Figure 2.11: Simulated, input-referred noise spectrum containing small signal at 200MHz. The signal power = 0.4 fW, system temperature = 400 K and $N_{avg} = 100$; the same as is shown in the red spectrum of Fig. 2.10. The 0.4 fW signal is shown as an orange point. This power is added to the random background, so the measured power in the bin at 200 MHz is a Gaussian random variable given by Eq. 2.33; the mean is shifted up by the power contained in the signal. The dashed red line shows $\mu + z\sigma$, where z was derived in section 2.2.1. The detection threshold (dashed green line) is the red line minus the mean, $(\mu + z\sigma) - \mu = z\sigma$. This shows that the detection threshold is set by *fluctuations* of the measured power spectrum and not its mean. Note the detection at approximately 75 MHz; this is a random fluctuation and is expected to occur in 5 out of 100 simulations of these spectra since the significance used to calculate the ST was set at 5%.

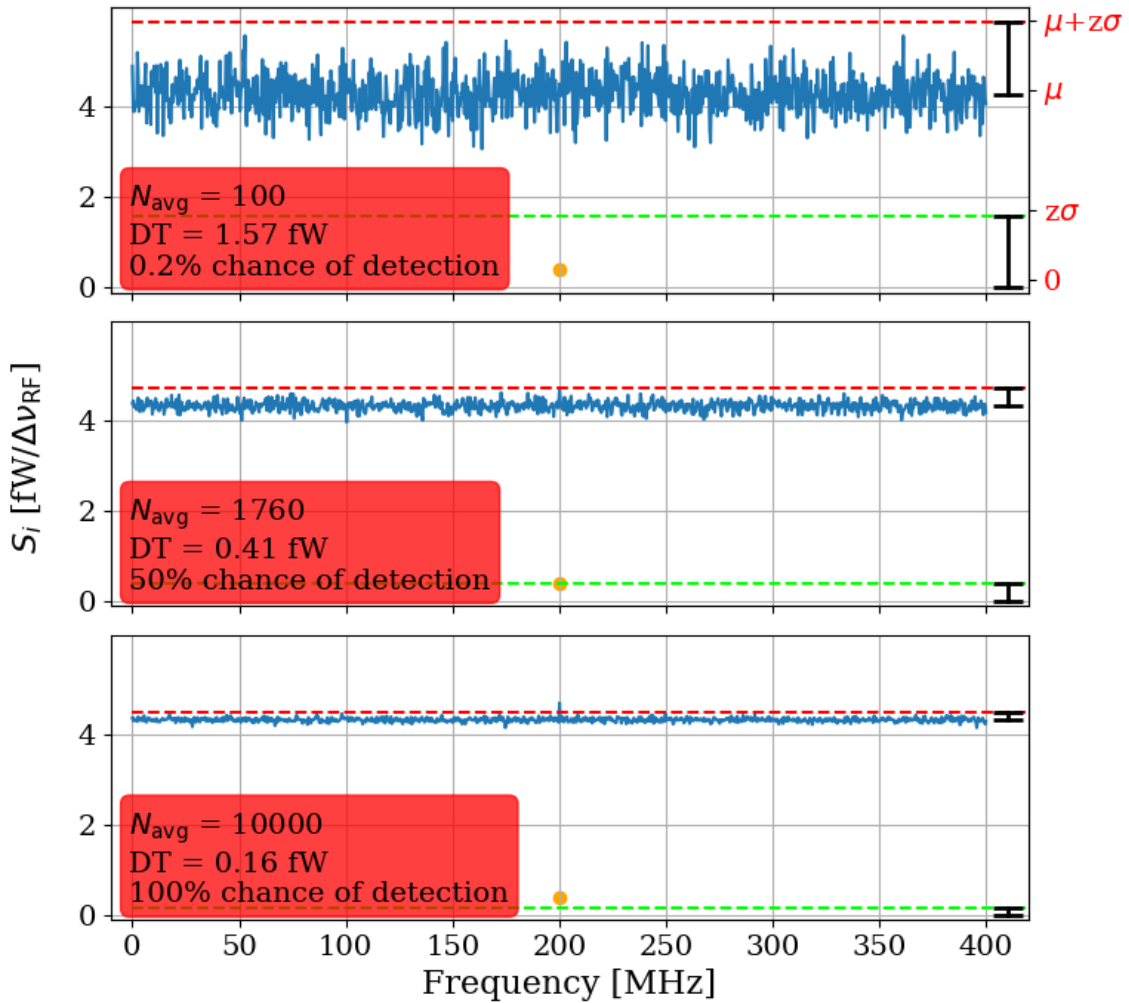


Figure 2.12: Simulated, input-referred noise spectrum containing small signal at 200MHz. The signal power = 0.4 fW, system temperature = 400 K and N_{avg} = 100, 1,760 and 10,000; the first and last are shown as the red and green spectra respectively in Fig. 2.10. The 0.4 fW signal is shown as an orange point. The chance of detection is computed via a simple Montie Carlo where 100,000 similar spectra containing noise and signal are generated, and the number of times the measured power at 200 MHz is greater than $\mu + z\sigma$ (red dashed line). The full set of statistics from this Montie Carlo is shown in Table 2.1. The detection threshold (DT, dashed green line) is $(\mu + z\sigma) - \mu = z\sigma$. Note that red labels on right Y-axis are suppressed for the second and third subplots to prevent clutter, but they are the same as the first subplot

840 **2.2.2 Predicted time to detection**

841 To conclude this subsection, Fig. 2.13 fills in the gaps between the three sub-plots shown
842 in Fig. 2.12. The continuous detection threshold is shown to decrease following $1/\sqrt{N}$
843 shape given by Eq. 2.16. The intersections with this curve and the $1-\sigma$ uncertainty of the
844 background give the $1-\sigma$ uncertainty on the number of averages required for a the known
845 signal and background. Table 2.1 summarizes the statistics for probability of detection for
846 a few numbers of averages.

Number of Averages	True Pos. [%]	False Neg. [%]	False Pos. [%]	True Neg. [%]
100	0.2	99.8	5.7	94.3
971	16.3	83.7	5.5	94.5
1,760	49.8	50.2	5.7	94.3
2,782	83.8	16.2	5.7	94.3
10,000	100.0	0.0	5.6	94.4

Table 2.1: Statistics of simple Monte Carlo simulation for the probability of signal detection in the toy analysis. Number of averages chosen based on Fig. 2.13. 100 and 10,000 averages show extreme cases, 1760 is a 50% chance of detection, and the two remaining values show the $\pm 1\sigma$ uncertainty band (shaded red region in Fig. 2.13).

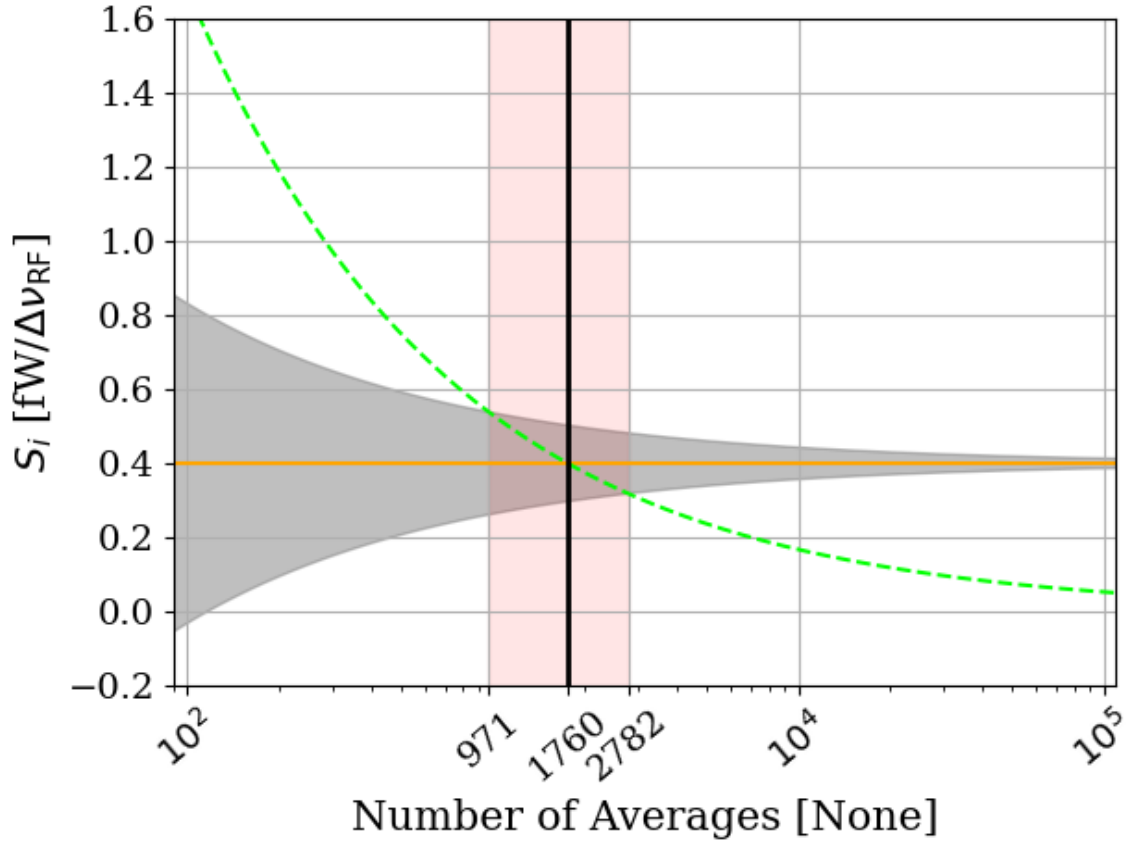


Figure 2.13: Predicted time to detection for the toy analysis spectra shown throughout this section. This is a companion to Fig. 2.12 and shows all numbers of averages between the three subplots shown in that figure, though only at a single frequency bin; 200 MHz in the case of the previous figures in this section. Orange line represents the known, injected signal, shown as orange points in Fig. 2.12. Gray shaded region shows the standard deviation of the noise σ , which is equivalent to the uncertainty on the measured power. It is given by Eq. 2.16, and scales with the square root of time. Dashed green curve is the exclusion limit defined in Sec. 2.2.1.1. It is also shown as a dashed green line in Fig. 2.12. Finally, red shaded region shows intersection of exclusion limit (dashed green) with measurement uncertainty (shaded gray), which gives the $\pm 1\sigma$ uncertainty on the number of averages required to detect the signal. The detection statistics from a simple Monte Carlo simulation at a few points from this plot are shown in Tab. 2.1. This figure is a recreation of Fig. 3 in [4].

847 2.3 Thermal Noise in a Cavity: Thermal Wiggles

848 This section is concerned with the topic of variations of thermal noise emerging from a cavity;
849 “Thermal Wiggles”. Throughout this experiment, this was a challenging concept since the
850 theory outlined in Sec. 2.3 predicts the experiment will measure a frequency-independent
851 noise spectrum, and it doesn’t. This theory will be expanded upon, the data that seem
852 not to conform to this theory will be presented, the reasons for this disagreement will be
853 discussed, and finally, an experiment that tests this understanding will be presented.

854 2.3.1 Theory of thermal radiation in a cavity

855 In his 1946 paper The Measurement of Thermal Radiation at Microwave Frequencies [28],
856 Robert Dickie presented a thought experiment to derive the aperture of a matched antenna
857 from thermodynamic arguments. This was previously discussed in Sec. 2.1.1.2.

858 To recap the argument; if an antenna (in a black cavity) and matched load are matched
859 to a transmission line and in thermal equilibrium (the situation presented in Fig. 2.3), the
860 net power flow in the line must be zero by the second law of thermodynamics. If there was
861 a power flow, one of the environments would warm up, resulting in spontaneous pumping of
862 heat. An interesting way to model this situation is by treating the antenna as an aperture
863 in the cavity, as pointed out in [41].

864 A simpler model removes the antenna and load altogether. Although removal of the
865 antenna also removes the ability to perform the measurement, this is a useful thought exper-
866 iment. In Fundamentals of Statistical and Thermal Physics [42], F. Reif uses four examples

867 to explore the radiation field $f_\alpha(\kappa, \mathbf{r})$ (wave vector κ at position \mathbf{r} with polarization α)
 868 within cavities connected by an aperture (see Fig. 2.14). All cavities and materiel contained
 869 within them are presumed to be in thermal equilibrium. As we shall see, this function is
 870 independent of position, direction, polarization and specifics of the cavity. It can be written
 871 simply as $f(|\kappa|)$, where the dependence on wave number is simply given by Eq. 2.6.

$$f_\alpha^{(1)}(\kappa) = f_\alpha^{(2)}(\kappa)$$

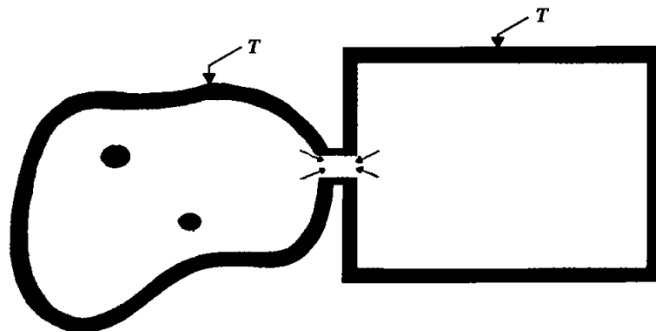


Figure 2.14: Two cavities in thermal equilibrium of arbitrary shape, material and physical contents contain equivalent radiation fields $f_\alpha(\kappa, \mathbf{r})$. Figure from Reif [42].

- 872 **1. Independence of Position:** The radiation field inside an enclosure is homogeneous,
 873 meaning $f_\alpha(\kappa, \mathbf{r}) = f_\alpha(\kappa)$, independent of position \mathbf{r} . If the radiation field depended
 874 on position, two identical bodies at temperature T placed at different points in the
 875 enclosure would absorb different amounts of radiation, leading to a temperature dif-
 876 ference.
- 877 **2. Independence of Direction:** The radiation field is isotropic, meaning it depends
 878 only on $|\kappa|$ and not its direction. If this were not true, then bodies placed in the
 879 enclosure would absorb different amounts of energy based on orientation.

880 3. **Independence of Polarization:** The radiation field is unpolarized, meaning $f(|\kappa|)$
881 is independent of the polarization index α . If it depended on polarization, bodies
882 surrounded by polarizing filters would absorb different amounts of radiation depending
883 on the orientation, leading to temperature differences.

884 4. **Independence of Enclosure Shape and Contents:** The function $f(|\kappa|)$ is inde-
885 pendent of the shape, volume, and material of the enclosure, as well as the bodies
886 contained within. The argument is that if $f^{(1)}(|\kappa|)$ and $f^{(2)}(|\kappa|)$ were different for two
887 enclosures at the same temperature T , then connecting them would result in unequal
888 radiation transfer. Therefore, $f(|\kappa|)$ must be the same across different enclosures.

889 To further flush out argument four, picture a photon entering a metallic cavity (emissivity
890 < 1) through a small hole as in Fig. 2.15. At each bounce, the photon has a probability of
891 absorption given by the emissivity (a photon hitting a perfect black body has a 100% chance
892 of being absorbed). As long as the geometries of the cavity and aperture allow a photon to
893 bounce many times before it escapes, even a highly reflective cavity will behave like a black
894 body. This is because when a photon enters, it is likely to be absorbed and a new photon will
895 be emitted with a random wavelength drawn from the blackbody spectrum corresponding
896 to the temperature of the walls. (Fig. 2.2).

897 The conclusion is rather surprising; a cavity with a small aperture will behave as a
898 black body, and the spectrum emanating from a black body is a universal function that is
899 independent of the cavity and its modes. Therefore, **a well-matched antenna in a cavity**
900 **will not measure the modal structure of the cavity.** This seems to defy intuition.

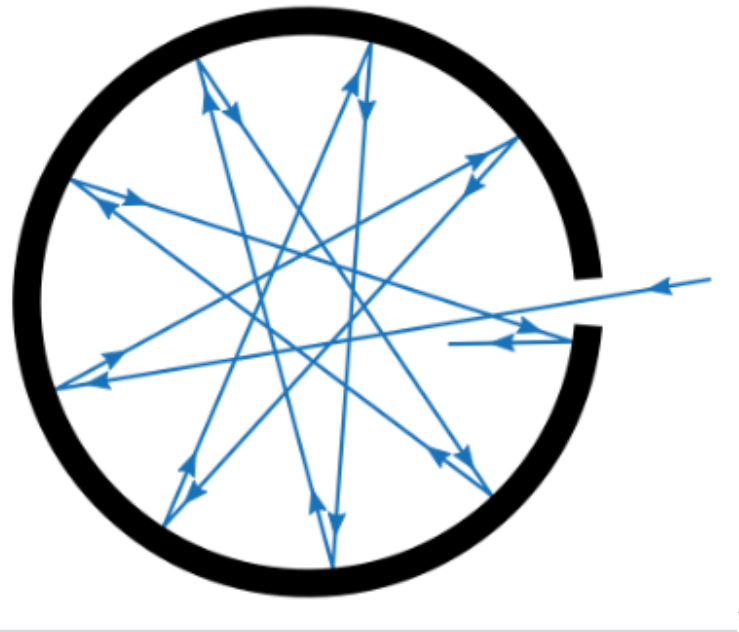


Figure 2.15: A cavity with a small hole behaves like a black body as long as the probability of absorption $\ll 1$. The probability of absorption at each reflection is given by the emissivity, so the total probability of *reflection* is the emissivity raised to the power of the average number of bounces. Figure from Wikipedia.

901 Cavities are resonators, and resonators... resonate?

902 The resolution to the seeming discrepancy is that this intuition only holds outside of
903 equilibrium, a situation that is nearly ubiquitous in engineering contexts. A resonant cavity
904 has the resonance it does because photons are being pumped in faster than they can be
905 absorbed by the walls and remitted with a thermal distribution. In this out-of-equilibrium
906 case, the photons interfere in such a way as to excite cavity modes. Turn the amplitude of the
907 source down to $\approx kT$ and the modes vanish. This case, among others, will be investigated
908 in the following subsections.

909 **2.3.2 Inspection of thermal noise spectra**¹⁰

910 The theory outlined above predicts the (input-referred) spectrum of an antenna in a cavity
911 should not vary with frequency if there is thermal equilibrium between the cavity and the
912 receiver system¹¹. A real measurement will take place after an amplifier (in other words,
913 will be output-referred), and will vary due to the gain and noise figure of the amplifier. A
914 simple way to correct for the amplifier is to compare the spectrum between an antenna and
915 a terminator since both will have identical gain and amplifier noise contributions. Since we
916 are more focused on the qualitative *shape* of the spectrum and not absolute input referred
917 power, this method is acceptable. A comparison of antenna and terminator data from an
918 identical amplifier chain is shown in Fig. 2.16.

919 The variations are unexpected in light of the theory presented in the previous subsection.

920 In the following subsection, the thermal spectrum emerging from a simple resonator will be
921 presented.

¹⁰Code for this section can be found at: https://github.com/josephmlev/darkRadio/tree/master/daqAnalysisAndExperiments/run1p4/thermalNoiseVsH/thermalWiggles_writeup.ipynb

¹¹this assumes $h\nu \ll kT$ (Rayleigh-Jeans limit), an ideal antenna aperture $\propto \lambda^2$, and an impedance match between the antenna and amplifier. The final assumption will be relaxed in Sec. 2.3.8.

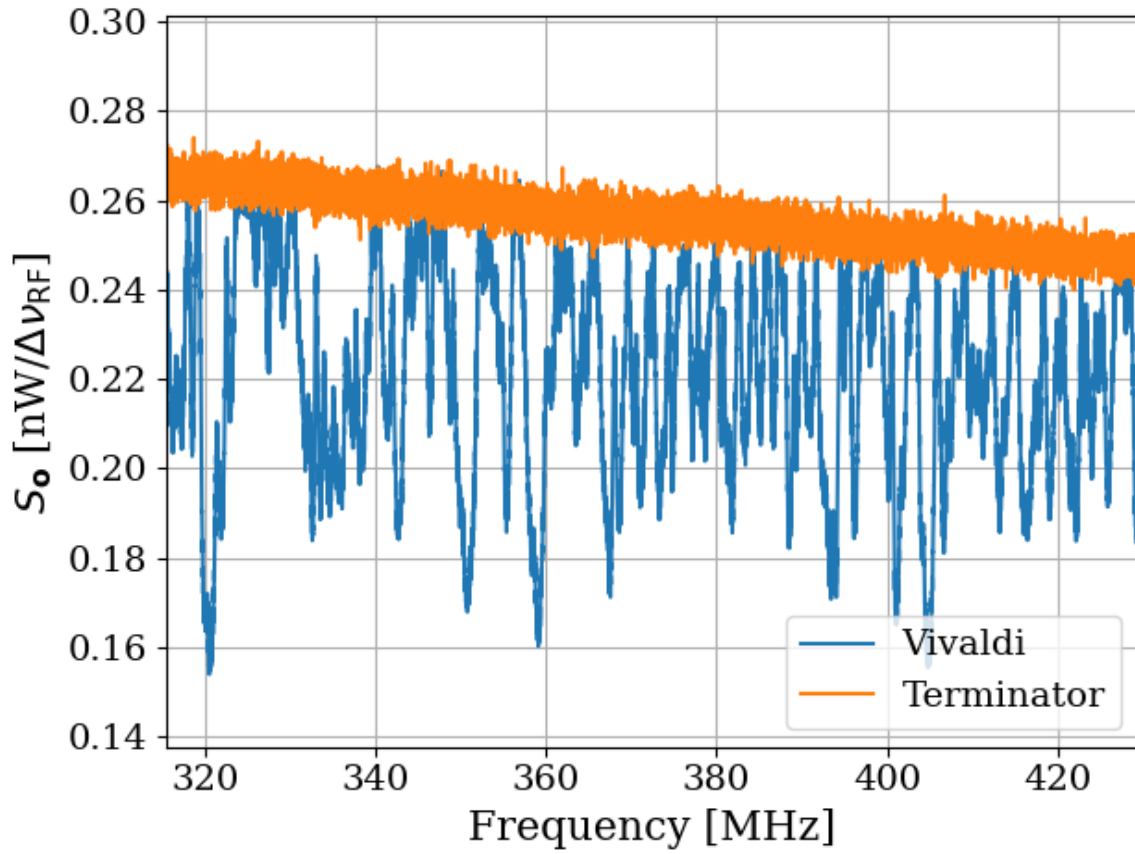


Figure 2.16: Output-referred Vivaldi antenna and terminator thermal spectra as measured through an amplifier chain ($G \sim 68$ dB, noise temperature ~ 120 K). Vivaldi is inside the shielded room. Both spectra represent about 1 second of data, with $\Delta\nu_{\text{RF}} = 9.5$ kHz. Vivaldi antenna is in a single position throughout all averaging, in contrast to the technique where it moves, outlined in later chapters.

922 2.3.3 A simple resonator: shorted coax cable

923 A coax cable that is shorted on one end and matched to a measurement device ¹² on the other
 924 is a simple resonator. The short provides a boundary condition demanding the voltage goes
 925 to zero¹³ while the measurement device, being matched, absorbs the wave. A “closed-open”

¹²In the entirety of this section, a Pasternack PE15A-1012 will be used as the front end amplifier.

¹³Similarly, an open termination will force the *current* to zero, resulting in a similar resonator, though with a 180-degree phase shift.

926 resonator such as this will resonate with frequency

$$\nu = \frac{v(2n - 1)}{4L}, \quad (2.35)$$

927 for integer $n > 0$, where v is the wave speed in the cable and L is the length. For a
928 185 cm cable with velocity factor = 69.5% (i.e. $v = 0.695 c$), this works out to a first mode
929 at 28.2 MHz and following modes every 56.4 MHz. A schematic of the setup is shown in
930 Fig. 2.17, and the output power spectrum is shown in ratio to a terminator in Fig. 2.18.
931 Also shown in Fig. 2.18 is an open termination at the end of the cable in place of the short.
932 Fitting the peaks ¹⁴ reveals the average spacing between peaks is 55.2 ± 2.4 MHz, in good
933 agreement with the prediction of 56.4 MHz of Eq. 2.35.

934 By the fluctuation-dissipation theorem, the loss of the cable will dissipate some thermal
935 noise into the system, which can excite the cable. As discussed in Sec 2.3.1, if the resonator
936 (cable) is in thermal equilibrium with the measurement device, a frequency-independent
937 power spectrum is expected. The deviation from this expectation is surprising because the
938 data seem to be in contradiction with thermodynamics. Now, a cable is not a particularly
939 good resonator ($Q \lesssim 10$), so the effects are rather small here, but the simplicity of the system
940 makes it one that is worth exploring.

941 One assumption which is critical to the above logic is that of equilibrium. The amplifier
942 is a likely culprit for breaking this equilibrium, so a test that can remove the amplifier's
943 ability to interact with the resonator is worth pursuing. Fortunately, such a test is quite
944 simple to implement using a circulator ¹⁵.

¹⁴Code for this section can be found at: https://github.com/josephmlev/darkRadio/tree/master/daqAnalysisAndExperiments/run1p4/thermalNoiseVsH/thermalWiggles_writeup.ipynb

¹⁵I got one for \$36 on Ebay!



Figure 2.17: A coax cable with a short on the end and a matched measurement device on the other behaves like a “closed-open” resonator. Replacing the short termination with an open (not shown here) produces a similar resonator, though with a 180-degree phase shift.

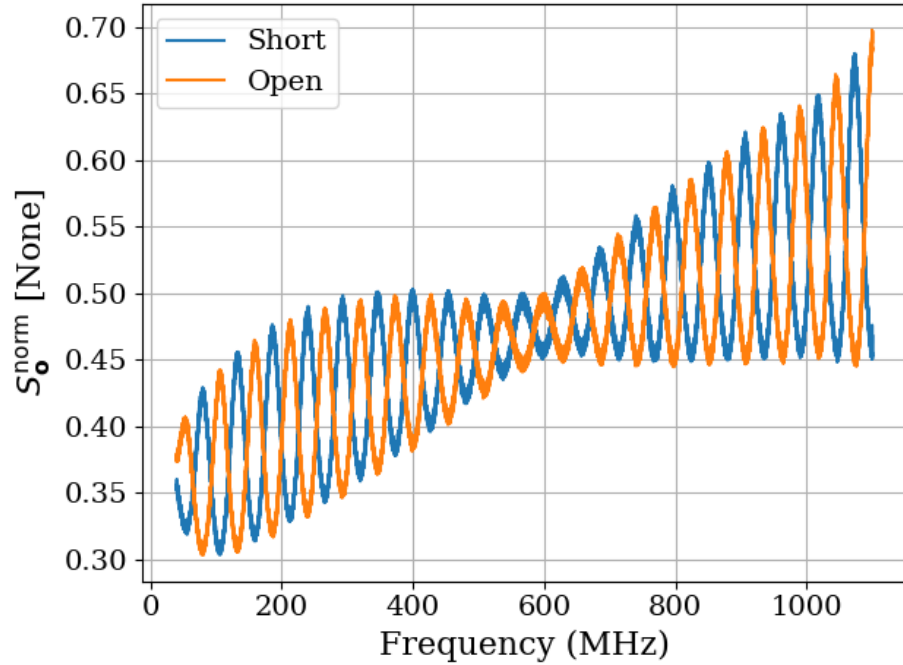


Figure 2.18: Power spectra of short (blue) and open (orange) terminations at the end of 1.85 m of RG400 coax cable (velocity factor = 69.5%). Schematic of this set-up is shown in Fig. 2.17. These spectra are normalized to the spectrum of a terminator, which was measured through the same amplifier chain. For example, when $S_o^{\text{norm}} = 0.5$, the power measured in this setup is half of the power measured by a terminator through the same amplifier chain. The average spacing between peaks is 55.2 ± 2.4 MHz, in good agreement with the prediction of 56.4 MHz of Eq. 2.35.

945 **2.3.3.1 RF circulators**¹⁶

946 A circulator is a three-port, non-reciprocal device that allows power to flow only in specific

947 ways between its ports. A schematic symbol is shown in Fig. 2.19.

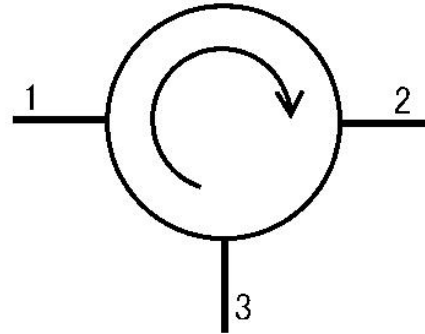


Figure 2.19: Schematic symbol of a circulator. Power can only flow from ports 1 to 2, 2 to 3 and 3 to 1. Image from Wikipedia.

948 The (linear) S-parameters of an ideal circulator are given by the matrix

$$S = \begin{pmatrix} 0 & 0 & 1 \\ 1 & 0 & 0 \\ 0 & 1 & 0 \end{pmatrix}. \quad (2.36)$$

949 In other words, in an ideal circulator, $S_{12} = 0$, so power can not flow from port 2 to port

950 1, while $S_{21} = 1$, so power can flow from 1 to 2. Also of note, the diagonal elements $S_{ii} = 0$,

951 meaning ports do not reflect power.

952 A Teledyne C-0S03A-3M RF circulator has an approximate bandwidth from 490-510 MHz

953 and was available inexpensively on eBay, so it is used for testing. A photo of it is shown in

¹⁶Code for this section can be found at: https://github.com/josephmlev/darkRadio/tree/master/thesis/ch2/circulatorData/SParameter_circulator/calc3portSPParam.ipynb

954 Fig. 2.20, and its S-parameter data are shown in Fig. 2.21. Note that a circulator with one
955 port terminated is sometimes known as an “isolator”, but I will refrain from using this term.



Figure 2.20: Photo of Teledyne C-0S03A-3M RF circulator. Lines in the background are collage-ruled lined paper (\approx 7mm spacing) for scale.

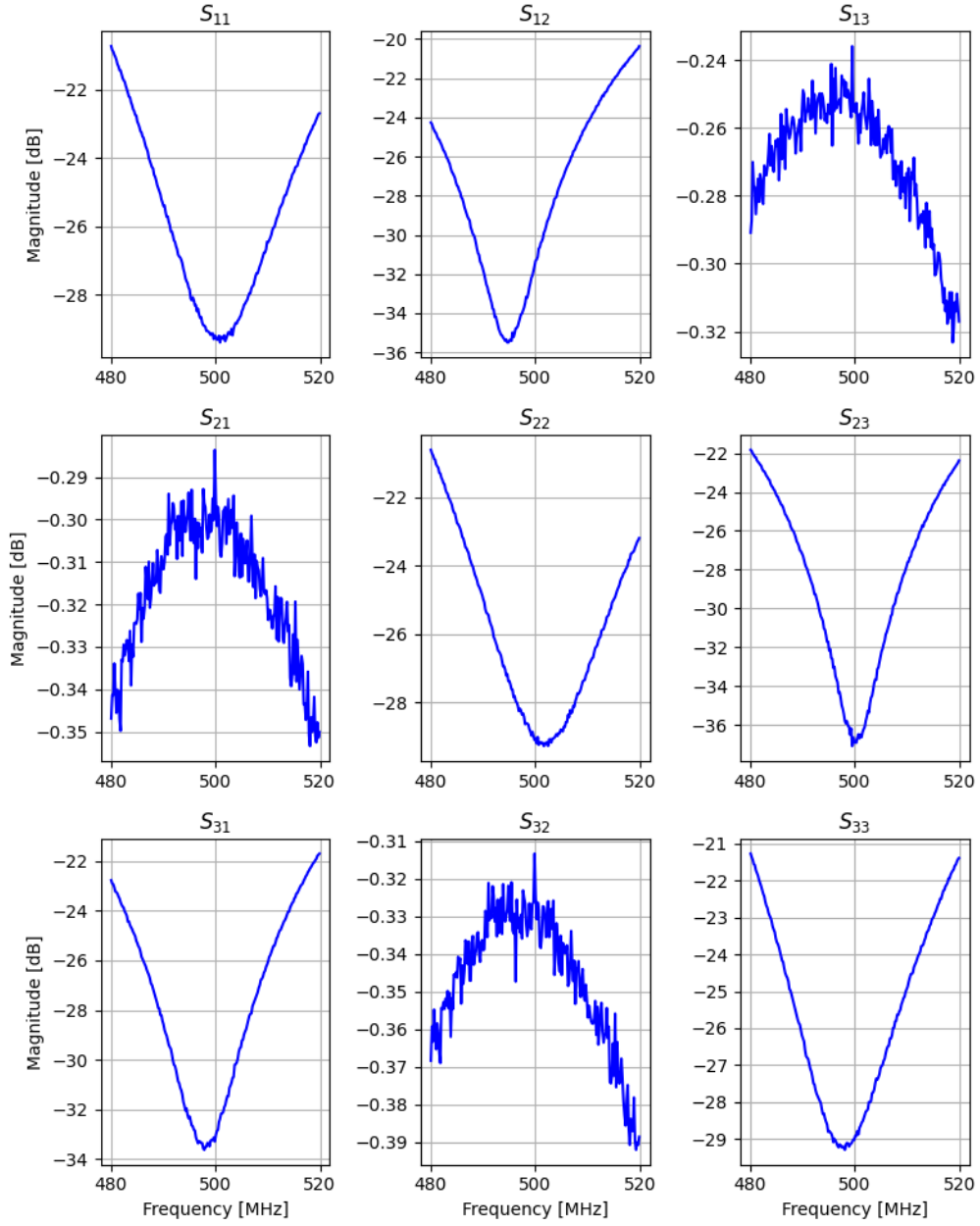


Figure 2.21: 3-port, frequency-dependent S-parameter data for Teledyne C-0S03A-3M circulator. Data taken by Ben Godfrey and Andrea Lopez Arguello with 2-port VNA with the circulator's unused port terminated. Circulator is rated for use between 490 and 510 MHz. These data show good agreement with Eq. 2.36. Note that magnitude is in dB, so these data are proportional to power, i.e. the square of linear S-parameters.

956 2.3.4 A simpler resonator: shorted coax cable and circulator

957 In light of the variations observed in Fig. 2.18, a similar measurement was made using
958 a circulator in order to isolate the coax resonator from any effects of the amplifier. The
959 schematic of this setup is shown in Fig. 2.22, and resulting the spectrum is shown in Fig. 2.23.
960 This is an interesting measurement because any net power flow from the amplifier will be
961 absorbed by the terminator on port three since it presents a good impedance match. This
962 net power flow has the potential to cause a temperature change in the terminator, however
963 it is in a thermally-conductive metal can exposed to the air which serves as a heat bath
964 and holds it very close to room temperature. The coax resonator will just see the Johnson
965 noise of the room temperature terminator in equilibrium with the Johnson noise caused by
966 its internal loss. The overall effect is a resonator that is in thermal equilibrium yet is able
967 to be measured by an extremely sensitive spectrum analyzer.

968 The result of introducing the circulator and matched load on port 3 is the removal of the
969 variations that were seen without the circulator (Fig. 2.23).

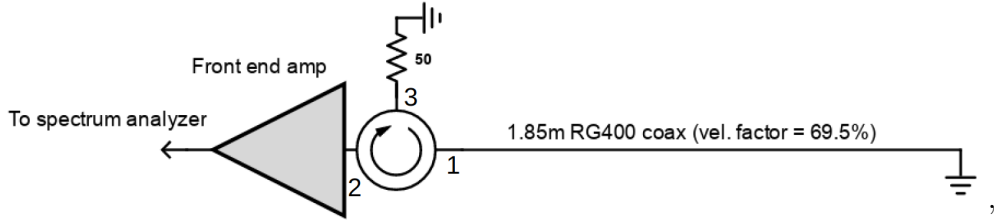


Figure 2.22: A coax cable with a short on one end and a circulator isolating the system from the amplifier.

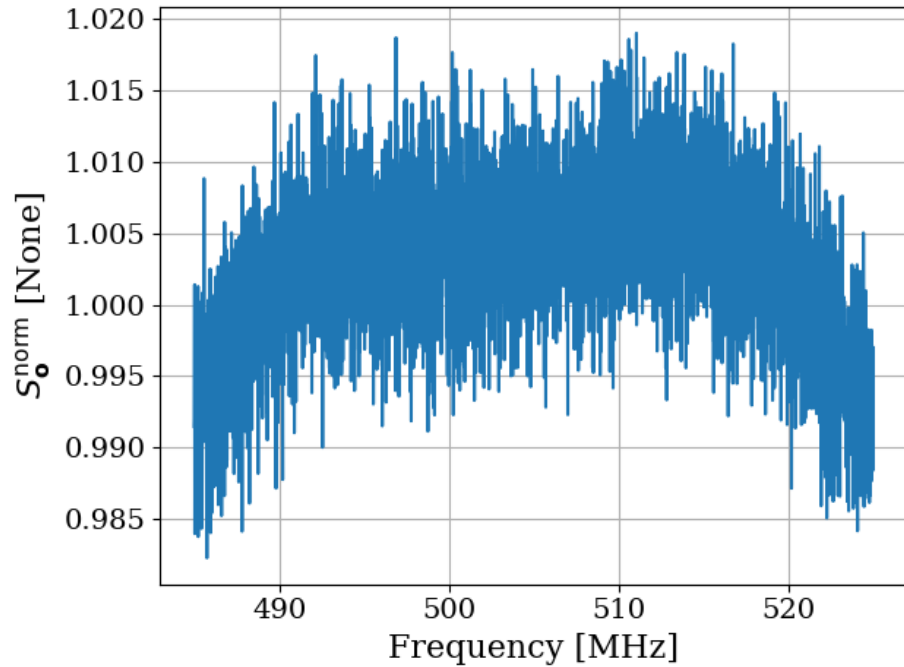


Figure 2.23: Power spectrum of 185 cm coax resonator as measured through a circulator. Short termination at the end of the cable as depicted in Fig. 2.22. The amplitude of the variations in this spectrum are on the order of half a percent and hardly visible under the noise. They are much smaller than those at the $\sim 15\%$ level without a circulator (Fig. 2.18). Also note this spectrum is normalized to a terminator through the same amplifier chain and very close to 1. The normalized spectrum without the circulator shown in Fig. 2.18 was significantly lower, around 0.5. Note that the peak-to-peak frequency variations of the cable without a circulator (Fig. 2.18) are ≈ 55 MHz, and would be visible in the ≈ 30 MHz span shown here. This span is limited by the circulator.

970 **2.3.5 A more complex resonator: antenna in room**

971 Similar to the coax resonator shown in Fig. 2.17, the antenna data presented in Fig. 2.16
972 are of a resonator (antenna-room system) which is being measured by an amplifier. The
973 experiment in the previous section suggests that the amplifier seems to have an effect on
974 the delicate thermal equilibrium which can be mitigated by including a circulator. The
975 experimental set-up for the antenna in the room is shown in Fig. 2.24, and the data from
976 this set up is shown in Fig. 2.25.

977 The result is striking. The theory outlined early in the chapter predicted the noise
978 power spectrum of an antenna in a cavity will look the same as a matched terminator;
979 -174 dBm/Hz, independent of frequency. The Dark E-Field Radio Experiment measures
980 just such a spectrum, but comparing a terminator and antenna in Fig. 2.16, they are remark-
981 ably different; the Vivaldi has large variations. However, introducing a circulator to the set
982 up such as in Fig. 2.24 removes these variations. Compare blue/orange curves in Fig. 2.25.

983 A nice test case would be to measure the thermal noise of an extremely high Q cavity
984 after carefully ensuring the radiation that is allowed to enter has a black body spectrum of
985 the same temperature of the cavity. This is nicely demonstrated in a few places, notably by
986 Cervantes et. al with a cavity of $Q = 10^{10}$ (!!!) [32]. When care is taken to create equilibrium
987 here, the resulting spectrum is flat, even on a frequency span that includes the resonance
988 (Fig. 2). When this equilibrium condition is broken, the cavity resonance becomes visible
989 (Fig. 10).

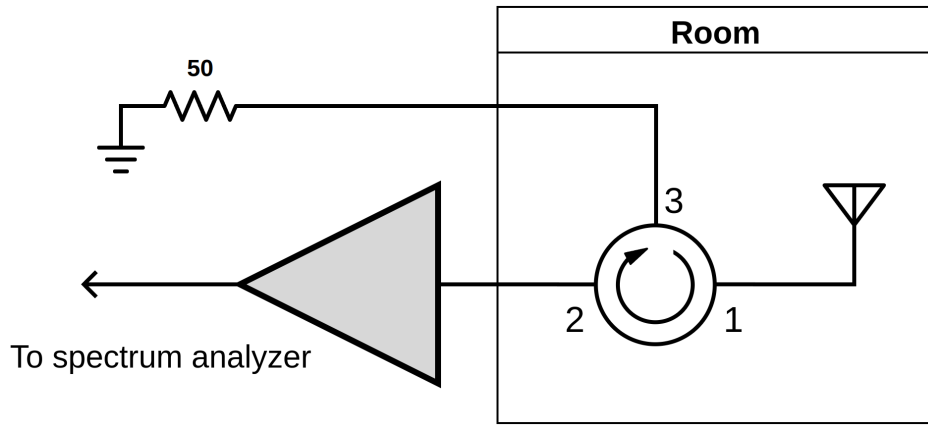


Figure 2.24: Schematic of experimental set-up using circulator to isolate antenna from amplifier effects.

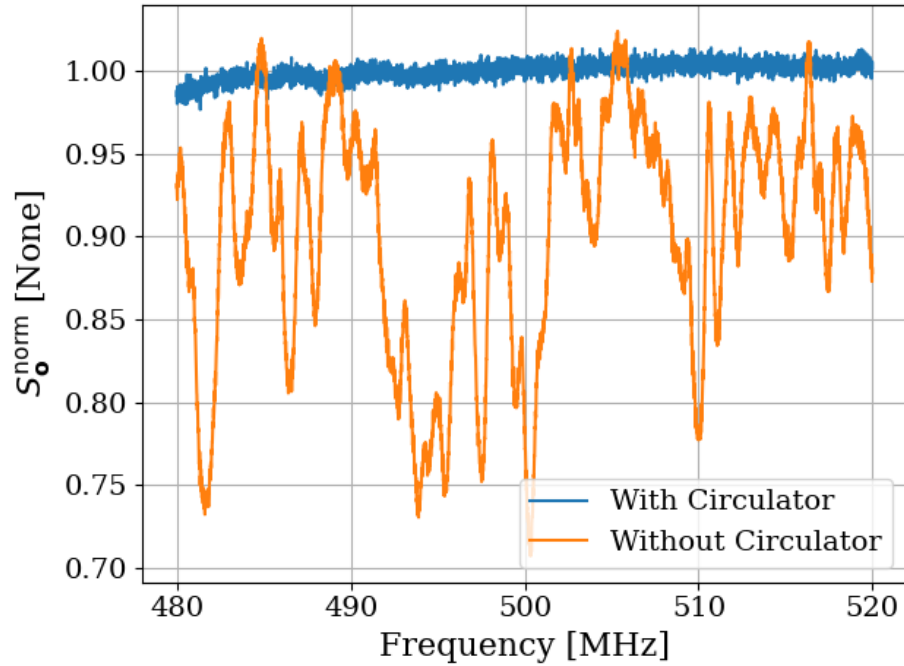


Figure 2.25: Normalized power spectrum for Vivaldi antenna in the room with/without circulator (blue/orange). This setup is shown schematically in Fig. 2.24. The normalized spectrum of the same antenna in the same position is shown with the circulator removed in orange for reference. This orange spectrum is the same as that shown in Fig. 2.16, but here it has been normalized to a terminator measured through the same amplifier chain. The terminator's spectrum is also shown in Fig. 2.16.

990 **2.3.6 Effective temperature of amplifier**

991 At this point, the seemingly obvious explanation is that the amplifier, being warm, is sourcing
992 more power than it's absorbing. To test this theory, two amplifiers can be placed input-to-
993 input as shown in Fig. 2.26. The noise power emerging *out* of the amp-under-test's input will
994 be measured by the front-end amplifier. This amplifier has a noise temperature $\sim 100\text{ K}$, so
995 it should be sensitive to very small variations in power. The data from the set-up is shown
996 in Fig. 2.27. Also shown in this figure are the spectra of the amp-under-test replaced by
997 both short and open terminations for reference.

998 An important number to keep in mind is the noise floor of this detector and what it looks
999 like in the dimensionless units shown. This is set by the noise temperature of the front end
1000 amp, $\sim 100\text{ K}$. If the load-under-test were at 0 K , the power measured $S_{0\text{K}}^{\text{meas}}$ would be only
1001 that of the front end amp. Taken in ratio to a 300 K matched terminator measured by the
1002 same amp chain,

$$\frac{S_{0\text{K}}^{\text{meas}}}{S_{300\text{K}}^{\text{meas}}} \approx \frac{0 + 100\text{ K}}{300 + 100\text{ K}} \quad (2.37)$$

$$= 0.25, \quad (2.38)$$

1003 where the factors of Boltzman's constant k and the measurement bandwidth $\Delta\nu_{\text{RF}}$ were
1004 suppressed since they cancel immediately.

1005 Thus, anything with an apparent noise temperature $\ll 100\text{ K}$ will appear with a dimen-
1006 sionless power spectral density of ~ 0.25 in Fig. 2.27.

1007 This phenomenon actually has been discussed in the literature[19].¹⁷, which I will provide
1008 a brief summary of.

1009 In this case, two amplifiers are placed back to back on either side of a transmission
1010 line. When a particle interacts with the transmission line, a pulse is detected at each of the
1011 amplifiers, and the difference in time provides a means to work out the position the particle
1012 came in along the line. It is advantageous in this case to minimize the noise emanating out
1013 of the inputs of these amplifiers. By tuning the reactance of the input of these amplifiers,
1014 they can absorb a net power, putting them at an “effective temperature” lower than their
1015 physical temperature.

1016 In the case of off-the-shelf Pasternack RF amplifiers, this was likely not an intentional
1017 effect. However, the data presented here seem to agree with the idea that the amplifiers have
1018 an effective temperature $\ll 100\text{ K}$.

1019 In the next subsection, I will demonstrate that by changing the temperature of the
1020 matched load outside the shielded room (shown in Fig. 2.24), the amplitude of the thermal
1021 wiggles can be controlled.

¹⁷I am very grateful to Greg Wright for pointing this out.

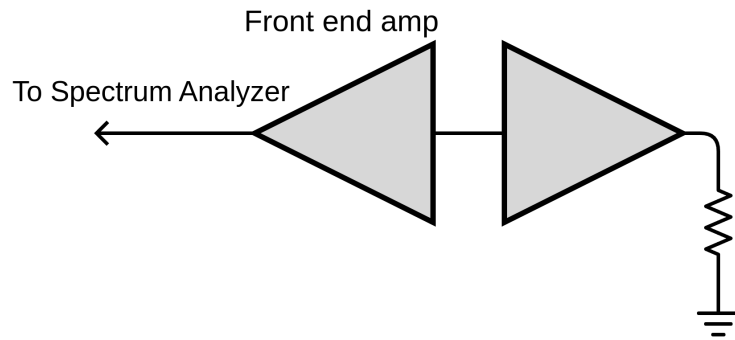


Figure 2.26: Schematic of set-up to measure the noise emerging *out* of an amplifier's input.

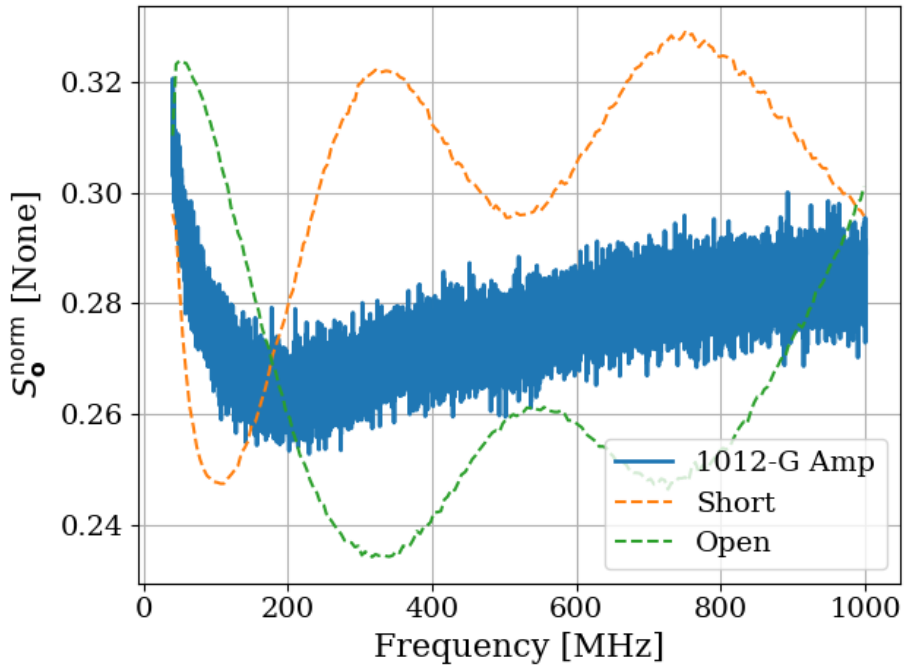


Figure 2.27: Power spectrum of noise emerging *out* of the input of an amplifier's (Paster-nack PE15A-1012-G) input, see Fig. 2.26. Normalized to a matched 50Ω terminator. Also shown as dashed curves are the spectra of a short and open termination. These spectra have a median fit applied to reduce visual clutter. Low-frequency behavior is due to the high noise figure of the amplifier at these frequencies; see Eq. 2.37.

1022 2.3.7 Intentional breaking of thermal equilibrium

1023 At this point, it has been demonstrated that an amplifier absorbs more thermal noise than
1024 it emits, likely due to the electronic cooling effect described by Radeka [19]. This causes the
1025 spectrum of a resonator, which is measured with such an amplifier, to exhibit wiggles, which
1026 disappear when a circulator is used to isolate the system from the amplifier. An interesting
1027 question naturally arises; what happens when the the thermal equilibrium is disturbed by
1028 varying the temperature of the 50Ω terminator on port 3 of the circulator (Fig. 2.24)? Since
1029 the terminator is outside the room, it is simple to conduct a highly controlled experiment
1030 where the terminator's temperature is varied without entering the room and disturbing
1031 sensitive boundary conditions.

1032 The hot terminator is created by using a noise source (red device in left panel of Fig. 2.28).
1033 The noise source has an effective noise ratio (ENR) of approximately 16.1 dB according to
1034 its calibration sheet. Noise temperature is related to ENR by the formula[43]

$$T_n = (10^{\text{ENR}/10} \times 290 K) + 290 K, \quad (2.39)$$

1035 where ENR is measured in dB and a reference temperature of 290 K has been assumed.
1036 Therefore, the noise source has a noise temperature of around 12,100 K ¹⁸.
1037 The cold terminator is a standard Pasternack 50Ω (with the blue rubber case removed),
1038 and the cable is semi-rigid and rated for cryogenic temperatures. This assembly is shown
1039 immersed in liquid nitrogen in the right panel of Fig. 2.28.

¹⁸This testing was performed before the Y-factor measurements of Sec. 3.1.1. The noise source worked correctly here but failed before the Y-factor measurements.

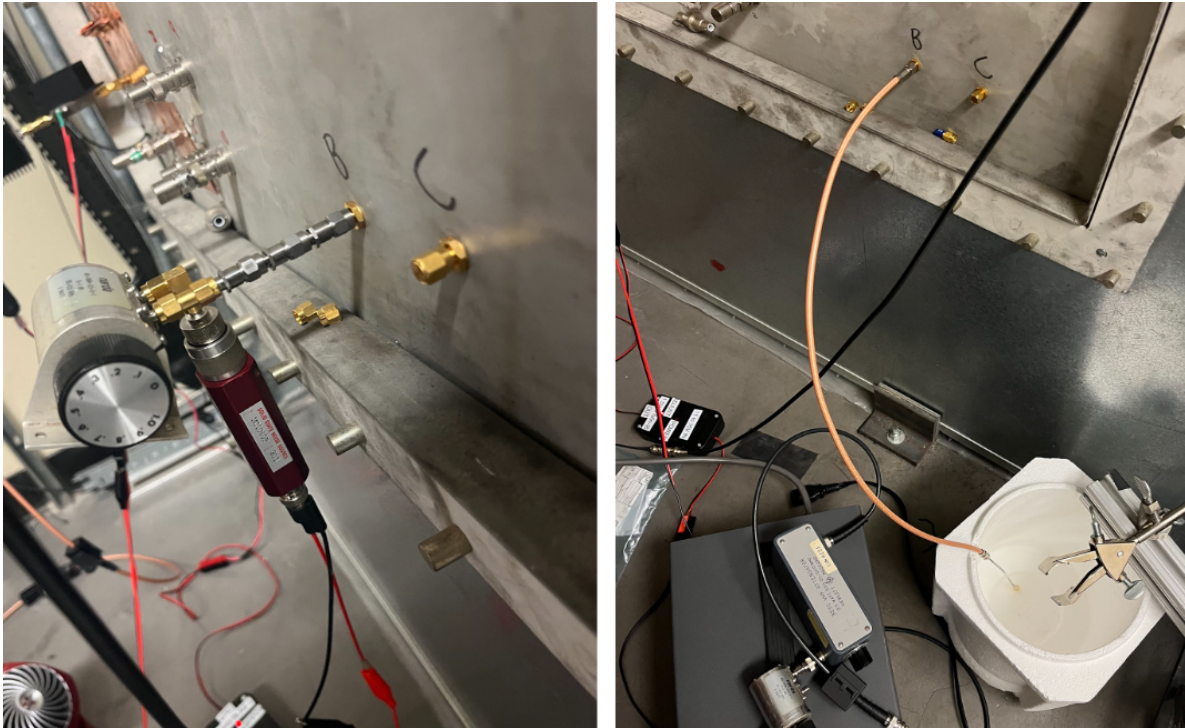


Figure 2.28: Setup to create hot and cold terminator. The hot/cold load is connected to port 3 of the circulator (as shown in Fig. 2.24). The circulator is in the room and not visible in this photo. Left panel shows the noise source ($16.1 \text{ dB ENR} \approx 12,000 \text{ K}$ noise temperature) and attenuators allowing the specific control of the hot temperature, see Eq. 2.40. Course attenuation is controlled by adding fixed attenuators, while fine control (0.1 dB steps) is provided by the step attenuator. Right panel shows the semi-rigid cryogenic-capable cable in liquid nitrogen to create a cold load.

1040 In both the hot and cold measurements, the loads were shown to have a good impedance
 1041 match to the 50Ω line using a VNA. The noise source is designed to have a good match,
 1042 but the terminator is not rated for cryogenic temperatures, so this is an important test.
 1043 The cryogenic test load (semi-rigid cable plus terminator) was measured to have $S_{11} <$
 1044 -35 dB at both room temperature and at 77 K (by submerging in liquid nitrogen), confirming
 1045 performance at cryogenic temperatures.

1046 The noise source looks like a terminator, which is a factor of ~ 40 times hotter than room

1047 temperature, while the cryogenic terminator is a factor of ~ 4 colder than room tempera-
1048 ture. To account for this, room temperature attenuators can be added to bring the effective
1049 temperature of the noise source down closer to room temperature. Therefore, the total noise
1050 temperature T_{out} of a terminator at physical temperature T_{in} in series with an attenuator at
1051 physical temperature T_{att} with (linear) loss L is a useful quantity. For brevity, the derivation
1052 outlined in the white paper by Whitham D. Reeve [44] is skipped, and the result is provided;

$$T_{\text{out}} = \frac{T_{\text{in}}}{L} + T_{\text{att}}\left(1 - \frac{1}{L}\right). \quad (2.40)$$

1053 Returning to the set-up in Fig. 2.24, replacing the terminator on port 3 with either a
1054 noise source (including an attenuator chain) or a terminator in liquid nitrogen provides a
1055 means to break thermal equilibrium in both the hot and cold direction by applying a matched
1056 load at a very precise temperature to port 3 of the circulator. Equation 2.40 converts the
1057 attenuation and noise source temperature into an output temperature.

1058 Figure 2.29 shows the resulting spectra from the set-up shown in Fig. 2.24 using a noise
1059 source/attenuator chain shown in the left panel of Fig. 2.28. The two panels show the spectra
1060 from the same set-up, but for different ranges and resolutions of T_{out} as defined by Eq. 2.40.

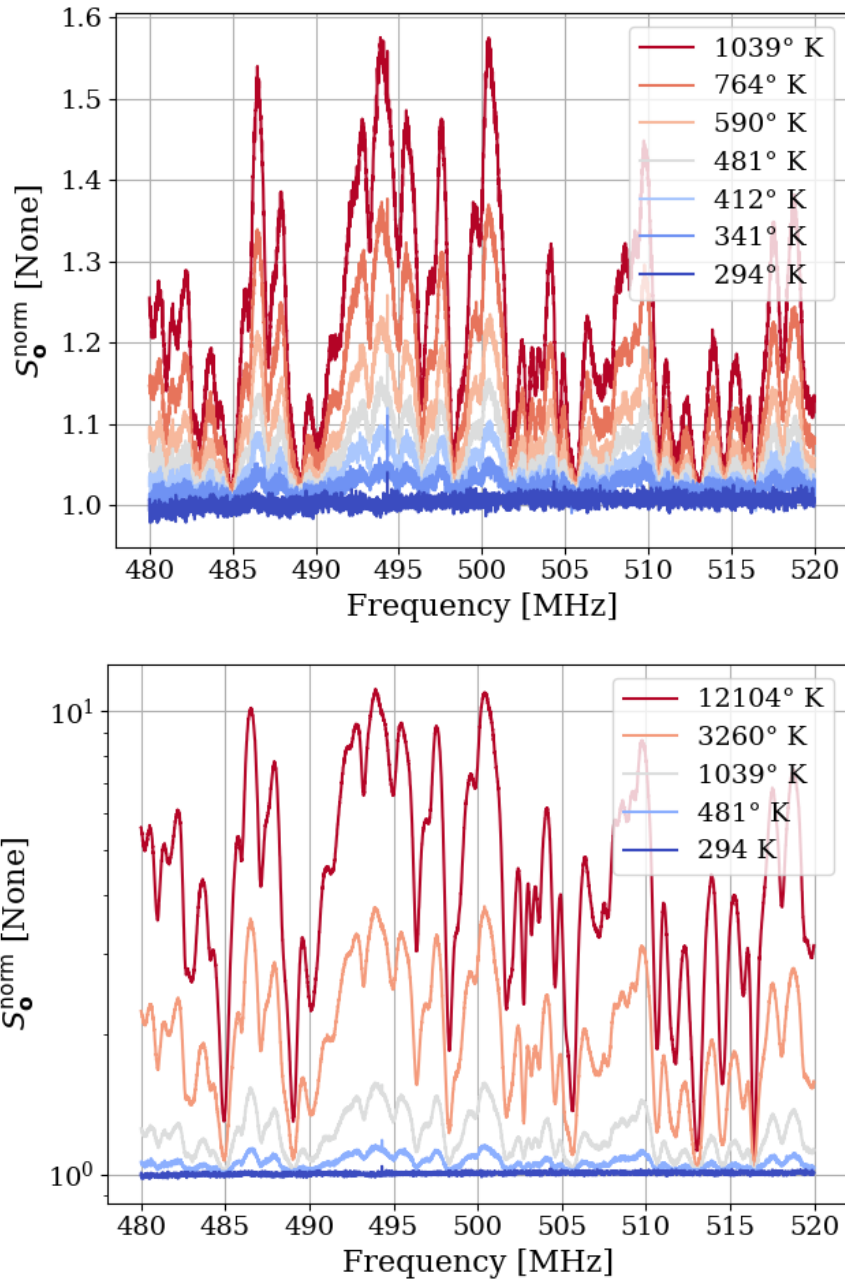


Figure 2.29: Spectra resulting from the antenna and circulator set up of Fig. 2.24 with the terminator on port 3 of the circulator at a variety of temperatures, as calculated by Eq. 2.40. Spectra are all normalized to a terminator through the same amplifier chain. The two panels show different ranges and resolutions of temperatures for clarity, but are the same setup.

1061 Figure 2.29 showed spectra from the set-up shown in Fig. 2.24 for a hot terminator, but
1062 a cold terminator can also be used by dunking a terminator into liquid nitrogen (Fig. 2.28).
1063 Neglecting the small attenuation of the cable, the noise temperature is simply 77 K. An
1064 interesting test case is to set the hot temperature such room temperature is halfway between
1065 T_{hot} and T_{cold} . In other words, let

$$T_{\text{hot}} = (T_{\text{room}} - T_{\text{cold}}) + T_{\text{room}} \quad (2.41)$$

$$\approx 511 \text{ K}. \quad (2.42)$$

1066 For $T_{\text{hot}} = 12, 100 \text{ K}$, $T_{\text{att}} = 294 \text{ K}$ and $T_{\text{out}} = 511 \text{ K}$, inverting Eq. 2.40 we expect L to
1067 be ~ 54.4 or 17.4 dB .

1068 The two spectra with the terminator at 504 K (the closest temperature accessible with the
1069 0.1dB step attenuator) and 77 K are shown in Fig. 2.30. Again, they have been normalized
1070 to the spectrum of a room-temperature terminator.

1071 The two spectra shown in Fig. 2.30 appear to be mirrored about $S_0^{\text{norm}} = 1$. In a test of
1072 this reflection, these spectra are added, and the resulting sum spectrum is flat to about 1%
1073 with another 1.5% offset from the expected value of 2. This is shown in Fig. 2.31. The offset
1074 is likely due to the amplifier gain or ambient temperature drift between measurements.

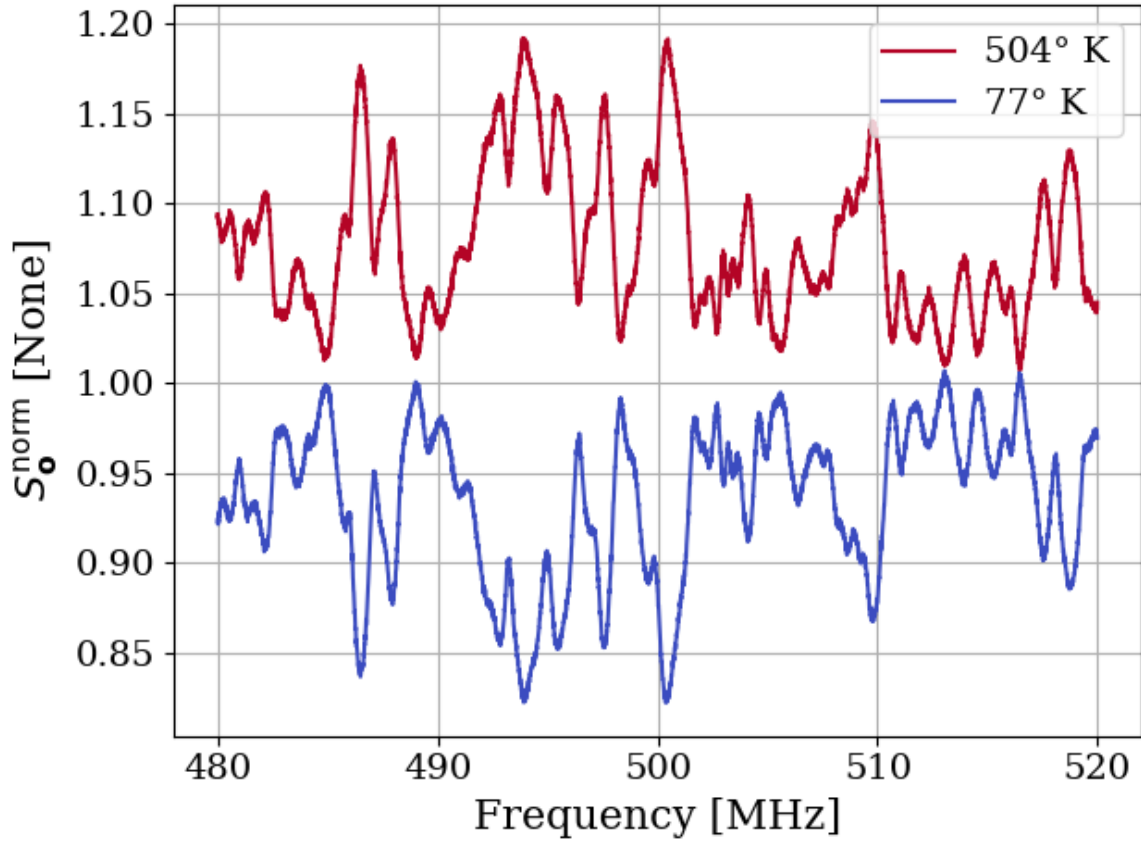


Figure 2.30: Spectra resulting from the antenna and circulator set up of Fig. 2.24 with the terminator on port 3 of the circulator $\approx 210\text{ K}$ above and below room temperature, as calculated by Eq. 2.40. Spectra are both normalized to a terminator through the same amplifier chain.

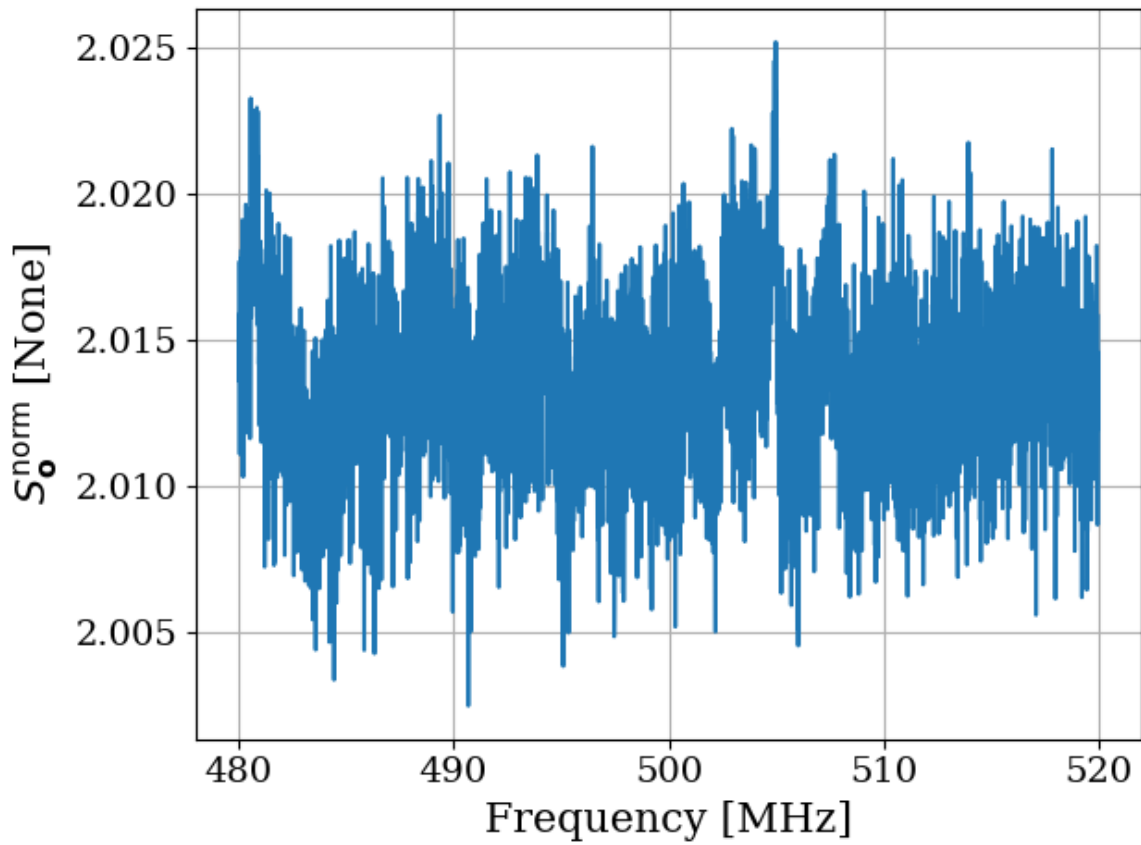


Figure 2.31: Sum of normalized spectra shown in Fig. 2.30. If the two normalized spectra in that figure were perfect reflections about 1, their sum would be a constant 2 in this figure. That is close to what is observed.

1075 **2.3.8 Relation of antenna S_{11} to thermal noise without a**

1076 **circulator**

1077 As pointed out in [41], the antenna impedance determines how much power is transferred
1078 from the cavity's electric field noise into the transmission line, and therefore what is mea-
1079 sured by the amplifier¹⁹. Indeed, impedance is a useful tool in understanding the situation
1080 outside equilibrium. However, viewing from this perspective misses a subtle point when con-
1081 sidering equilibrium; while an impedance mismatch will prevent the antenna's noise power
1082 from entering the transmission line, it will also prevent the noise in the line from leaving!
1083 This power will reflect off of the mismatch at the antenna and be absorbed by the matched
1084 amplifier, resulting in a flat spectrum. This can be seen in the coax resonator when mea-
1085 sured with the circulator in Sec. 2.3.4, specifically Figs. 2.22 and 2.23. Figure 2.32 shows a
1086 comparison of $1 - |S_{11}|^2$ and the noise spectrum of an antenna measured with a Pasternack
1087 low noise amplifier (LNA). There is no circulator in the setup, so variations are observed.
1088 Figure 2.33 shows the strong correlation between the curves in Fig. 2.32.

¹⁹The amplifier has a small impedance mismatch as well ($S_{11} \lesssim -15$ dB), but this is a small effect and is neglected.

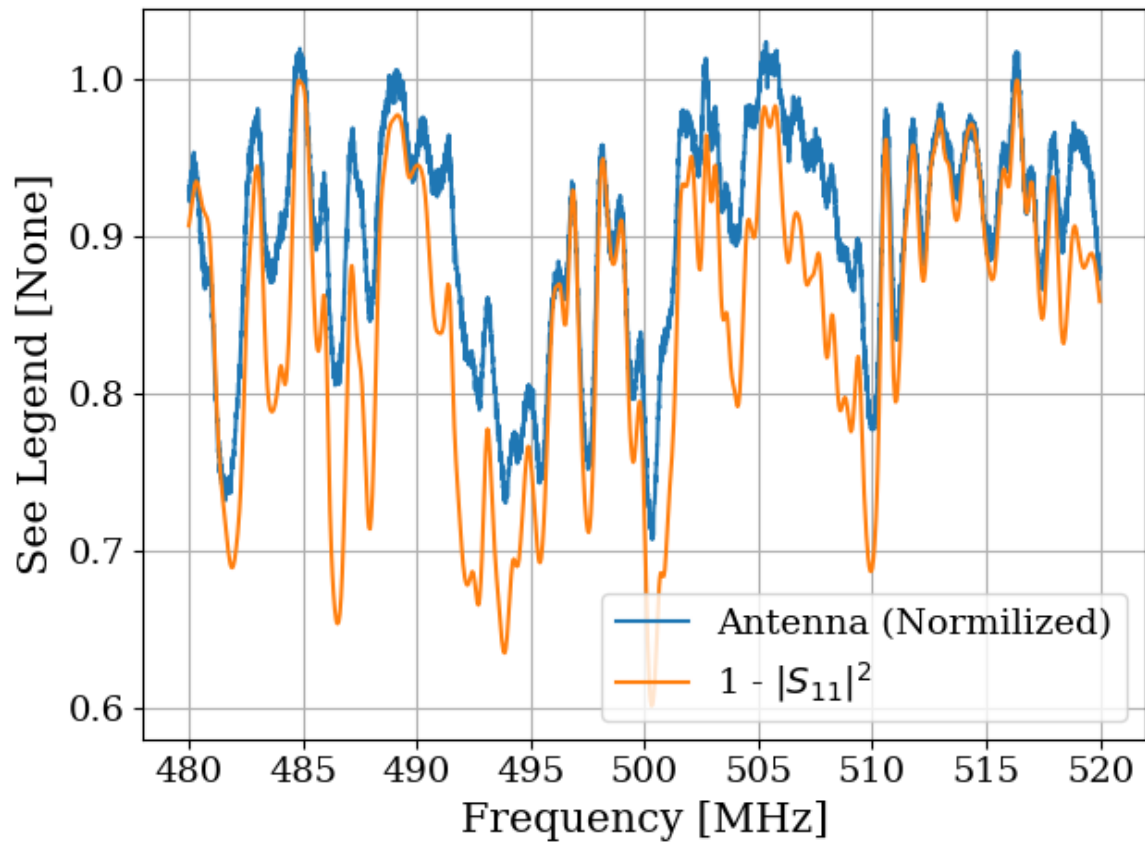


Figure 2.32: $1 - |S_{11}|^2$ and the normalized antenna spectrum without circulator. Shown at significant zoom to show detail. A much wider span is used to generate the correlation shown in Fig. 2.33.

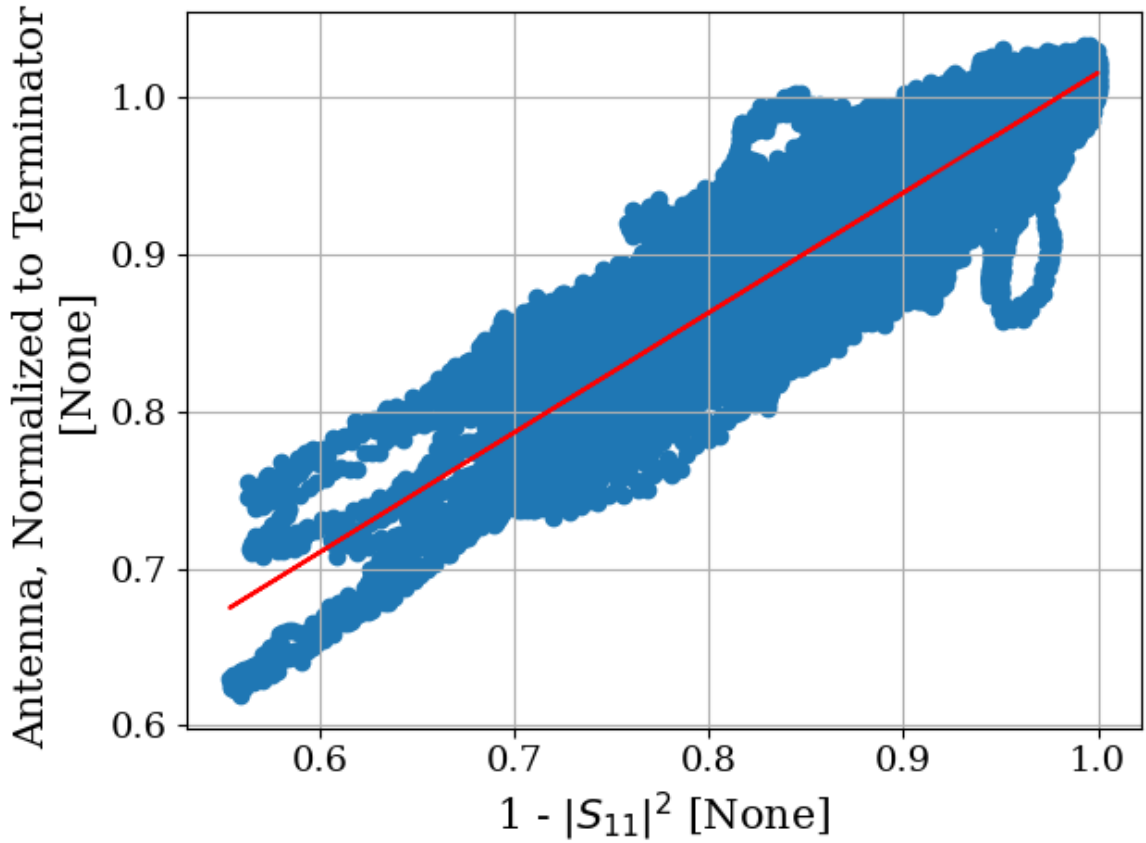


Figure 2.33: Correlation of $1 - |S_{11}|^2$ and the normalized antenna spectrum without the circulator. The data are taken between 300 and 800 MHz, a much wider span than shown in Fig. 2.32. The antenna is connected directly to the low noise amplifier (LNA), i.e. with the circulator shown in Fig. 2.19 removed. The line of best fit is shown in red. Pearson correlation coefficient = 0.92.

1089 **2.3.9 Discussion of Thermal Wiggles**

1090 Inspection of the output of the experiment (S_o , Fig. 2.16) reveals small variations in PSD
1091 (power spectral density) over spans of tens of kHz. Given an antenna in a cavity in thermal
1092 equilibrium with the input of an LNA, whose input is assumed to be real and matched,
1093 one would expect an output PSD which is constant with respect to frequency (up to small
1094 variations in system gain and noise temperature). The theory for this is outlined in Sec 2.3.1.
1095 These observed variations are not noise; for a given antenna position, the same shape is
1096 repeatedly measured (though the noise riding on these variations *is* random). The origin of
1097 the observed small variations lies in the effective temperature difference between the room
1098 and the LNA, causing a net power flow from the antenna into the LNA (Fig. 2.26). This
1099 effective temperature difference partially excites modes of the antenna/cavity system, causing
1100 the observed variations. This effect likely originates from a small reactive component of the
1101 LNA's input causing the electronic cooling described originally by Radeka [19]. This effect
1102 can be eliminated by adding a circulator between the antenna and LNA [45, 46] though for
1103 this experiment, it is impractical to get an isolator that covers such a wide band at relatively
1104 low frequency. Furthermore, the relatively wide (tens of kHz) variations can be handled by
1105 fitting to them, which is discussed in Sec. 4.2.

1106 **2.4 Reverberation Chambers and Statistical**

1107 **Uniformity**

1108 The Dark E-Field Radio experiment consists of an antenna in a cavity. An averaged noise
1109 power spectrum is measured and an exclusion limit is set on the amount of power excess
1110 that would have been detected if it were there. In order to convert this limit on power into
1111 a limit on kinetic mixing ϵ , the antenna/cavity detector system must be calibrated.

1112 In many situations, an electromagnetic cavity can be treated with a "spherical cow"
1113 approach; they contain one mode with a few simple properties that can be analytically
1114 computed. This works well enough for a smooth, empty cavity that resonates near its
1115 first mode, but for complex cavities, this treatment turns out to be insufficient. At high
1116 frequencies (where the wavelength is much smaller than the cavity), many modes, each with
1117 a finite spread in frequency, overlap. Each of these modes depends on very specific boundary
1118 conditions of the cavity and everything within it. The configuration of the cavity and its
1119 contents simply cannot be known to a level of precision that would allow for an analytic or
1120 simulated solution. Qualitatively, placing a small conducting object²⁰ in a cavity greatly
1121 impacts the cavity's resonances as measured by its S-parameters (Fig. 2.36).

²⁰This is a point made by Hill [47], with the example of placing a soda can in a reverb chamber. Ben Godfrey and I independently discovered this by measuring S_{21} of an antenna in our shielding room with and without a small SMA terminator on the ground with surprisingly different results.

1122 The problem is summarized nicely by Price et al. [48];

1123 The solution cannot depend in detail on such things as whether a small metallic
1124 can has been set down somewhere inside the test article, or the position of the
1125 pilot's arms, or whether some mechanical widget has moved from position A
1126 to position B, changing the mode structure. If the answer did depend on those
1127 things, all of the measurements would be useless, defeated by the minutiae present
1128 in all systems.

1129 The answer to this dilemma is found in the study of mode-stirred reverberation chambers,
1130 such as those studied by Price, whose quote appears directly above. These are electromag-
1131 netic or acoustic cavities in which a large volume is occupied by an object that is highly
1132 reflective and designed to move, a so-called *mode stirrer*. Making the geometry more com-
1133 plex seems counter-intuitive. However, the payoff is in the transition from a deterministic
1134 theory to a statistical one. The fields in the cavity at any given configuration are complex
1135 and are not known, but the statistics of the fields subject to the stirring can be rather simple.

1136 This section provides a mostly qualitative overview of the subject. The de facto reference
1137 is David Hill's 2009 book [47] which consolidates his many papers spanning his ~ 30 -year
1138 career. There is little I can do to explain the theory of electromagnetic reverberation cham-
1139 bers, which is not in this book, so I will focus on their application to the experiment and
1140 cite Hill where appropriate. The reader is encouraged to consult this book and its references
1141 for a more detailed exploration of the subject.

2.4.1 Deterministic solutions to electromagnetic waves in cavities

The electromagnetic fields within a cavity can be modeled by applying Maxwell's equations with the appropriate boundary conditions. In principle, with enough knowledge about the contents of the cavity, this treatment could calculate fields in any cavity. Unfortunately, it quickly becomes untenable for all but the simplest cases. Therefore, we will restrict ourselves to an empty cavity with perfectly conducting surfaces. The resulting fields have simple analytic solutions which vary sinusoidally in both space and time. They are derived in many places. See for example [47, 49]. While this treatment will not solve the problem at hand, it is a good starting point and will illustrate important features leading to the statistical treatment in the following subsection.

For a rectangular cavity of linear dimensions a , b and d , the frequencies of resonance are given by

$$\nu_{mnp} = \frac{c}{2} \sqrt{\left(\frac{m}{a}\right)^2 + \left(\frac{n}{b}\right)^2 + \left(\frac{p}{d}\right)^2}, \quad (2.43)$$

for integer mode numbers m , n and $p \geq 0$ and wave speed c . The lowest frequency of resonance requires at least two non-zero mode numbers. Thus, for $a < b < d$ the lowest frequency is at TE_{011} . For an ideal cavity with dimensions equal to that of the shielded room in this experiment ($8 \times 10 \times 12$ feet), the lowest mode is 63.6 MHz. An important consideration is the degeneracy of electric and magnetic fields for any mode where all three mode numbers are non-zero. For example, TE_{111} and TM_{111} occur at the same frequency, and both of these modes must be counted in the following section. See page 28 of Hill [47] for a discussion.

1162 A quantity of interest is the functional form of the cumulative number of modes at
 1163 frequencies below a given frequency $N(\nu)$. This is rather simple by brute force computer
 1164 counting²¹, though an analytic solution can be computed by looking at the volume enclosed
 1165 in a sphere of k -space [50], where k is the wave vector²². This analytic form is given by

$$N_s = \frac{8\pi}{3} abd \frac{\nu^3}{c^3} - (a + b + d) \frac{\nu}{c} + \frac{1}{2}. \quad (2.44)$$

1166 Differentiation of Eq. 2.44 results in a functional form for the mode density, i.e. the
 1167 number of modes contained in a frequency band,

$$\frac{dN_s}{d\nu} = 8\pi abd \frac{\nu^2}{c^3} - \frac{a + b + d}{c}. \quad (2.45)$$

1168 Equations 2.44 and 2.45 are plotted in Fig. 2.34

1169 This is useful because as the mode density becomes high, modes in a cavity of finite
 1170 conductivity begin to overlap. The modification of modal structure by conductors is demon-
 1171 strated in Figs. 2.35 and 2.36 by placing different conductors in the room and measuring
 1172 S_{11} .

1173 From these measurements it can be seen that modes can be pulled around, even by
 1174 conductors occupying a small percentage of room volume. This is especially true for high
 1175 frequencies. However, by using a large volume of conductors such as a mode-stirrer (sim-
 1176 ulated here with scrap metal), high-frequency modes are pulled around so much that they
 1177 overlap. This is the intuition behind reverb chambers and the idea of statistical uniformity.

²¹As long as you don't forget the degeneracy!

²²This whole business of mode counting is directly analogous to the calculation of density of states in statistical mechanics. It shouldn't come as a surprise that the calculation is carried out in the same way.

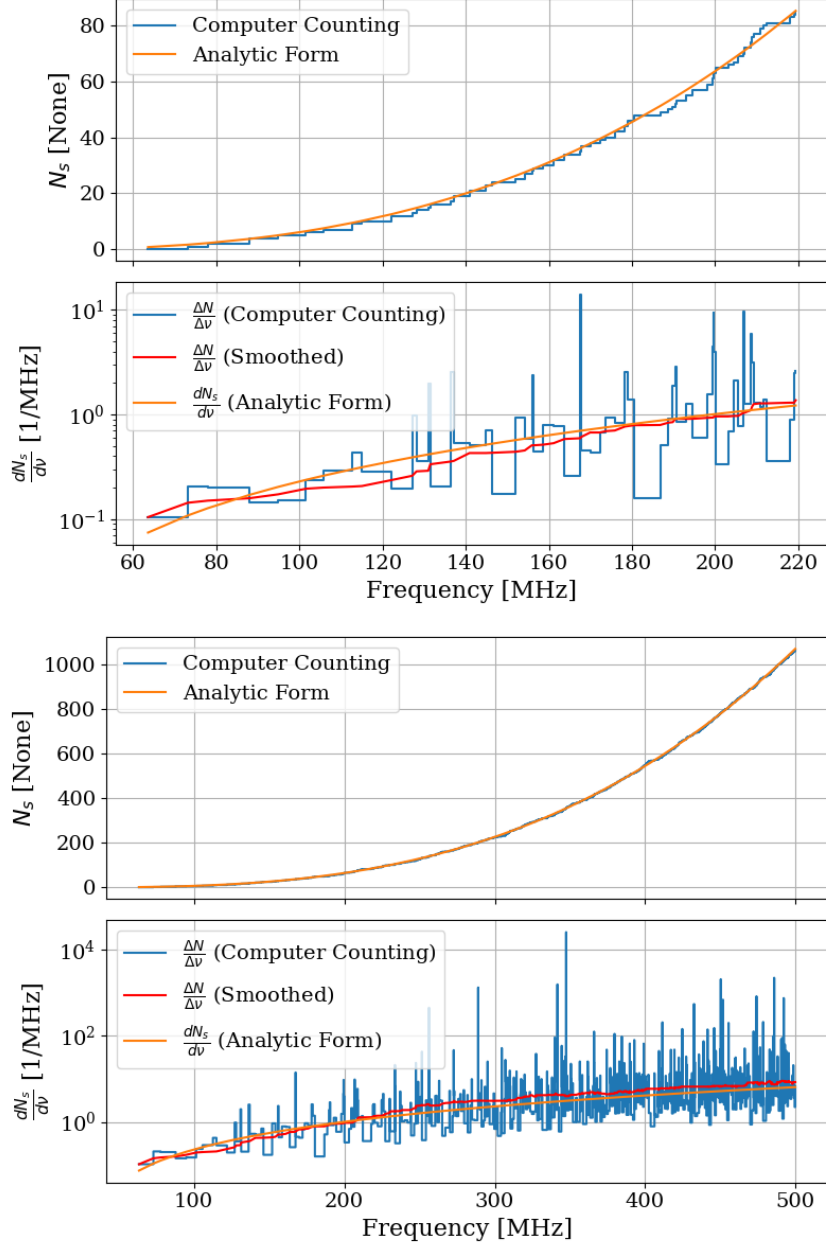


Figure 2.34: Modal density for an electromagnetic cavity with dimensions of the shielding room (nominally $8 \times 10 \times 12$ ft, see table 2.2). Upper sub-plot shows $N_s(\nu)$, the cumulative number of modes below a given frequency. Lower sub-plot shows the derivative of $N_s(\nu)$. Upper and lower panel show same data at two different frequency spans. These plots are a recreation of Figs. 3, 4 and 5 from [50] for a cavity with dimensions of the shielding room. Note that large spikes in $\Delta N/\Delta\nu$ should be interpreted as binning artifacts, and are only shown for reference. The analytic derivative is more useful.



Figure 2.35: Pictures of conductor configurations in shielded room. Antenna is in the same position between photos. Left panel shows tin foil hat, and right shows random placement of scrap metal. Hat and scrap metal courtesy of Tyler Erjavec.

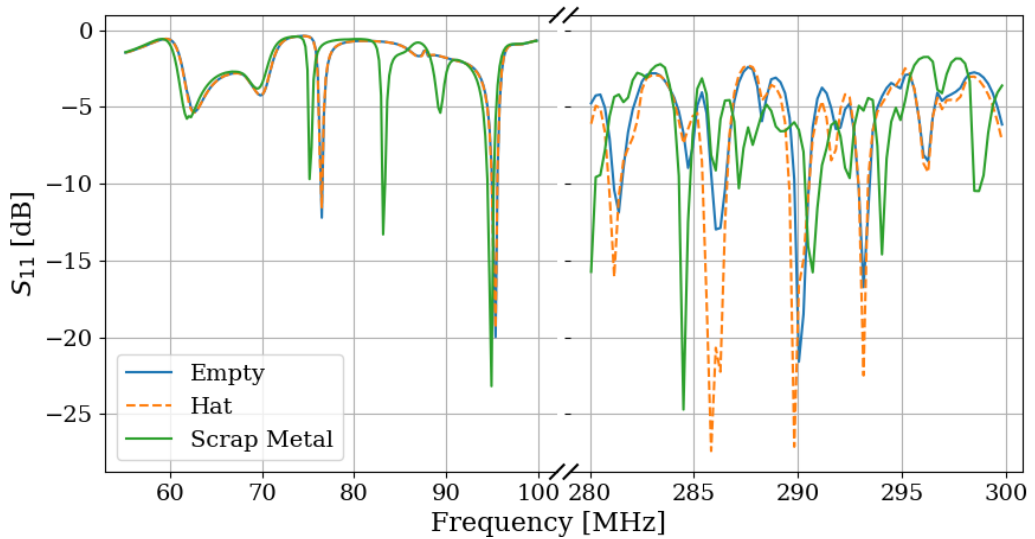


Figure 2.36: Measured S_{11} with different conductors in shielded room, as pictured in Fig. 2.35. Modes visible at low frequency agree nicely with the predictions of Eq. 2.43, though they are pulled around by the scrap metal. Note, scale changes slightly after X-axis break.

1178 2.4.2 Statistical approach to electromagnetic waves in cavities

1179 By using a mode stirrer, modes are intentionally pulled around in frequency, and the average
1180 response of the cavity begins to converge to be relatively flat. The regime where this occurs is
1181 known as being well-stirred. It requires the stirrer to be large enough and obey some design
1182 principles, and that the frequency to be above a threshold. This lowest usable frequency
1183 (LUF) is determined by a minimum modal density since the modes must be close enough
1184 together in order to overlap. For a room-sized reverberation chamber with a lowest resonance
1185 of around 60 MHz (~ 3 or 4 meters per side), the rule of thumb cited by Hill among others
1186 is the LUF is close to where the modal density is about 1 mode/MHz. Therefore, according
1187 to Fig. 2.34, the LUF of our shielded room is about 200 MHz.

1188 A simple alternative to using a purpose-built mode stirrer is moving a receive antenna
1189 around in the room. Instead of moving the spatial structure of the modes around the antenna,
1190 the antenna is moved through the modes. While not as effective, it is simpler to implement,
1191 so this was the method used in Run 1A. Note that Run 1A does not rely on statistical
1192 uniformity. Simulations provide a means to calibrate the system as discussed in Sec. 4.3.
1193 However, using these statistical ideas provides a much more stable simulation with a much
1194 better agreement with measurement.

1195 One final remark that is relevant to the experiment is the concept of composite Q . This
1196 parameter represents a resonant enhancement factor that corresponds to the antenna/room
1197 system's tendency to "ring up" in the same way any resonator will. It is referred to as *com-*
1198 *posite Q* and represented as \tilde{Q} . It is analogous to the standard quality factor of a resonator

1199 with one important modification; the experiment is operated across a wide frequency range,
1200 so \tilde{Q} is defined across the continuum of these resonances, not only on classical eigenmodes
1201 of the system.

1202 2.5 System Design

1203 This section outlines the subsystems which make up the experiment. While specifics and
1204 basic calculations are provided as they apply to design choices of subsystems, testing and
1205 characterization of the system as a whole is left to Ch. 3. A simplified schematic of the
1206 entire experiment is shown in Fig. 2.37 and a photo of the lab is shown in Fig. 2.38.

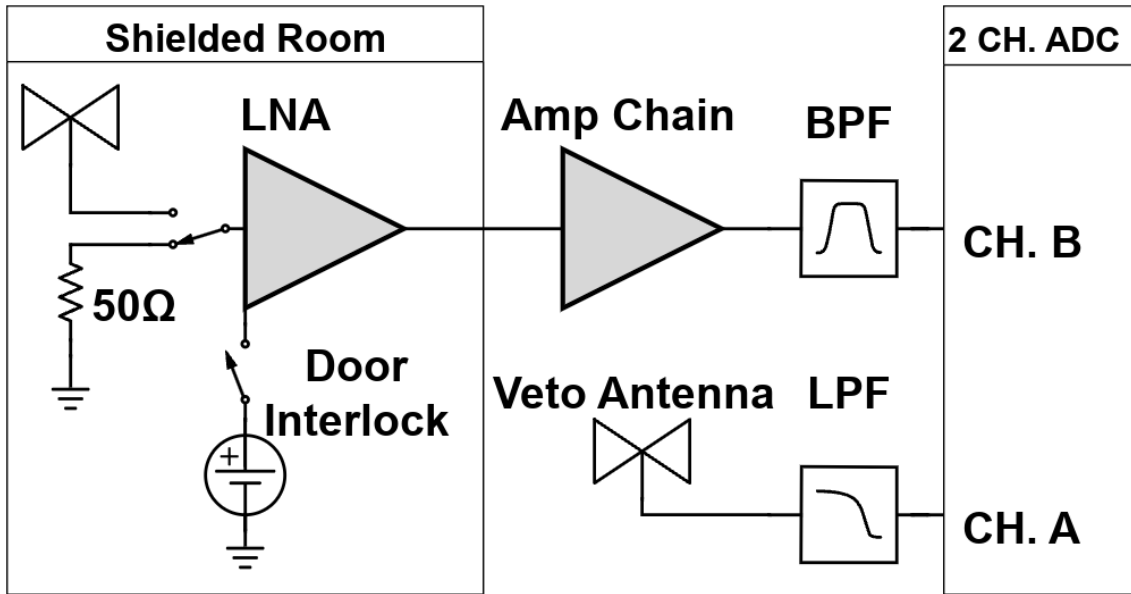


Figure 2.37: Schematic of the RF receiver system. An RF coax switch allows the PC to control the source (antenna or terminator). The amplifier chain is shown with more detail in Fig. 2.42. The switch is controlled by optical fiber to maintain isolation of the room. The LNA (Pasternack PE15A1012) has a nominal gain and noise temperature of 40dB and 100K (measurements shown in Sec. 3.1.1). It is interlocked (Fig. 2.43) to the door to protect amp B and the ADC from large signals when the door is open. The secondary amplifier is a Mini-Circuits (MC) ZKL-1R5+ and has a nominal gain of 38dB. Not pictured after this amplifier is a fixed 4dB of attenuation. The band pass filter (BPF) defines the experiment's bandwidth, $-3 \text{ dB} \approx 40 - 320 \text{ MHz}$ and is discussed in Sec. 2.5.4. The veto antenna is outside of the room and interference is not reduced by the $\approx 100 \text{ dB}$ SE of the room, so no gain is required. The low pass filter (LPF) on the veto is for anti-aliasing.



Figure 2.38: Photo of dark radio lab. The shielded room contains the main antenna as well as the LNA and power supply (not visible). The veto antenna can be seen hanging outside of the shielded room. Photo taken looking south.

1207 **2.5.1 Shielded room**

1208 The shielding room [51] serves two purposes. The first is straightforward; to shield the
1209 antenna, keeping radio frequency interference (RFI) *out*. The second purpose is a bit more
1210 subtle; to keep any converted dark photons *in*. This second point is addressed further as an
1211 aspect of system calibration in Ch. 4, but roughly can be described by the loaded quality
1212 factor [52–54] of the antenna/room system. Namely, a more resonant system will be more
1213 sensitive to coherent signals. This subsection will focus on the first point, keeping RFI out.

1214 Shielding effectiveness SE is a measurement of a shielding enclosure's ability to attenuate
1215 electromagnetic waves from entering,

$$\text{SE} \equiv 10 \log_{10} \left(\frac{P_{\text{open}}}{P_{\text{closed}}} \right) = P_{\text{open}, \text{dB}} - P_{\text{closed}, \text{dB}} \quad (2.46)$$

1216 where $P_{\text{open}}/P_{\text{closed}}$ are powers received with the door open/closed. The ratio of powers
1217 allows all the specifics of antenna matching to cancel allowing for a very simple differential
1218 measurement. The results of this are described in Sec. 3.2.

1219 Another important measurement are the dimensions, shown in table 2.2. I carefully
1220 measured the room with a laser range finder which I checked against a tape and gives good
1221 agreement to 1 mm²³. The room is out of square by a few mm, especially height measured
1222 in the south-west corner compared to the height measured everywhere else. This is the most
1223 extreme deviation, and is about 5 mm.

²³After a year I dropped it and it now gives crazy readings which jump around by 10s of cm. Be careful!

Direction	Coordinate	Nominal Length [ft]	Measured Length [m]
West-East	x	10	3.070
Vertical	y	8	2.457
North-South	z	12	3.684

Table 2.2: Direction, coordinate, and length measurements of shielded room in lab 314. Note that Fig. 2.38 is looking south, so x is right-left and z is into the page. Note that these are the mean values of several measurements. The room was found to be about 5mm out of square, so these should be interpreted as ± 5 mm.

1224 2.5.2 Antenna

1225 The antenna plays an important roll in the experiment as the matching device between
 1226 electromagnetic waves in the cavity and the 50Ω receiver system. For a broadband search
 1227 such as the 50-300 MHz run (a 6:1 bandwidth), a broadband antenna must be used. The
 1228 chosen antenna must provide a good impedance match and high efficiency since an inefficient
 1229 antenna would convert a substantial amount of the converted dark photon's power into heat
 1230 within the antenna's structure. The antenna is connected to the RF switch via a low loss
 1231 (0.45dB at 300 MHz) 21 ft. LMR400 cable. This contributes about 31.6 K to the ≈ 400 K
 1232 antenna noise, see Eq. 2.27. Note that the final limit on epsilon scales with the square root
 1233 of system temperature, so this is only a few percent degradation in the final limit after a 9
 1234 day run.

1235 For the 50-300 MHz run, a ≈ 131 cm biconical antenna (bicon) was chosen. The selected
 1236 model is manufactured by COMPOWER, model AB-900A [55]. In a phone call with the
 1237 manufacturer as well as testing of the isolated balun, it was determined that the balun used
 1238 in the antenna was 1:1. This allows for simple simulation of a free-space aperture which

1239 agrees remarkably well with manufacturer data, Fig. 2.39. In COMSOL [56], the lumped
1240 port option allows for a balanced drive of an antenna. A match to a 50Ω transmission line
1241 through a 1:1 balun is simply modeled as a lumped port, a very simple object in COMSOL
1242 featured in nearly all of the antenna tutorials²⁴. Additionally, there is good agreement
1243 between simulated and measured antenna impedance, see Fig. 2.40.

²⁴See for example the dipole antenna tutorial, available at <https://www.comsol.com/model/dipole-antenna-8715>

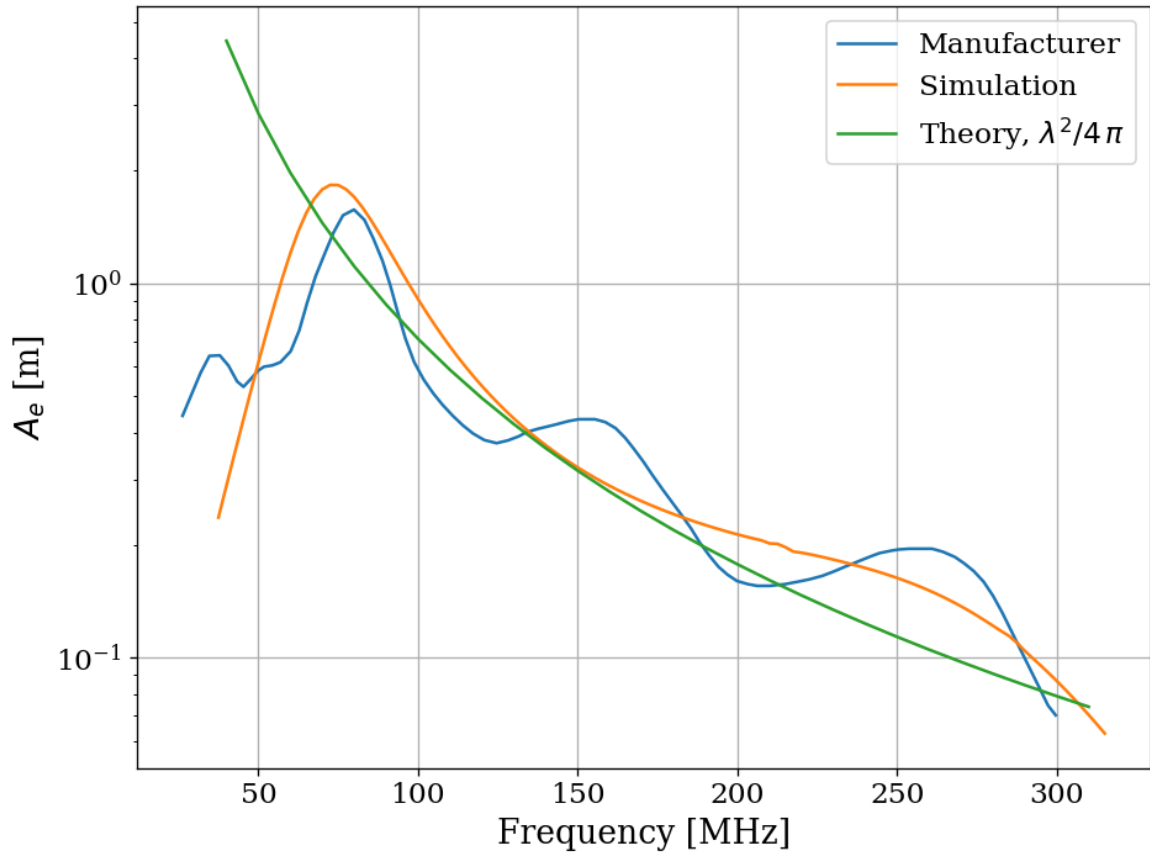


Figure 2.39: AB-900A biconical antenna effective aperture, simulated, measured and theoretical in free space. Simulation performed in COMSOL [56]. The measurement was provided by manufacture [55] as an antenna factor and was converted to aperture. Variations observed in manufacturer's measured data are the result of testing over a ground plane and are a known discrepancy between simulations and measurements of “free space” antenna factor. See for example [57] [comment: aperture units wrong, reprint plot](#)

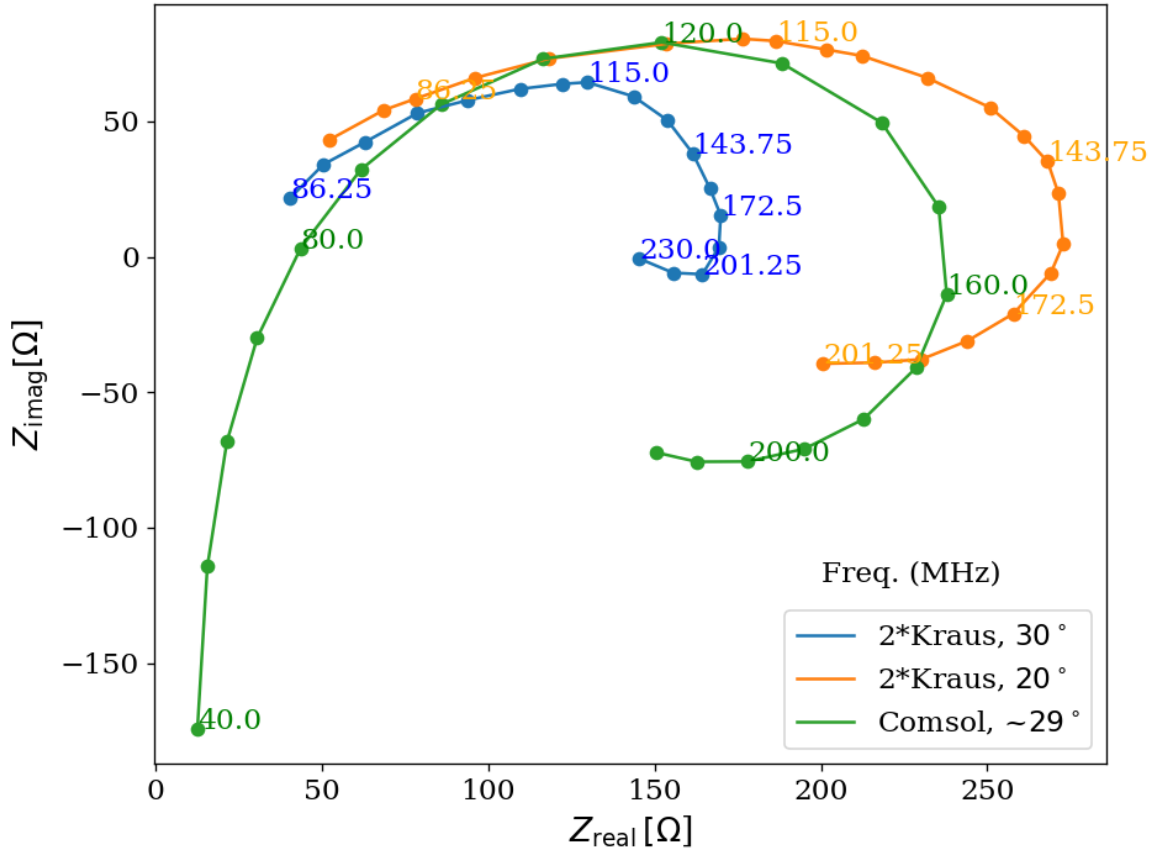


Figure 2.40: Simulated AB-900A biconical antenna free space complex input impedance shown in blue. Simulation was performed in COMSOL. Measurement from Kraus' Antennas, second edition, Fig 8-13 [58]. Measured data is for a monoconical antenna and must be multiplied by 2 to compare to a biconical antenna as discussed in Kraus. Numbers along curve indicate frequency in MHz.

1244 **2.5.3 Terminator and fiber-optic switch control**

1245 Experience has shown that it is advantageous to have a stable noise reference at the begin-
1246 ning of the signal chain to monitor system performance. One may think the antenna can
1247 provide this following Sec. 2.1.1.2, but in practice, the antenna is not that stable, Sec. 2.3.
1248 Furthermore, while RFI was not significant in the actual run, it very well could have been,
1249 introducing some uncontrolled, coherent power into the spectrum which would have had an
1250 unknown origin. A terminator will give a very constant noise power density $S_{\text{term}} = kT$
1251 regardless of RFI and antenna position. For this reason one is included. It is at the same
1252 temperature as the walls, and is a nice passive solution. The RF switch shown in Fig. 2.37
1253 is actuated periodically during the run to measure the terminator's noise power through the
1254 same amplifier chain as the antenna. The terminator is connected to the switch via a 21
1255 foot cable (LMR 400) which is identical to that of the antenna. The switch is controlled via
1256 a fiber-optic link in order to reduce RFI. The fiber optic is an extremely important feature
1257 which was overlooked for several years at the beginning of the experiment leading to lots of
1258 RFI.

1259 **2.5.4 Signal conditioning**

1260 As discussed in Sec. 2.1.5, the ADC has internal signals which are mitigated by introducing
1261 gain before the ADC. The amount of gain must be carefully chosen, since too much will cause
1262 the ADC to clip. Additionally, high frequencies must be limited before digitizing to prevent
1263 aliasing. To accomplish this, several RF components must be selected to condition the analog

1264 signal: an LNA, a secondary amplifier, band pass filter and several attenuators.

1265 2.5.4.1 Low noise amplifier

1266 The important concepts of the LNA have been introduced in Sec. 2.1.4. The key takeaway
1267 is that low noise gain helps to mitigate signal-to-noise degradation that occurs later in the
1268 signal path. Relevant specifications for the Pasternack PE15A1012 [36] are summarized in
1269 table 2.3.

Specification	Value	Uncertainty (50-300MHz)	Units
Frequency Range	50-1,000	-	MHz
Gain	40	± 1	dB
Noise Temperature	110	± 10	K
Input Return Loss	< -15	-	dB
Output Return Loss	< -15	-	dB
Price	500	-	USD
Voltage	9-15		V
Current	100	10	mA

Table 2.3: Specifications for the Pasternack PE15A1012-E. The voltage is regulated internally, so the exact voltage supplied is not critical, though there is a slight gain dependence on voltage since a higher voltage causes the amp to run warmer, see Fig 3.8.

1270 We have several identical amplifier which are labeled with letters. At the time of writing,
1271 amplifiers A-D are out of commission. Amplifier E was used for run 1.4.

1272 2.5.4.2 Secondary amplifier

1273 As discussed in 2.1.4, the noise temperature of a secondary amplifier has negligible impact
1274 on the total system noise temperature. For this reason a cheaper secondary amplifier is
1275 used. The specifications for the Mini-Circuits ZKL-1R5+ [59] are outlined in Table 2.4.

1276 This amplifier has no internal regulator, so gain and noise temperature depend strongly on
 1277 the bias voltage. Voltage was set to 9.05 V for run 1.4 using an external regulator (built
 1278 around a TI LM317 [60]).

Specification	Value	Uncertainty (50-300MHz)	Units
Frequency Range	50-1,000	-	MHz
Gain	40.5	.3	dB
Noise Temperature	275	15	K
Input VSWR	<1.14	-	dB
Output VSWR	<1.37	-	dB
Price	235	-	USD
Voltage	9-15	-	V

Table 2.4: Specifications for the Mini-Circuits ZKL-1R5+ as measured with 9.05 V bias.
 There is no internal regulator, so the voltage is set using an external regulator (built
 around a TI LM317 [60]).

1279 2.5.4.3 Band pass filter

1280 The band pass filter has two purposes. The first purpose is to minimize the bandwidth
 1281 entering the ADC. This allows for introducing as much gain as possible without wasting
 1282 power amplifying frequencies where the antenna doesn't offer a good match. This will be
 1283 computed below in Sec. 2.5.4.4. The second purpose is to prevent aliasing²⁵. Aliasing occurs
 1284 when the analog signal contains frequency components at frequencies greater than half the
 1285 sample rate, in otherwords when the signal and ADC don't obey a condition called the
 1286 Nyquist criterion, $\nu_s/2 \geq \nu$, where ν_s is the sample frequency and ν is the frequency of the
 1287 analog signal.

²⁵Aliasing is rather complex topic which is greatly simplified here. Wikipedia's aliasing page is an excellent reference. For a more rigorous treatment, see Ch. 7 Sec. 3 of the second edition of Signals and Systems by Oppenheim et. al [61]

1288 When this criterion is not met, higher frequencies are mapped back down to a lower
1289 frequency, described by the aliasing formula:

$$\nu_{\text{alias}} = |\nu_{\text{signal}} - n \times \nu_s|, \quad (2.47)$$

1290 where ν_{alias} is the aliased frequency, ν_{signal} is the original signal frequency, ν_s is the
1291 sampling rate, and n is an integer which specifies the Nyquist zone. In the simple case
1292 with bandpass filters that roll off well within the first Nyquist zone, only $n = 1$ must be
1293 considered.

1294 As an example, a $\nu_{\text{signal}} = 500$ MHz signal sampled at $\nu_s = 800$ MHz (the run 1.4 sample
1295 rate), it would alias to $\nu_{\text{alias}} = 300$ MHz. This also means that 1,300 MHz (residing in the
1296 second Nyquist zone) would alias down to 300 MHz, but again this and higher frequencies
1297 won't be considered. This means that by choosing only to analyze frequencies less than 300
1298 MHz, only frequencies greater than 500 MHz will alias into this analysis span.

1299 The Mini-Circuits ZX75LP-288-S+ low pass filter[62] serves as the anti-aliasing filter in
1300 run 1.4. It has an insertion loss of 68 dB at 500 MHz, while being flat to within 2dB from
1301 50 to 300 MHz. Additionally, the Mini-Circuits SHP-50+ [63] is used as the high pass filter.
1302 When connected in series, these two filters constitute the band pass filter shown in Fig. 2.37.

1303 2.5.4.4 Putting together a signal conditioning chain

1304 The total gain required can be estimated by setting the output referred power of bandlimited,
1305 400 K noise source times the gain equal to the maximum power the ADC can handle,

1306 $V_{\text{RMS}}^2/Z = 0.63 \text{ mW}$ for $Z = 50 \Omega$. Assuming a perfect filter from 50-300MHz (a 250 MHz
1307 bandwidth), the gain required is

$$G = \frac{0.63 \text{ mW}}{k 400\text{K} 250 \text{ MHz}} = 4.5 \times 10^8 = 87\text{dB}. \quad (2.48)$$

1308 Noise is a Gaussian random process however. This much gain ensures 1σ of the time
1309 domain samples are below clipping. Since many samples are collected ($2^{24} \approx 1.6 \times 10^7$ in
1310 run 1.4), and each has a probability of about 16% of clipping, many samples will clip with
1311 87 dB of gain. However, it gives a good estimation for what to expect.

1312 The band pass filter is not a brick wall from 50 - 300 MHz as was assumed in 2.48. The
1313 effective bandwidth of a filter is defined here as the integral of the square magnitude of it's
1314 through gain,

$$B_{\text{eff}} \equiv \int_{-\infty}^{\infty} d\nu 10^{S_{21}/10}. \quad (2.49)$$

1315 Where S_{21} is measured in dB and we are interested in integrating a quantity that is
1316 proportional to linear power, so it is divided by 10 rather than 20. The linear S parameters
1317 of components connected in series multiply, but since dB are logarithmic, this is equivalent
1318 to adding their S-parameters (in dB). Also note that $S_{21} \equiv \text{IL}$, the insertion loss. Insertion
1319 loss is frequently given on data sheets.

1320 With all this in mind, we can compute $B_{\text{eff}} = 237.06 \text{ Hz}$ for the actual filters (Mini-
1321 Circuits SLP-50+ high pass filter and Mini-Circutis ZX75LP-288-S+ low pass filter) from
1322 their data sheets. Curves of S_{21} for the real band pass filter and an ideal brick wall filter are

1323 shown in Fig. 2.41. Note that it is actually slightly less than the ideal 250 MHz bandwidth
1324 since there is some loss in band.

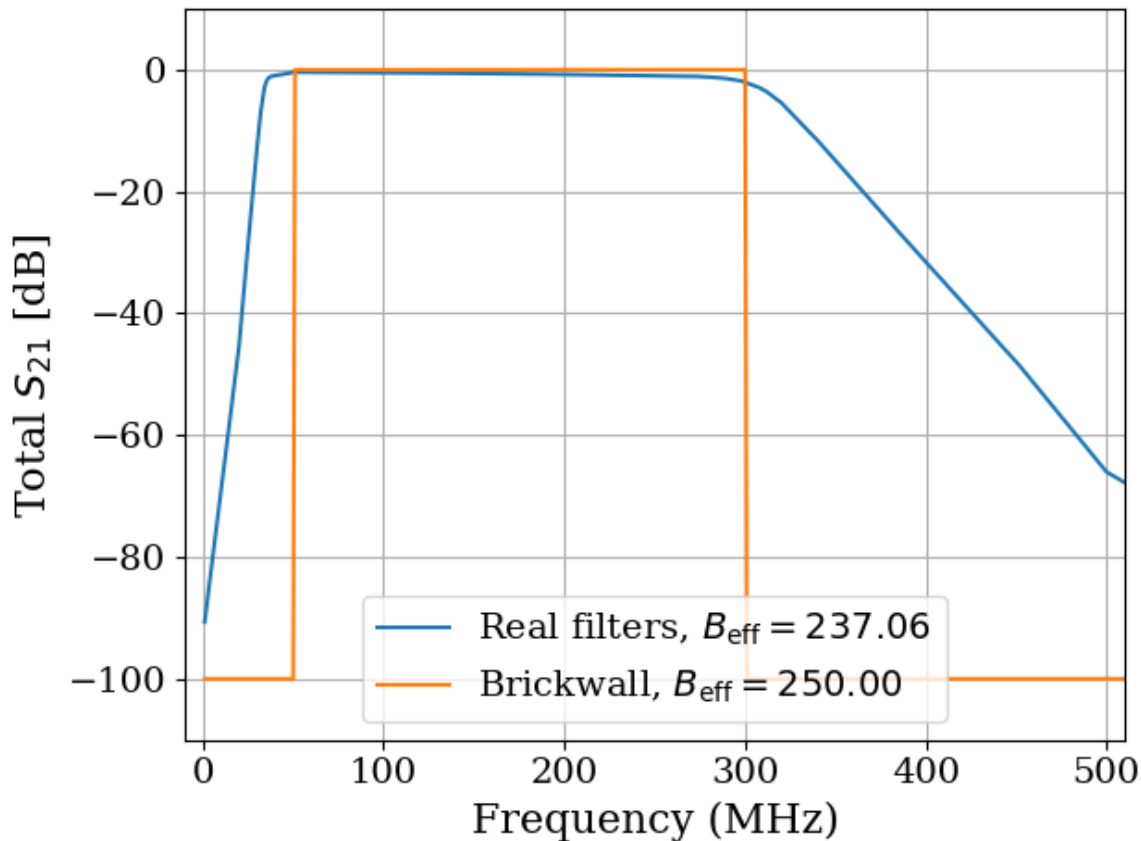


Figure 2.41: Through gain (S_{21}) of bandpass filter. Shown in dB, however B_{eff} is computed with linear S_{21} as in Eq. 2.49. Ideal brickwall filter shown for reference.
comment: Add Hz in legend

1325 Setting the gain is ultimately done by trial and error; taking a scan, adding some atten-
1326 uation if it clips, taking a scan, etc. Experience and preliminary simulations have shown
1327 that a few dB of clipping for an noise-dominated signal actually doesn't matter much, but
1328 this was not fully explored. If future runs are to scan for longer, they may have a significant
1329 contamination from ADC spurs (see Sec. 2.1.5.1), so additional gain driving into clipping

1330 may be fruitfully explored. Every dB of gain added allows for $10^{1dB/5} \approx 44\%$ more averaging
 1331 before ADC effects are at the same relative level²⁶, so a little extra gain goes a long way.

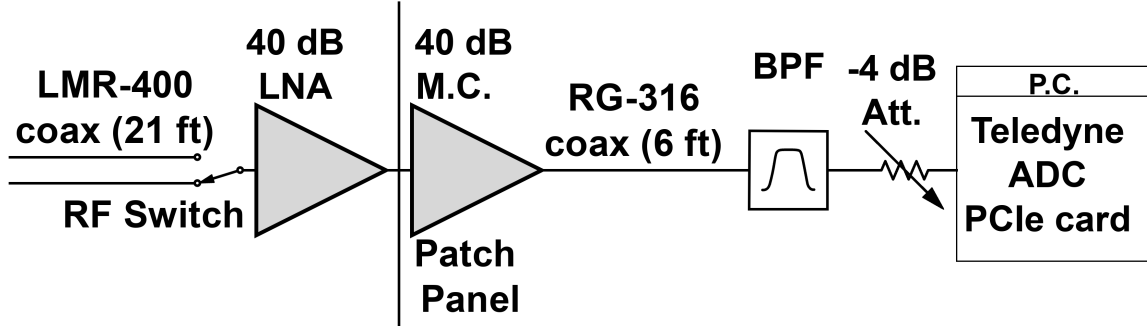


Figure 2.42: Schematic of Run 1A amplifier chain. Antenna (Sec. 2.5.2) and terminator (Sec. 2.5.3) are not part of the amplifier chain, and therefore not shown, but would be at far left of schematic. All RF connectors are SMA, except the connection between the bicon antenna and its cable which is N type (though that cable has SMA on the switch-side). RF switch is Teledyne CR-33S8D-T. 40 dB LNA is Pasternack PE15A1012-E (Table 2.3). Patch panel uses an SMA bulkhead connector labeled “A” (far left-hand side when standing outside the shielding room, as shown in Fig. 2.38). 40 dB Mini-Circuits (M.C.) is Mini-Circuits ZKL-1R5+ (Table 2.4). Band pass filter (BPF) is made up of Mini-Circuits SLP-50+ high pass filter and Mini-Circutis ZX75LP-288-S+ low pass filter. Note that filters and attenuator are directly connected to the SMA port of the Teledyne ADC (Sec. 2.5.7) to mitigate RFI received in the RG-316 cable run.

1332 2.5.5 Veto antenna

1333 The veto antenna is an identical Compower AB900 bicon antenna [64] as is used in the
 1334 shielded room. It is connected to channel A of the ADC, with no amplification. However,
 1335 it has a Mini-Circuits ZX75LP-288-S+ low pass filter [62] to prevent aliasing. This is the
 1336 same model low pass filter which is used for the main channel. The antenna is hung a few

²⁶Calculations in dB like this are handy once they are understood, but can seemingly come out of nowhere. This can be worked out by a careful reading of section 2.2, using properties of logarithms and definition of the dB.

1337 feet in front of the door from some pipes on the ceiling. The proximity to these pipes likely
1338 give the antenna a strange response, but it's purpose is simply to look for large RFI signals,
1339 so this isn't that important.

1340 **2.5.6 12 V power system**

1341 The LNA and switch are active component which require power to operate. The experiment
1342 is incredibly sensitive to RFI, so while there is 120 VAC in the room, it is simpler to provide
1343 the power from a 12 V battery than use a AC/DC regulator. Originally a 12 V lithium-ion
1344 (LiFePO4) battery was used. Lithium-ion batteries contain several cells and a controller
1345 to regulate charge/discharge between the cells. In order to remove the possibility of this
1346 controller emitting RFI in the room (which would create candidates that would be extremely
1347 difficult to veto), the lithium-ion was replaced with a 12 V lead acid golf cart battery²⁷.

1348 The LNA is interlocked to the door such that power is cut when the door is opened. This
1349 prevents the large radio signals being amplified once they enter the room and protects the
1350 ADC. The circuit that controls this is shown in Fig. 2.43. Note that it takes a few seconds
1351 for the slow turn on circuit to discharge, so the door should be opened slowly

²⁷This was done between run 1.2 and 1.3 due to interference resulting in many candidate detections. Most of these were likely external RFI which were eliminated by cleaning the door (discussed in Sec. 3.2. Two variables were changed (cleaning of the door and replacement of the battery) so it's unclear if a lead acid is necessary. It works however, and if it aint broke don't fix it.

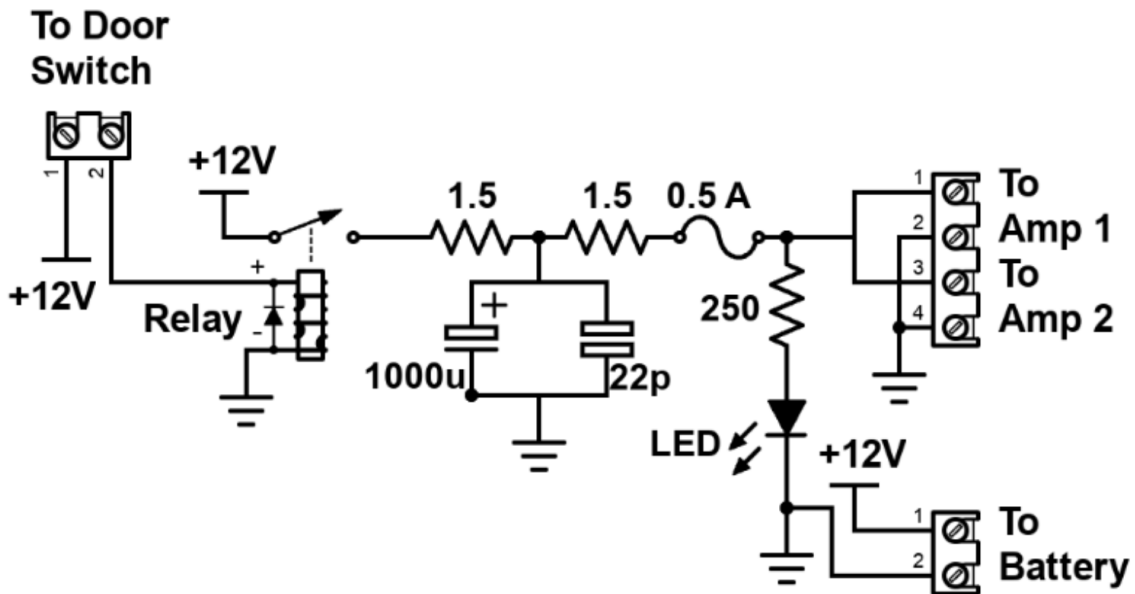


Figure 2.43: Schematic of Interlock board. No voltage regulation is provided because it is designed to work with amplifiers containing internal regulation (Pasternack PE15A1012 [36]). Not shown is a simple “slow turn on circuit” consisting of a 0.68 F capacitor and a 8Ω , 10 W resistor (time constant = 5.4 seconds) which was installed to protect the amplifier from transient voltages when the door is closed. This circuit can be seen in Fig. 2.44. Experience has shown the liberal use of fuses to be prudent when working with car batteries in a metal room.

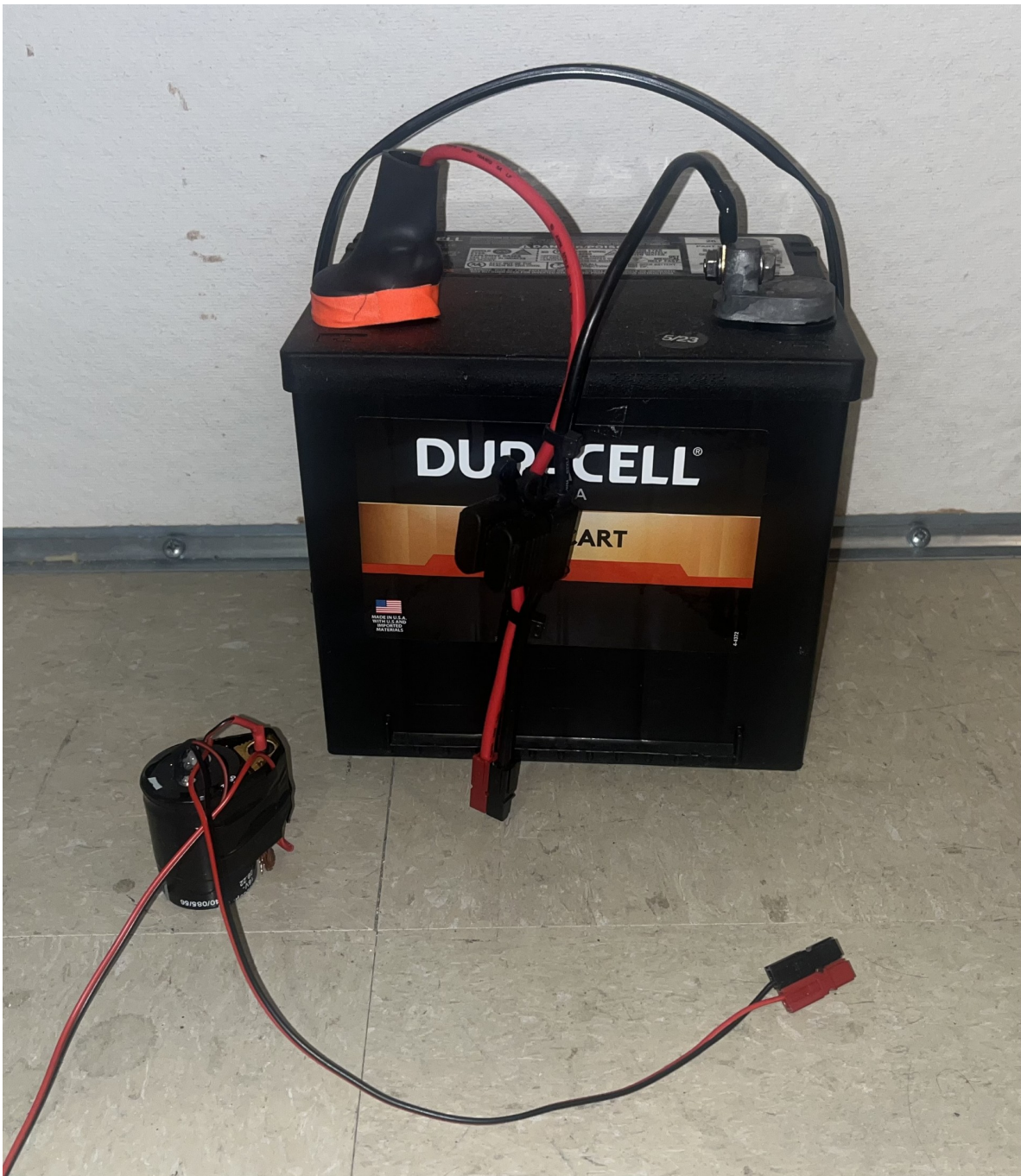


Figure 2.44: Photo of 12V lead-acid battery and slow turn on circuit. Both connect directly to the interlock board shown in Fig. 2.43. Slow turn on circuit is connected between interlock board and amplifier. Battery includes a 2A fast fuse installed in commercial Anderson power pole assembly.

1352 **2.5.7 GPU-Based Real-Time Spectrum Analyzer**²⁸

1353 The use of commercial Spectrum Analyzers (SAs) which feature so-called real time spectrum
1354 analyzer (RTSA) mode come with several restrictions which limit the efficiency with which
1355 they are able to perform wide-band scans with narrow frequency resolution, as as pointed
1356 out the dark radio pilot run [4]. The number of frequency bins output by a real discrete
1357 Fourier transform (DFT) is equal to half of the number of time domain samples, while the
1358 bandwidth is given by half of the sample rate. Furthermore, the ability to acquire data in real
1359 time requires a DFT algorithm (generally implemented as a fast Fourier transform, FFT)
1360 and computational resources which can operate on time domain data at least as fast as it is
1361 acquired. In practice, real-time DFTs with high frequency resolution and wide bandwidth
1362 require modest memory, transfer rates and processing resources. Commercial “real time
1363 spectrum analyzers” tend to cheat a bit to reduce hardware requirements. Frequency mixers
1364 reduce required sample rate (and therefore span), limits on FFT lengths reduce either span
1365 or resolution, and limits on rate of scans make it so that these SAs aren’t real-time (at least
1366 in the sense that we require them to be).

1367 For this reason, I have constructed a custom SA based on the Teledyne ADQ32 PCIE
1368 digitizer[37], which is wide-bandwidth (up to 1.25 GHz frequency span), high resolution
1369 (2^{24} point FFT), and nearly 100% real-time (see Fig. 3.16). I have been unable to find a
1370 commercial SA with comparable capabilities. Specifications are shown in table 2.5.

²⁸Code for this section can be found at: <https://github.com/josephmlev/darkRadio/tree/master/daqAnalysisAndExperiments/teledyne>

Bit depth	12 bits
Sample rate	800MHz
DFT input length	2^{24} samples
FFT compute time	2 ms
Channel count	2
Efficiency	99.765%

Table 2.5: Specifications for the custom, real time spectrum analyzer used for run 1A.

1371 After passing through and amplifier and filter chain outlined in Sec. 2.5.4, both the main
 1372 and veto antenna's RF signals are digitized by the ADQ32's two independent ADCs. This
 1373 raw, digitized time series is sampled at the digitizer's clock rate. Since the discrete Fourier
 1374 transform (DFT) of a perfect sinusoid sampled by an unstable clock will have a finite spectral
 1375 width, clock stability must be better than the expected spectral width of candidate signals,
 1376 which in our case is set by the expected $Q_{DP} \approx 10^6$. To achieve the required stability,
 1377 we synchronize the sample clock (Valon 5009 RF synthesizer) of our ADC to a 10 MHz
 1378 rubidium frequency standard (Stanford Research Systems FS725) which is further steered
 1379 by the one pulse-per-second (pps) signal from a GPS receiver. Clock performance is discussed
 1380 in Sec. 3.3.3.

1381 This system utilizes a GPU direct write in order to minimize CPU-GPU copies tends to
 1382 be significantly slower than the FFT itself. This GPU direct write is implemented by the digi-
 1383 tizer's C++ API which is called from python. This happens in the `teledyneTemplate/drDaq.py`
 1384 script (within the directory linked as a footnote at the beginning of this subsection). The
 1385 GPU is a Nvidia A5000. The process is shown graphically in Fig. 2.45

1386 First, several buffers are allocated in GPU memory. A record is acquired (2^{24} time domain

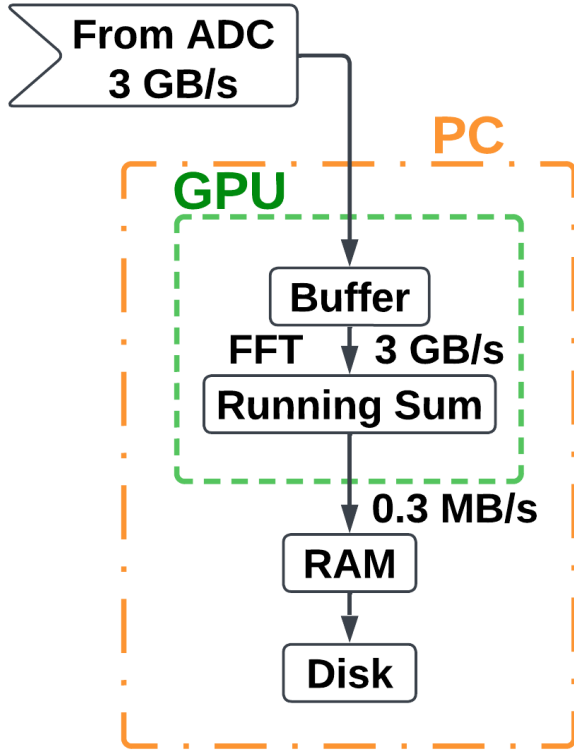


Figure 2.45: Real time DAQ data stream. Approximately 10^4 time series records (about 3 minutes of real time data) are written from the ADC directly to GPU buffers. FFTs are performed on these records resulting in a pre-averaged spectrum which can be saved to disk. This set up is duplicated for channels A and B, though the data rates indicate the sum of both channels.

1387 samples for run 1.4). This record is written to a pre-allocated, time-domain buffer in the
 1388 GPU's memory. Next, an FFT is performed using Pytorch which I found to be the fastest
 1389 algorithm, at least on a Nvidia GPU. 8,600 FFTs are performed and added to a cumulative
 1390 sum on the GPU (representing about 3 minutes of real time data). Dividing by the number of
 1391 FFTs provides an averaged spectrum that is saved for offline processing. This *pre-averaging*
 1392 reduces the raw $\approx 1.5 \text{ GB/s}/\text{channel}$ data stream to $\approx 0.15 \text{ MB/s}/\text{channel}$, which greatly
 1393 reduces storage requirements. However, this comes at the cost of temporal resolution of

1394 transient candidates. Since we are interested in constant (or at least very slowly varying)
1395 signals, this is not a problem, but in other radio astronomy applications, this step should be
1396 avoided. Pre-averaging is set using the NOF_BUFFERS_TO_RECEIVE variable, see Appendix A .

¹³⁹⁷ **Chapter 3**

¹³⁹⁸ **System Characterization and Data**

¹³⁹⁹ **Acquisition System**

¹⁴⁰⁰

“When you can measure what you are speaking about and express it in numbers you know something about it; but when you cannot measure it, when you cannot express it in numbers your knowledge is of meagre and unsatisfactory kind; it may be the beginning of knowledge but you have scarcely progressed in your thoughts to the stage of science whatever the matter may be.”

Lord Kelvin

1401 This chapter covers the characterization of the system as a whole, including the shielded
1402 room (Introduced in Sec. 2.5.1), amplifier chain (Sec. 2.5.4) and real-time spectrum analyzer
1403 system (RTSA, Sec. 2.5.7). This section provides data and information about how they
1404 were collected from tests that were performed, but that distract from the narratives of the
1405 preceding and following chapters. This chapter can be skimmed and referenced with further
1406 care during the reading of Ch. 4.

1407 **3.1 Measurement of Amplifier Chain Performance**

1408 The amplifier chain conditions the analog signal (described in Sec. 2.5.4). The following data
1409 show some measurements that are useful in confirming the system is operating as expected.
1410 Similar data should be collected and inspected before, during and after a new data run so
1411 that any performance degradation can be monitored. At the very least, one should take
1412 note of the power spectrum from a room temperature terminator (Fig. 3.10) and monitor it
1413 throughout the run for any changes. The heads-up display (Fig. A.1) makes this very easy.

1414 **3.1.1 Y-factor method¹**

1415 The Y-factor method [65] [66] is a common technique for measuring the gain and noise
1416 temperature of an amplifier chain (details in Sec. 2.1.4). A matched terminator is placed at
1417 the end of a transmission line, which is connected to the input of an amplifier chain under
1418 test. The output of the amplifier chain is measured with the terminator at two different

¹Code for this section can be found at: <https://github.com/josephmlev/darkRadio/tree/master/daqAnalysisAndExperiments/run1p4/yFactorTest/yFactorTest.ipynb>

1419 temperatures². These temperatures must be known, and the larger the difference the better
1420 the measurement because it is easier to extrapolate the slope and intercept from these data
1421 (see Fig. 3.1).

1422 There are a few different ways to handle the algebra, but the simplest is to fit a line of
1423 the form

$$T_{\text{out}}(\nu) = G T_{\text{term}} + B, \quad (3.1)$$

1424 where all terms are dependent on frequency. The x-intercept (and therefore the negative
1425 amplifier temperature) is simply G/B . This is shown as a cartoon for a single frequency in
1426 Fig. 3.1.

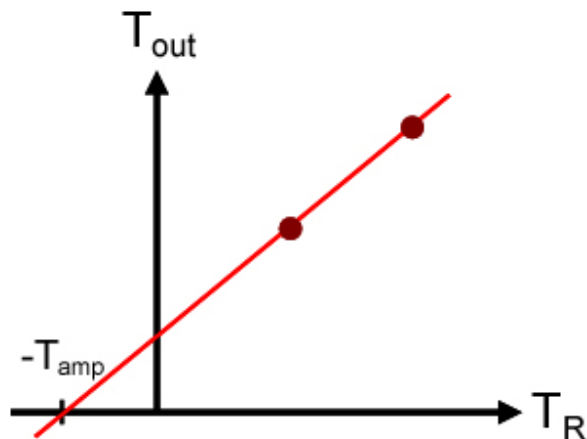


Figure 3.1: Cartoon showing Y-factor data. The (negative of) amplifier temperature is read off of the x-intercept. The gain is given by the slope. Figure from Wikipedia [67].

1427 To make this measurement, I wanted to use liquid nitrogen for the cold temperature

²Alternatively, a calibrated noise source can be used to simulate a very hot terminator, usually thousands of degrees Kelvin.

1428 (77 K) and a calibrated noise source for the hot temperature (\sim 12,000 K). The test was
1429 conducted using the noise source and a 30 dB attenuator placed directly before the ADC.
1430 This attenuation was later accounted for, yielding a calibrated measurement. However,
1431 while the test was set up to use this noise source, it gave unreliable results. I was able
1432 to confirm it became uncalibrated using a spectrum analyzer so I did not use that data
1433 point. Additionally, I made the measurements with a much wider bandpass filter (0-1 GHz)
1434 compared to the span of this Run 1.4 (0-0.3 GHz) so that the same data would also give
1435 the gain and noise temperature up to 1 GHz (though this is not shown in this thesis). Both
1436 the 30 dB attenuator and the 0-1 GHz bandpass filter will be calibrated out. As a check this
1437 is done correctly, the gain was measured again using a tracking generator with the actual
1438 setup, avoiding corrections. This is shown in Fig 3.7. The two gain curves agree quite well.

1439 The test setup is nearly identical to the Run 1A amplifier chain (see Fig. 2.42). The
1440 differences are the 30 dB attenuator and band pass filter (discussed above) and the short,
1441 semi-rigid, cryogenic-capable cable between the terminator and LMR 400 cable. The cryo-
1442 genic setup is the same as shown in the right panel of Fig. 2.28. The raw data (including
1443 only liquid nitrogen and room temperature) are shown in Fig. 3.2.

1444 The spectra of Fig. 3.2 contain hot and cold measurements at 2^{18} frequency points. At
1445 each point, a fit is performed according to Eq. 3.1. To demonstrate, this is shown for a single
1446 frequency (625 MHz) in Fig. 3.3.

1447 Finally, fitting the raw spectra shown in Fig. 3.2 with Eq. 3.1 at each of the frequency
1448 points, the frequency-dependent gain and noise temperature of the amplifier chain is ex-
1449 tracted. These are shown (after correcting for the 30 dB attenuator) in Figs. 3.4 and 3.5.

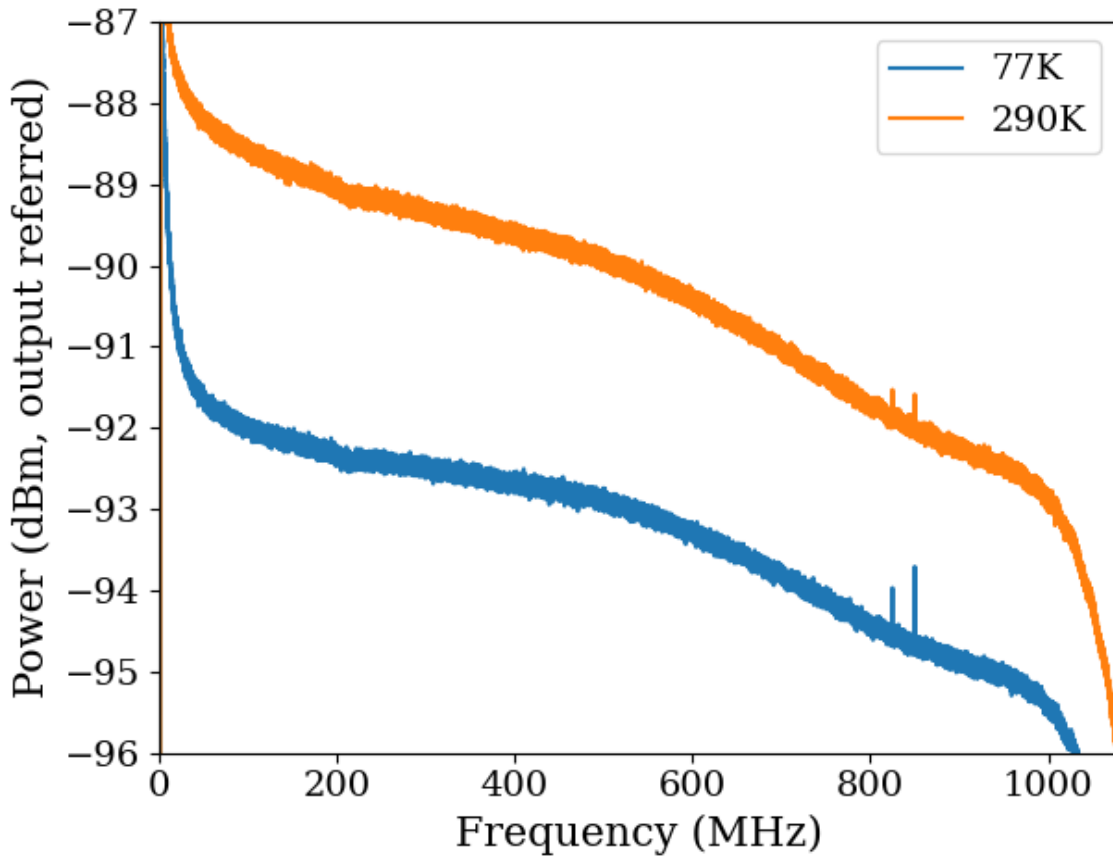


Figure 3.2: Raw output power spectra used to compute the gain and noise temperature for the Run 1.4 amplifier chain using the Y-factor method. $\Delta\nu_{\text{RF}} \approx 9.5 \text{ kHz}$, and 10,000 averages were taken. These data are only used to characterize the system between 50 and 300 MHz, so the low frequency ADC effects and RFI around 800 MHz do not affect the calculation. Note that the amplifier chain under test has a 30 dB attenuator directly before the ADC which is discussed in the text. This had an impact on the measured gain, and it is corrected for in the following analysis. It has negligible impact on the noise figure however, as shown in Eq. 2.29.

1450 As a final check, I took the Run 1.4 terminator data and corrected it for the gain and noise
 1451 figure found using the Y-factor method of this section, expecting to recover the -174 dBm/Hz
 1452 as predicted by Johnson's formula for a terminator at room temperature. The agreement is
 1453 quite good as shown in Fig. 3.6.

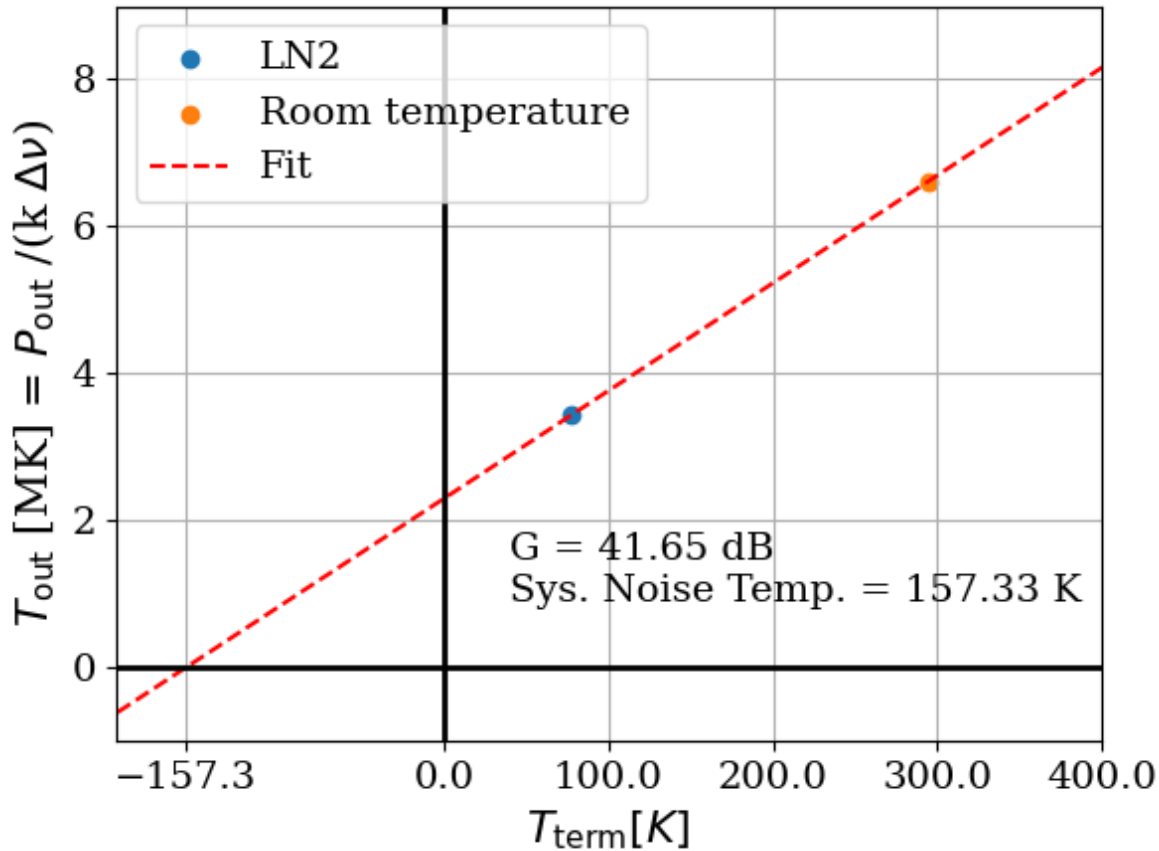


Figure 3.3: Y-factor data from Run 1.4 amplifier chain at a single frequency (625 MHz). Note that T_{out} is in MK or millions of degrees Kelvin. This is expected since there is approximately 41 dB of gain on an input temperature of a few hundred Kelvin. Reminder, there is a 30 dB attenuator which has not yet been corrected for.

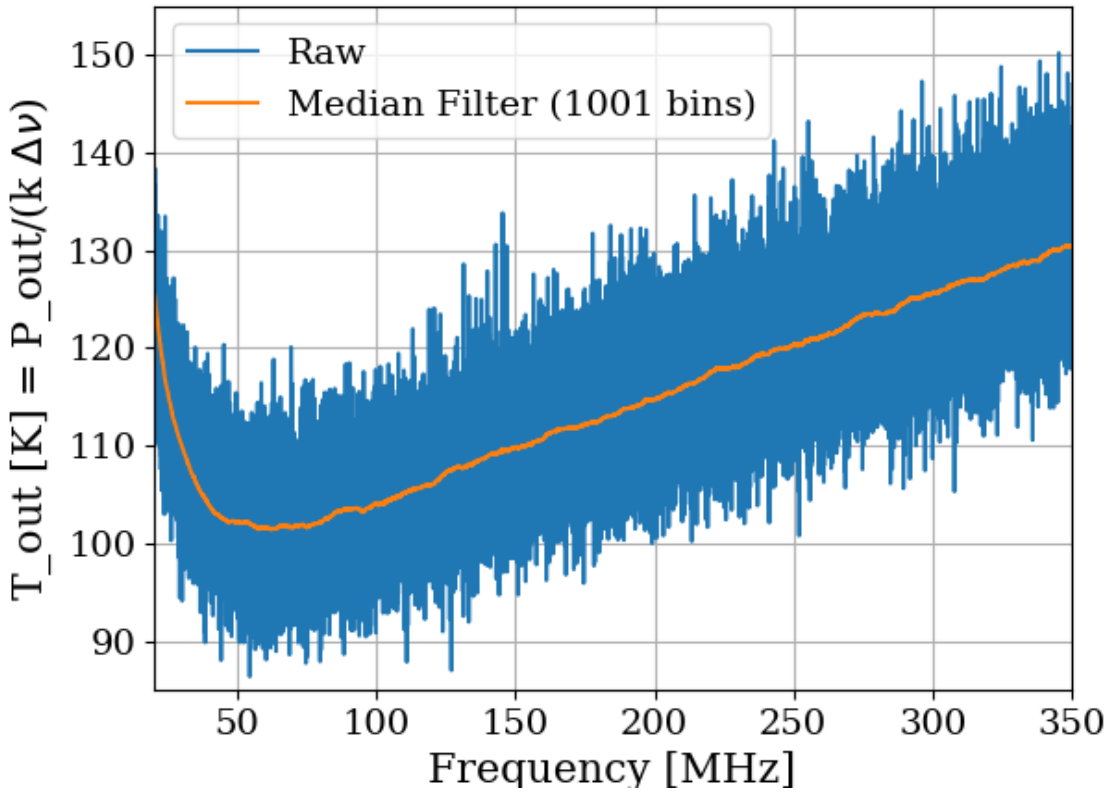


Figure 3.4: Frequency-dependent noise temperature of the Run 1.4 amplifier chain, measured using the Y-factor method. Low-frequency behavior is consistent with the data sheet of the LNA [36]. The increase at high frequency is due to the attenuation of the cable before the LNA. Future runs may place the LNA directly on the antenna to minimize this issue, though other complications will be introduced. The median filter is a simple rolling median to smooth out the noisy measurements.

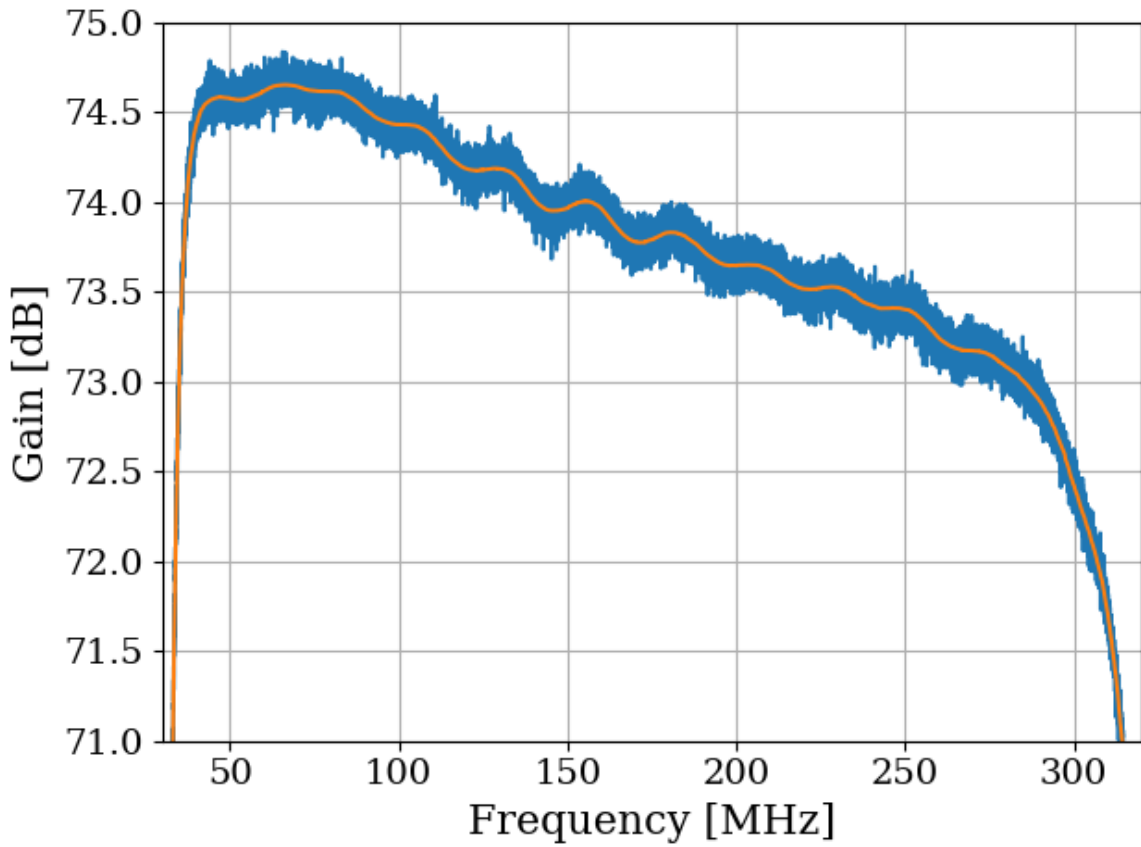


Figure 3.5: Frequency-dependant gain of the Run 1.4 amplifier chain, measured using the Y-factor method. The 30 dB attenuator and band pass filter have been corrected for in this plot. The slow decrease of gain with frequency is consistent with the data sheets for the LNA [36] and secondary amplifier [59]. Roll-off at high and low frequencies is due to the bandpass filter (see 2.5.4.3). Bumpy behavior is due to the small impedance mismatch of the terminator to the 50Ω system.

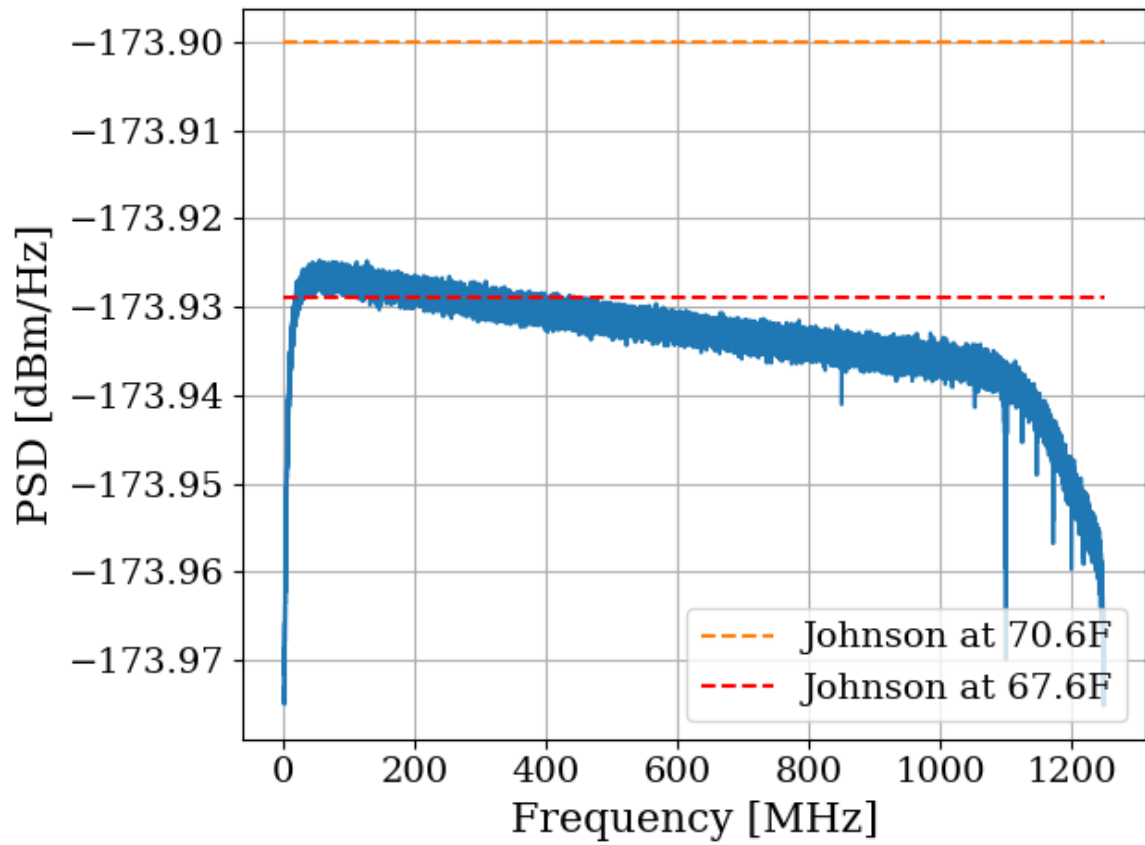


Figure 3.6: Run 1.4 terminator, input-referred power spectral density. Excellent agreement with the predicted value from the formula for Johnson noise at room temperature. Two reference temperatures are given with the dashed lines.

1454 **3.1.2 Confirming gain with tracking generator measurement**

1455 As a sanity check for the Y-factor method, the system gain was measured again using the
1456 tracking generator on the Rigol RSA-5065-TG [68], with good agreement. This measurement
1457 was useful since there were some corrections involved in the Y-factor measurement (the 30 dB
1458 attenuator and band pass filter).

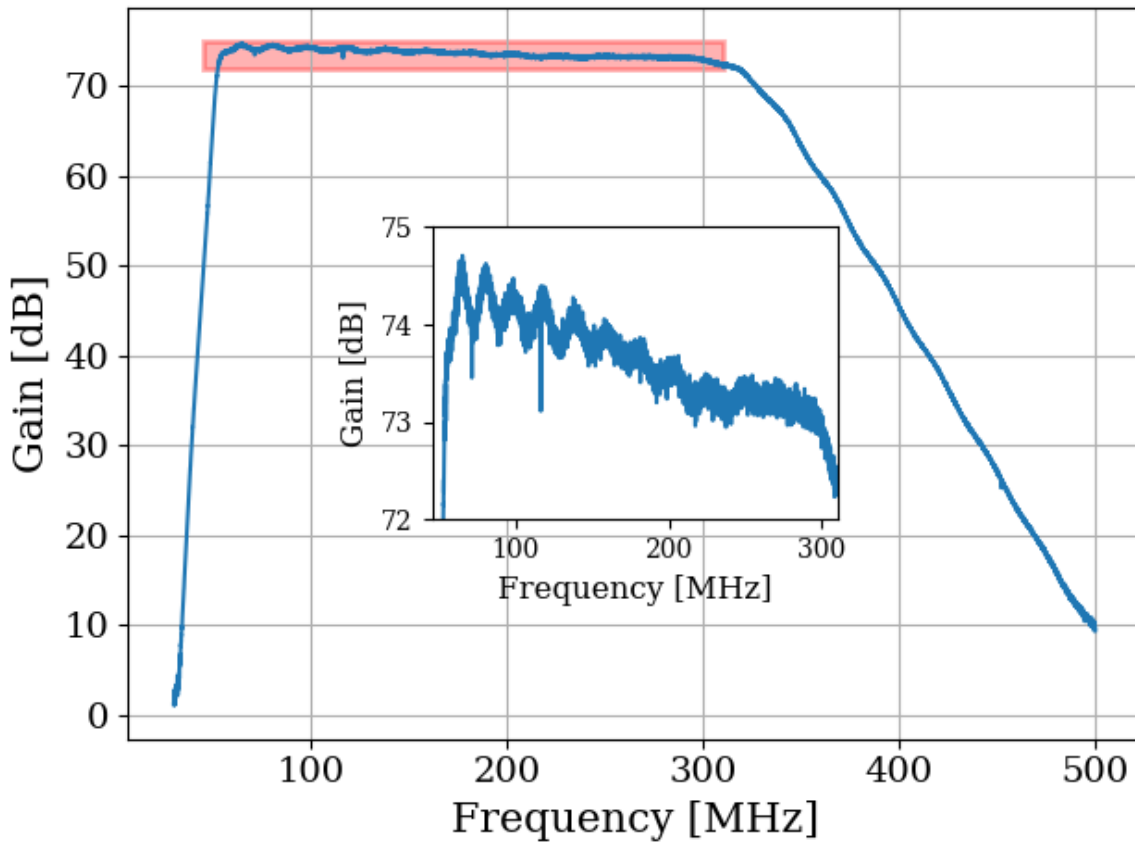


Figure 3.7: Gain vs. frequency of Run 1.4 amplifier chain, including LNA, secondary amplifier, bandpass filter and attenuators. Inset shows zoom of region enclosed in red box. This was measured using the tracking generator on Rigol RSA-5065-TG [68]. Wiggles visible in inset are a known artifact due to an impedance mismatch between the Rigol's tracking generator and the system under test. Gain was confirmed by comparing to Y-factor method (Sec. 3.1.1)

1459 **3.1.3 System stability over a run period**³

1460 The system's gain will vary slightly over the course of a run. An obvious culprit is the
1461 battery voltage decreasing with time⁴. At first glance, one may conclude that since the
1462 LNA is equipped with an internal voltage regulator, it is insensitive to the battery voltage
1463 as long as it is above some minimum value. However, at higher voltage, the regulator must
1464 dissipate more power which will make the LNA warmer. Temperature does have an effect
1465 on the gain of the LNA. Tests of gain vs. LNA voltage show that this is a minor issue. This
1466 is shown in Fig. 3.8.

1467 Knowing the gain vs voltage is only useful if it is understood how the battery voltage
1468 will behave over the course of the run. These data are shown in Fig. 3.9.

1469 As a final check of system performance during the run, Fig. 3.10 shows the output-referred
1470 power (averaged from 50-300 MHz) over the course of the 9-day Run 1.4. The gain varies by
1471 about 0.7%, an insignificant amount given the other uncertainties involved (especially that
1472 of simulation and calibration, Sec. 4.3).

³Code for this section can be found at: [https://github.com/josephmlev/darkRadio/tree/master/daqAnalysisAndExperiments/run1p4/run1p4_timeDependence.ipynb](https://github.com/josephmlev/darkRadio/tree/master/daqAnalysisAndExperiments/run1p4/run1p4_analysis/run1p4_timeDependence.ipynb)
https://github.com/josephmlev/darkRadio/tree/master/daqAnalysisAndExperiments/run1p4/gainAndNf/gainAndNF_analysis.ipynb

⁴The LNA is powered by a battery. The secondary amplifier is outside of the room and powered with a voltage regulator.

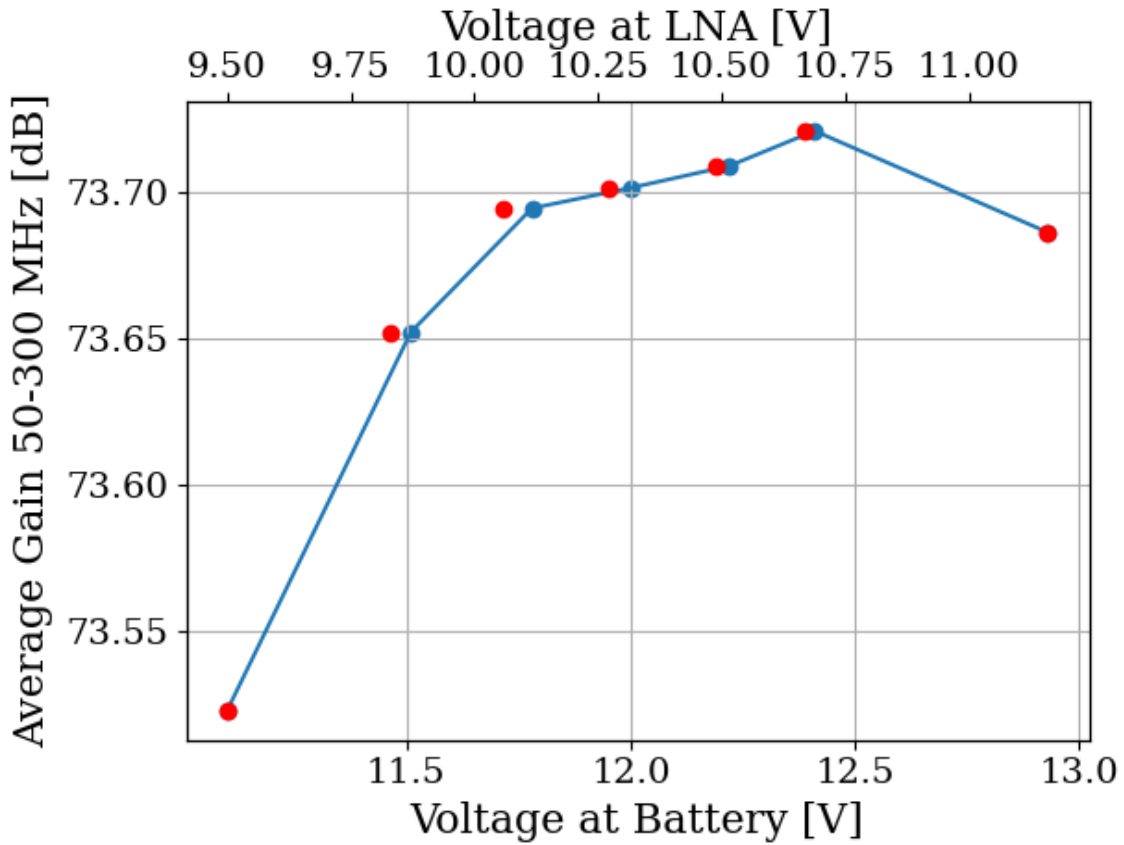


Figure 3.8: Gain vs. LNA voltage of Run 1.4 amplifier chain, including LNA, secondary amplifier, bandpass filter and attenuators. This was measured using the tracking generator on Rigol RSA 5065TG [68]. Gain is frequency dependent; its average value between 50 and 300 MHz is shown here. Voltage at the amplifier was measured directly at its terminals, after significant voltage drop due to interlock and slow turn-on circuits (described in Sec. 2.5.6). Gain is in good agreement with the previous two subsections, 3.1.1 and 3.1.2. The operating voltage range specified on LNA data sheet [36] is 10-15 V. The voltage at the LNA (red) does not exactly line up with voltage at battery (blue), so there is a slight offset. The scale of the x-axes scale has been set so that the maximum and minimum voltages line up.

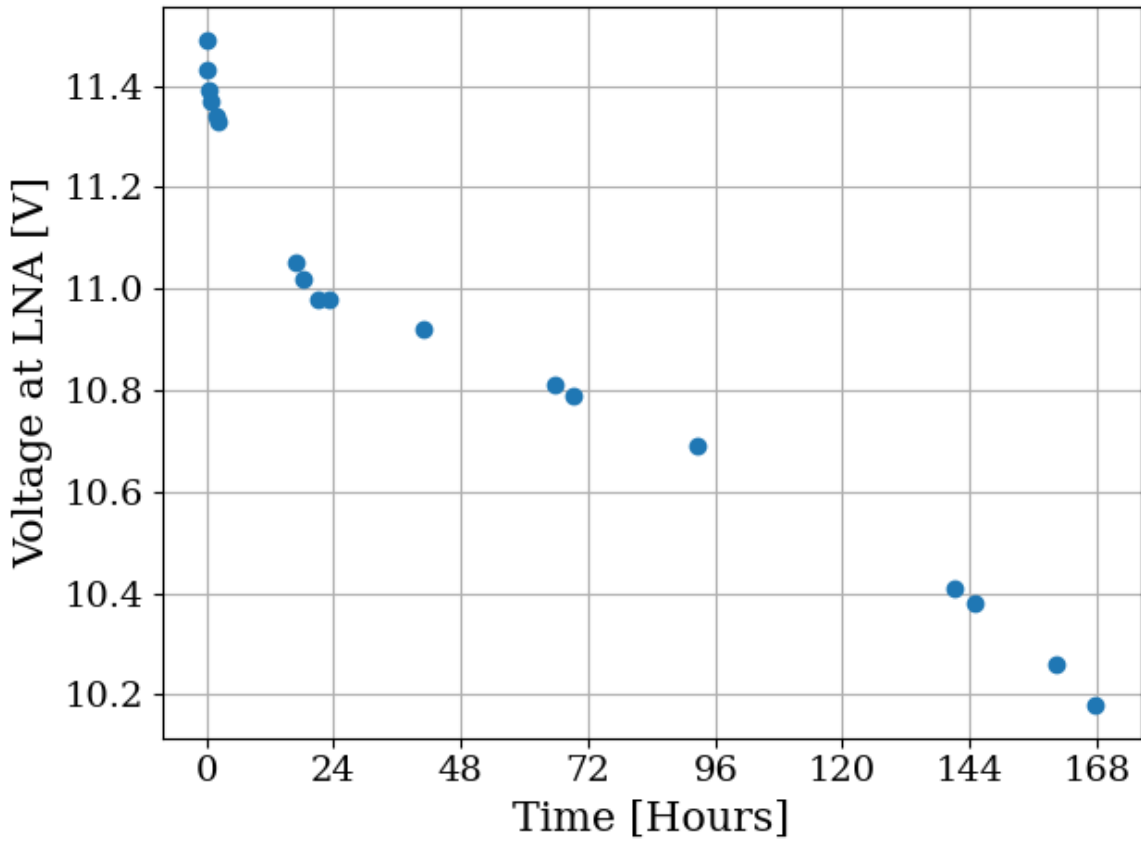


Figure 3.9: Voltage at LNA vs. time. Data were acquired 7/15/2024 through 7/22/2024 using battery number 2 immediately after being charged. The system was set up as it was for Run 1.4, including the switching cycle (on for 3 minutes, off for 45 minutes). The battery supplies 177 mA when the switch is off, and 370 mA when the switch is on. There is an additional data point (not shown) around 196 hours where the voltage has dropped to 6.2 V, well below the minimum required voltage. The battery had approximately 20 charge/recharge cycles at the time of this test and was about 14 months old. A repeat of this test may be required to use the battery for longer periods between charges.

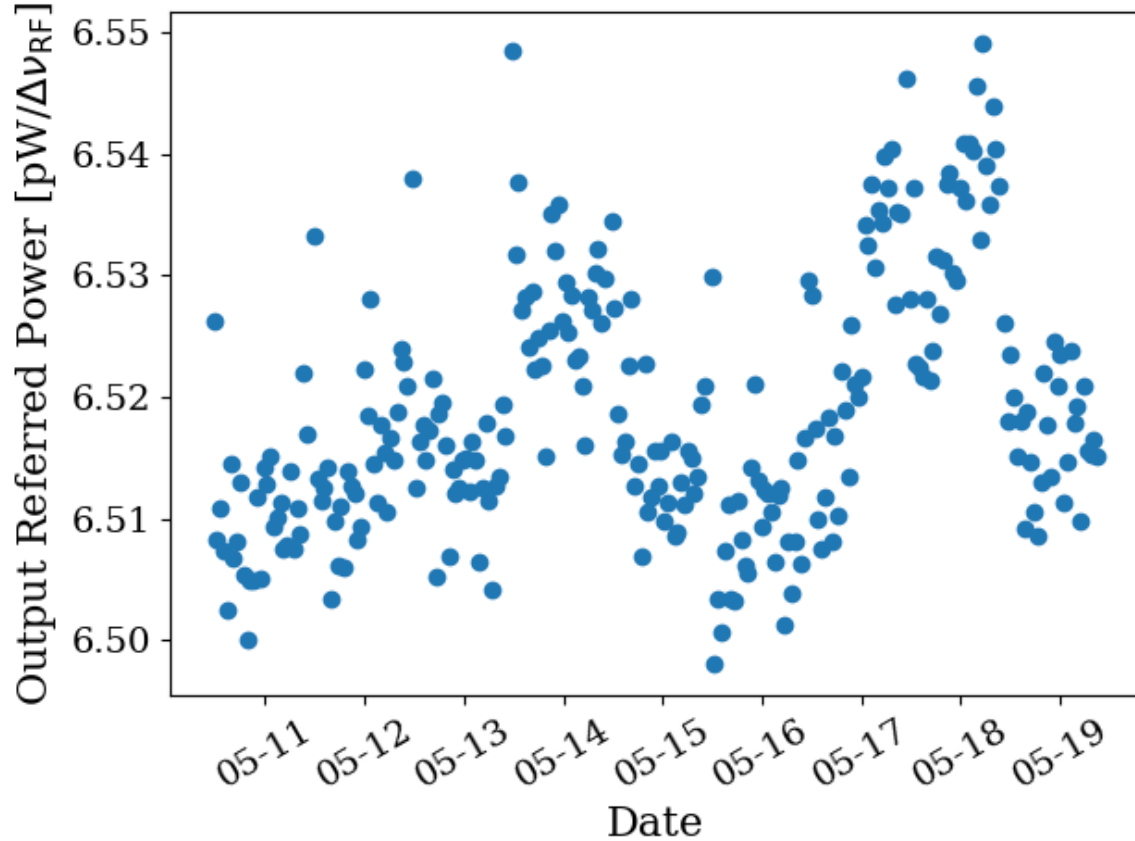


Figure 3.10: Frequency-averaged power spectral density vs. time of the terminator from Run 1.4 (schematically shown in Fig. 2.37). Each data point represents the mean power between 50 and 300 MHz of the terminator. In Run 1.4, a \sim 3 minute long scan of the terminator took place after \sim 45 minutes of antenna scans. Dates shown are all May 2023 (month-day format, year suppressed), and x-axis ticks are shown at midnight.

1473 **3.2 Measurement of shielding effectiveness and radio**

1474 **frequency interference**

1475 Shielding effectiveness (SE) and radio frequency interference (RFI) were introduced in Secs.

1476 2.1.3 and 2.5.1. Their measurement is introduced here.

1477 Similar to the warning given in the previous section, SE should be measured before
1478 starting a data run or after entering a new frequency range/modifying anything on the
1479 patch panel. In addition, it is best practice to clean the door's RF seal before beginning a
1480 run (the procedure is described in the text of this section).

1481 Due to reciprocity between antennas, measuring the shielded room's ability to keep radi-
1482 ation *out* is equivalent to measuring how well the room can keep it *in*. The latter method is
1483 simpler and was performed. The IEEE standard prescribing a very detailed SE measurement
1484 procedure [69] was used as a rough guideline, but the simple results presented here should
1485 be viewed as an estimate. While simplified, the results do tend to agree with predictions of
1486 when RFI should become detectable, based on comparisons to the veto antenna spectrum ⁵.

1487 The SE was measured by placing a Rigol DSG830 signal generator and 25 Watt RF power
1488 amplifier inside the room, both powered by the filtered 120 VAC Edison outlets inside the
1489 room, shown in Fig. 3.11. An antenna was connected to the signal generator. Outside of
1490 the room, an identical antenna was connected to a Rigol RSA-5065-TG spectrum analyzer
1491 [68]. The spectrum is scanned to find a frequency without local interference which would

⁵Or at least they did agree before cleaning the door. With the excellent isolation values, no RFI was detected in Run 1.4.

1492 confuse the results. The spectrum analyzer was set to attenuate its input to prevent clipping
1493 ⁶, and the signal generator was set to output a sine wave near the maximum power of the
1494 RF amplifier ($20\text{ W} = 43\text{ dBm}$). The power measured on the spectrum analyzer is P_{open} in
1495 Eq. 2.46. The door was closed, attenuation removed and P_{closed} was measured. In some
1496 cases the SE was so high a signal was buried below the noise floor of the spectrum analyzer.
1497 These data are shown in red in Figs. 3.12 3.13 and should be interpreted as an upper limit
1498 on isolation, since the true value is lower (better).

1499 SE can drop off to less than 80 dB if the RF gasket around the door is not clean. Previous
1500 day-long test runs detected several hundred signals that originated from RFI emitted from
1501 the PC and several local radio stations. Cleaning was performed by scrubbing the copper
1502 finger stock and steel mating surfaces with red Scotch-Brite using denatured alcohol as a
1503 lubricant ⁷. After two passes of polishing were complete, a layer of DeoxIT D100L liquid
1504 was added. Maintenance cleanings were performed using only DeoxIT D5 spray. These
1505 signals were not detected after the gasket was cleaned, which is consistent with calculations
1506 of Sec. 2.1.3

1507 The primary RFI in the 50-300 MHz span are from local radio broadcasts. The electric
1508 field of the strongest signals is $\sim 100\text{ }\mu\text{V/m}$ when measured in the lab. There are also many
1509 lower level peaks which span the entire frequency range, though are more pronounced in a
1510 few frequency bands (60-75 MHz, 130-140 MHz, and 270-290 MHz). These peaks come from

⁶The spectrum analyzer automatically calibrates the displayed spectrum to its internal attenuator and pre-amplifier. If external gain/attenuation are used, they must be accounted for manually. Since this is a relative measurement (i.e., a ratio of $P_{\text{open}}/P_{\text{closed}}$), this calibration does not matter much.

⁷Alcohol fumes are nasty. Be careful to open the hallway door and use a fan to blow in air from the hall. Take frequent breaks. Don't get dizzy while standing on a chair!



Figure 3.11: Photo showing setup to measure SE of 314. Photo taken using Vivaldi antennas for data shown in Fig. 3.13. The same setup was used with bicon antennas for the 50-300 MHz data shown in Fig. 3.12. The bicon antenna shown in the background of this photo was not used for this test.

1511 the PC which is an integral part of the spectrum analyzer system, housing the ADC, so it
1512 can not be removed. Before the door was cleaned, many of these signals were detectable
1513 after a few hours of integration, but cleaning the door resulted in a clean spectrum for the
1514 9-day data Run 1.4. The spectrum from the veto antenna (discussed in Sec. 2.5.5) is shown
1515 in Fig. 3.14

314 Shielding Effectiveness

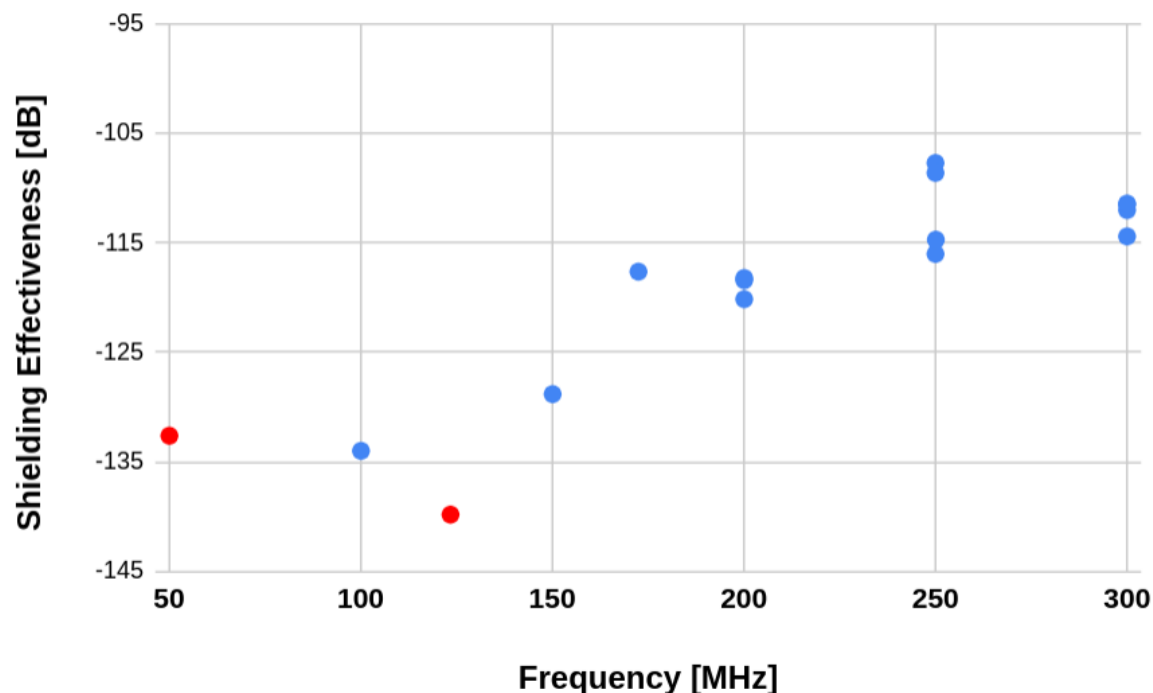


Figure 3.12: Shielding effectiveness of shielded room measured with bicon antenna. Red points indicate measurements limited by the noise floor of the spectrum analyzer located outside the shielded room and are an upper limit. The true SE is lower (better). To get the true SE for these points, measurement would require a higher gain amplifier inside the room. SE measurements are all better than required for Run 1.4, and no RFI candidates were detected. At a few frequencies, the antenna inside the room was moved to get a sense of the uncertainty of the measurement.

314 Shielding Effectiveness

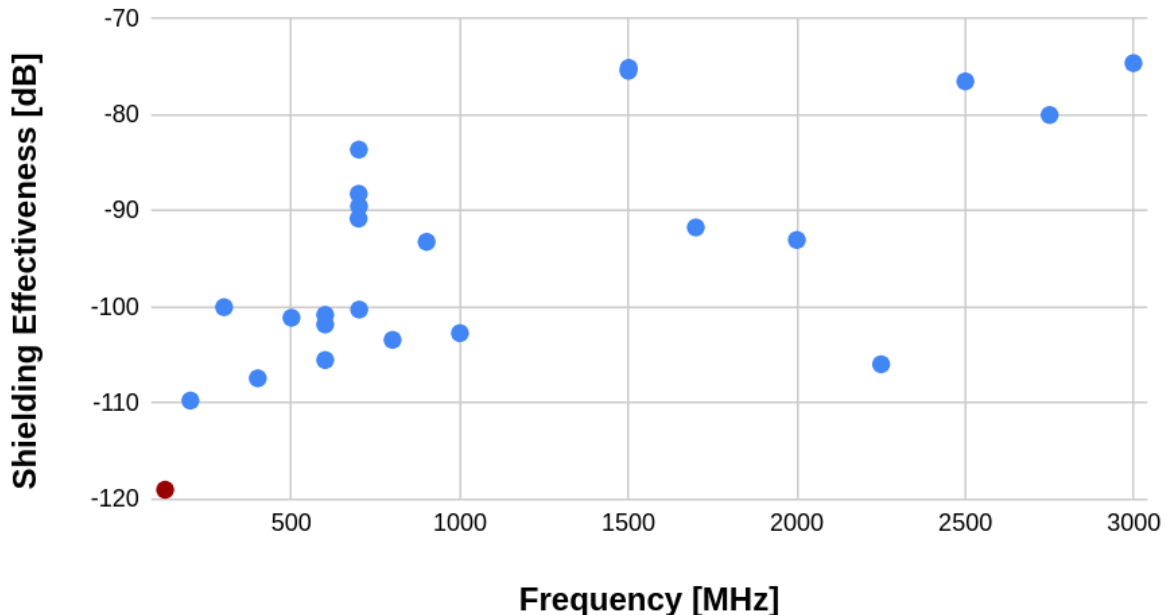


Figure 3.13: Shielding effectiveness of shielded room measured with Vivaldi antenna. Red points indicate measurements limited by the noise floor of the spectrum analyzer located outside and are an upper limit; true SE is lower (better). Measurement would require a higher gain amplifier inside the room. At a few frequencies, the antenna inside the room was moved to get a sense of the uncertainty of the measurement.

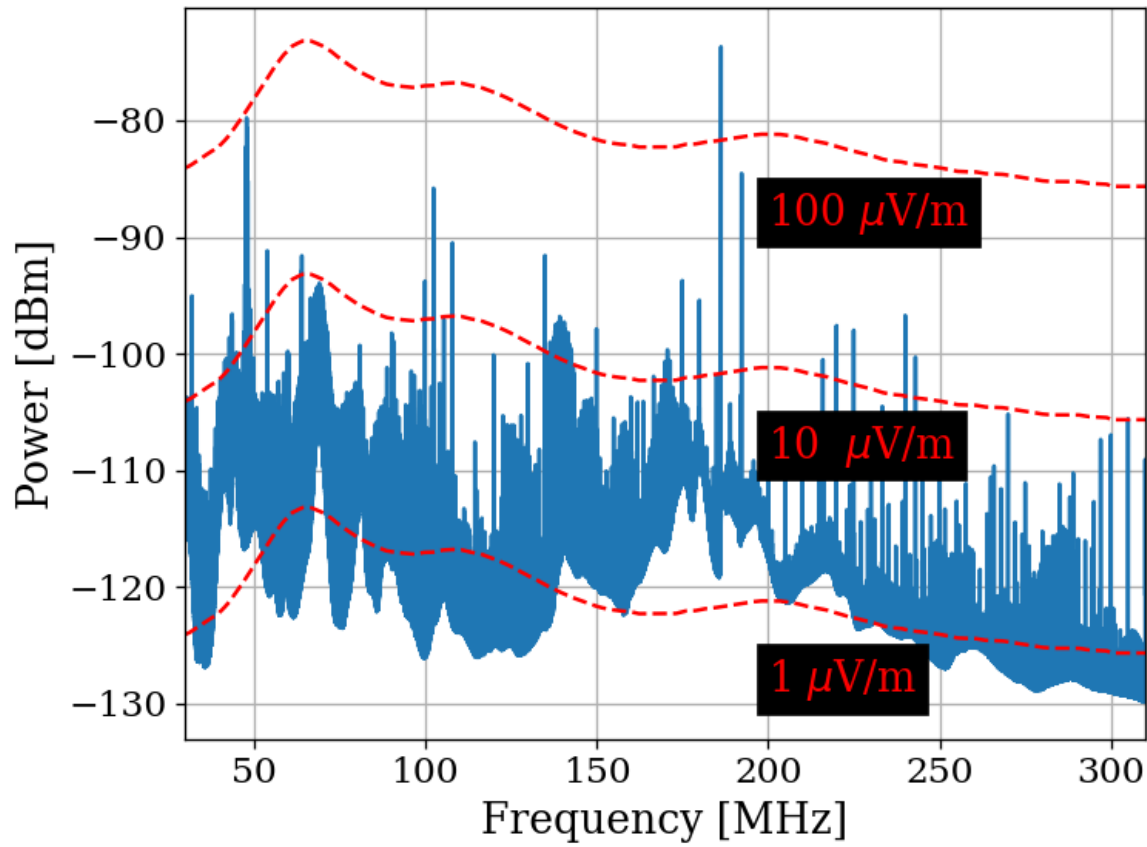


Figure 3.14: Spectrum from veto antenna during the 300 MHz data run. Spectrum plotted as measured power in dBm. Red curves indicate the equivalent field strength. These curves track the free-space antenna factor with frequency for the Com-Power AB900 [55] bicon. Two identical AB900-A antennas are used, one to search for dark photons in the shielded room, and a second to monitor the local RFI background.

1516 3.3 Spectrum Analyzer Characterization

1517 This section outlines several tests performed to ensure the GPU-based real-time spectrum
1518 analyzer (RTSA) system performs as expected. Background information that relates to
1519 this system is described in Sec. 2.5.7.

1520 3.3.1 Spectrum analyzer calibration

1521 The first step in determining if the RTSA system is working adequately is to make sure
1522 it is able to correctly identify known, injected signals and noise. This calibration step is
1523 important since the FFT is normalized manually (see Eq. 2.15), and it is rather easy to
1524 mess up. The test signals were generated with a Rigol DSG830 signal generator. The time-
1525 domain peak-to-peak voltage measured by the RTSA system agreed with the injected voltage
1526 to about 2 %. The signal generator's output frequency and power were verified in both the
1527 frequency and time domain using a separate oscilloscope and spectrum analyzer. This is an
1528 important step since cable losses are significant at this level of precision. They can be taken
1529 into account by consulting the data sheet for the cable⁸.

1530 Next, it is important to understand how the system handles noise spectra, since this is the
1531 primary use of the system. This is tested by amplifying the Johnson noise of a terminator (see
1532 Sec. 2.1.1.2) and measuring the power spectral density. Knowing the gain and noise figure
1533 of the amplifier chain allows for calibration using the procedure outlined in detail earlier in
1534 this chapter, see Sec. 3.1, specifically Fig. 3.6. These results were confirmed several times

⁸There are several cheap black SMA cables which are great for testing, but not for calibration. They have more than 5 dB of loss above 1 GHz. Use a nice cable for these tests, and blow out the SMA connector with compressed air while you are at it.

1535 preceding the data run. Note that due to windowing, other spectrum analyzers will disagree
1536 with the theoretical calculation by a few dB if the equivalent noise bandwith (ENBW) of
1537 the window function is not included. Also remember to take cable effects into account as
1538 discussed in the previous paragraph.

1539 **3.3.2 Spurious signal performance of the ADC**

1540 Any practical spectrum analyzer will have small, coherent, signals which sneak into the the
1541 analog signal path and, after being digitized and Fourier transformed, manifesting as spurious
1542 signals or *spurs* (see Sec. 2.1.5.1). These spurs likely come from clock signals within the same
1543 enclosure as the ADC. They can also come from local oscillators bleeding through mixers in
1544 a mixed, high-frequency system such as the Rigol RSA 5065TG [68] or the future, upgraded
1545 dark radio system discussed in Ch. 5.

1546 Regardless of their origin, the spurs must be characterized such that if a known spur is
1547 detected it can be classified as such and rejected quickly. Ideally, the system has enough
1548 gain that any spurs are subdominant to the amplified thermal noise, as discussed in Eq. 2.1.
1549 However, since there is a maximum amount of gain that can be added before clipping the
1550 ADC (see Sec. 2.5.4.3, this is not always possible.

1551 Experience with the Teledyne RTSA system has shown that spurs are rather simple to
1552 classify because they do not change much with time in either frequency or amplitude. Their
1553 frequency drifts by $\sim 1 \text{ kHz}$ and their amplitude changes by a few dB.

1554 To classify them, the input of the Teledyne is terminated and a scan is performed few

1555 minutes using the exact same system configuration as for the run (with the possible exception
1556 of the number of averages). See Appendix A for details. The averaged spectra of the
1557 terminated inputs are shown in Fig. 3.15.

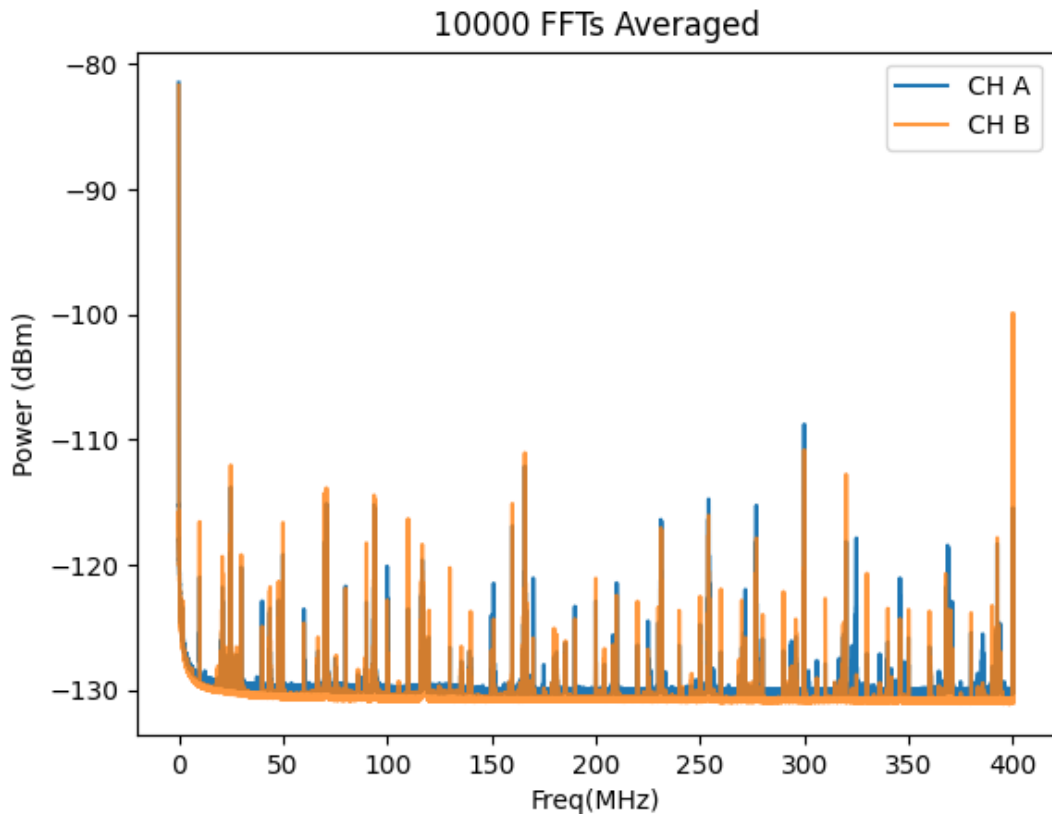


Figure 3.15: Scan of terminated input of Teledyne spectrum analyzer system to measure spur performance. The spectra were acquired with run 1A parameters ($\Delta\nu_{RF} = 47.7$ Hz) with 10,000 averages (~ 3.5 minutes). This plot is taken directly from test mode of the system (not post-processed in any way). The largest spur in the 50-300 MHz range is at 299.97 MHz and is also the single significant signal in Run 1.4 (see Sec. 4.2.5).

1558 Once a test scan is acquired, comparing the largest spurs (≈ -110 dB) to the expected
1559 output-referred background ([Johnson noise + LNA noise] * Gain ≈ -81 dBm/ $\Delta\nu_{RF}$) allows
1560 the calculation of the number of averages which are required before the spurs are significant.

1561 Working this out is a good test of understanding of Sec. 2.2. This spur should be detectable
1562 with 95% confidence after about 4 days, which is exactly what happened in Run 1.4. The
1563 false positive candidate is described in Sec. 4.2.5.

1564 **3.3.3 ADC clock performance**

1565 Any ADC requires a clock which dictates the precise time a sample should be acquired. This
1566 subsection deals with the evaluation of the performance of that clock.

1567 Determining the performance of a clock generally relies on having a better (read: more
1568 expensive) clock known as a *standard* and measuring the clock under test against the stan-
1569 dard. The Valon 5009 RF synthesizer was tested against a rubidium frequency standard and
1570 was found to be just on the threshold of stable enough to work (this threshold is explained in
1571 Sec. 2.5.7). To ensure the measurement is not limited by clock instability, the sample clock
1572 of the ADC is synchronized to a 10 MHz rubidium frequency standard (Stanford Research
1573 Systems FS725) which is further steered by the one pulse-per-second (pps) signal from a
1574 GPS receiver. This system has medium and long term fractional frequency stability (Allan
1575 deviation [70, 71]) of $\sigma_y(\tau) < 3 \times 10^{-12}$ (where τ is the averaging time) and phase noise of
1576 less than -65 dBc/Hz at offset frequencies > 50 Hz from the carrier [72]. This means that
1577 over the course of a single acquisition, the power contained in a bin will spread to an adjacent
1578 bin by less than 1 part in 10^6 which is more than sufficient for our experiment.

1579 This is a rare example of something in this experiment where we trust the data sheet.
1580 We do not have access to a clock which is better than this, so confirming its performance

1581 is difficult. Furthermore, even if the specs are an order of magnitude worse than advertised
1582 there is still more than enough stability for the experiment. This statement holds at higher
1583 frequencies. Since the Q of the signal is fixed, higher frequencies have wider bins so the
1584 relevant offset frequency at which the phase noise is measured increases with frequency. The
1585 dimensionless Allan deviation is also not affected.

1586 3.3.4 Real-time data collection efficiency

1587 As a final test, one would like to know how efficiently data scans can be acquired and
1588 averaged. We call a 100 % efficient system *real-time* as described in Sec. 2.5.7. Figure 3.16
1589 illustrates this efficiency. For Run 1.4, it is $\sim 99.765\%$. However, in practice run logistics
1590 such as moving the antenna prevent the full efficiency of the system from being realized.

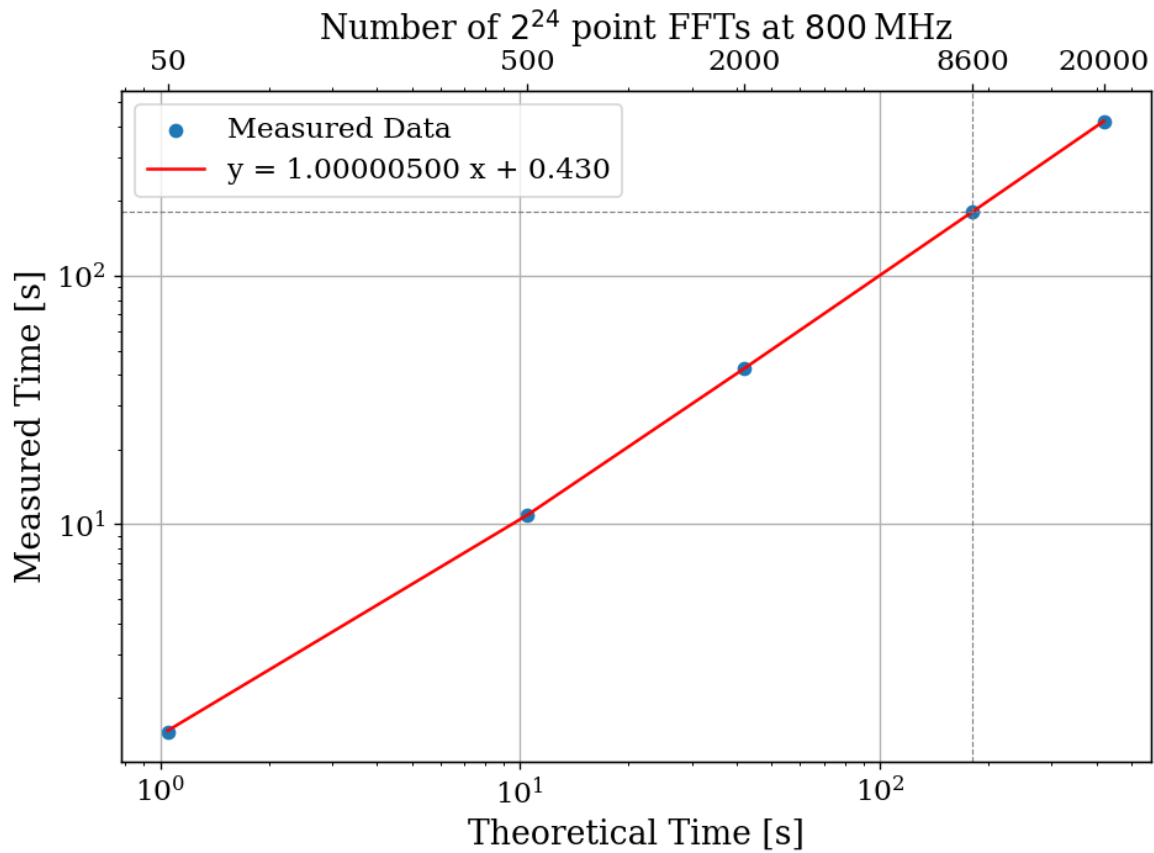


Figure 3.16: Acquisition efficiency for GPU-based real-time spectrum analyzer computed from measured vs. theoretical times. The constant offset of 0.43 s corresponds to a small set-up period when starting an acquisition containing, in the case of run 1A, 8600 FFTs. In the limit of an infinite length acquisition, the system's efficiency may be read off from the slope and is 99.9995%. The more realistic efficiency is a function of the number of FFTs per acquisition and for Run 1.4 = $180.3551 \text{ [s]} / 180.7782 \text{ [s]} = 99.765\%$.

₁₅₉₁ Chapter 4

₁₅₉₂ Data Acquisition, Data Analysis and
₁₅₉₃ Calibration

1594 Thus far this thesis has focused on building up a background on the dark radio technique
1595 as well as the design and testing of the experiment and its sub-systems. This chapter outlines
1596 the process of acquiring actual data, analyzing that data to search for a small power excess,
1597 and, in the absence of that excess, converting the null result into an exclusion limit on the
1598 dark photon mass/epsilon parameter space. Section 4.4 describes an injection test which
1599 detect a realistic, hardware-injected, dark photon signal. This chapter borrows heavily from
1600 my paper, *New Limit on Dark Photon Kinetic Mixing in the 0.2-1.2 μ eV Mass Range From*
1601 *the Dark E-Field Radio Experiment*[39], which was published in August 2024.

1602 The cleanest way to model the contents of this chapter is by compartmentalizing the
1603 steps outlined above. For this reason, the chapter is organized as follows. In Sec. 4.1 the
1604 data are acquired over a 9-day period. The procedure is outlined, and, where appropriate,
1605 references to previous sections are provided which are helpful in understanding how different
1606 procedures were developed. This section concludes with the output-referred power spectral
1607 density S_o , which must be searched for a power excess. We call this search *analysis* and it is
1608 covered in Sec. 4.2. The task of analysis is to extract a dark photon signal from this spectrum
1609 if it is present. Otherwise, in its absence, we set a limit on the amount of output-referred
1610 power one would be able to detect *most of the time* were a narrow signal to be present in
1611 this averaged dataset. We quantify the meaning of “most of the time” by conducting a series
1612 of Monte Carlo “pseudo-experiments” on artificial signal-containing spectra for synthetic
1613 signals of varying powers and frequencies. With a limit on dark photon power extracted,
1614 Sec. 4.3 works back through the system to determine a limit on ϵ above which we have some
1615 confidence we would have observed a signal. This produces the exclusion limit, which is

1616 ultimately the deliverable of this experiment. This limit is shown in Sec. 4.5.

1617 4.1 Data Acquisition

1618 Data were collected during a 9-day run from May 10 to May 19, 2023. This data run is
1619 referred to as run 1.4 throughout this thesis, and its details are shown in Table ??.

Specification	Value
Analysis span	50-300 MHz
Antenna	AB-900A biconical antenna
RTSA	Teledyne GPU system (Sec. 2.5.7)
Frequency resolution ($\Delta\nu_{RF}$)	47.7 Hz
Length of record	2^{24} samples
Sample rate	800 MHz
Window type	None (flattop)
Acquisition time per spectrum	20.96 ms
Run start time	2023-05-10 11:29:48
Total time of run	8 days, 21.13 hours
Efficiency (Time spent scanning antenna/total time)	92.03%

Table 4.1: Run 1.4 Details. Many specifications are related and can be computed from each other but are listed for reference. The efficiency differs from that calculated in Fig. 3.16 mainly because of switching to terminator and brief daily pauses to move the antenna.

1620 Each day was subdivided into data-collection (23 hours 15 minutes) and setup (45 min-
1621 utes) periods. The setup period includes moving the antenna, changing a 12 V battery for
1622 the LNA (Sec. 2.5.6), file management and documentation. In order to reduce the data
1623 rate and storage requirements, all data were pre-averaged into 3-minute chunks and then
1624 saved. This pre-averaging is shown in Fig. 2.45. Additionally, an RF switch (see Fig. 2.37)
1625 is actuated for a 3-minute scan for every 15 antenna scans in order to monitor the status

1626 of the amplifier chain. For the data analysis, all 9 days of data were averaged together to
1627 create a single spectrum S_o (Fig. 4.1). If candidates are found, their time dependence are
1628 observed by looking at the 3-minute pre-averages. All further analysis is performed on the
1629 full 9-day S_o spectrum and is described below (Sec. 4.2).

1630 4.1.1 Raw data, S_o

1631 All 9 days of pre-averaged data from the run are averaged together. The stability of the
1632 sample clock (Sec. 3.3.3) ensures that this is a simple process. Frequency bins ($\Delta\nu_{RF} =$
1633 47.7 Hz) corresponding to a given frequency are added and normalized by the total number
1634 of pre-averaged spectra. This process produces the raw spectrum, S_o (Fig. 4.1), on which
1635 we will perform a search for power excess.

1636 Inspection of S_o reveals small power variations over spans of tens of kHz. The origin of
1637 these variations is explored in Sec. 2.3, but it is summarized here. Given an antenna in a
1638 cavity in thermal equilibrium with the input of an LNA, whose input is assumed to be real
1639 and matched, one would expect an output PSD which is constant with respect to frequency
1640 up to small variations in LNA gain. The theory for this is outlined by Dicke in [73]. These
1641 variations are not noise; for a given antenna position we repeatedly measure the same shape
1642 (though the noise riding on these variations *is* random). The origin of the observed small
1643 variations lies in the effective temperature difference between the room and LNA causing a
1644 net power flow from the antenna into the LNA. This effective temperature difference partially
1645 excites modes of the antenna/cavity system, causing the observed variations. We suspect this

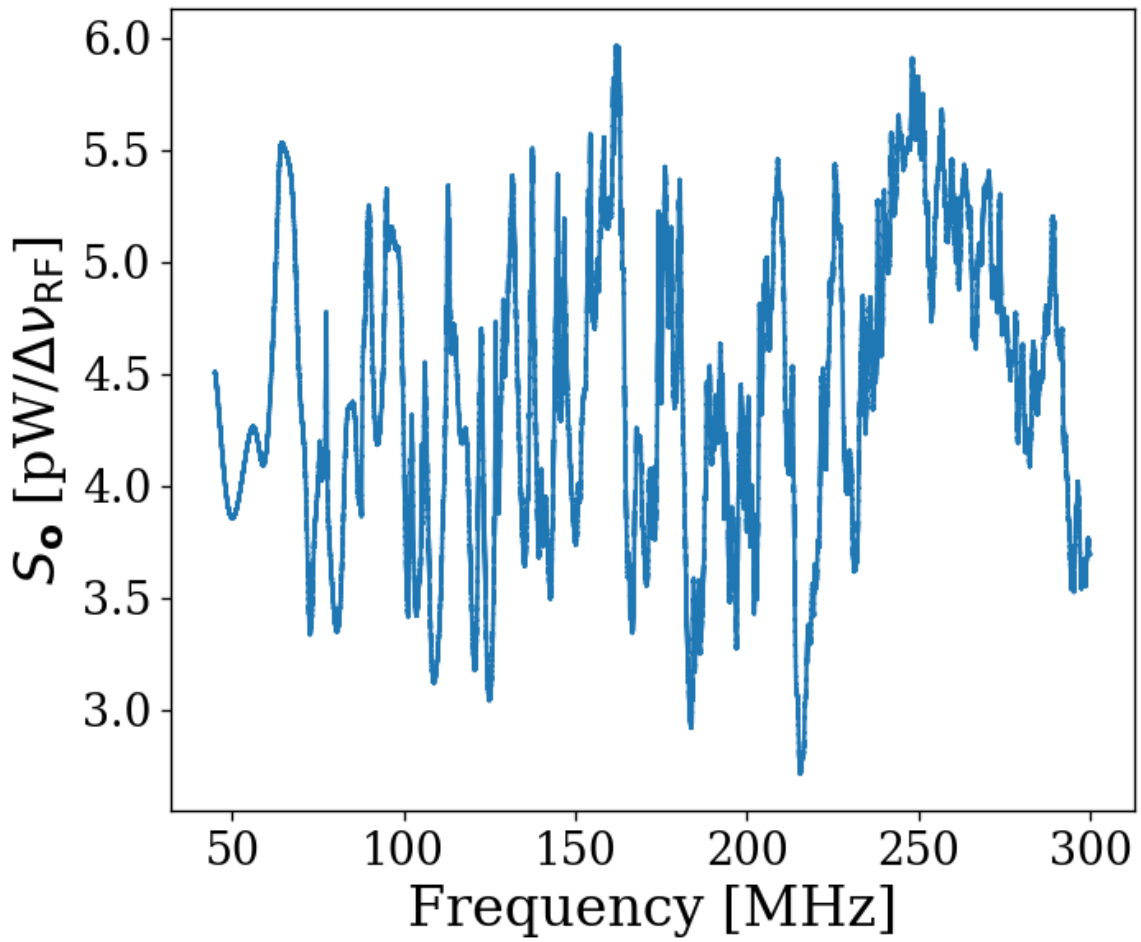


Figure 4.1: Run 1A averaged, output-referred antenna power spectrum S_o . Data were taken over a 9-day period at 9 antenna positions. The narrow variations are mainly due to the effective temperature difference between the room and LNA (Sec. 2.3), though there is a small contribution due to amplifier gain and noise temperature variations (Sec. 4.1.1). The variations seen here are not noise; their shape is repeatable for a given antenna position. The noise on this background is not visible at this level of zoom, but is seen in Fig. 4.4, which shows a zoomed-in view of the spectrum at 240 MHz. The noise is also seen nicely in Fig. 4.17



Figure 4.2: Run 1A averaged, output-referred, antenna and terminator power spectra

1646 effect originates from a small reactive component of the LNA's input causing the electronic
1647 cooling described originally by Radeka [19]. This effect can be eliminated by adding an
1648 isolator between the antenna and LNA [32, 74] though for our experiment, it is impractical
1649 to get an isolator that covers such a wide band at relatively low frequency. Furthermore, the

1650 relatively wide (tens of kHz) variations can be handled by fitting to them which we discuss
1651 in Sec. 4.1.

1652 **4.2 Data Analysis**

1653 At this point, we have compiled a single, averaged, output-referred power spectrum, S_o
1654 (Fig. 4.1). The task of *analysis* is to extract a dark photon signal from this spectrum if
1655 it is present. Otherwise, in its absence, we would like to set a limit on the amount of
1656 output-referred power one would be able to detect *most of the time* were a narrow signal
1657 to be present in this averaged dataset. We quantify the meaning of “most of the time”
1658 by conducting a series of Monte Carlo “pseudo-experiments” on artificial, signal-containing
1659 spectra for synthetic signals of varying powers and frequencies. The following subsections
1660 are organized as follows:

1661 4.2.1: Fit S_o to extract an estimate of the background B (which we call \hat{B}) whose origin was
1662 discussed in Sec. 4.1.1. See Fig. 4.4.

1663 4.2.2 Divide the spectrum by \hat{B} to generate the *normalized spectrum*, which very nearly
1664 follows a Gaussian distribution. Discuss statistics of the normalized spectrum and
1665 choose a global significance level and its associated *significance threshold*. See Fig. 4.5.
1666 Also note this was derived in Sec. 2.2.

1667 4.2.3 Apply a matched filter to the normalized spectrum and establish a significance thresh-
1668 old on its output using the same method defined in the previous section. See Fig. 4.6.

1669 The previous three steps comprise our *detection algorithm* which is shown in Fig. 4.3.

1670 4.2.4 Perform a Monte Carlo analysis to simulate the required power of a signal that can be
1671 detected above the significance threshold 95% of the time. We use this to recover a
1672 95% exclusion limit on the output referred power spectrum.

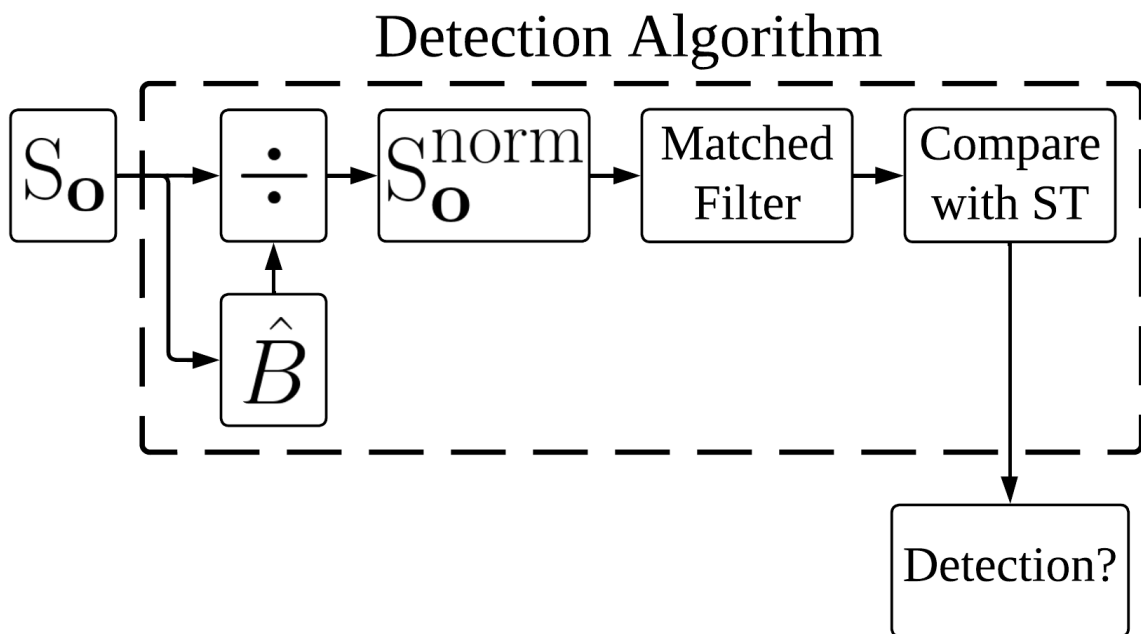


Figure 4.3: Flow chart outlining the logic of signal processing in the detection algorithm of sections 4.2.1 through 4.2.3. \hat{B} is the smoothed fit to S_o generated by low pass filtering. The output, *Detection?*, is a Boolean array which signifies a detection or lack thereof at each frequency bin. We detect a candidate if a bin contains more power than a significance threshold (ST) (Sec. 4.2.2).

1673 In Sec. 4.3 we convert this threshold on S_o into an actual limit on ϵ .

1674 Throughout the figures of this section we will follow a relatively large (40 fW, output-
1675 referred) software-injected, synthetic dark photon signal at 240 MHz to illustrate what a
1676 candidate would look like as it passes through the analysis procedure. This signal is added

1677 to S_o . For clarity, a single interfering candidate has been removed. This is discussed in
1678 Sec. 4.2.5.

1679 As a final note, at this point if you are unfamiliar with the data analysis, it would be
1680 advantageous to spend a few minutes looking through Figs. 4.17 through 4.19 to get a sense
1681 of the task at hand. It can be disorienting dealing with a spectrum that contains 8 million
1682 frequency points. Zooming in on a signal is very informative.

1683 **4.2.1 Fit background, $\hat{B}(\nu)$** ¹

1684 As shown in Fig. 4.1, the measured power spectrum looks like flat thermal noise *multiplied* by
1685 some frequency-dependent background, $B(\nu)$ ². However, for this section we will not concern
1686 ourselves with the origin of B or any details of the experiment aside from two assumptions:

1687 1. The measured background is the product of a normally distributed spectrum and some
1688 background. This is enforced by the central limit theorem due to the large number of
1689 averaged spectra, independent of any experimental specifics.

1690 2. The line shape of the signal is known and the width of this signal is much narrower
1691 than the width of features on the background, viz. $\Delta\nu_{DP} \ll \Delta\nu_B$

1692 The first assumption (1) implies that if we were able to extract the background, dividing
1693 S_o by this extracted background would yield a *dimensionless*, normally distributed power

¹Code for this section can be found at: https://github.com/josephmlev/darkRadio/tree/master/daqAnalysisAndExperiments/run1p4/run1p4_analysis/analysisClass.ipynb

²When I was first working on this, I used $H(\nu)$ to represent this background. This naming convention persists in the analysis code.

1694 spectral density on which a search for a dimensionless signal is performed. The second
1695 assumption (2) will be critical in both performing the fit to the background (this section),
1696 and performing matched filtering (Sec. 4.2.3).

1697 In light of these assumptions, we attempt to fit for the background power spectrum. Since
1698 this fit estimates B , we use the symbol \hat{B} to refer to it. As discussed in [20], a particularly
1699 effective fitting technique that can discriminate between the wide bumps of S_o and a narrow
1700 signal is to use a low pass filter. We implement this filter in two stages:

- 1701 1. A median pre-filter (51 bins or about 2.4 kHz wide) attenuates any very narrow, very
1702 large excursions which would interfere with any following filters, causing them to
1703 “ring”³
- 1704 2. A 6th-order Butterworth low pass filter (corner frequency of 210 bins or 10 kHz)

1705 These bin widths/frequencies should be interpreted as the width of spectral features on
1706 S_o that are attenuated and will, therefore, not show up in the background fit. A narrow
1707 zoom of this fit with a synthetic signal is shown in orange in Fig. 4.4.

³I recommend that this pre-filtering step is omitted if the spectrum analyzer in use doesn’t produce large spurs. It is the slowest part of the analysis chain. It also causes the filtered spectrum to deviate slightly from Gaussian.

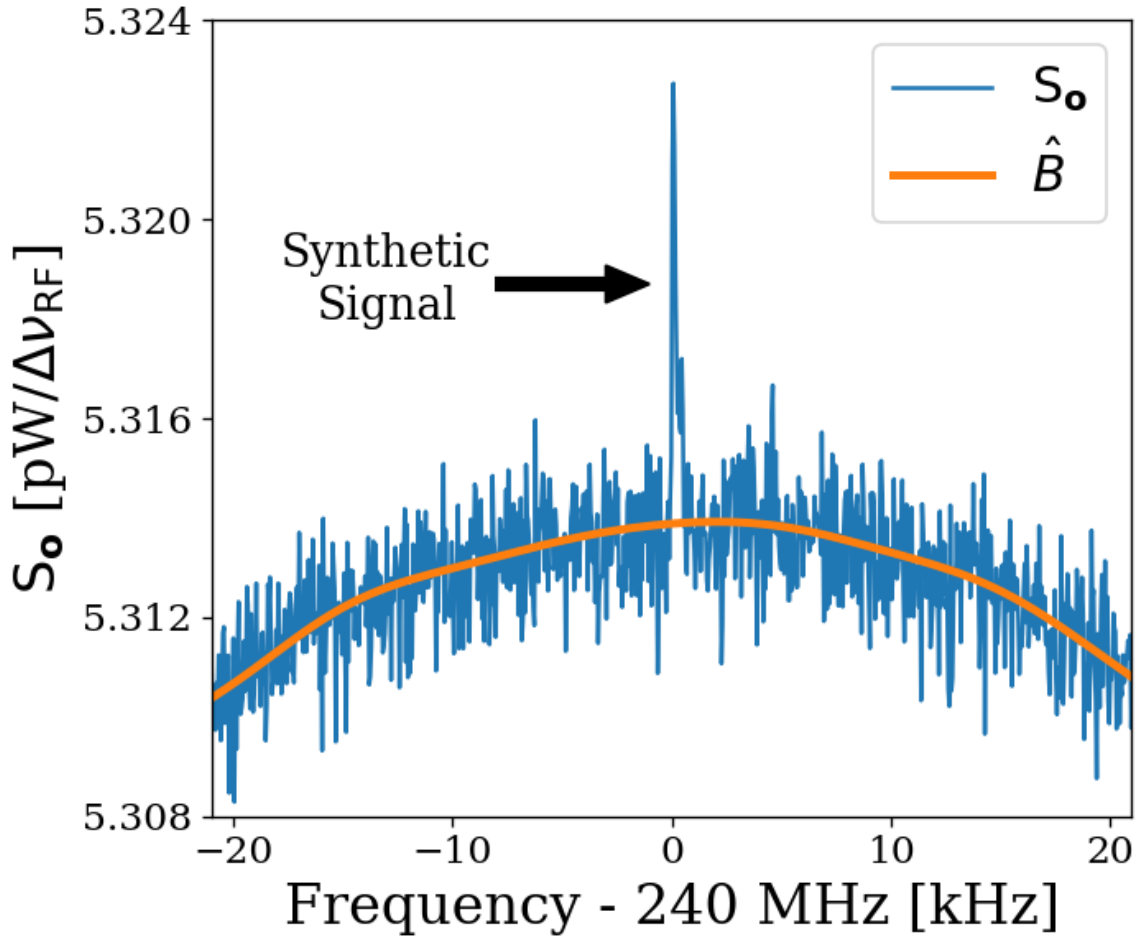


Figure 4.4: Fitting background \hat{B} in the presence of a synthetic signal injected at 240 MHz. Starting from the averaged, output-referred spectrum (S_o), we fit the background using a series of filters (section 4.2.1, and Fig. 4.3). This figure is a highly zoomed in view (240 MHz \pm 20 kHz) in order to show the noisy Rayleigh signal shape.

₁₇₀₈ **4.2.2 Normalized spectrum, S_o^{norm}**

₁₇₀₉ Once we have a fit to the background, \hat{B} , division of S_o by this fit yields a dimensionless,

₁₇₁₀ Gaussian distributed spectrum

$$S_o^{\text{norm}} \equiv \frac{S_o}{\hat{B}}. \quad (4.1)$$

1711 As discussed in Sec. 2.1.1.3, this normalized spectrum (Fig. 4.5) should have a mean $\mu_{\text{norm}} = 1$
 1712 and a standard deviation given by the Dicke radiometer equation $\sigma_{\text{norm}} = (\tau \Delta\nu_{\text{RF}})^{-1/2}$ where
 1713 τ is the total integration time (≈ 9 days) and $\Delta\nu_{\text{RF}}$ is the width of a bin (47.7 Hz). This
 1714 works out to a predicted σ_{norm} of 1.727×10^{-4} . μ_{norm} and σ_{norm} calculated from the data
 1715 are $1 - 1.2 \times 10^{-5}$ and 1.741×10^{-4} respectively, which agree with the predicted values
 1716 to better than 1%. Knowing the statistics of the background allow us to set a threshold
 1717 above which we have some confidence that a candidate is not a random fluctuation. This
 1718 significance threshold was derived in Sec. 2.2.1. As a reminder, the probability that all N
 1719 bins are less than z standard deviations, $z\sigma$, for a standard normal distribution is given
 1720 by $\left\{ \frac{1}{2} [1 + \text{erf}(z/\sqrt{2})] \right\}^N$, where $\text{erf}(z)$ is the standard error function and z is real. A 5%
 1721 ST for 5.2×10^6 bins (our 50-300 MHz analysis span) works out to 5.6σ . This is shown in
 1722 Fig. 4.5.

1723 It is possible to set a simple limit using this significance threshold on the normalized
 1724 spectrum, which was our method in [4]. However, knowing the line shape of the dark photon
 1725 signal provides additional information that improves sensitivity (up to a factor of ≈ 2) at
 1726 the higher frequency end of the spectrum, as shown in Fig. 4.8.

1727 **4.2.3 Signal-matched filter**

1728 As discussed in 4.2.2, one simple method to set a limit is to look for single-bin excursions
 1729 above some threshold. However, galactic dynamics impart a dark photon candidate with
 1730 a Rayleigh-distributed, spectral signature, which has a dimensionless width $Q_{\text{DP}} \approx 10^6$

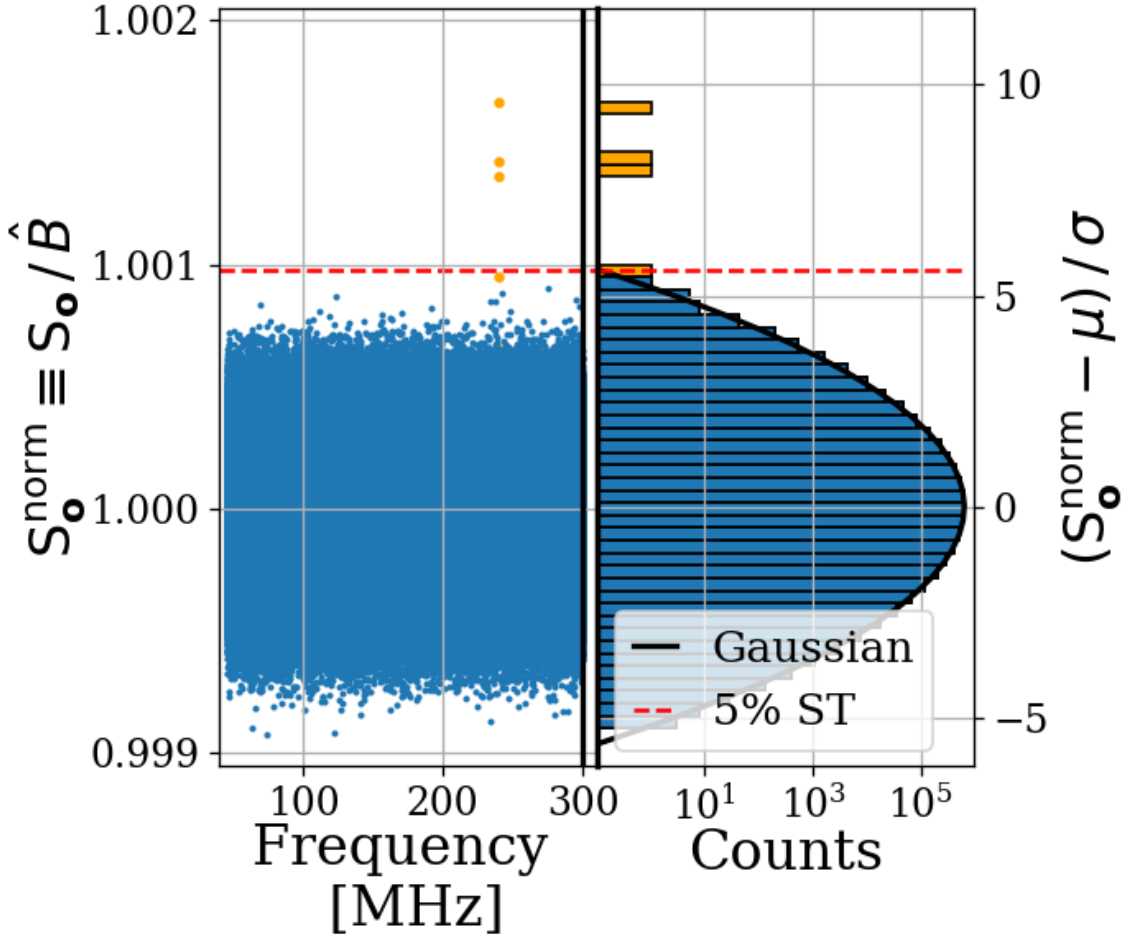


Figure 4.5: Dividing S_o by \hat{B} yields a dimensionless, normally distributed power spectrum that we define as S_o^{norm} . We show S_o^{norm} in two ways: a normalized power/frequency spectrum (*left*) and rescaled into z-score units and collapsed into a histogram (*right*). The histogram shows power excess and Gaussian fit, but frequency information is lost. We compute a 5% significance threshold ST (*dashed red*), above which we will detect a candidate by chance 5% of the time. Bins adjacent to the 240 MHz synthetic signal show up in orange on both plots. A single interfering signal has been removed for clarity. We discuss this further in Sec. 4.2.5

1731 [33]. This means that the expected width of a candidate signal over our analysis span (50-
 1732 300 MHz) varies between 50-300 Hz. We set $\Delta\nu_{\text{RF}} = 47.7 \text{ Hz}$ to maximize SNR for the lowest
 1733 expected signal width. However, this divides signal power between adjacent bins, an effect

1734 that becomes more pronounced at higher frequencies, leading to a decrease in sensitivity.
1735 By using a signal processing technique known as *signal-matched filtering* [75, 76], we restore
1736 some of the sensitivity lost due to the splitting of signal between the fixed-width frequency
1737 bins of the FFT. A similar “optimal weighting” procedure has been well established in axion
1738 haloscope experiments, notably by [20, 77]. Below, the signal-matched filter is referred to
1739 simply as a *matched filter*.

1740 For a known signal shape, the detection technique which optimizes SNR is the matched
1741 filter. This is implemented on the normalized power spectrum using the Rayleigh-distributed
1742 spectral line shape of [33] as a template. Since we have a constant $\Delta\nu_{\text{RF}}$ and expect the width
1743 of the signal to vary across our span, we must calculate several templates of varying width to
1744 match the expected line shape. Every 10% of fractional frequency change, a new template
1745 is generated and used to search that small sub-span of the normalized spectrum, each of
1746 which is also normally distributed though with its own standard deviation. This results in
1747 20 subspans (50-55 MHz, 55-60.5 MHz etc.). The normalized spectra of all 20 subspans and
1748 the histogram of the 227-250 MHz subspan are shown in Fig. 4.6.

1749 As the width of the templates increase, the standard deviation of the output decreases,
1750 resulting in the $\nu^{-1/2}$ shape of the 5% significance threshold shown in Fig. 4.6. It should be
1751 noted that since the total number of bins remains 5.2 million, the 5% significance threshold
1752 still corresponds to 5.6σ ; the shaping in Fig. 4.6 is due to the variation in σ for different
1753 templates, not a change in the $z = 5.6$ pre-factor.

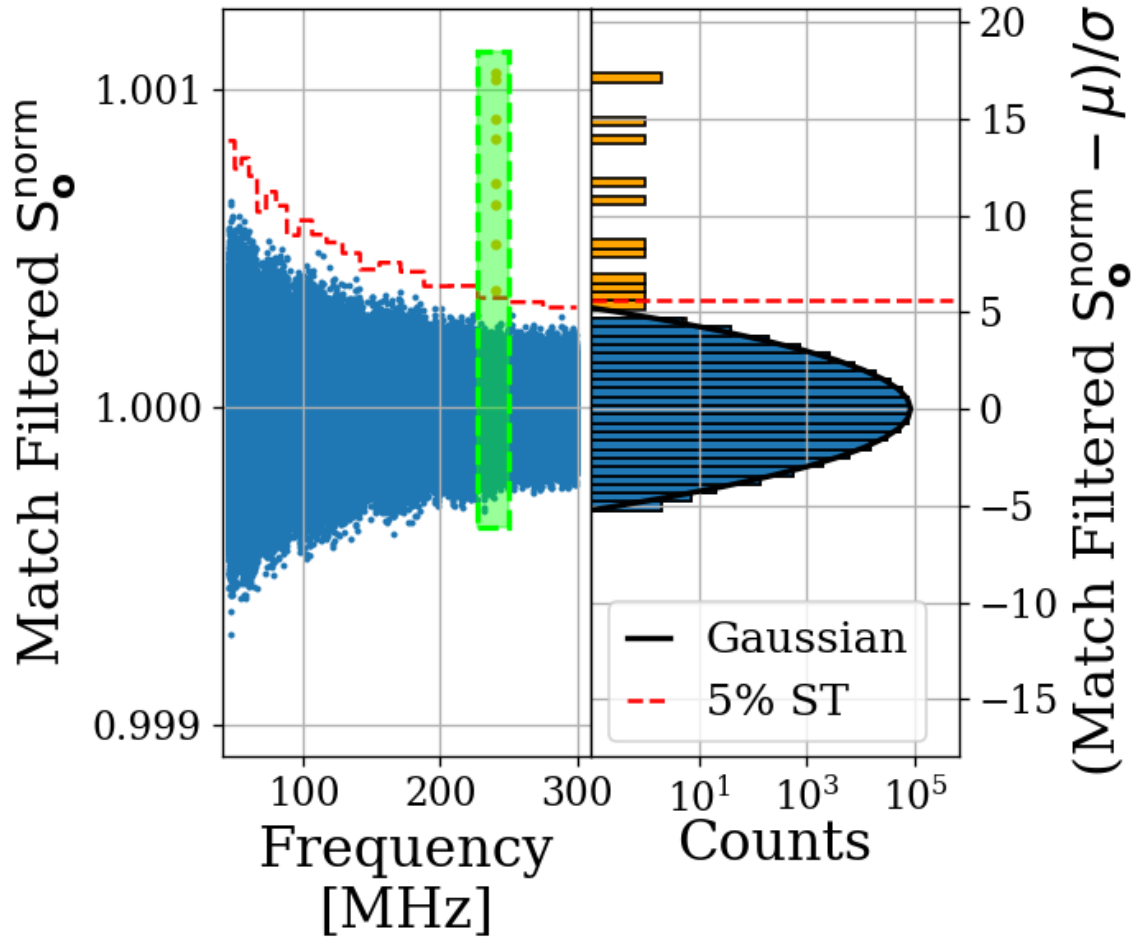


Figure 4.6: S_o^{norm} after it has been passed through a matched filter. The template varies in width throughout the frequency span resulting in 20 subspans, each with a constant 5% significance threshold ST (*dashed red*). Histogram only includes 227-250 MHz subspan (enclosed in the green box). The signal-to-threshold ratio of the synthetic signal (orange) improves by a factor of about 1.8 as compared to Fig. 4.5 without a matched filter. The frequency dependence of this effect is shown in Fig. 4.8. A single interfering signal has been removed for clarity.

¹⁷⁵⁴ 4.2.4 Monte Carlo: pseudo experiments

¹⁷⁵⁵ The previous three sub-sections outline the procedure for detecting the presence of a signal

¹⁷⁵⁶ of known spectral line shape embedded in wide-band noise. We refer to this procedure as a

1757 *detection algorithm* (see Fig. 4.3) which we now calibrate through a Monte Carlo method.

1758 A synthetic spectrum is constructed by multiplying some B by randomly generated Gaussian white noise characterized by μ_{norm} and σ_{norm} , as discussed in section 4.2.2. A signal of known, total integrated, output-referred power and frequency, $\lambda(p, \nu)$, can now be added to this spectrum to create a test spectrum which can be passed through the detection algorithm. The frequencies of the synthetic signals are evenly spaced (approximately every 10 MHz). However because the signal spans a limited number of bins (one to six), the shape of the discretized signal is very sensitive to where its peak lands relative to the bins. To compensate for the fact we don't know where a dark photon's peak would land relative to the frequency bins, the frequency of the synthetic signal is randomly jittered by $\pm\Delta\nu_{\text{RF}}/2$, which is drawn from a uniform probability distribution at each iteration of the Monte Carlo. By repeating this with randomly generated Gaussian noise and various synthetic signals (including a small jittering of signal frequency outlined above), statistics are built up about how much total integrated power is required to detect a signal as a function of frequency *most of the time*. We quantify this as the statistical power of the detection algorithm and denote it $100\% - Y = 95\%$ following the standard convention of hypothesis testing.

1773 This Monte Carlo allows us to treat the detection algorithm as a black box which can be calibrated by passing it a known input (a synthetic S_0 containing a synthetic signal, both software-generated) and looking at its output; a Boolean array of frequency bins representing signal detection. These data along with a simple linear fit to the 95% confidence interval are shown in Fig. 4.7.

1778 The output MC_{lim} , normalized to standard deviation can simply be converted back to the

	Only Noise	Noise + Signal
Detection	X	100% – Y
No Detection	100% – X	Y

Table 4.2: Threshold parameters that are part of the detection algorithm and Monte Carlo. X is the significance of the analysis. It is a parameter passed to the detection algorithm which specifies the significance threshold. The quantity 100% – Y is the statistical power of the analysis. It is a parameter in the MC, which specifies a threshold on signal power where a given signal is detected in 100% – Y of the MC iterations. We choose both X and Y = 5%.

1779 limit on the total output-referred power contained in injected signals which can be detected
 1780 95% of the time,

$$P_o^{\lim} = MC_{\lim} \sigma_{\text{norm}} \hat{B}. \quad (4.2)$$

1781 MC_{\lim} is then a measure of how much the analysis' efficacy is reduced compared to an
 1782 ideal analysis where a signal with 5.6σ of power is detected at 95% significance half of the
 1783 time (remember, it's still a random process. Refer back to Sec 2.2).

1784 P_o^{\lim} is shown in Fig. 4.8 in blue. Also shown in Fig. 4.8 is a limit that does not include
 1785 any matched filtering (orange) to highlight the frequency dependent improvement of the
 1786 matched filter. This limit is only for illustration and not used in the following sections.

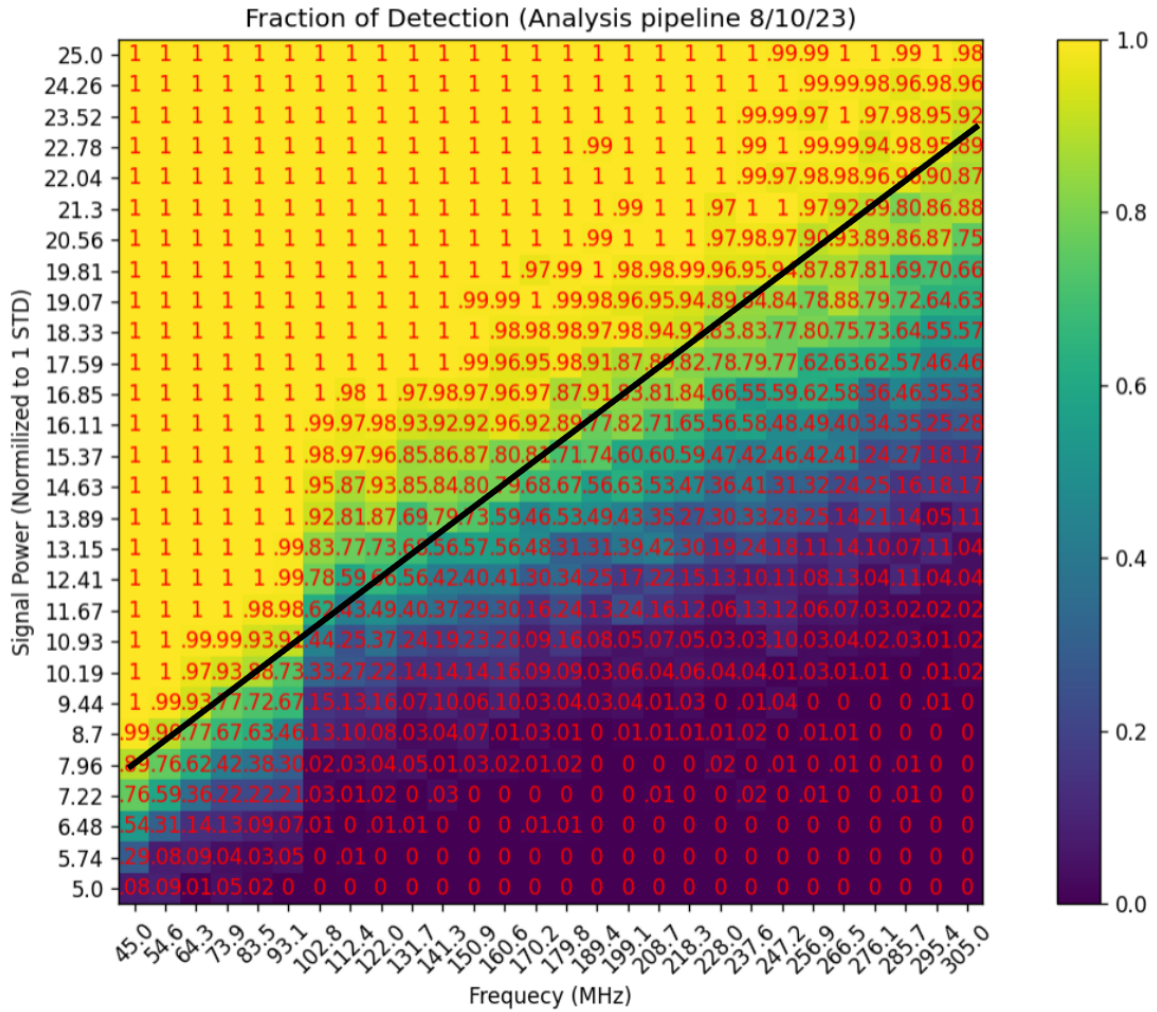


Figure 4.7: Result of Monte Carlo pseudo experiments on signal detection. Color/red numbering show fraction of detection for each frequency/injected signal power of the 784 combinations tested. Black line inserted by eye and gives an approximate fit to the frequency vs. injected signal power which results in a detection 95% of the time. Approximate form of back line is $y = 0.0686x + 2.411$

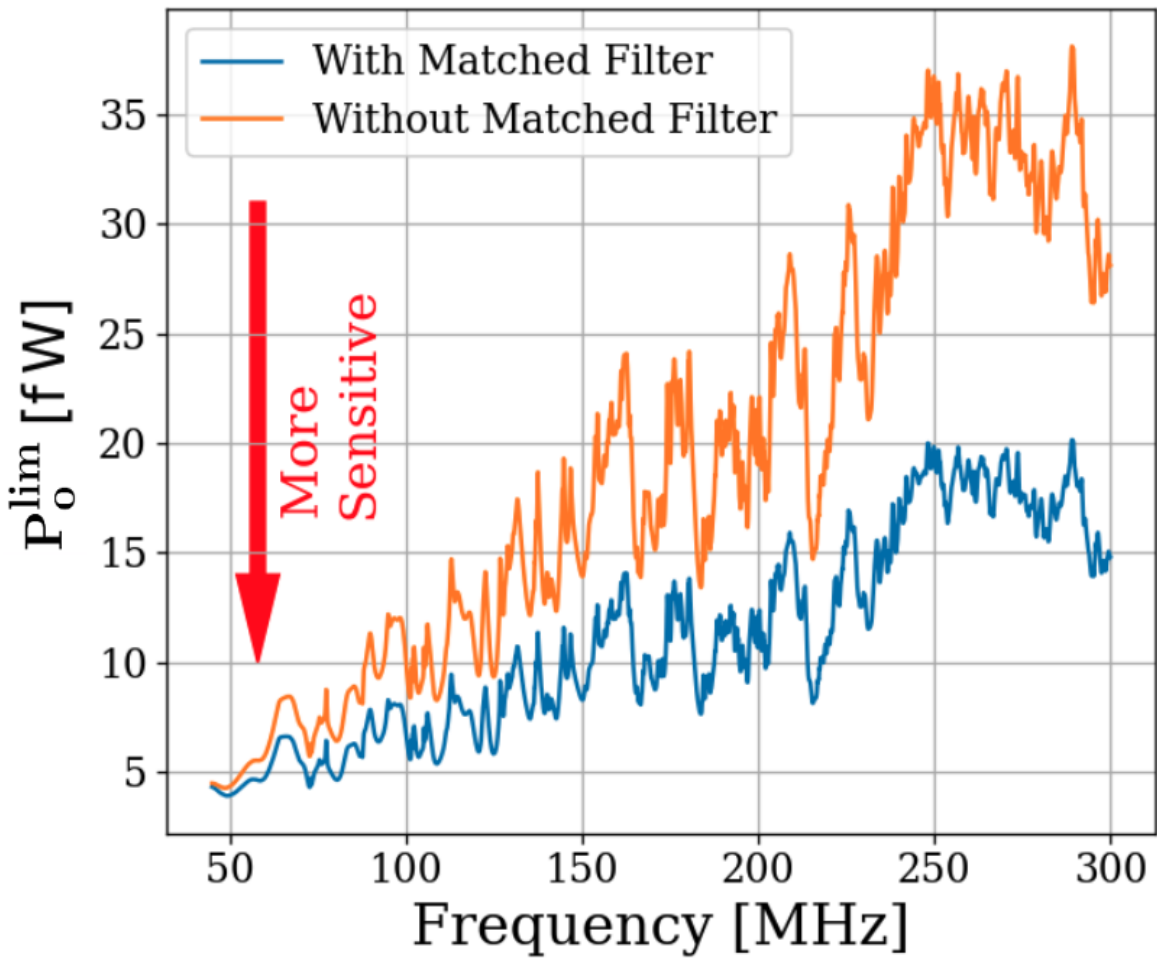


Figure 4.8: Limit on output-referred total integrated signal power, P_o^{\lim} . Limits computed with (blue) and without (orange) a matched filter (Sec. 4.2.3). The limits are similar at lower frequencies, but the matched filter improves sensitivity at higher frequencies where the signal power is split among more bins. The blue curve is used in the following sections.

1787 **4.2.5 Rejection of a single candidate**

1788 Passing S_o through the detection algorithm diagrammed in Fig. 4.3 yields a single candidate
1789 at 299.97 MHz which is approximately 1 kHz wide. This candidate first became detectable
1790 above the noise after about 4 days of averaging, indicating it is just on the threshold of what
1791 we are able to detect. Four factors cause us to conclude the candidate is an interfering signal
1792 originating from within the PC or ADC, allowing us to remove it:

- 1793 • The candidate is present not only in the main spectrum, but also the veto and termi-
1794 nator spectrum.
- 1795 • Inspection of the time evolution of this signal shows a narrow signal (about two bins,
1796 or \sim 100 Hz wide) which seems to wander in frequency periodically over the course of a
1797 day and therefore with temperature. This is expected behavior for a quartz oscillator.
- 1798 • Reducing the gain of the system causes the SNR of the candidate to *increase*, indicating
1799 it enters the signal path after the gain stages.
- 1800 • Changing the clock rate causes the frequency of the candidate to change.

1801 The limit set in this section is referred to the output of the amplifier chain. A single
1802 significant candidate was found, but the method of ruling it out was outlined above. The
1803 topic of the next section will be to work back through the amp chain, to an E-field limit in
1804 the cavity and ultimately to a limit on ϵ .

1805 4.3 Calibration

1806 In this section we describe the calibration of our experiment and estimate our uncertainty.

1807 The previous section concluded with a limit on the output-referred power P_o^{\lim} (Fig. 4.8),

1808 which we now must convert into a frequency dependent limit on ϵ .

1809 We begin by inverting Eq. 1.7,

$$\epsilon(\nu) < \sqrt{\frac{|\mathbf{E}_{\text{ant}}^{\lim}|^2 \varepsilon_0}{2 \rho_{DM}}}, \quad (4.3)$$

1810 where the *lim* superscript indicates a limit, below which a detectable electric field may be

1811 hiding. The $<$ should be taken to mean that in setting a limit on $|\mathbf{E}_{\text{ant}}^{\lim}|$, ϵ is constrained to

1812 be less than the right hand side (if it exists at all).

1813 The first step of calibration is to convert from output-referred power to *antenna-referred*

1814 *power*. This represents the signal power presented to the LNA by the antenna via a matched

1815 transmission line and is given by

$$P_{\text{ant}}(\nu) = \frac{P_o}{G} - T_{\text{amp}} k_B \Delta\nu_{\text{RF}}, \quad (4.4)$$

1816 where G and T_{amp} are the frequency-dependent amplifier gain and noise temperature (74–75 dB

1817 and 100–120 K respectively, measured via the Y-factor method, see Sec. 3.1.1) and k_B is

1818 Boltzmann’s constant.

1819 Ultimately, the exclusion limit is set by fluctuations on this baseline described by

$$\begin{aligned}
P_{\text{ant}}^{\lim}(\nu) &= \frac{P_{\text{o}}^{\lim}}{G} - \left(\frac{2}{n} \right)^{1/2} T_{\text{amp}} k_B \Delta\nu_{\text{RF}} \\
&= \frac{P_{\text{o}}^{\lim}}{G} - \left(\frac{2 \Delta\nu_{\text{RF}}}{\tau} \right)^{1/2} T_{\text{amp}} k_B,
\end{aligned} \tag{4.5}$$

1820 where the *lim* superscript indicates an exclusion limit, n is the total number of spectra
 1821 averaged together, and τ is the total integration time. In the second line we have used
 1822 $n = \Delta\nu_{\text{RF}} \tau$. In practice, the LNA correction is small; the first term divided by the second
 1823 varies with frequency between 7 and 50. The $\tau^{-1/2}$ dependence of P_{o}^{\lim} is implicit because it
 1824 was calculated from S_{o} which is itself an averaged spectrum. As mentioned above, this $\tau^{-1/2}$
 1825 dependence implies that the limit on ϵ scales as $\tau^{-1/4}$.

1826 In the remainder of this section we explore the relationship between P_{ant}^{\lim} and $|\mathbf{E}_{\text{ant}}^{\lim}|$
 1827 allowing us to use our experimental data to set a constraining limit on ϵ by employing
 1828 Eq. 4.3.

1829 4.3.1 Average effective aperture, $\langle A_e(\nu) \rangle$

1830 An antenna's effective aperture, $A_e [\text{m}^2]$, represents the effective area that it has to collect
 1831 power density or irradiance [W/m^2] from an incident Poynting vector. It was defined in
 1832 Eq. 2.9.

1833 A_e is useful for an antenna in free space, however some modifications must be made to
 1834 construct an analogous quantity for an antenna in a cavity.

1835 The first modification is to average over many configurations of the system. The back-
 1836 ground for this is given in Sec. 2.4. As discussed, we denote this averaging with $\langle \rangle$ so that the

1837 average, effective aperture is denoted $\langle A_e \rangle$. It is interesting to note that by averaging over
1838 configurations (namely antenna direction), $\langle A_e \rangle$ simplifies since $\langle D(\Omega) \rangle = 1$ by construction
1839 [23].

1840 The second modification is to introduce a resonant enhancement factor that corresponds
1841 to the system's tendency to "ring up" in the same way any resonator will. We refer to
1842 this as *composite Q* and represent it as \tilde{Q} . It is analogous to the standard quality factor
1843 of a resonator with one important modification; we operate our experiment across a wide
1844 frequency range so we define \tilde{Q} across the continuum of these resonances, not only on classical
1845 eigenmodes of the system.

1846 These modifications allow us to construct a relationship between an observable E-field
1847 (\mathbf{E}_{ant} in Eq. 4.3) and the power available at the port of an antenna for a given aperture

$$\langle P_{\text{ant}} \rangle = \frac{|\mathbf{E}_{\text{ant}}|^2}{\eta_0} \langle \tilde{Q} A_e \rangle, \quad (4.6)$$

1848 where η_0 is the impedance of free space. With this in mind, we perform an RF simulation
1849 to compute $\langle \tilde{Q} A_e \rangle$.

1850 4.3.2 Simulation of $\langle \tilde{Q} A_e \rangle$

1851 It is difficult to make claims about statistical uniformity in the "undermoded" regime where
1852 modes are not sufficiently mixed [78], so we have employed a commercial, electromagnetic,
1853 finite-element modeling software package (COMSOL Multiphysics RF module [56]). The
1854 original paper explicitly on modeling reverb chambers seems to be [79], though it only

1855 considers a 2-dimensional model and is rather rudimentary. Within the simulation, a model
1856 of the antenna (with a 50Ω feed) is placed in a simplified room with wall features removed.
1857 Spot testing at various frequencies has shown that averaging results from various antenna
1858 positions using this simplified simulation behaves very similarly to one with the room features
1859 included at a fraction of computational complexity.

1860 Two similar simulations are run; driving an E-field while measuring the antenna's re-
1861 sponse and driving a second small monopole antenna and measuring the response of the
1862 primary antenna.

1863 In the first simulation, we drive currents on the walls which correspond to a surface E-
1864 field magnitude of 1 V/m (made up of equal components in the x, y and z directions) using
1865 COMSOL's source electric field option. This field takes the place of \mathbf{E}_{ant} in Eq. 4.6. The
1866 antenna/cavity system resonates and causes an enhancement by \tilde{Q} . The power received at
1867 the antenna's port is measured, allowing the calculation of $\tilde{Q} A_e$, again from Eq. 4.6. By
1868 repeating this simulation for several positions, averaging allows us to compute $\langle \tilde{Q} A_e \rangle$.

1869 The second simulation shares the same geometry, but is used to compute a correction
1870 factor to account for differences between simulation and measurement and to estimate un-
1871 certainty on the first simulation through comparison to physical measurement. Rather than
1872 driving the system through currents on the walls, power is injected into the system with
1873 a 40 cm monopole. From this simulation, two-port scattering parameters (S parameters,
1874 defined in 4.3.3) are computed. A similar test is performed on the physical system using a
1875 vector network analyzer (VNA) which provides a physical measurement of the S parameters
1876 to compare with the simulation. The processing of the simulated and measured S parameter

1877 datasets are discussed in the following sub-section. A screenshot of the COMSOL model GUI
 1878 is shown in Fig. 4.9. The resulting S parameters from the simulation are plotted against the
 1879 measured S parameters in Fig. 4.10

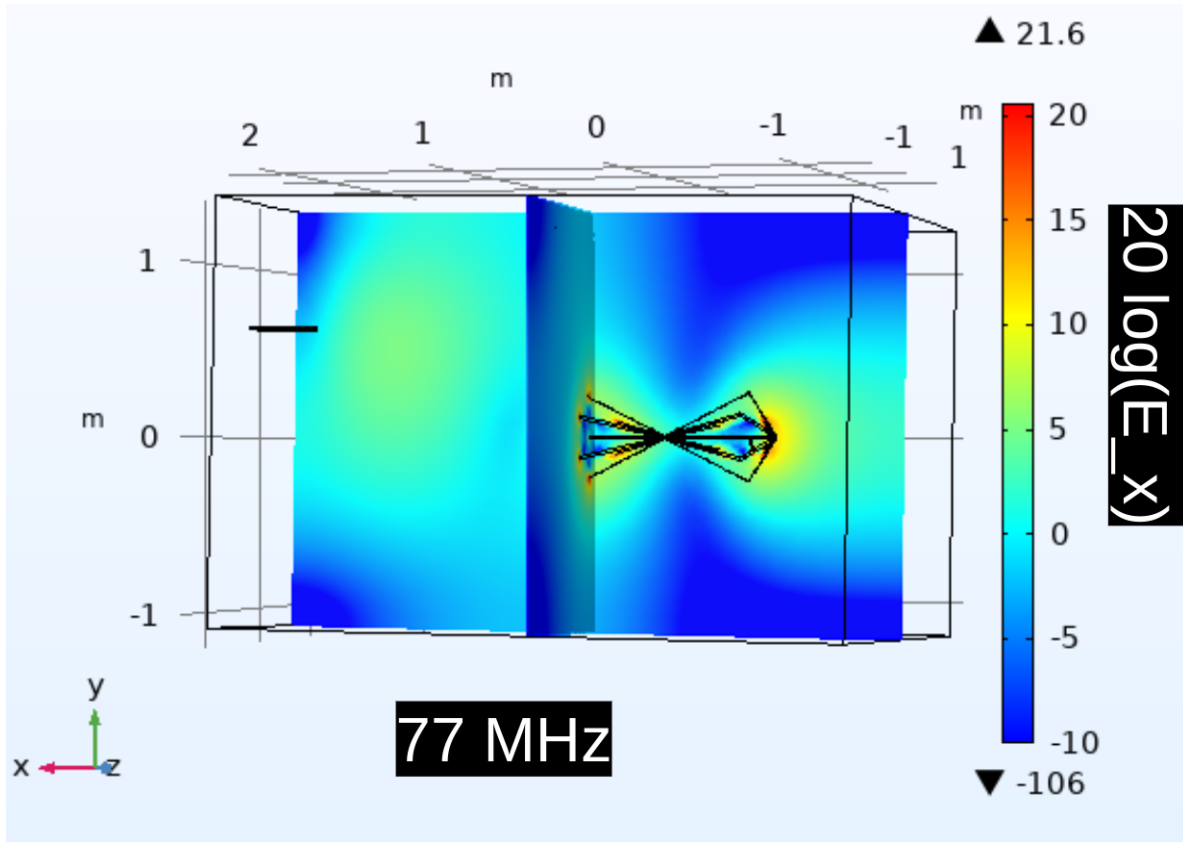


Figure 4.9: Screenshot of COMSOL simulation GUI for two-antenna validation. Shown only at a single position and single frequency (77 MHz). There are 18 antenna positions, 3 E-field components, and ~ 1000 frequency points, so there are many similar figures to this one. The relative x-component of the electric field in dB is shown in color compared to 1 V/m.

1880 Both simulations are run at the same 18 positions; 9 of which are approximately equiv-
 1881 alent to the physical antenna positions while the other 9 are different in order to estimate
 1882 how many positions are required for decent convergence of $\langle \tilde{Q} A_e \rangle$. Repeatedly averaging 9

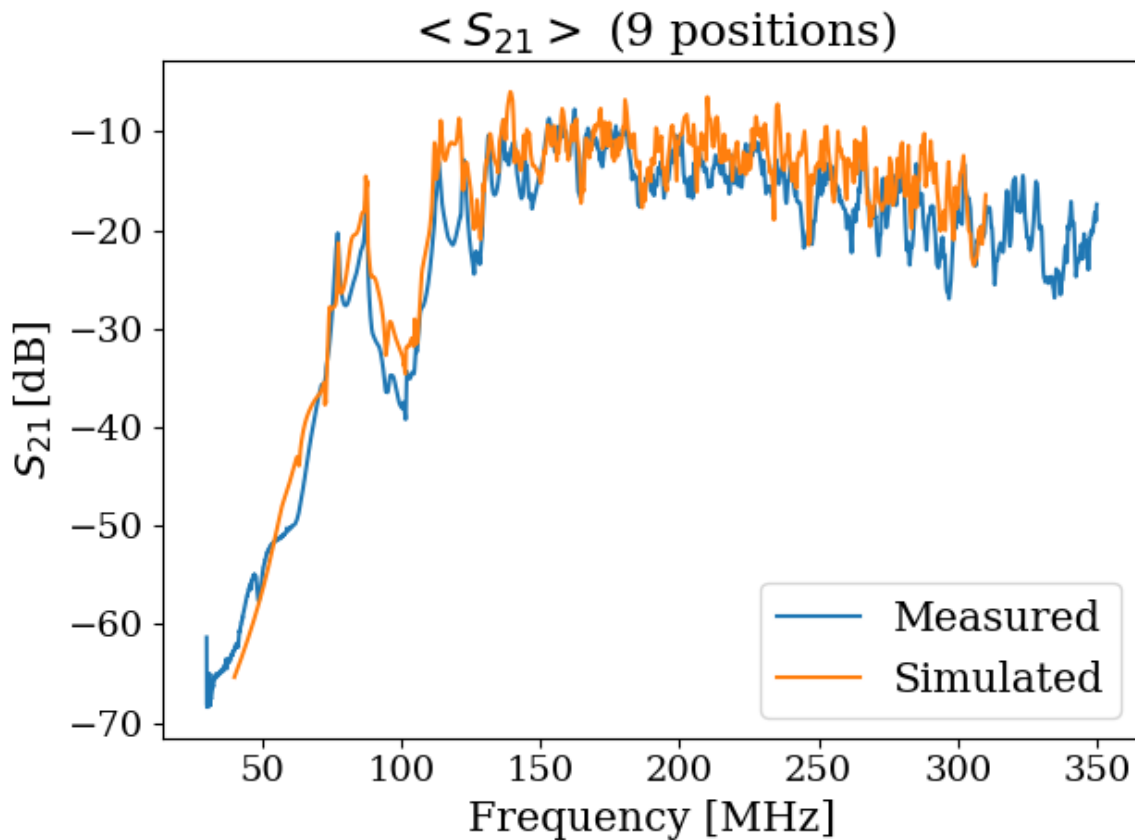


Figure 4.10: Simulated vs measured $\langle S_{21} \rangle$.

1883 different, random positions (with replacement) results in about 20% variation on their aver-
 1884 aged S_{12} coefficients at each frequency, allowing us to conclude 9 positions and polarizations
 1885 provides acceptable convergence.

1886 4.3.3 Correction and uncertainty of $\langle \tilde{Q} A_e \rangle$

1887 As outlined above, we approximate the uncertainty of the simulation by injecting power into
 1888 the system via a second antenna and comparing the results to simulation.

1889 For a two port microwave device, the ratio between the voltage presented at port one
 1890 and the voltage measured at port two is known as S_{21} . For our system, S_{21} is a measurable
 1891 quantity which is similar to a dark photon detection in that it requires the antenna to convert
 1892 an electric field (which has interacted with the room) into a port voltage. Having frequency
 1893 dependent measurements of S_{21} for simulation and measurement give us a correction to
 1894 the simulation (to account for discrepancies in geometry) and estimate the uncertainty on
 1895 $\langle \tilde{Q} A_e \rangle$.

1896 The difference between the measured and simulated values of $\langle |S_{21}| \rangle$ can be described by

$$\langle |S_{21}^{\text{meas}}|^2 \rangle = \alpha \langle |S_{21}^{\text{sim}}|^2 \rangle, \quad (4.7)$$

1897 where meas/sim indicates measured/simulated and the average is over all 18 measured/sim-
 1898 ulated positions and orientations of the antenna. We have taken the square since we are
 1899 interested in the aperture, which is proportional to the square of the voltage. This equa-
 1900 tion implies α is a frequency dependent, multiplicative correction factor which results in a
 1901 corrected $\langle |S_{21}^{\text{sim}}|^2 \rangle$. We find α to have a mean of 0.6, a minimum of 0.1 and a maximum of
 1902 2.

1903 To determine uncertainty on effective aperture, we define the following test statistic

$$\Delta = \frac{\langle |S_{21,n}^{\text{meas}}|^2 \rangle - \alpha \langle |S_{21,n}^{\text{sim}}|^2 \rangle}{\langle |S_{21}^{\text{meas}}|^2 \rangle}, \quad (4.8)$$

1904 where n refers to the subset of n measured/simulated positions sampled randomly with re-
 1905 placement. Δ defines the fractional difference between corrected, simulated S_{21} and measured
 1906 S_{21} . The test statistic, Δ , is calculated 1000 times, providing a distribution of frequency

1907 dependent Δ s. The curves bounding 63% of these curves are taken to be the uncertainty on
 1908 Δ . Thus we can calculate the corrected $\langle \tilde{Q} A_e \rangle$ as well as its uncertainty. This is shown as
 1909 a function of frequency in Fig. 4.11. The uncertainty on it is shown in gray, and is simply

$$\delta\langle \tilde{Q} A_e \rangle = \langle \tilde{Q} A_e \rangle \delta\Delta. \quad (4.9)$$

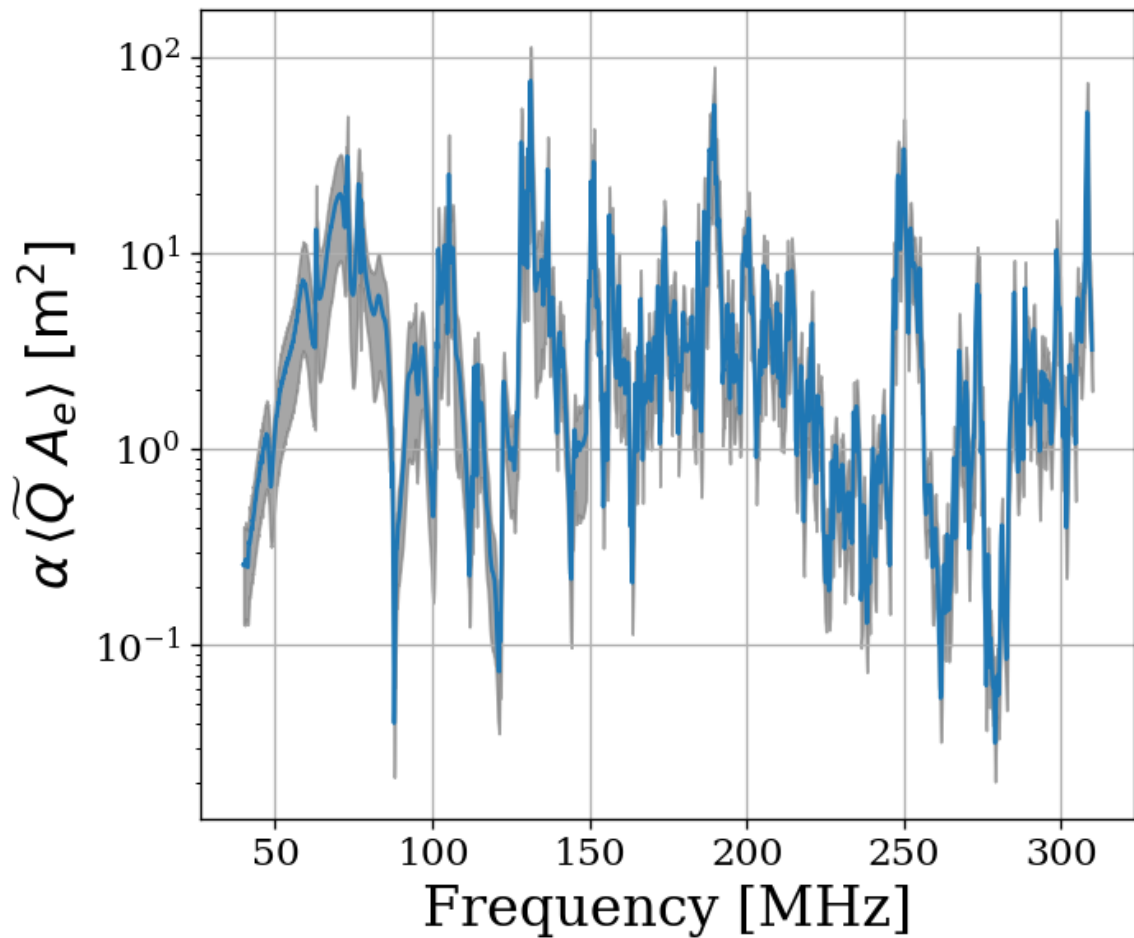


Figure 4.11: Corrected average effective aperture. Calculated with COMSOL RF. The aperture correction α (Eq. 4.7) and its uncertainty (*gray*) are estimated by comparing simulations to measured S parameters.

1910 A brief summary of the system's aperture is in order. In free space an antenna's ability
 1911 to couple an incoming wave's power density into a transmission line is given by it's effective
 1912 aperture, Eq. 2.9. An antenna in a cavity acts as a coupled oscillator which exhibits very
 1913 complex resonances above the first few modes (around 100 MHz for our system). Attempts
 1914 to simulate an aperture for the antenna-cavity system are difficult because of the system's
 1915 extreme dependence on placement of any conductor in the room, especially the antenna.
 1916 Averaging over system configurations (antenna positions and polarizations in our case) allows
 1917 for a significantly more repeatable *statistical* treatment of the aperture/quality factor, which
 1918 we call $\langle \tilde{Q} A_e \rangle$. Comparison of simulated and measured S_{21} gives a small, dimensionless
 1919 correction factor α , Eq. 4.7.

1920 Armed with $\alpha \langle \tilde{Q} A_e \rangle$ we are now able to compute a limit on epsilon using measured and
 1921 simulated quantities via Eqs. 4.5 and 4.6,

$$\epsilon(\nu) < \sqrt{\frac{1}{2c\rho_{\text{DM}}} \frac{P_{\text{ant}}^{\text{lim}}}{\alpha \langle \tilde{Q} A_e \rangle}}, \quad (4.10)$$

1922 where c is the speed of light, ρ_{DM} is the local dark matter density and $P_{\text{ant}}^{\text{lim}}$ is defined in
 1923 Eq. 4.5. We have separated the equation into constants (or in the case of ρ_{DM} , values which
 1924 we fix) and values which we measure or simulate.

1925 In order to validate our entire detection system, we inject sub-threshold signals into the
 1926 shielded room to verify we are able to detect them.

1927 **4.4 Hardware Injection Test**⁴

1928 To validate detection methodology, a separate, proof-of-concept run with a proxy dark
1929 photon signal injected into the shielded room was performed. Apart from the injection
1930 antenna (a 40 cm monopole, see Sec. 4.3.2), the setup was equivalent to run 1.4, including
1931 the data analysis. The proxy dark photon signal (detailed in Sec. 4.4.1.2) was injected at a
1932 frequency set by a colleague and was unknown to me at the time of analysis, constituting a
1933 “blind” analysis.

1934 **4.4.1 Injection test prerequisites**

1935 **4.4.1.1 Determination of required injected power**

1936 **comment:** S parameters need to be squared. Check on this. See Besnier [80] To accomplish
1937 the test, a minimum detectable power required for injection P_{inject} must be computed. P_{inject}
1938 should correspond to a signal that can be detected in a predictable amount of time (with
1939 some uncertainty, discussed in detail in Sec. 2.2.2). A simple way to begin is to read off the
1940 detectable, total integrated, power from Fig. 4.8. In other words the power contained in a
1941 dark photon line, integrated over the few bins spanned by the line ($Q_{\text{DP}} \approx 10^6$, discussed in
1942 Sec. 2.1.2). This gives the amount of output-referred power that would be detectable 95%
1943 of the time after 9 days of integration. Since we don’t want to wait 9 days for this test, it is
1944 simple to convert this detection limit into one which would be produced in a shorter time by
1945 the Dicke radiometer equation, Eq. 2.16. Namely, the limit on power scales like the square

⁴Code for this section can be found at: <https://github.com/josephmlev/darkRadio/tree/master/daqAnalysisAndExperiments/run1p4/injectionTesting/injectionTesting.ipynb>

1946 root of time ⁵, so a one hour integration will require a factor $\sqrt{9 \text{ days}/1 \text{ hour}} = 14.7$ more

1947 power than is shown in Fig. 4.8.

1948 At this point the simplest way to proceed is to measure the the average through-power
1949 of the monopole to the bicon in several antenna positions $\langle |S_{21}|^2 \rangle$. This is the same as the
1950 set up described in Sec. 4.3.2. The bicon was moved to 9 positions and the resulting S
1951 parameters were measured at the reference planes shown in Fig. 4.12. They are shown in
1952 Fig. 4.13 after being averaged together.

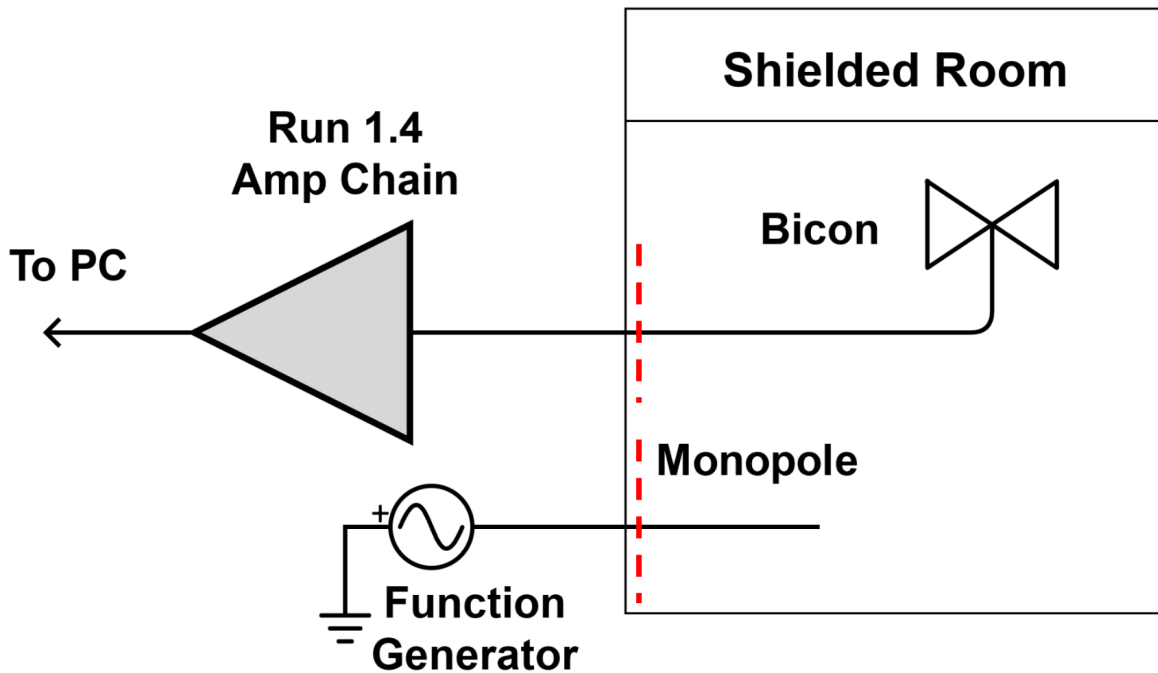


Figure 4.12: Schematic of hardware injection test. Dashed red lines indicate reference planes used to measure S parameters, shown in Fig. 4.13. “Amp Chain” includes amplifiers, attenuators and filters as described in Sec. 2.5.4.

⁵It is important to point out that one needs to test whether or not the system in question actually behaves as predicted by the Dicke equation for the amount of averaging in question. After lots of averaging, one may encounter non-thermal backgrounds which do not scale properly. It is shown in Fig. 4.16 that the dark radio system follows the Dicke radiometer equation at least for 9 days.

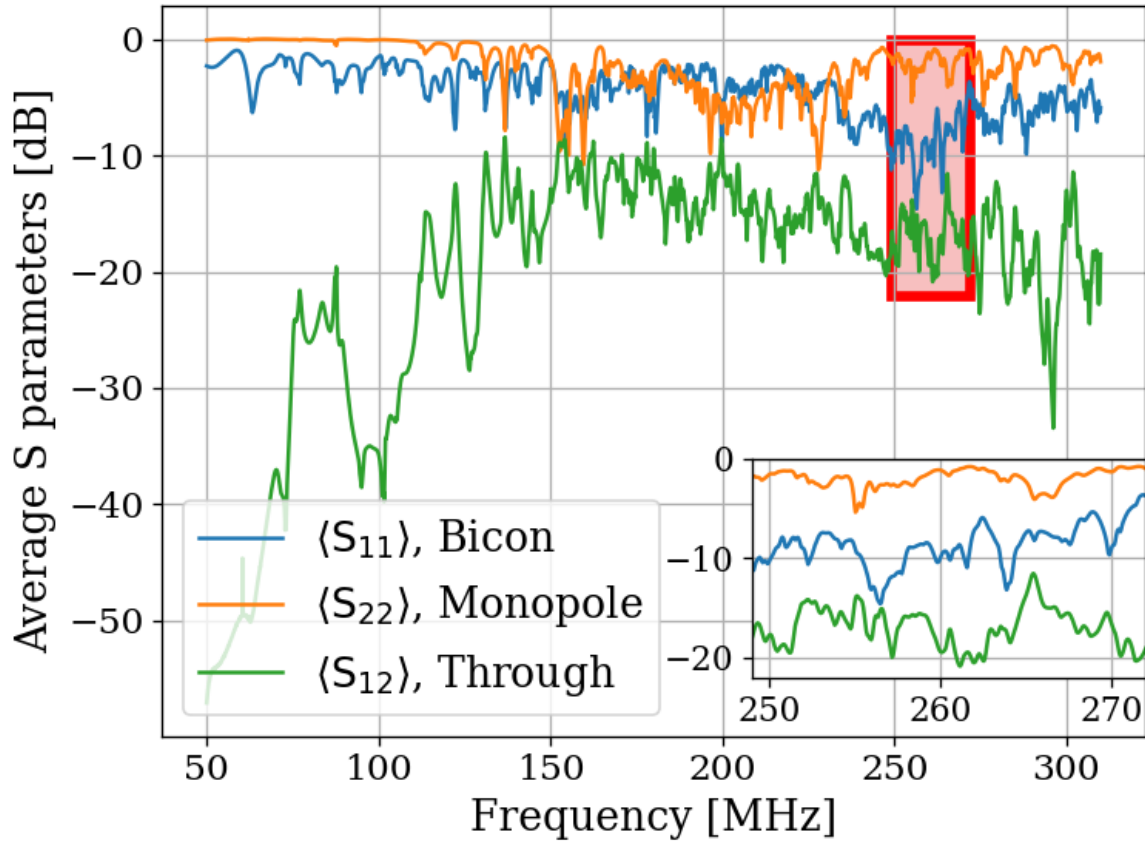


Figure 4.13: Average S parameters of hardware injection test. Taken at 9 positions of the bicon antenna and averaged together (linearly). Ports 1 and 2 are defined to be for the bicon and monopole respectively. Note that $\langle S_{12} \rangle = \langle S_{21} \rangle$ so only $\langle S_{12} \rangle$ is shown. Inset shows zoom on area enclosed by red box.

1953 Knowing the output-referred limit, the system's average $\langle |S_{21}|^2 \rangle$, and the gain G, allows
 1954 for a calculation of the required signal strength (as a function of frequency) which will become
 1955 detectable after a known amount of time. In order to simplify the test, a smaller 1 MHz
 1956 band is chosen between 268 and 269 MHz for the blind injection, where $\langle |S_{21}|^2 \rangle$ is constant
 1957 to about 1dB. At first glance, this seems to be cheating, however there are still approximately
 1958 21,000 frequency bins in this span, so a detection is very unlikely to be random. Furthermore,

1959 the entire 50-300 MHz span is sent to the detection algorithm (Discussed in Sec. 4.2 and
1960 illustrated in Fig. 4.3) which produces an output without knowing about this frequency
1961 restriction.

With all this in mind, the signal power required is simply

$$P_{\text{inject}} = \frac{P_{\text{o}}^{\text{lim}}}{G \langle S_{21} \rangle},$$

1962 where each term is a function of frequency. For the parameters described in this sec-
1963 tion (including the increase in the power limit $\sqrt{9 \text{ days}/1 \text{ hour}} = 14.7$), this works out to
1964 $\approx 6 \times 10^{-19} \text{ W}$ or -152.5 dBm. The Rigol DSG830 signal generator is not calibrated to
1965 such low levels, so this was achieved through attenuation ⁶.

1966 4.4.1.2 Proxy dark photon signal injection

1967 Now that the power for signal injection has been established, the finite-width proxy-signal
1968 ($Q_{\text{DP}} \approx 10^6$) can be generated. This is discussed in Sec. 2.1.2. An intuitive way to accomplish
1969 this would be with an arbitrary waveform generator injecting a time domain signal which is
1970 the Fourier transform of the the expected Rayleigh line shape, Eq. 2.24. This is the method
1971 of the ADMX experiment (see for example [81]). Another option would be to frequency-
1972 modulate a sine wave such that it slowly sweeps out the line shape, spending am amount of
1973 time at each frequency weighted by Eq. 2.24. While intuitive, I was unable to get this to
1974 work. Zhu et al.'s method of frequency hopping [82] is the discretized version of this and
1975 it was very simple to implement. The signal generator is set to change frequencies at some

⁶Experience with this signal generator has shown it exhibits the best performance is when it is set around -30 dBm. Higher than this, large non-harmonic distortions appear contaminating the run. Smaller, and the signal-to-spurious-noise-floor of the generator is poor, also contaminating the run.

1976 interval (discussed below). The frequency which is set is randomly drawn from the PDF of
1977 Eq. 2.24.

1978 There are two considerations that determine the frequency hop period τ_{FH} that the
1979 frequency is changed⁷. First, τ_{FH} should be much longer than the acquisition time of a single
1980 buffer τ_{FFT} ⁸. On the Rigol signal generator, the power is briefly shut off while the frequency
1981 is changed. $\tau_{\text{FFT}} \ll \tau_{\text{FH}}$ ensures that most FFTs of data don't contain a frequency-hop.
1982 Second, τ_{FH} should be small compared to the total time of integration τ , so that there are
1983 many frequencies represented in the entire run. In the limiting case, $\tau_{\text{FH}} = \tau$ will yield an
1984 averaged spectrum containing a single injected frequency; the proxy-signal will be a delta
1985 function in the frequency domain.

1986 Testing has shown that $\tau_{\text{FH}}/\tau_{\text{FFT}} \approx 10$ is more than adequate to address the first consider-
1987 ation. For run 1A (and therefore, this test which shares settings with run 1A), $\tau_{\text{FFT}} = 2^{24}/800$
1988 MHz = 21 ms, so τ_{FH} was set to 250 ms. This means that over 1 hour, the frequency will be
1989 set to $\approx 1.4 \times 10^4$, which addresses the second concern. A histogram of this signal is shown
1990 in Fig. 4.14.

⁷Zhu et al. randomized this period to prevent any unintentional periodic signals entering. I didn't find this to be necessary.

⁸One can likely bypass this restriction by coordinating the signal generator and ADC such that there is some dead time between collection of buffers, in which the frequency is set. Testing has shown that this restriction is adequate to avoid this extra programming step

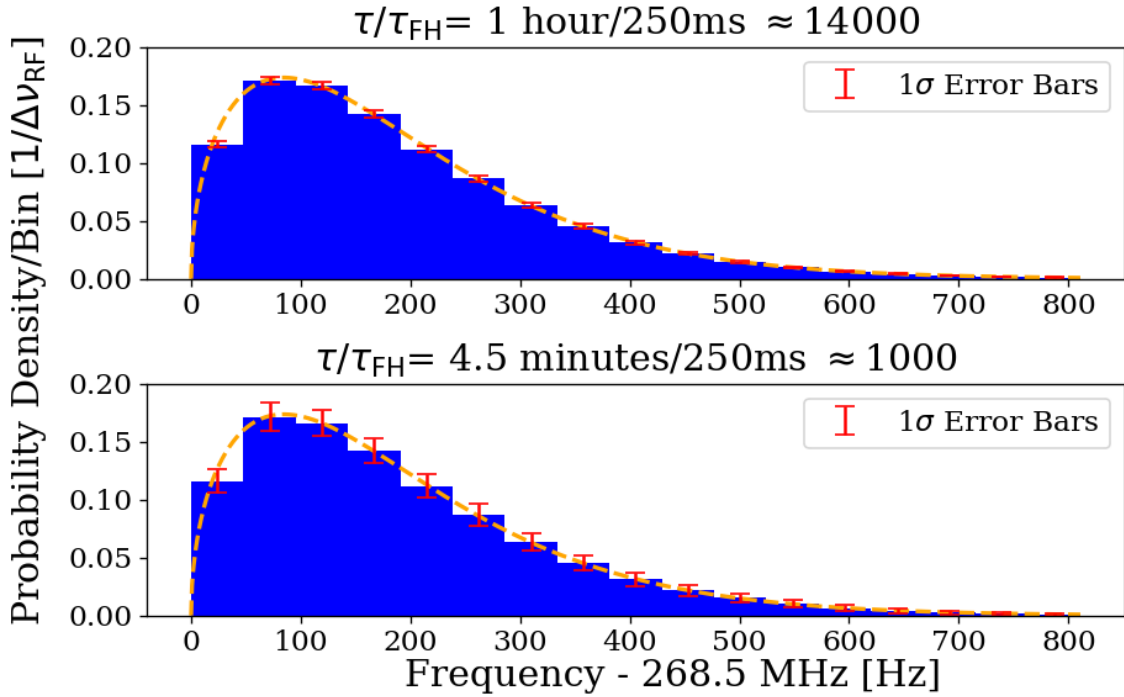


Figure 4.14: Histogram of frequencies used for hardware injection test, with realistic $\Delta\nu_{RF} = 47.7$ Hz. Orange dashed curve is expected line shape from 2.24, and is the PDF frequencies are drawn from. Blue histogram and error bars generated from Monte Carlo simulation and shows the mean value per bin, with 1σ error bars in red. This involves generating 1000 lists of random frequencies (each of length τ/τ_{FH}), binning the data and calculating the standard deviation of each bin. τ is the total acquisition time and τ_{FH} is the amount of time spent on each frequency before “hopping” to the next. Their ratio, τ/τ_{FH} is the number of frequencies which are injected in a given injection test, and was approximately 1.4×10^4 for the one hour test outlined in this section. Two plots give an idea of how error scales with τ/τ_{FH} .

1991 4.4.2 Performing the injection test

1992 Due to the uncertainties involved, more data were taken than the required 1 hour. This also
1993 helped produce the pretty plot in Fig. 4 of Levine et al. [39]. 3.6 hours of data were collected,
1994 and saved in 30 second pre-averages so that progressively more data could be averaged if
1995 the signal was not detected at the predicated time. As mentioned above, the signal injected

1996 was at a relatively high frequency withing the span so that it would be split up into 5 or 6
1997 bins, testing the matched filter's effectiveness. The bicon was moved to 9 positions. Spectra
1998 resulting from 9 antenna positions and 30 seconds of pre-averaging at each position were
1999 averaged together giving 4.5 minute time resolution. Three of these spectra are shown in
2000 Fig. 4.15. The standard deviation of these spectra average down with the square root of time,
2001 closely following the Dicke radiometer equation (discussed in Sec. 2.1.1.3). This scaling is
2002 shown in Fig. 4.16.

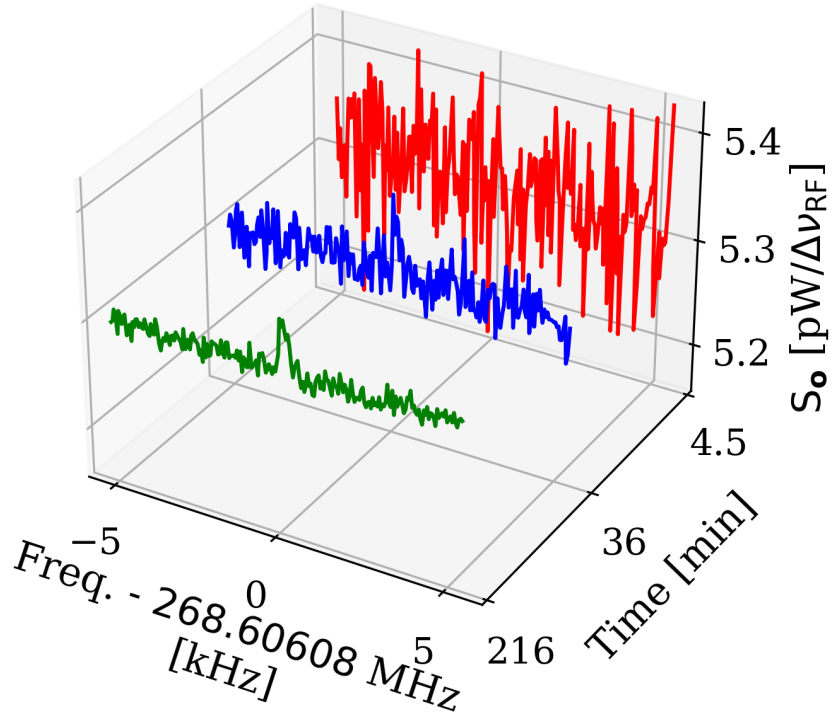


Figure 4.15: Output-referred power spectral density from the hardware injection test illustrating noise averaging down to reveal a persistent, hardware-injected, dark photon proxy signal. Spectra shown are highly zoomed around the injected frequency, 268.60608 MHz. The red, blue and green spectra represent 4.5, 36 and 216 minutes of integration time respectively. The standard deviation of these spectra (excluding the bins containing the injected signal) average down with the square root of time as expected. The blue spectrum shows the amount of averaging required for the signal to be detected by the detection algorithm (including the matched filter) at 5% significance. The tight zoom shown here is less than 1 part in 10^4 of the full 50-300 MHz spectrum analyzed.

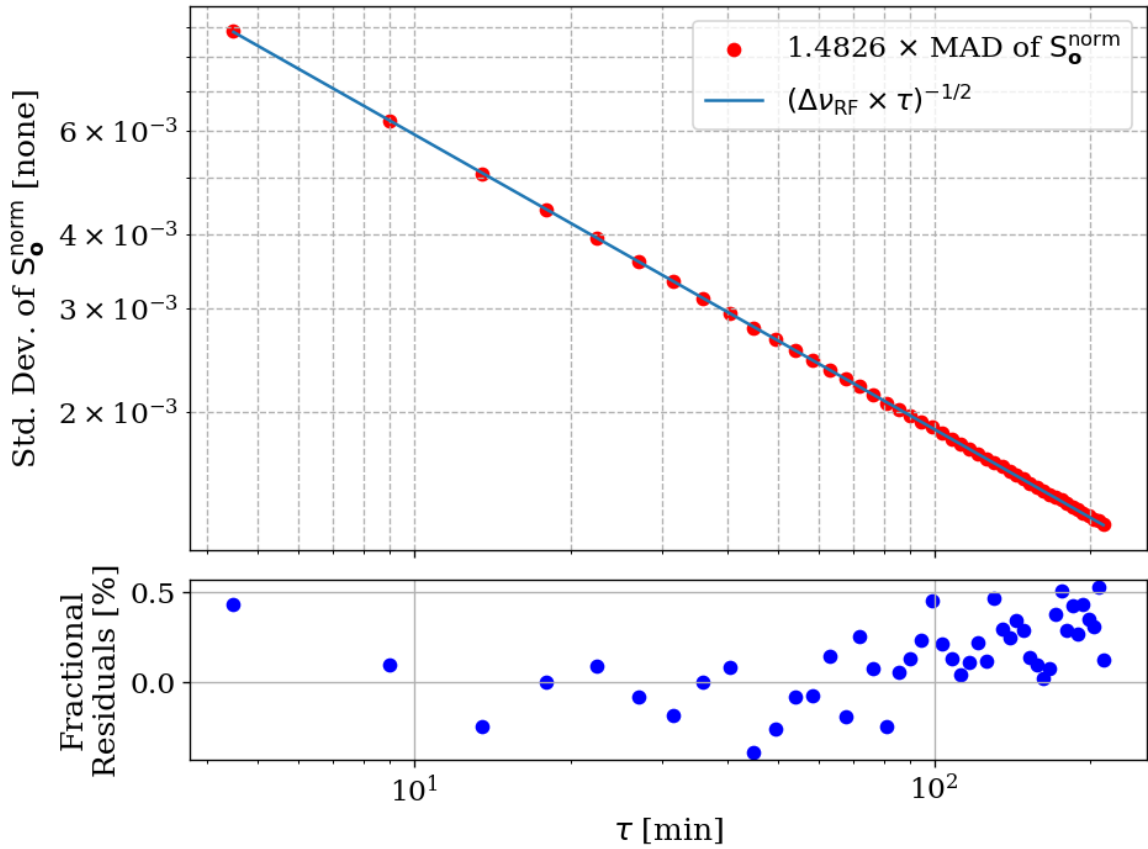


Figure 4.16: Standard deviation of output-referred power spectral density from the hardware injection test, computed with median absolute deviation (MAD). The blue curve represents the predicted standard deviation from the Dicke radiometer equation, Eq. 2.16. Each point corresponds to 9 antenna positions with an additional 4.5 minutes of data averaged (see Sec. 4.4.2). MAD provides a more robust measure of variability, reducing the influence of outliers and offering a better fit than direct standard deviation calculations.

2003 These spectra were generated one at a time and passed through the detection algorithm.
2004 The first spectrum where a signal was detected was at 36 minutes, shown in blue in Fig. 4.15.
2005 Although hardly detectable to the eye, the matched filter detects the signal with 5% signifi-
2006 cance. At the point the signal was detected (i.e. before all data were averaged together), the
2007 injection frequency was confirmed to have been correctly identified, resulting in a success-
2008 ful, blind, hardware injection test. Only after this confirmation were all the date averaged
2009 together to make Fig. 4.15.

2010 **4.4.3 Inspection of Data**

2011 This final subsection simply contains some full page figures which show data from the injec-
2012 tion test. They are all the same 34 minutes of data, but at different stages of processing,
2013 closely following the three main steps of Analysis, Sec. 4.2. They are meant to simulate the
2014 experience of inspecting a 2^{24} point FFT's power spectrum in a matplotlib widget window.
2015 The zoom is seemingly unending, a feature that is difficult to appreciate in a printed docu-
2016 ment. These figures should provide some context for how futile a manual search of unfiltered
2017 data would be. Try and pick out the signal in the top left panel of Fig. 4.17!

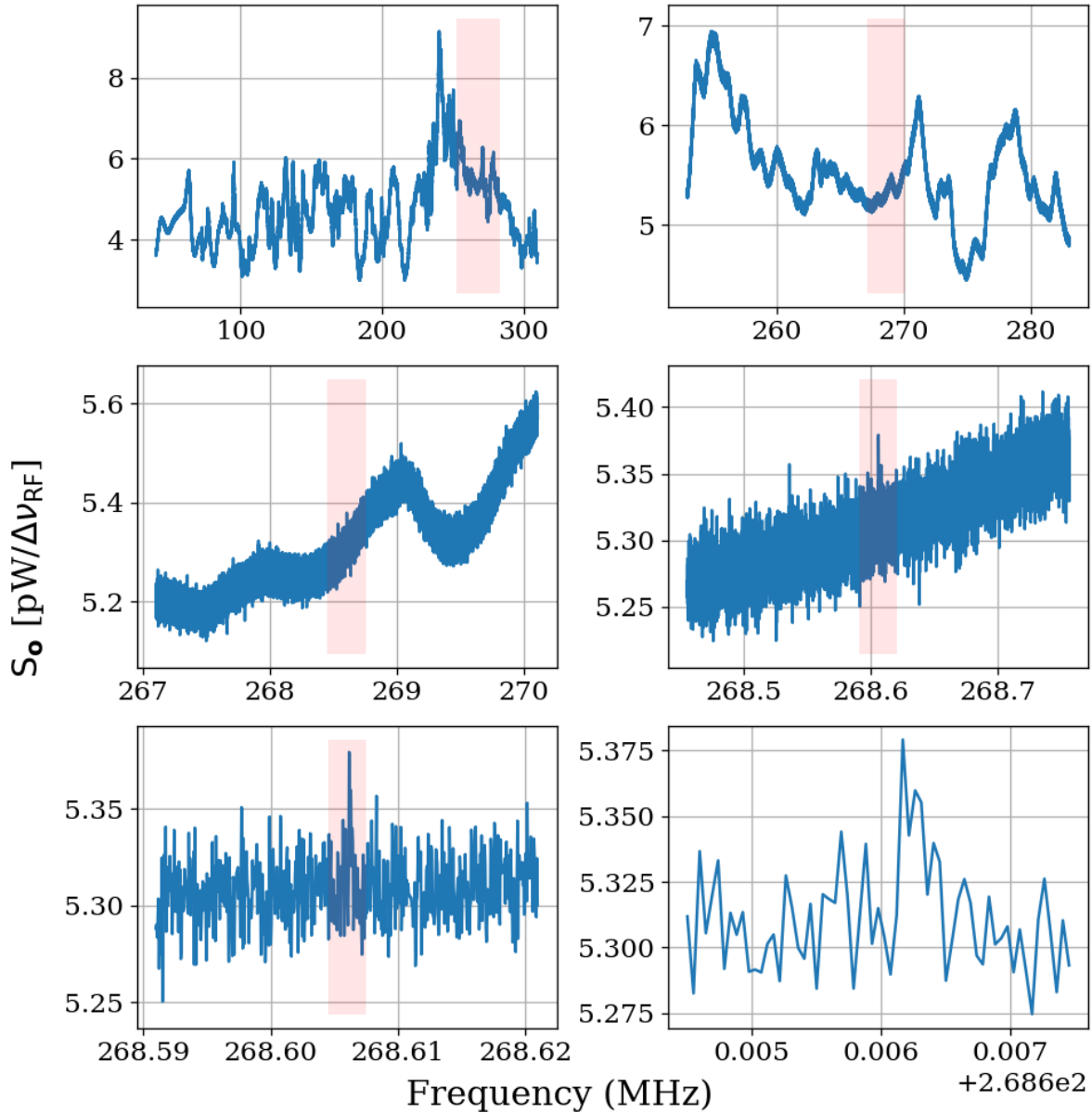


Figure 4.17: Output-referred power spectrum from hardware injection test. Injected signal at 268.60608 MHz. All spectra correspond to a total of 36 minutes of averaging, split evenly between 9 antenna positions. Full 50-300 MHz span contains $\approx 5.2 \times 10^6$ bins. Light pink boxes show zoom level on following plot.

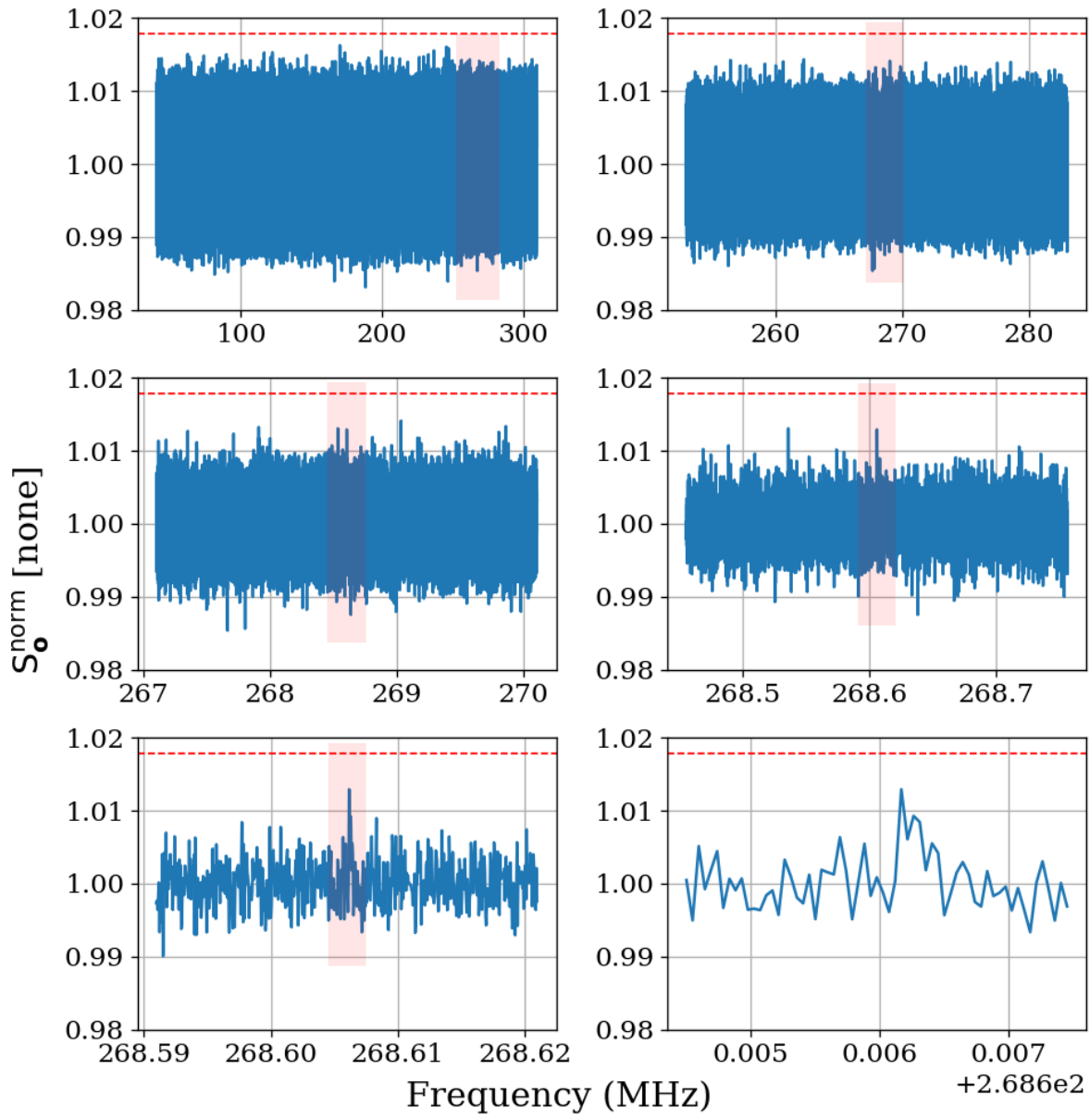


Figure 4.18: Normalized, output-referred power spectrum from hardware injection test. Injected signal at 268.60608MHz. Light pink boxes show zoom level on following plot. Red dashed line indicates the 5% significance threshold, derived in Sec. 2.2.1. Signal is not detectable above threshold.

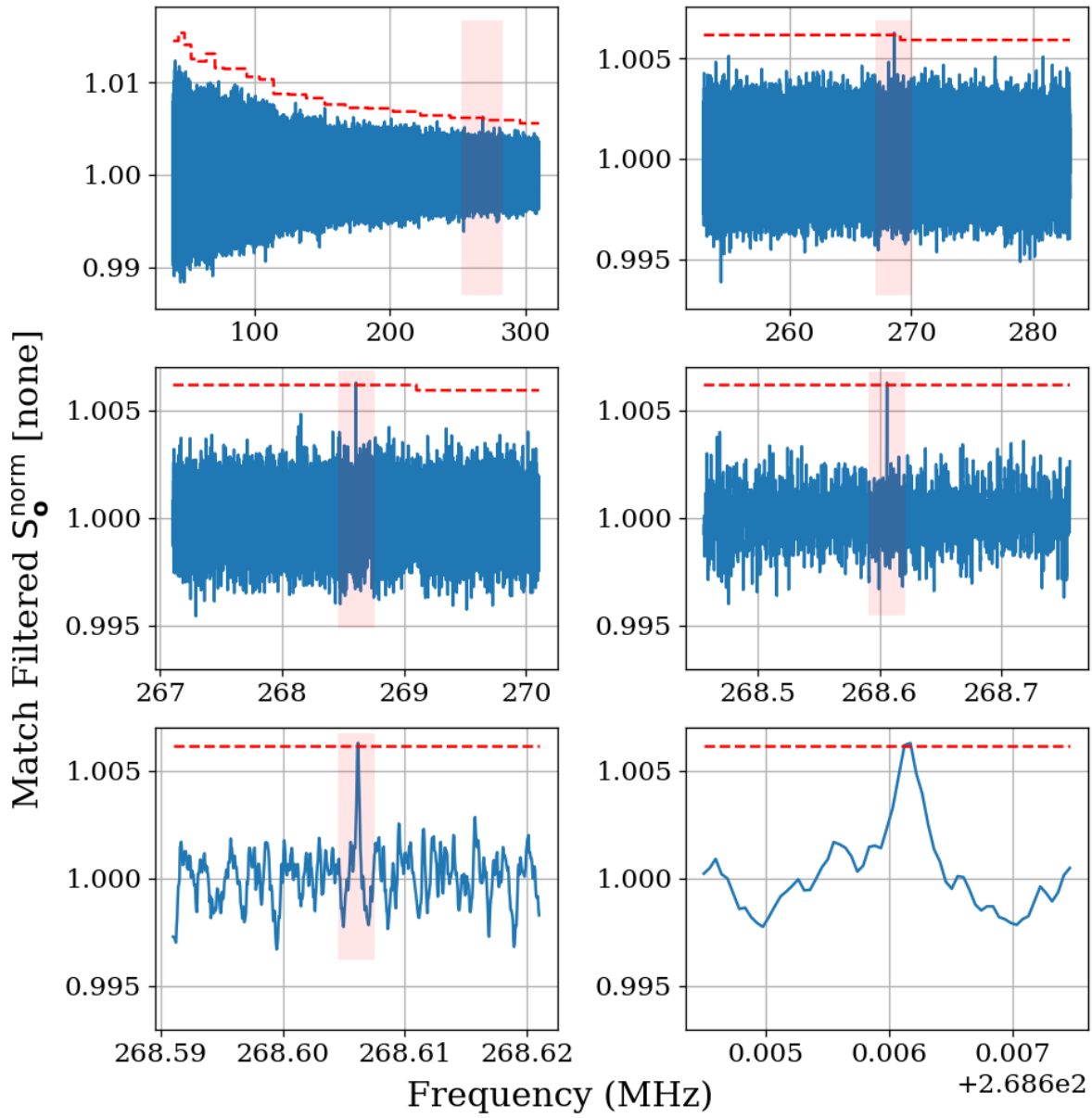


Figure 4.19: Matched filtered, output-referred power spectrum from hardware injection test. Injected signal at 268.60608MHz. Light pink boxes show zoom level on following plot. Red dashed line indicates the 5% significance threshold, derived in Sec. 2.2.1. Introducing the matched filter pushed signal above detectable above threshold compared to Fig. 4.18.

2018 **4.5 Results**⁹

2019 In this section, we report a 95%, frequency-dependent, exclusion limit on the kinetic mixing
2020 strength ϵ of the dark photon (Fig. 4.20). We discuss uncertainties on measured data, identi-
2021 fication of a candidate signal and our process to exclude it. Finally, we display our results in
2022 context by plotting these new limits on top of an aggregation of existing limits in Fig. 4.21.
2023 Future runs of this experiment from 0.3-14 GHz in similar room temperature RF enclosures
2024 and 100 K noise temperature LNAs are indicated (the foundation for such a system is out-
2025 lined in Ch. 5). We have only indicated planned runs, however at microwave frequencies,
2026 highly resonant cryogenic cavities and cryogenic LNAs as well as sub-THz instrumentation
2027 are feasible and could result in an order of magnitude improvement in the limit over the
2028 indicated frequency range and beyond.

2029 **4.5.1 Discussion of uncertainties**

2030 The systematic uncertainty in this experiment comes primarily from three sources, listed in
2031 order of their contribution from greatest to least:

- 2032 1. Fractional uncertainty on the simulated antenna aperture, which is discussed in Sec. 4.3.3,
2033 $\approx 60\%$
- 2034 2. Fractional uncertainty on the first-stage amplifier noise temperature, $\approx 10\%$
- 2035 3. Fractional uncertainty on the gain of the amplifier chain, $\approx 5\%$

⁹Code for this section can be found at: <https://github.com/josephmlev/darkRadio/tree/master/COMPUTELIMIT>

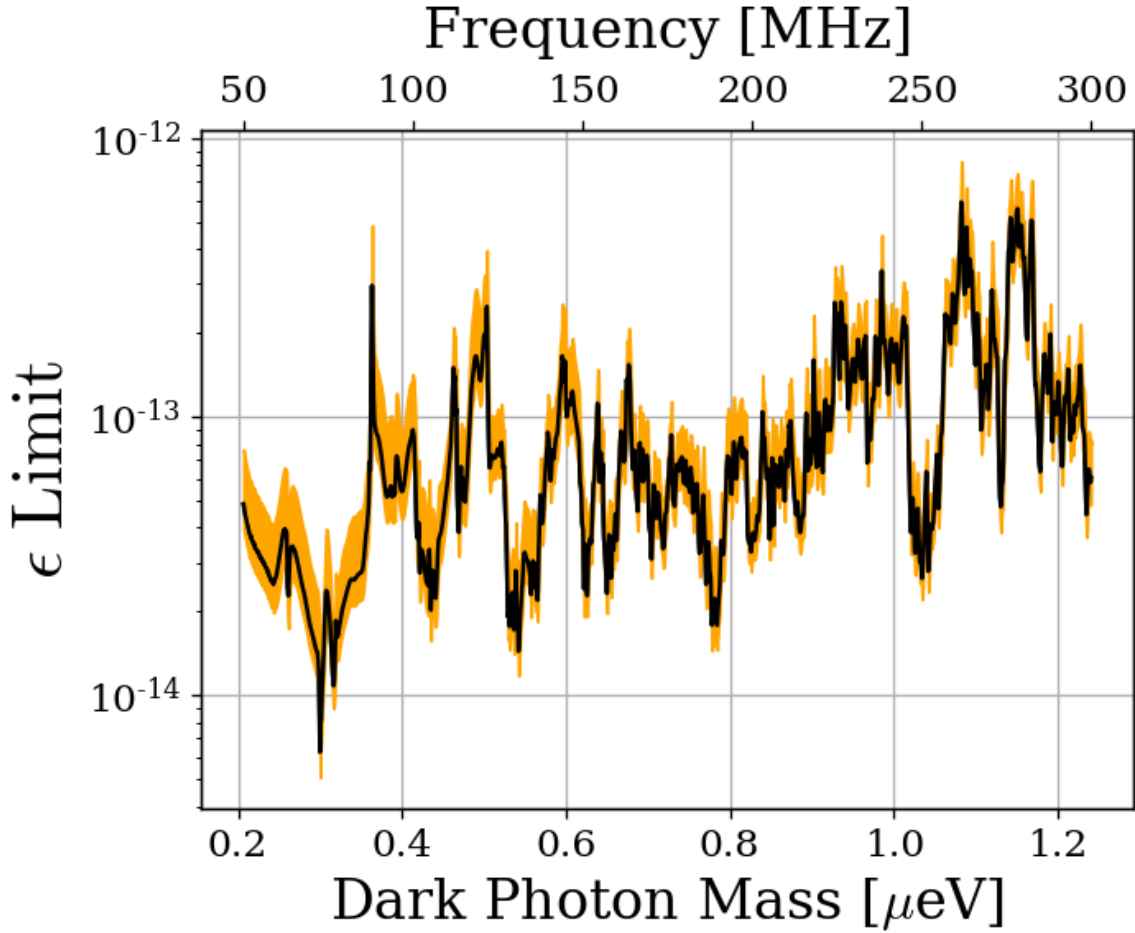


Figure 4.20: 95 % exclusion limit on ϵ with uncertainty shown in orange shaded region. This is based on a local dark matter density of $\rho_{\text{DM}} = 0.45 \text{ GeV/cm}^3$. The error estimate does not take the comparatively small gain and amplifier noise temperature errors into account.

2036 The uncertainty on the simulated antenna aperture is significantly larger than the other

2037 two, and so we neglect them in the uncertainty in the ϵ limit.

2038 We follow the convention of similar experiments where we fix the value of ρ_{DM} and

2039 solve for an ϵ limit given this value. Therefore we treat ρ_{DM} as a known constant with no

2040 uncertainty.

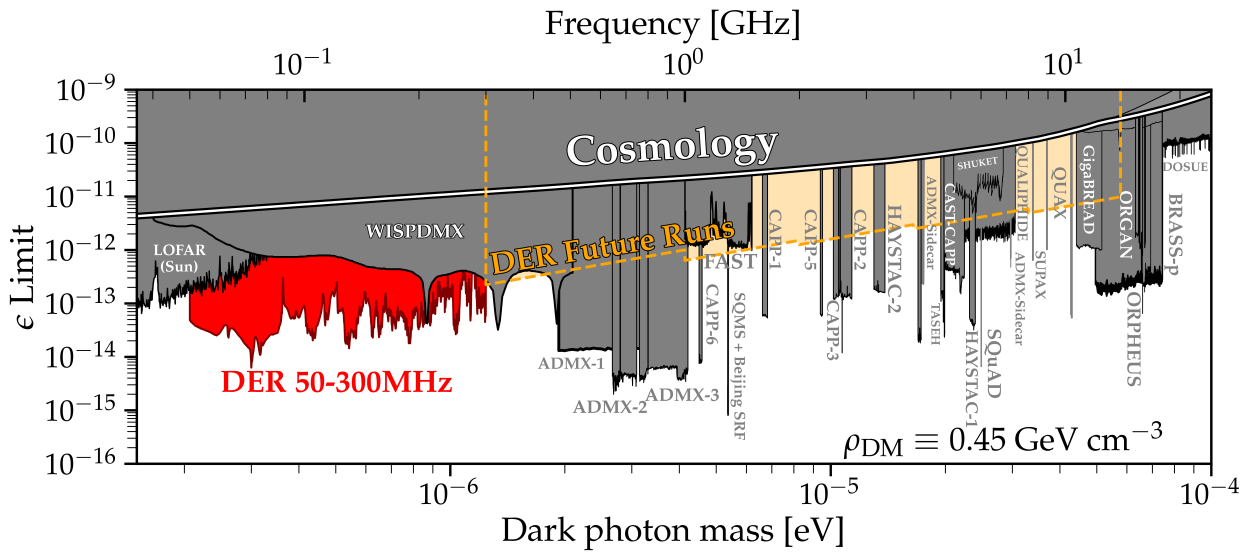


Figure 4.21: Dark photon limits of various experiments circa August 2024, with this work shown in red. The ragged lower bound is due to the complex structure of the resonant modes of the shielded room. Plot adapted by Ben Godfrey from [83] using code found at [84] and includes limit projections of various axion experiments. Astrophysical limits such as CMB interactions with the dark photon are in the region labeled *Cosmology*. Planned wideband extensions of our experiment search from 0.3-14 GHz in similar room temperature RF enclosures are indicated (*yellow*).

₂₀₄₁ Chapter 5

₂₀₄₂ Beyond 300 MHz

To infinity and beyond!

₂₀₄₃

Buzz Lightyear

2044 Where does this experiment go in the future?

2045 **5.1 Preliminary Run 1B results**

2046 **5.2 Mixer System**

2047 **5.3 Cryogenics**

2048 **Appendix A**

2049 **Overview of RTSA code base**

2050 A basic overview of the code which are used to acquire and process data are outlined here.

2051 The version control is very simple and each experiment has it's own directory containing

2052 several key files. The general usage template from which other experiments can be developed

2053 is in the `teledyneTemplate` directory. The important files, in order of importance, are

2054 • `settings.py`: Settings are controlled from this file. If the DAQ code isn't to be
2055 modified, this is all the user must interact with in normal usage. While it is a python
2056 script, it functions more like a text file. Descriptions and notes about allowed values
2057 are included as comments. Read them carefully, settings can conflict.

2058 • `drDaq*.py`: Main script which calls all the helper functions. To take data, run this
2059 script after modifying (and saving) `settings.py`. There is usually a suffix indicating
2060 the date and information about version.

2061 • `avgFftModule.py`: This is modified code from teledyne. It handles all the heavy

lifting: Interfacing with the C++ API, pinning GPU memory, transfer of data from PCIE card to the GPU, computation of the FFT on the GPU. This is all wrapped in a class called `avgFft`. An instance of this class is called `avgSpec` and is the workhorse of `drDaq.py`

- `daqHelpers.py`: Lots of helper functions which are separated here to keep other code clean. It is imported as a module in other files. Lots of useful code lives in here, including the code that converts time series to power spectra (normalization is non-trivial, see Eq. 2.15), writes info to `database.txt`, saves the pre-averaged spectra including metadata in an HDF5 file.
- `plotTesting.py`: This uses `dash` to host a web app which allows interactive `plotly` graphs for simple visualisation of run data. This is extremely useful as it can tell you if amplifiers die. Without this, all data would have to be averaged and more fully analyzed, but this is a good light-weight option. There is some creative use of data down sampling so it runs quickly while not removing any candidates. An example window is shown in Fig. A.1.
- `backup.sh`: Simple shell script which backs up run data to locations of your choosing. In the `teledyneTemplate` directory, it is set up to back up to the secondary hard disk drive in the DR2 machine, and to peloton, but this can be easily modified. When taking real data, this script should not be run at the same time as `drDaq.py`. `backup.sh` should be run first, so it completes while the antenna is moved and batteries changed. This ensures there is not a heavy load on the hard drive due to back ups while data

2083 acquisition is ongoing. `valonInit.py`: sets up the valon signal generator to work as a
2084 clock. This should probably be a function inside of `daqHelpers.py`, but there may have
2085 been a reason I kept it separate.

2086 • `gdrapi.py` Comes from Teledyne. Defines functions for the api. I have not modified
2087 it at all.

2088 • `helperCupy.py` Comes from Teledyne. Defines functions for the GPU. I have not
2089 modified it at all.

2090 • `streamingHelpers.py` comes from Teledyne. Defines functions for streaming from
2091 PCIE card to GPU. I have not modified it at all.

2092 A Tips for using the RTSA system

2093 • As of September 2024, you must boot into kernel version 5.15.

2094 • Make sure to run `insmod.sh` in the `teledyneInstall/gdrcopy` directory after restart-
2095 ing the machine.

2096 – look at `teledyneInstall/installGuide.txt` on how to handle common errors
2097 involving this process.

2098 • Read through the `settings.txt` file carefully! Some settings will conflict with others,
2099 but they are mostly noted. There are also some notes about possible upgrades which
2100 could be made, some of which without much effort.

2101 B Data structure and processing

2102 Figure 2.45 shows the handling of data as it comes in as an RF time series and is converted
2103 to pre-averaged spectra. While significantly less cumbersome than the raw data, processing
2104 these spectra still represents a challenge. This subsection outlines how I have attempted to
2105 handle it. While it is a little convoluted, this is the third iteration of how to handle this
2106 data processing and is likely simpler than it seems on first blush. In other words, there is
2107 probably a better way to do this, but don't knock it til you try it.

2108 B.1 Writing data

2109 Once a pre-averaged spectrum is computed by dividing the running sum by `NOF_BUFFERS_TO_RECEIVE`,
2110 this can be written to an HDF5 file. Whether or not it is, can be controlled by the `SAVE_H5`
2111 boolean variable¹. Each pre-averaged spectrum is uniquely specified by `ACQ_NUM` in a given
2112 data run. In order to simplify backups and avoid placing all our eggs in one HDF5 basket,
2113 `NUM_SPEC_PER_FILE`² pre-averaged spectra are saved into a single HDF5 file, before starting
2114 a new file. These files are simply named as a zero-indexed number followed by their `.hdf5`
2115 extension. These files are saved in `SAVE_DIRECTORY`³. I usually make this save directory in
2116 a secondary SSD named `drBiggerBoy` in order to preserve the main drive. I think the stress

¹This variable exists because when testing things or taking miscellaneous measurements, you will frequently want to acquire a single spectrum without engaging the complex machinery of the HDF5 saving procedure.

²I have kept this around 16 and not experimented much outside of this range, but it's probably fine. This keeps the files around 1 GB. For run 1.4, this is about 45 minutes of antenna data and 3 minutes of terminator data per file, so if a file is corrupted it's not a big deal. I have never had a problem, this is paranoia inherited from Ben.

³A reminder that this is specified, like all other variables, in `settings.py`. Note you must create this directory ahead of time and include a sub-directory called `data`. It says this in the comments of `settings.py` which you are reading, right?

2117 of continuous reads and writes will probably kill this drive, so I prefer to keep it separate
2118 from the main boot drive, drBigBoy.

2119 When `SAVE_H5 == 1`, a `database.txt` file is created in `SAVE_DIRECTORY`, shown in Table
2120 A.1.

Attribute	Pre-averaged spectrum 0	Pre-averaged spectrum 1
ACQ_NUM	0	1
DATETIME	2023-05-10 11:32:48.365	2023-05-10 11:35:49.193
SWITCH POS	0	1
ANT POS IDX	0	0
TEMP	295.64	295.54
LEN FFT LOG2	24	24
SAMPLE RATE MHZ	800.0	800.0
NOF BUFFERS	8600	8600
AMP1	1012_E_PbAcid	1012_E_PbAcid
AMP2	ZKL_9p05VReg	ZKL_9p05VReg
LPF	HSP50+	HSP50+
HPF	288S+	288S+
ATTENUATOR	4dB_FIXED	4dB_FIXED
ADC	ADQ32	ADQ32
CLOCK	SRS_VIA_VALON	SRS_VIA_VALON
File Number	0	0

Table A.1: Example database file from run 1.4. In this run, `ACQ_NUM` counts up to 4175, and these spectra are saved between 261 HDF5 files. Some of the values are auto-generated (`temp`, `DATETIME`, etc.) while others are manually entered into `settings.txt` (`AMP1`, `LPF`, etc.) Note that this table has been transposed in order to fit on the page.

2121 When setting up a data run, you must test that the data are saved how you expect. I have
2122 had success by reducing `NOF_BUFFERS_TO_RECEIVE` to a small number⁴, and taking a simu-
2123 lated data run. The process of switching is hacked together and can give you unpredictable

⁴`NOF_BUFFERS_TO_RECEIVE` times the time per buffer must be larger than around 2 seconds or it will crash

2124 results. Did I mention to read the comments in `settings.py`?

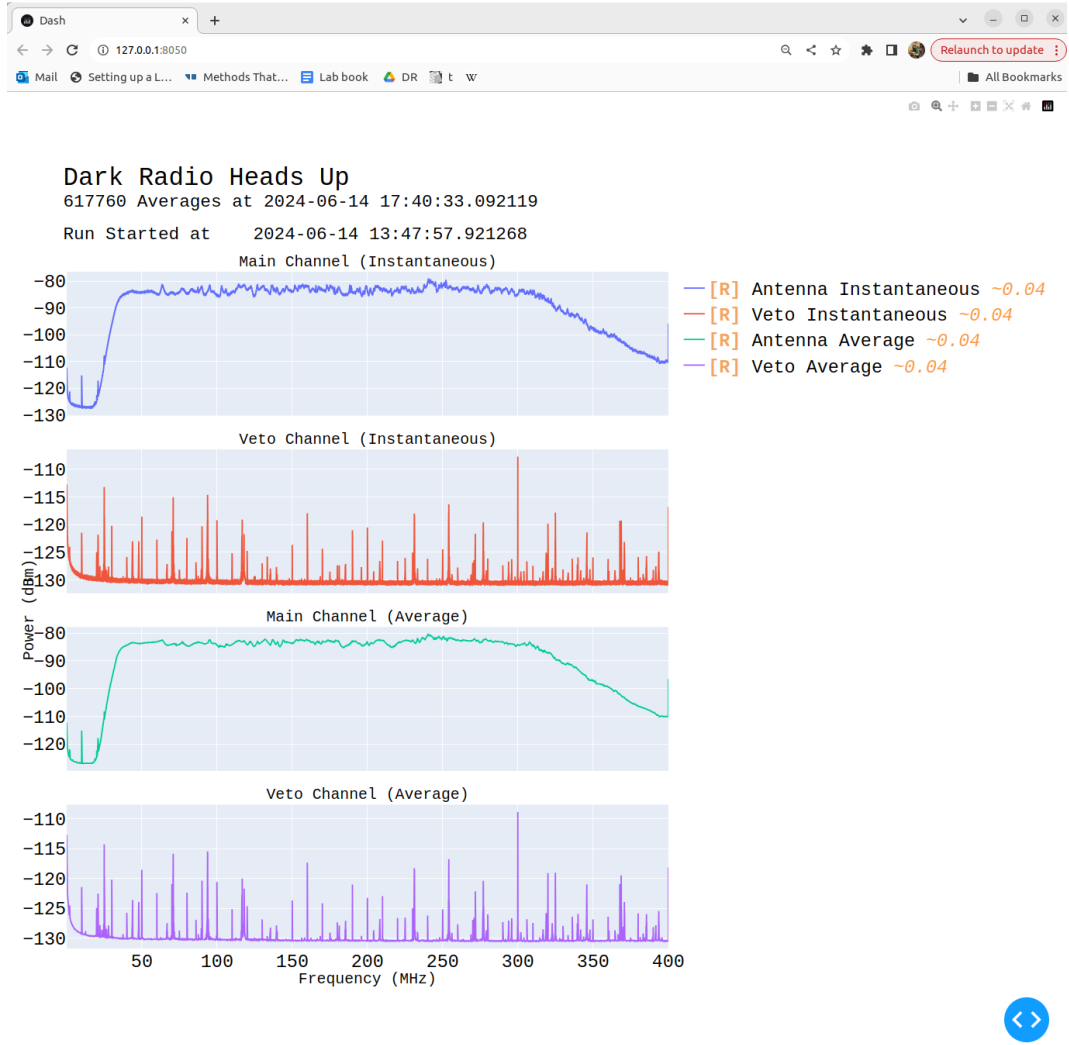


Figure A.1: Real time heads up window for data acquisition. Built with Plotly and Dash, and displays in web browser, in this case Google Chrome. Spectra contain 2^{23} frequency bins, so are down-sampled so as to display 10^4 bins at any given level of zoom. This allows for interaction with the plot in real time with very little lag. The resolution currently displayed (in MHz) is shown in yellow next to the legend (right of first plot). This down-sampling is "smart" in that it will show any excursions, and is implemented with the `plotlyResampler` package in `MinMaxAggregator` mode. Mousing over a curve causes a "Tooltip" to appear, indicating the frequency and power at that point in the curve. The frequency axes are all linked, so zooming on one plot will cause all plots to display the same frequency range. Icons on upper right allow for navigation of plot. Frustratingly there is no back button, so be careful when zooming on a very narrow feature; a wrong move means you have to go all the way back out and start over.

2125 **B.2 Reading and averaging data**⁵

2126 After taking a data run, you should have a `SAVE_DIRECTORY` containing a directory full of
2127 many HDF5 files and a `database.txt` file (and possibly a directory of plotting spectra if
2128 that is chosen in `settings.txt`. The basic idea is to “pre-process” the HDF5 files into a
2129 single, large HDF5 file which can be more quickly accessed to compute a single, averaged
2130 S_o spectrum for further analysis (see next chapter). The `database.txt` file is loaded into
2131 python as a pandas dataframe in order to find specific spectra in this large data structure.

2132 I tried (for a while) to keep the files separate to allow for multi-processing to speed up
2133 the averaging, but I ran into issues. The most serious issue is that all the files live on the
2134 same drive, so you can’t get much of a speed up since the drive is read-limited to around
2135 500 MB/s. I found multiprocessing is more effort than it’s worth. It takes about 20 minutes
2136 to pre-average run 1.4 (9 days of data, 3 minute pre-averages yields 4175 spectra which take
2137 about 280 GB), and you only have to do this once after a run.

2138 Following the example of `run1p4_packAvgAllAnalysis.ipynb`, the first step is to load
2139 `database.txt` as a pandas dataframe which can be used to index the pre-processed file.
2140 Next, a list of which `ACQ_NUMs` correspond to an antenna and terminator must be computed,
2141 after removing any which are known to be contaminated⁶. The list of indices which are
2142 to be averaged together is called either `antIdx` or `termIdx`. Note that you can devise any
2143 number of ways to generate these lists, or even hard code them. The code given is just an

⁵Code for this section can be found at: https://github.com/josephmlev/darkRadio/tree/master/daqAnalysisAndExperiments/run1p4/run1p4_analysis/run1p4_packAvgAllAnalysis.ipynb

⁶In run 1.4, the first antenna and terminator spectra are thrown out, since the computer monitor was on to verify the run started successfully. This was out of paranoia and probably didn’t do anything.

2144 example.

2145 Next, info in the dataframe (no power spectra data yet) are analyzed as a sanity check.

2146 These are not super important but a good check.

2147 The cell beginning with the comment `#pack pre proc dataset` is where the heavy lifting

2148 happens. A large HDF5 file is initialized. It contains two datasets, one for each channel

2149 (main experiment and veto in run 1.4). Note that in this example, it is hard coded to expect

2150 8388609 frequency bins ($2^{23} + 1$), and this must be changed if doing something other than a

2151 2^{24} -point FFT. The HDF5 sub-files are iterated over, their data is read, and written into the

2152 pre-processed HDF5 file. Make sure not to remove the error handling for closing the HDF5

2153 file, or you will corrupt it and have to rerun the pre-processing.

2154 Now that the pre-processed HDF5 file has been packed with data and a list of indices

2155 to be averaged has been generated, averaging is trivial (though still takes a few minutes, so

2156 maybe test it with a sub set of `antIdx`. The code is provided below:

```
2157
21581 def avgSpecFromPacked(avgIdxs, specStr):
21592     sum = np.zeros(2**23+1)
21603     for i in avgIdxs:
21614         sum += f[specStr][:,i]
21625     avgSpec = sum/(len(avgIdxs))
21636     return avgSpec
2164
```

Listing A.1: Python function for averaging spectra from pre-processed data

2165 Note that this assumes a single HDF5 file, `f`, is in scope. `specStr` is a string which

2166 specifies which channel to average, for example `spec_W_chA`.

2167 The output of this function is S_o which can be passed to following functions for further
2168 analysis.

²¹⁶⁹ Bibliography

- 2170 [1] Fritz Zwicky. “The Redshift of Extragalactic Nebulae”. In: (1933).
- 2171 [2] Vera C. Rubin and Jr. Ford W. Kent. “Rotation of the Andromeda Nebula from a
2172 Spectroscopic Survey of Emission Regions”. In: (1970).
- 2173 [3] Marco Battaglieri *et al.* *US Cosmic Visions: New Ideas in Dark Matter 2017: Com-*
2174 *munity Report*. 2017. DOI: 10.48550/ARXIV.1707.04591. URL: <https://arxiv.org/abs/1707.04591>.
- 2175
- 2176 [4] Benjamin Godfrey et al. “Search for dark photon dark matter: Dark E field radio pilot
2177 experiment”. In: *Phys. Rev. D* 104 (1 July 2021), p. 012013. DOI: 10.1103/PhysRevD.
2178 104.012013. URL: <https://link.aps.org/doi/10.1103/PhysRevD.104.012013>.
- 2179 [5] E. E. Barnard and A. C. Ranyard. “Structure of the Milky Way”. In: *Knowledge: An*
2180 *Illustrated Magazine of Science* 17 (Nov. 1894), p. 253.
- 2181 [6] Kelvin, William Thomson, Baron. *Baltimore Lectures on Molecular Dynamics and the*
2182 *Wave Theory of Light*. English. Collection: University of California Libraries. London,
2183 Baltimore: C. J. Clay and sons; Publication agency of the Johns Hopkins University,
2184 1904, pp. xxi, 703. URL: <https://archive.org/details/baltimorelecture00kelvrich>.

- 2185 [7] Richard H. Maurer. “The Idea Man”. In: *SLAC Beam Line* 31.1 (2001). Accessed:
2186 2024-06-23. URL: <https://www.slac.stanford.edu/pubs/beamline/31/1/31-1-maurer.pdf>.
- 2188 [8] Anthony Tyson. “Mapping Dark Matter with Gravitational Lenses”. In: *Physics Today*
2189 45.6 (June 1992), pp. 24–32. ISSN: 0031-9228. DOI: 10.1063/1.881309. eprint: <https://pubs.aip.org/physicstoday/article/45/6/24/407200/Mapping-Dark-Matter-with-Gravitational-LensesMost>. URL: <https://doi.org/10.1063/1.881309>.
- 2193 [9] R. Clausius. “XVI. On a mechanical theorem applicable to heat”. In: *The London, Edinburgh, and Dublin Philosophical Magazine and Journal of Science* 40.265 (1870),
2194 pp. 122–127. DOI: 10.1080/14786447008640370. eprint: <https://doi.org/10.1080/14786447008640370>. URL: <https://doi.org/10.1080/14786447008640370>.
- 2197 [10] Herbert Goldstein, Charles P. Poole, and John L. Safko. *Classical Mechanics*. 3rd. San
2198 Francisco: Addison-Wesley, 2002. ISBN: 9780201657029.
- 2199 [11] A. S. Eddington. “The Kinetic Energy of a Star Clusters”. In: *Monthly Notices of
2200 the Royal Astronomical Society* 76.6 (Apr. 1916), pp. 525–528. ISSN: 0035-8711. DOI:
2201 10.1093/mnras/76.6.525. eprint: <https://academic.oup.com/mnras/article-pdf/76/6/525/18494199/mnras76-0525.pdf>. URL: <https://doi.org/10.1093/mnras/76.6.525>.
- 2204 [12] Gianfranco Bertone and Dan Hooper. “History of dark matter”. In: *Reviews of Modern
2205 Physics* 90.4 (2018), p. 045002.

- 2206 [13] F. D. Kahn and L. Woltjer. “Intergalactic Matter and the Galaxy.” In: *American*
2207 *Journal of Physics* 130 (Nov. 1959), p. 705. DOI: 10.1086/146762.
- 2208 [14] Hugo van Woerden and Richard G. Strom. “The beginnings of radio astronomy in
2209 the Netherlands”. In: *Journal of Astronomical History and Heritage* 9.1 (June 2006),
2210 pp. 3–20.
- 2211 [15] J.I. Read. “The Local Dark Matter Density”. In: *J. Phys.* G41 (2014), p. 063101. URL:
2212 <https://arxiv.org/abs/1404.1938>.
- 2213 [16] S Sivertsson et al. “Estimating the local dark matter density in a non-axisymmetric
2214 wobbling disc”. In: *Monthly Notices of the Royal Astronomical Society* 511.2 (Apr.
2215 2022), pp. 1977–1991. ISSN: 0035-8711. DOI: 10.1093/mnras/stac094.
- 2216 [17] Sung Hak Lim et al. *Mapping Dark Matter in the Milky Way using Normalizing Flows*
2217 and *Gaia DR3*. 2023. arXiv: 2305.13358 [astro-ph.GA]. URL: <https://arxiv.org/>
2218 [abs/2305.13358](https://arxiv.org/abs/2305.13358).
- 2219 [18] Virginia Trimble. “History of Dark Matter in Galaxies”. In: *Planets, Stars and Stel-*
2220 *lar Systems: Volume 5: Galactic Structure*. Ed. by Gerard Gilmore. New York, NY:
2221 Springer, 2013, pp. 1093–1116.
- 2222 [19] V. Radeka. “Signal, Noise and Resolution in Position-Sensitive Detectors”. In: *IEEE*
2223 *Transactions on Nuclear Science* 21.1 (1974), pp. 51–64. DOI: 10.1109/TNS.1974.
2224 4327444.

- 2225 [20] B. M. Brubaker et al. “HAYSTAC axion search analysis procedure”. In: *Physical Re-*
2226 *view D* 96.12 (Dec. 2017). DOI: 10.1103/physrevd.96.123008. URL: <https://doi.org/10.1103%2Fphysrevd.96.123008>.
- 2227
- 2228 [21] C. Boutan et al. *Axion Dark Matter eXperiment: Run 1A Analysis Details*. 2023. arXiv:
2229 2312.16668.
- 2230 [22] Maximiliano Silva-Feaver et al. “Design Overview of DM Radio Pathfinder Experi-
2231 *ment*”. In: *IEEE Transactions on Applied Superconductivity* 27.4, 2631425 (June 2017),
2232 p. 2631425. DOI: 10.1109/TASC.2016.2631425.
- 2233 [23] David Hill. “Plane Wave Integral Representation for Fields in Reverberation Cham-
2234 bers”. en. In: 40 (1998-08-01 00:08:00 1998).
- 2235 [24] W. L. Stutzman and G. A. Thiele. *Antenna Theory and Design*. John Wiley Sons,
2236 1998.
- 2237 [25] J.D. Kraus. *Antennas*. McGraw-Hill, 1950. ISBN: 07-035410-3.
- 2238 [26] H. Nyquist. “Thermal Agitation of Electric Charge in Conductors”. In: *Phys. Rev.* 32
2239 (1 July 1928), pp. 110–113. DOI: 10.1103/PhysRev.32.110. URL: <https://link.aps.org/doi/10.1103/PhysRev.32.110>.
- 2240
- 2241 [27] J. B. Johnson. “Thermal Agitation of Electricity in Conductors”. In: *Phys. Rev.* 32 (1
2242 July 1928), pp. 97–109. DOI: 10.1103/PhysRev.32.97. URL: <https://link.aps.org/doi/10.1103/PhysRev.32.97>.
- 2243

- 2244 [28] Robert H Dicke. “The measurement of thermal radiation at microwave frequencies”.
2245 In: *Review of Scientific Instruments* 17.7 (1946), pp. 268–275.
- 2246 [29] Albert Einstein. “Über die von der molekularkinetischen Theorie der Wärme geforderte
2247 Bewegung von in ruhenden Flüssigkeiten suspendierten Teilchen”. In: *Annalen der
2248 Physik* 322.8 (1905), pp. 549–560.
- 2249 [30] Herbert B. Callen and Theodore A. Welton. “Irreversibility and Generalized Noise”.
2250 In: *Phys. Rev.* 83 (1 July 1951), pp. 34–40. DOI: 10.1103/PhysRev.83.34. URL:
2251 <https://link.aps.org/doi/10.1103/PhysRev.83.34>.
- 2252 [31] C. L. Mehta. “Coherence-time and effective bandwidth of blackbody radiation”. In:
2253 *Il Nuovo Cimento (1955-1965)* 28.2 (1963), pp. 401–408. DOI: 10.1007/BF02828589.
2254 URL: <https://doi.org/10.1007/BF02828589>.
- 2255 [32] Raphael Cervantes et al. *Deepest Sensitivity to Wavelike Dark Photon Dark Matter
2256 with SRF Cavities*. 2022. arXiv: 2208.03183 [hep-ex].
- 2257 [33] Alexander V. Gramolin et al. “Spectral signatures of axionlike dark matter”. In: *Physi-
2258 cal Review D* 105.3 (Feb. 2022). ISSN: 2470-0029. DOI: 10.1103/physrevd.105.035029.
2259 URL: <http://dx.doi.org/10.1103/PhysRevD.105.035029>.
- 2260 [34] Michael S. Turner. “Periodic signatures for the detection of cosmic axions”. In: *Phys.
2261 Rev. D* 42 (10 Nov. 1990), pp. 3572–3575. DOI: 10.1103/PhysRevD.42.3572. URL:
2262 <https://link.aps.org/doi/10.1103/PhysRevD.42.3572>.
- 2263 [35] Greg Durgin. *Lecture on Noise Figure*. Accessed: 2024-06-23. 2017. URL: https://www.youtube.com/watch?v=M_SRUF4TQgA.

- 2265 [36] Pasternack Enterprises. *PE15A1012: 1 Watt Amplifier Operating From 0.01 GHz to*
2266 *6 GHz*. Accessed: 2024-05-17. 2024. URL: <https://www.pasternack.com/images/ProductPDF/PE15A1012.pdf>.
- 2268 [37] SP Devices. *ADQ32 Datasheet*. Accessed: 2024-06-23. 2024. URL: https://www.spdevices.com/en-us/Products_/Documents/ADQ32/20-2378%20ADQ32%20datasheet.pdf.
- 2271 [38] Benjamin Godfrey. “A Novel Search for Dark Photons”. Ph.D. dissertation. UC Davis,
2272 2022. URL: <https://escholarship.org/uc/item/72b776v4>.
- 2273 [39] Joseph Levine et al. *New Limit on Dark Photon Kinetic Mixing in the 0.2-1.2 μeV Mass Range From the Dark E-Field Radio Experiment*. 2024. arXiv: 2405.20444
2274 [hep-ex]. URL: <https://arxiv.org/abs/2405.20444>.
- 2276 [40] L.A. Wainstein and V.D. Zubakov. *Extraction of Signals from Noise*. Englewood Cliffs,
2277 NJ: Prentice-Hall, 1962. ISBN: 9780132981330.
- 2278 [41] Andy Marvin and Simon Jonathan Bale. “Thermal Noise Measurements in a Rever-
2279 beration Chamber”. English. In: *IEEE Transactions on Electromagnetic Compatibility*
2280 64.3 (June 2022). © 2022 IEEE. This is an author-produced version of the published
2281 paper. Uploaded in accordance with the publisher’s self-archiving policy. Further copy-
2282 ing may not be permitted; contact the publisher for details, pp. 893–896. ISSN: 0018-
2283 9375. DOI: [10.1109/TEMC.2022.3142937](https://doi.org/10.1109/TEMC.2022.3142937).
- 2284 [42] F. Reif. *Fundamentals of Statistical and Thermal Physics*. Long Grove, IL: Waveland
2285 Press, 2009. ISBN: 9781577666127.

- 2286 [43] NoiseWave. *NoiseWave FAQ Document*. Accessed: 2024-06-23. 2024. URL: <https://noisewave.com/faq.pdf>.
- 2287
- 2288 [44] Whitham D. Reeve. *Noise Tutorial Part III: Attenuator and Amplifier Noise*. Revision
2289 0.1, Updated: July 7, 2014. Reeve Engineers. 2014. URL: https://www.reeve.com/Documents/Noise/Reeve_Noise_3_AttenAmpNoise.pdf.
- 2290
- 2291 [45] S. Al Kenany et al. “Design and operational experience of a microwave cavity axion
2292 detector for the 20-100 μeV range”. In: *Nuclear Instruments and Methods in Physics*
2293 *Research Section A: Accelerators, Spectrometers, Detectors and Associated Equipment*
2294 854 (May 2017), pp. 11–24. ISSN: 0168-9002. DOI: [10.1016/j.nima.2017.02.012](https://doi.org/10.1016/j.nima.2017.02.012).
2295 URL: <http://dx.doi.org/10.1016/j.nima.2017.02.012>.
- 2296 [46] Raphael Cervantes et al. *Deepest Sensitivity to Wavelike Dark Photon Dark Matter
2297 with SRF Cavities*. 2022. arXiv: 2208.03183 [hep-ex].
- 2298 [47] David A. Hill. “Wall Losses and Cavity Q”. In: *Electromagnetic fields in cavities:
2299 Deterministic and statistical theories*. John Wiley & Sons Inc., 2009, pp. 31–33.
- 2300 [48] R.H. Price, H.T. Davis, and E.P. Wenaas. “Determination of the statistical distribution
2301 of electromagnetic-field amplitudes in complex cavities”. In: *Physical Review E* 48
2302 (1993), pp. 4716–4729. DOI: [10.1103/PhysRevE.48.4716](https://doi.org/10.1103/PhysRevE.48.4716).
- 2303 [49] John David Jackson. *Classical Electrodynamics*. 3rd. New York: Wiley, 1998. ISBN:
2304 9780471309321.
- 2305 [50] Bing-Hope Liu, David C. Chang, and Mark T. Ma. *Eigenmodes and the Composite Q
2306 Factor of a Reverberating Chamber*. Tech. rep. Aug. 1983.

- 2307 [51] *Series 83 RF Shielded Enclosure*. Lindgren R.F. Enclosures, Inc. 2021. URL: <https://www.ets-lindgren.com/datasheet/shielding/rf-shielding-and-accessories/11003/1100307>.
- 2310 [52] David A. Hill. *Electromagnetic Theory of Reverberation Chambers*. Technical Note
2311 1506. Gaithersburg, MD: National Institute of Standards and Technology, 1998. URL:
2312 https://tsapps.nist.gov/publication/get_pdf.cfm?pub_id=24427.
- 2313 [53] D.A. Hill. “A reflection coefficient derivation for the Q of a reverberation chamber”. In:
2314 *IEEE Transactions on Electromagnetic Compatibility* 38.4 (1996), pp. 591–592. DOI:
2315 [10.1109/15.544314](https://doi.org/10.1109/15.544314).
- 2316 [54] Lawrence Krauss et al. “Calculations for cosmic axion detection”. In: *Physical Review
2317 Letters* 55.17 (1985), pp. 1797–1800. DOI: [10.1103/PhysRevLett.55.1797](https://doi.org/10.1103/PhysRevLett.55.1797). URL:
2318 <https://doi.org/10.1103/PhysRevLett.55.1797>.
- 2319 [55] *Biconical Antenna AB-900A*. Rev. D05.19. Com-Power Corporation. May 2019. URL:
2320 <https://documentation.com-power.com/pdf/AB-900A-1.pdf>.
- 2321 [56] *COMSOL Multiphysics*. 5.4. Available at <https://www.comsol.com/>. COMSOL, Inc.
2322 One First Street, Suite 4 Los Altos, CA 94022.
- 2323 [57] Zhong Chen and Michael D. Foegelle. “A numeric investigation of ground plane effects
2324 on biconical antenna factor”. In: *Electromagnetic Compatibility, 1998. 1998 IEEE In-
2325 ternational Symposium on*. Vol. 2. IEEE. IEEE, 1998, pp. 802–806. DOI: [10.1109/ISEMC.1998.750302](https://doi.org/10.1109/ISEMC.1998.750302). URL: <https://ieeexplore.ieee.org/document/750302>.
- 2327 [58] John D. Kraus. *Antennas*. 2nd. New York: McGraw-Hill, 1988, p. 892. ISBN: 9780070354227.

- 2328 [59] Mini-Circuits. *ZKL-1R5: 50 Ω Gain Block Amplifier*. Accessed: 2024-06-23. 2024. URL:
2329 <https://www.minicircuits.com/pdfs/ZKL-1R5.pdf>.
- 2330 [60] Texas Instruments. *LM317: 3-Terminal Adjustable Regulator*. Accessed: 2024-06-23.
2331 2024. URL: <https://www.ti.com/lit/ds/symlink/lm317.pdf?ts=1720749307506>.
- 2332 [61] Alan V. Oppenheim, Alan S. Willsky, and S. Hamid Nawab. *Signals and Systems*. 2nd.
2333 Upper Saddle River, NJ: Prentice Hall, 1996. ISBN: 978-0138147570.
- 2334 [62] Mini-Circuits. *ZX75LP-288-S+: Low Pass Filter*. Accessed: 2024-06-23. 2024. URL:
2335 <https://www.minicircuits.com/pdfs/ZX75LP-288-S+.pdf>.
- 2336 [63] Mini-Circuits. *SHP-50+: High Pass Filter*. Accessed: 2024-06-23. 2024. URL: <https://www.minicircuits.com/pdfs/SHP-50+.pdf>.
- 2338 [64] *Biconical Antenna*. AB-900A. Rev. D. Com-Power Corporation. May 2019.
- 2339 [65] *The Y Factor Technique For Noise Figure Measurements*. 1MA178. Version 5e. Rhode
2340 & Schwarz. Oct. 2021.
- 2341 [66] *Noise Figure Measurement Accuracy: The Y-Factor Method*. 1MA178. Version 5e.
2342 Keysight Technologies. Oct. 2021.
- 2343 [67] Wikipedia contributors. *Y-factor Sketch*. Accessed: 2024-06-23. 2024. URL: https://en.wikipedia.org/wiki/Y-factor#/media/File:Y-factor_sketch.jpg.
- 2345 [68] Rigol Technologies. *RSA5000 Series: Real-Time Spectrum Analyzer Datasheet*. Ac-
2346 cessed: 2024-06-23. 2024. URL: https://beyondmeasure.rigoltech.com/acton/attachment/1579/f-0816/1/-/-/-/RSA5_datasheet.pdf.

- 2348 [69] “IEEE Standard Method for Measuring the Effectiveness of Electromagnetic Shielding
2349 Enclosures”. In: *IEEE Std 299-1997* (1998), pp. 1–48. DOI: 10.1109/IEEESTD.1998.
2350 88115.
- 2351 [70] David W. Allan. “Statistics of atomic frequency standards”. In: *Proceedings of the
2352 IEEE* 54.2 (1966), pp. 221–230.
- 2353 [71] Keysight Technologies. *Analyzing Frequency Stability in the Frequency and Time Do-
2354 mains*. Tech. rep. 5991-4797EN, August 11, 2014. USA: Keysight Technologies, 2014.
- 2355 [72] Stanford Research Systems. *FS725 Rubidium Frequency Standard Manual*. Accessed:
2356 2024-06-23. 2024. URL: <https://www.thinksrs.com/downloads/PDFs/Manuals/FS725m.pdf>.
- 2358 [73] R. H. Dicke. “The Measurement of Thermal Radiation at Microwave Frequencies”.
2359 In: *Rev. Sci. Instrum.* 17 (1946), p. 268. DOI: 10.1063/1.1770483. URL: <https://aip.scitation.org/doi/10.1063/1.1770483>.
- 2361 [74] S. Al Kenany et al. “Design and operational experience of a microwave cavity axion de-
2362 tector for the 20-100 micro-eV Range”. In: *Nuclear Instruments and Methods in Physics
2363 Research Section A: Accelerators, Spectrometers, Detectors and Associated Equipment*
2364 854 (May 2017), pp. 11–24. ISSN: 0168-9002. DOI: 10.1016/j.nima.2017.02.012.
2365 URL: <http://dx.doi.org/10.1016/j.nima.2017.02.012>.
- 2366 [75] G. Turin. “An introduction to matched filters”. In: *IRE Transactions on Information
2367 Theory* 6.3 (1960), pp. 311–329. DOI: 10.1109/TIT.1960.1057571.

- 2368 [76] Robert N McDonough and Anthony D Whalen. *Detection of signals in noise*. Academic
2369 Press, 1995.
- 2370 [77] S. Asztalos et al. “Large-scale microwave cavity search for dark-matter axions”. In:
2371 *Phys. Rev. D* 64 (9 Oct. 2001), p. 092003. DOI: 10.1103/PhysRevD.64.092003. URL:
2372 <https://link.aps.org/doi/10.1103/PhysRevD.64.092003>.
- 2373 [78] G. Orjubin et al. “Statistical model of an undermoded reverberation chamber”. In:
2374 *IEEE Transactions on Electromagnetic Compatibility* 48.1 (2006), pp. 248–251. DOI:
2375 10.1109/TEMC.2006.870705.
- 2376 [79] Charles F. Bunting. *Statistical Characterization and Simulation of a Reverberation
2377 Chamber Using Finite-Element Techniques*. Tech. rep. 20060022547. NASA Technical
2378 Reports Server (NTRS), 2006. URL: <https://ntrs.nasa.gov/citations/20060022547>.
- 2380 [80] Philippe Besnier, Christophe Lemoine, and Jerome Sol. “Various estimations of com-
2381 posite Q-factor with antennas in a reverberation chamber”. In: *2015 IEEE Interna-*
2382 *tional Symposium on Electromagnetic Compatibility (EMC)*. 2015, pp. 1223–1227. DOI:
2383 10.1109/ISEMC.2015.7256344.
- 2384 [81] R. Khatiwada et al. “Axion Dark Matter Experiment: Detailed design and operations”.
2385 In: *Review of Scientific Instruments* 92.12 (Dec. 2021), p. 124502. ISSN: 0034-6748.
2386 DOI: 10.1063/5.0037857. eprint: https://pubs.aip.org/aip/rsi/article-pdf/doi/10.1063/5.0037857/16136265/124502\1_online.pdf. URL: <https://doi.org/10.1063/5.0037857>.

- 2389 [82] Yuqi Zhu et al. “An improved synthetic signal injection routine for the Haloscope
2390 At Yale Sensitive To Axion Cold dark matter (HAYSTAC)”. In: *Review of Scientific*
2391 *Instruments* 94.5 (May 2023). ISSN: 1089-7623. DOI: 10.1063/5.0137870. URL: <http://dx.doi.org/10.1063/5.0137870>.
- 2392
- 2393 [83] Andrea Caputo et al. “Dark photon limits: A handbook”. In: *Phys. Rev. D* 104 (9
2394 Nov. 2021), p. 095029. DOI: 10.1103/PhysRevD.104.095029. URL: <https://link.aps.org/doi/10.1103/PhysRevD.104.095029>.
- 2395
- 2396 [84] Ciaran O’Hare. *cajohare/AxionLimits: AxionLimits*. <https://cajohare.github.io/AxionLimits/>. Version v1.0. July 2020. DOI: 10.5281/zenodo.3932430.
- 2397